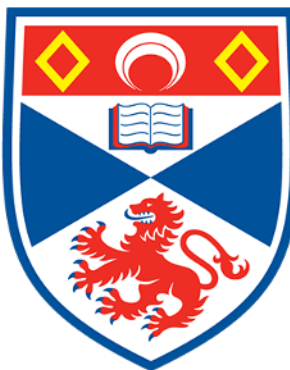


# Partial differential equation modelling in cancer and development

Chiara Villa



University of  
St Andrews

This thesis is submitted in partial fulfilment for the degree of  
Doctor of Philosophy (PhD)  
at the University of St Andrews

December 2021

# Declarations

## Candidate's declaration

I, Chiara Villa, do hereby certify that this thesis, submitted for the degree of PhD, which is approximately 55,000 words in length, has been written by me, and that it is the record of work carried out by me, or principally by myself in collaboration with others as acknowledged, and that it has not been submitted in any previous application for any degree. I confirm that any appendices included in my thesis contain only material permitted by the 'Assessment of Postgraduate Research Students' policy.

I was admitted as a research student at the University of St Andrews in September 2018.

I received funding from an organisation or institution and have acknowledged the funder(s) in the full text of my thesis.

## **Supervisor's declaration**

I hereby certify that the candidate has fulfilled the conditions of the Resolution and Regulations appropriate for the degree of PhD in the University of St Andrews and that the candidate is qualified to submit this thesis in application for that degree. I confirm that any appendices included in the thesis contain only material permitted by the ‘Assessment of Postgraduate Research Students’ policy.

## Permission for publication

In submitting this thesis to the University of St Andrews we understand that we are giving permission for it to be made available for use in accordance with the regulations of the University Library for the time being in force, subject to any copyright vested in the work not being affected thereby. We also understand, unless exempt by an award of an embargo as requested below, that the title and the abstract will be published, and that a copy of the work may be made and supplied to any bona fide library or research worker, that this thesis will be electronically accessible for personal or research use and that the library has the right to migrate this thesis into new electronic forms as required to ensure continued access to the thesis.

I, Chiara Villa, have obtained, or am in the process of obtaining, third-party copyright permissions that are required or have requested the appropriate embargo below.

The following is an agreed request by candidate and supervisor regarding the publication of this thesis:

## Printed copy

No embargo on print copy.

**Electronic copy**

No embargo on electronic copy.

## **Underpinning research data or digital outputs**

### **Candidate's declaration**

I, Chiara Villa, hereby certify that no requirements to deposit original research data or digital outputs apply to this thesis and that, where appropriate, secondary data used have been referenced in the full text of my thesis.

Date

Signature of Candidate

To my parents.

# Acknowledgements

## General acknowledgements

First and foremost, I wish to thank my supervisors Mark and Tommaso for their guidance and support over the years, not only concerning my studies and career but also in the face of life's unexpected obstacles. Thank you for believing in me and for the many words of encouragement. A big thank you also goes to Alf Gerisch, for the valuable collaboration. It has been a pleasure working with you and I hope we will have the chance to discuss more projects together.

I would like to thank my family and friends for always rooting for me, for the many laughters and loud dinners, and for putting up with me whenever I complained about being stressed. Unfortunately, I cannot promise it won't happen again.

A particular thank you goes to Alessio, for the enthusiasm with which he has always discussed with me the biological wonders I have encountered in my studies.

I would like to thank Ashley, Raad and Veronica for being my family away from home and my companions in this journey. I already miss our coffee chats, post-lunch crosswords and improvised dinners.

A special mention goes to Giorgia and Lorenza, for their heartfelt sisterhood. I cherish the countless laughters and adventures growing up, and I am truly thankful for the profound friendship I have found in you, who at times know me better than I know myself.

I wish to thank my brother, Francesco, for being my rock and my inspiration: I am constantly amazed by the restless enthusiasm and determination with which you lead your life. Thank you for your profound affection, and for pushing me to get out of my comfort zone.

Finally, I dedicate this work to my parents, who have dedicated their lives to raising me with the values and ambition that have lead me to where I am today. Thank you for your love and your patience. Thank you for showing me how to cherish life in spite of adversities, and how to learn from them. Thank you for supporting my dreams.

I feel blessed for having been gifted with such amazing people in my life, and I could not have gotten this far without each of you.

## Funding

This work was supported by the University of St Andrews (School of Mathematics and Statistics).

## Publications and collaboration

The following four papers, in collaboration with Mark A. J. Chaplain, Alf Gerisch and Tommaso Lorenzi, form the core around which this thesis is built.

- C. Villa, M. A. J. Chaplain and T. Lorenzi. Evolutionary dynamics in vascularised tumours under chemotherapy: Mathematical modelling, asymptotic analysis and numerical simulations. *Vietnam Journal of Mathematics*, **49**(1):143–167 (2021).
- C. Villa, M. A. J. Chaplain and T. Lorenzi. Modelling phenotypic heterogeneity in vascularised tumours. *SIAM Journal on Applied Mathematics*, **81**(2):434–453 (2021).
- C. Villa, M. A. J. Chaplain and A. Gerisch. A novel nonlocal partial differential equation model of endothelial progenitor cell cluster formation during the early stages of vasculogenesis. *Journal of Theoretical Biology*, **534**(1):110963 (2022).
- C. Villa, M. A. J. Chaplain, A. Gerisch and T. Lorenzi. Mechanical models of pattern and form in biological tissues: the role of stress-strain constitutive equations. *Bulletin of Mathematical Biology*, **83**(4):1-38 (2021).

# Abstract

This thesis explores various partial differential equation (PDE) models of the spatiotemporal and evolutionary dynamics of cell populations in different problems in cancer and development. In particular, these models are used to investigate: (i) the emergence of intratumour phenotypic heterogeneity and the development of chemotherapeutic resistance in vascularised tumours; (ii) the formation of endothelial progenitor cell clusters during the early stages of vasculogenesis; (iii) mechanical pattern formation under different linear viscoelasticity assumptions for the extracellular matrix. The mathematical models proposed for these problems are formulated as systems of nonlinear and nonlocal PDEs, which provide a mean-field representation of the underlying cellular dynamics and pose a series of interesting analytical and numerical challenges. These are tackled by means of formal asymptotic methods, linear stability analyses and appropriate numerical schemes preventing the emergence of spurious oscillations. Numerical simulations, relying on parameter values drawn from the extant literature, complement the analytical results and are employed for *in silico* investigations qualitatively testing the model assumptions against empirical observations. The obtained results help us shed light on the hidden mechanisms responsible for the emergence of the studied phenomena in biology and medicine, suggesting promising research perspectives.

# Contents

<b>I Preface</b>	<b>1</b>
<b>II Modelling evolutionary dynamics in vascularised tumours</b>	<b>7</b>
<b>1 Biological and modelling background</b>	<b>9</b>
1.1 Intratumour phenotypic heterogeneity in vascularised tumours . . . . .	9
1.1.1 Cancer overview . . . . .	9
1.1.2 Therapeutic issues associated with cancer . . . . .	11
1.1.3 Intratumour phenotypic heterogeneity . . . . .	13
1.2 Mathematical models of phenotypic evolution in cancer . . . . .	15
1.2.1 The ecological argument and evolutionary principles . . . . .	15
1.2.2 Modelling the evolutionary dynamics of cancer . . . . .	18
1.2.3 Nonlocal PDE models of well-mixed phenotype-structured populations . . . . .	20
1.2.4 Nonlocal PDE models of space- and phenotype-structured populations . . . . .	23
<b>2 A space- and phenotype-structured PDE model of the emergence of intratumour phenotypic heterogeneity in vascularised tumours</b>	<b>26</b>
2.1 The mathematical model . . . . .	28
2.1.1 Dynamics of tumour cells . . . . .	29
2.1.2 Dynamics of abiotic factors . . . . .	33
2.2 Analytical investigations . . . . .	35
2.2.1 Analytical results in the absence of spatial diffusion . . . . .	35
2.2.2 Formal results in the limit of small spatial diffusion and rare phenotypic changes . . . . .	38
2.2.3 Biological interpretation of analytical results . . . . .	41
2.3 Numerical investigations . . . . .	43
2.3.1 Set-up of numerical simulations and numerical methods . . . . .	43
2.3.2 1D numerical results under stationary concentrations of oxygen and chemotherapeutic agent . . . . .	47

2.3.3	2D numerical results under dynamical concentrations of oxygen and chemotherapeutic agent . . . . .	52
2.3.4	Numerical results assessing the impact of tumour tissue vascularisation on intratumour phenotypic heterogeneity . . . . .	54
<b>3</b>	<b>Discussion and research perspectives</b>	<b>61</b>
3.1	Summary and discussion . . . . .	61
3.1.1	The emergence of intratumour phenotypic heterogeneity and the development of chemotherapeutic resistance . . . . .	62
3.1.2	Vascularisation and phenotypic heterogeneity . . . . .	63
3.1.3	The role of spatial diffusion . . . . .	63
3.2	Research perspectives . . . . .	64
3.2.1	Alternative temporal scales and stochasticity . . . . .	64
3.2.2	Environmental fluctuations and additional abiotic factors . . . . .	65
3.2.3	Optimal therapeutic strategies . . . . .	65
3.2.4	A nonlocal PDE model of metastatic spread . . . . .	66
<b>III</b>	<b>Modelling cluster formation in vasculogenesis</b>	<b>67</b>
<b>4</b>	<b>Biological and modelling background</b>	<b>69</b>
4.1	Endothelial progenitor cell cluster-based vasculogenesis . . . . .	69
4.1.1	Homotypic and heterotypic interactions . . . . .	70
4.1.2	<i>In vivo</i> processes of vascular network formation . . . . .	72
4.1.3	<i>In vitro</i> single-cell vasculogenesis . . . . .	74
4.1.4	<i>In vivo</i> and <i>in vitro</i> cluster-based vasculogenesis . . . . .	74
4.2	Mathematical models of vasculogenesis . . . . .	79
4.2.1	PDE models of single-cell vasculogenesis . . . . .	79
4.2.2	Cellular Potts models of single-cell vasculogenesis . . . . .	81
4.2.3	Modelling the early stages cluster-based vasculogenesis . . . . .	83
<b>5</b>	<b>A novel nonlocal PDE model of endothelial progenitor cell cluster formation</b>	<b>85</b>
5.1	The mathematical model . . . . .	86
5.1.1	Dynamics of endothelial progenitor cells . . . . .	86
5.1.2	Dynamics of extracellular factors . . . . .	88
5.1.3	Boundary and initial conditions . . . . .	89
5.1.4	Nondimensional model . . . . .	90
5.2	Linear stability analysis results . . . . .	91
5.3	Numerical investigations . . . . .	93

5.3.1	Set-up of numerical simulations and numerical methods . . . . .	93
5.3.2	Cluster formation under the baseline parameter set . . . . .	96
5.3.3	Numerical investigation of cluster formation . . . . .	98
5.3.4	Numerical investigation of cluster size . . . . .	100
5.3.5	2D clusters . . . . .	102
<b>6</b>	<b>Discussion and research perspectives</b>	<b>109</b>
6.1	Summary and discussion . . . . .	109
6.1.1	Chemotaxis, degradation and their link to hypoxia . . . . .	109
6.1.2	Cell-to-cell adhesion and cluster stability . . . . .	111
6.2	Research perspectives . . . . .	111
6.2.1	Model validation . . . . .	111
6.2.2	Further analytical investigations . . . . .	112
6.2.3	The inclusion of persistence of motion . . . . .	113
6.2.4	Modelling the late-stages of cluster-based vasculogenesis . . . . .	113
<b>IV</b>	<b>Modelling the extracellular matrix in mechanical pattern formation</b>	<b>115</b>
<b>7</b>	<b>Background and linear viscoelasticity models</b>	<b>117</b>
7.1	PDE models of pattern formation . . . . .	117
7.1.1	Reaction-diffusion models . . . . .	117
7.1.2	Mechanochemical models . . . . .	118
7.1.3	Linear viscoelasticity assumptions on the ECM . . . . .	119
7.2	Essentials of viscoelastic materials and stress-strain constitutive equations	120
7.2.1	Essentials of viscoelastic materials . . . . .	120
7.2.2	1D stress-strain constitutive equations . . . . .	121
7.2.3	2D stress-strain constitutive equations . . . . .	126
<b>8</b>	<b>The role of stress-strain constitutive equations in mechanical models of biological pattern formation</b>	<b>127</b>
8.1	A mathematical model of mechanical pattern formation . . . . .	128
8.1.1	Dynamics of the cells . . . . .	128
8.1.2	Dynamics of the ECM . . . . .	128
8.1.3	Force-balance equation for the cell-ECM system . . . . .	129
8.1.4	Boundary conditions . . . . .	130
8.1.5	Extension to 2D . . . . .	131
8.2	Linear stability analysis and dispersion relations . . . . .	132
8.2.1	Linear stability analysis . . . . .	132

8.2.2	Dispersion relations . . . . .	134
8.3	Numerical investigations . . . . .	143
8.3.1	Set-up of numerical simulations and numerical methods . . . . .	143
8.3.2	1D patterns . . . . .	144
8.3.3	2D patterns . . . . .	146
<b>9</b>	<b>Discussion and research perspectives</b>	<b>148</b>
9.1	Summary and discussion . . . . .	148
9.1.1	Summary . . . . .	148
9.1.2	Empirically informed mechanical models . . . . .	149
9.2	Research perspectives . . . . .	149
9.2.1	Model extensions, further analytical and numerical work . . . . .	149
9.2.2	Experimentally motivated studies . . . . .	151
<b>V</b>	<b>Potential future directions</b>	<b>153</b>
<b>Appendices</b>		<b>157</b>
<b>A</b>	<b>Analytical details</b>	<b>158</b>
A.1	Proof of Proposition 1 in Chapter 2 . . . . .	158
A.2	Proof of Theorem 1 in Chapter 2 . . . . .	159
A.3	Formal analysis presented in Chapter 2 . . . . .	161
A.4	Linear stability analysis presented in Chapter 5 . . . . .	164
A.4.1	Linear stability analysis of the 1D problem . . . . .	164
A.4.2	Linear stability analysis of the 2D problem . . . . .	170
A.5	Derivation of the constitutive equations of the models of linear viscoelasticity in Chapter 7 . . . . .	172
A.5.1	Derivation of the 1D Kelvin-Voigt and Maxwell models . . . . .	173
A.5.2	Derivation of the 2D Kelvin-Voigt and Maxwell models . . . . .	174
A.6	Creep and stress relaxation tests on the constitutive equations of the Kelvin-Voigt and Maxwell models in Chapter 7 . . . . .	175
<b>B</b>	<b>Numerical details</b>	<b>178</b>
B.1	Numerical schemes used in Chapter 2 . . . . .	180
B.1.1	Numerical schemes for 1D spatial domains . . . . .	180
B.1.2	Numerical schemes for 2D spatial domains . . . . .	182
B.2	Numerical method used in Chapter 5 . . . . .	184
B.3	Numerical schemes used in Chapter 7 . . . . .	186
B.3.1	Numerical schemes for the 1D problem . . . . .	186

<b>B.3.2 Numerical scheme for the 2D problem</b>	190
<b>C Parameter details</b>	<b>195</b>
C.1 Parameter values used in Chapter 2	195
C.2 Parameter values used in Chapter 5	197
C.3 Parameter values used in Chapter 7	199
<b>D Supplementary figures</b>	<b>202</b>
<b>Bibliography</b>	<b>209</b>

# Part I

## Preface

# Mathematical modelling

Recent advances in many fields of biology and medicine, including cancer and development, have been driven by a synergistic approach involving not only empirical observations and experiments, but also mathematical modelling (Servedio et al., 2014). Experimental assays include *in vitro* and *in vivo* approaches, which can be used to obtain empirical data in controlled and realistic settings respectively. Experimental studies, however, can be expensive and time consuming. For this reason, mathematical models have been increasingly used as theoretical tools to investigate the mechanisms at the basis of a variety of problems in biology and medicine by means of *in silico* investigations. These models complement empirical research, serving as a proof of concept for newly developed theories, bridging the gap between *in vitro* and *in vivo* observations, and steering experimental investigations towards the most promising research perspectives (Anderson and Quaranta, 2008; Anderson and Maini, 2018; Tomlin and Axelrod, 2007; Servedio et al., 2014). By integrating the model with empirical data, the model's applicability to empirical systems can be tested. This step is known as model validation as it provides a means for testing the biological relevance of the model assumptions. Nonetheless, much theoretical work can be conducted prior to the integration of empirical data to improve model design (Vera et al., 2021): analytical and numerical results of the mathematical models can be qualitatively compared with empirical observations for an initial selection of model assumptions. Altogether, this supports the creation of new modelling frameworks to address complex problems in biology and medicine, and improved mathematical methods leading to better characterisations of the solution's properties. This thesis is concerned with such theoretical work, together with the analytical and numerical challenges posed by these models.

Each part of this thesis focusses on a different problem in cancer and development and it is composed of three chapters: the first one provides relevant biological and modelling background to inform the reader on the empirical evidence and previous studies motivating the model assumptions; the second one is dedicated to the presentation of the mathematical model together with analytical and numerical results; the final chapter is dedicated to the discussion of the model and promising research perspectives, both in terms of applicability to empirical systems and mathematical tractability.

# Modelling techniques

In this thesis we are interested in studying the spatiotemporal and adaptive (in Part II) dynamics of populations of cells of different types. Cellular processes exhibit multiscale properties, with relevant interactions occurring at different scales. In particular, intracellular processes such as mutations and signalling pathways occur at the molecular scale ( $\text{nm}-\mu\text{m}$ ), extracellular interactions such as those with other cells or the extracellular matrix (ECM) occur at the microscopic scale ( $\mu\text{m-mm}$ ), and tissue level processes occur at the macroscopic scale ( $\text{mm-cm}$ ) (Deisboeck et al., 2011). Note that these scales are sometimes referred to, respectively, as microscopic, mesoscopic and macroscopic instead (Scianna and Preziosi, 2013). The spatial scale at which the processes of interest occur, together with the relevant timescale, can be used as criteria to select the most appropriate modelling framework. Models of cell population spatiotemporal and adaptive dynamics can involve discrete, continuum and hybrid techniques (Anderson and Quaranta, 2008; Durrett and Levin, 1994; Preziosi and Tosin, 2009).

**Discrete modelling.** Discrete models rely on an explicit representation of individual cells in space and time, and are therefore known as individual-based (IB) models, or agent-based models (Anderson et al., 2007; Metzcar et al., 2019; Scianna and Preziosi, 2013). These may be off lattice or on lattice, in which case cells are placed on a grid and either regarded as point particles which may (cellular automata) or may not (lattice gas cellular automata) share the same grid position with other cells, or each occupy multiple grid positions (cellular Potts). They are particularly suited to processes occurring at the microscopic scale and over short timescales (minutes-hours) involving populations of low cell numbers, particularly thanks to the possibility to easily incorporate the stochasticity of the dynamics observed in these regimes. At the same time, IB models are generally computationally expensive and less amenable to analytical investigations.

**Continuum modelling.** Continuum models give a macroscopic description of the system under study, as the terms in the model equations provide a mean-field representation of the underlying cellular dynamics (Altrock et al., 2015; Deisboeck et al., 2011). Continuum macroscopic descriptions are particularly suited for dynamics involving populations of large cell numbers, where the small scale stochastic effects can be neglected. For this reason models formulated as systems of partial differential equations (PDEs) are particularly popular for tissue level spatiotemporal and evolutionary dynamics over longer timescales (days-years). A range of asymptotic techniques have been developed and used to derive several PDE models from their stochastic discrete counterpart – see for instance (Baker et al., 2019; Byrne and Drasdo, 2009; Buttenschön et al., 2018; Champagnat

---

et al., 2008, 2006; Lorenzi et al., 2020; Chaplain et al., 2020; Stevens and Othmer, 1997; Stevens, 2000) and references therein. Such derivations ensure that the model equations provide a faithful mean-field representation of the underlying cellular dynamics. Moreover, comparing the solution of a PDE model with that of the corresponding IB model, one may observe that stochastic effects are significant at low cell numbers, while the solutions match well for high cell numbers – see for instance (Bubba et al., 2020; Lorenzi et al., 2019; Macfarlane et al., 2020; Nardini et al., 2021; Simpson and Baker, 2011) and references therein. A wide range of methods and techniques from different areas of mathematics may be harnessed to overcome the analytical and numerical challenges posed by initial-boundary-value problems. For this reason, compared to IB models, PDE models are generally more amenable to analytical investigation and may be less computationally expensive, although their computational cost and analytical tractability do depend on the complexity of the model, as will be discussed throughout this thesis.

**Hybrid modelling.** Since many biological systems involve processes spanning different spatiotemporal scales, in the past twenty years many models combining discrete and continuum approaches have been proposed, known as hybrid or multiscale models (Deisboeck et al., 2011; Scianna and Preziosi, 2013). For example, hybrid models using a discrete stochastic approach for the cell dynamics, at low cell numbers, and a continuum deterministic one for the molecular concentration of abiotic factors, are particularly popular. Hybrid models, similarly to IB models, may still be computationally expensive and less amenable to analytical investigations.

The biological processes studied in this thesis are concerned with spatial sorting of cell populations at the tissue level, occur over longer timescales (days) and involve cell populations which are actively proliferating. For this reason the models presented henceforth are of the continuum deterministic type. These are formulated as systems of nonlinear, and at times nonlocal (Parts II and III), PDEs and they pose a series of analytical and numerical challenges, which make them interesting mathematical objects *per se*.

## Thesis structure and topics

This thesis is composed of three main parts (II–IV), each dedicated to a different application in cancer and development, and a brief discussion of potential future directions (Part V). The contents of Parts II–IV have been published in Villa et al. (2021a,b,c, 2022).

**Part II - Modelling evolutionary dynamics in vascularised tumours.** Part II focusses on the emergence of intratumour phenotypic heterogeneity in vascularised tumours and its consequences for the development of chemotherapeutic resistance, which is often responsible for treatment failure and disease relapse. The problem is addressed in an eco-evolutionary perspective, and studied by means of a nonlocal PDE model of a space- and phenotype-structured population of cancer cells. Equations of this type – i.e. nonlocal reaction-diffusion equations of the Lotka-Volterra type – have attracted the attention of the mathematical community and we will see how under simplifying assumptions we can construct explicit solutions, while in more complex cases a formal Hamilton-Jacobi approach can be used to obtain weak solutions in appropriate asymptotic limits. The analytical results will be complemented with numerical simulations, based on an explicit finite difference scheme, employed for *in silico* investigations testing eco-evolutionary hypotheses against empirical evidence. While it is known that in vascularised tumours new blood vessels may form, in this study we make the simplifying assumption of a fixed vascular distribution in order to focus on the cancer cell evolutionary dynamics. Mathematical modelling of neovascularisation processes, in fact, presents a series of challenges which make it an interesting problem to address on its own, as we do in Part III.

**Part III - Modelling cluster formation in vasculogenesis.** Part III focusses on a neovascularisation process referred to as cluster-based vasculogenesis, for which an underlying mechanism has recently been proposed. This is characterised by the formation of endothelial progenitor cell clusters during the early stages of the process, which allow for an extensive vascular network to form, not only in tumours but also in embryos and ischemic tissues. We theoretically investigate the determinants of cluster formation and size by means of a novel nonlocal PDE model. The nonlocal nature of the PDE system introduces significant analytical and numerical difficulties. We thus conduct linear stability analysis of the system and a parametric analysis on the numerical simulations, obtained using an implicit finite volume scheme developed by Alf Gerisch (TU Darmstadt), to test modelling assumptions against experimental observations. In this study we ignore mechanical interactions, which are negligible during the early stages of vasculogenesis, but a series of mechanochemical models similar to that presented in Part IV have been proposed and might provide an initial framework for the late-stage dynamics.

**Part IV - Modelling the extracellular matrix in mechanical pattern formation.** Part IV focusses on mechanochemical models of pattern formation in biological tissues, employed to study not only vasculogenesis but also a series of problems in development and physiology. In these models the ECM is generally regarded as a linear viscoelastic material and modelled using the Kelvin-Voigt model of linear viscoelasticity, but other

constitutive models exist which might be better suited to represent the ECM. We thus present a study of the role that different constitutive equations have in the pattern formation potential of a generic mechanical model of this type, relying on a parametric analysis of the dispersion relations obtained from a LSA and numerical simulations. The stiff PDE system poses significant numerical challenges, and we construct numerical solutions with an implicit mixed finite volume and finite difference scheme.

**Part V - Potential future directions.** Part V concludes this thesis by briefly presenting new modelling frameworks at the interface of adaptive dynamics and pattern formation, with promising research perspectives that would combine the strengths and complexities of the models presented in Parts II-IV.

## List of acronyms

The following acronyms will be used in this document:

1D	One-dimensional
2D	Two-dimensional
3D	Three-dimensional
ATP	Adenosine triphosphate
CAM	Cell adhesion molecule
CP	Cellular Potts
D-OCT	Dynamic optical coherence tomography
EC	Endothelial cell
ECFC	Endothelial colony-forming cell
ECM	Extracellular matrix
EMT	Epithelial-to-mesenchymal transition
EPC	Endothelial progenitor cell
eEPC	Embryonic EPC
FWHM	Full width at half maximum
HUVEC	Human Umbilical Vein EC
IB	Individual-based
LSA	Linear stability analysis
MMPs	Matrix-metalloproteases
ODE	Ordinary differential equations
PDE	Partial differential equations
PEC	Persistence and Endogenous Chemotaxis
SLS	Standard linear solid
VEGF	Vascular Endothelial Growth Factor

## **Part II**

# **Modelling evolutionary dynamics in vascularised tumours**

This part focusses on the evolutionary dynamics of cancer cells in vascularised tumours, before and during chemotherapeutic treatment. Tumour vascularisation constitutes a critical stage of cancer progression, supporting further tumour growth and metastasis. Moreover, intratumoural vasculature supports the emergence of intratumour-phenotypic heterogeneity and the development of therapeutic resistance, often responsible for treatment failure and relapse. Previous empirical and theoretical works indicate that the nonlinear interaction between abiotic factors and tumour cells can lead to the creation of different ecological niches in which cells with different phenotypic characteristic can be selected. Mathematical models of adaptive dynamics have been increasingly used in the study of phenotypic evolution in cancer, with particular attention being given to nonlocal PDE models of phenotype-structured populations. Despite the many insights provided by works in the extant literature, we are still far from a complete and systematic understanding of the evolutionary processes at the basis of the aforementioned phenomena. We here present a mathematical study of the evolutionary dynamics of tumour cells in vascularised tumours under chemotherapy. The model comprises a system of coupled spatially explicit nonlocal PDEs for the phenotypic distribution of tumour cells, including terms modelling spontaneous phenotypic changes and spatial movement, the concentration of oxygen and the concentration of a chemotherapeutic agent, which undergo nonlinear interactions with the tumour cells and are released from the intratumoural vascular network. The study is based on both asymptotic analysis and numerical simulations of the system, where a detailed quantitative characterisation of the long-time asymptotic behaviour of the solutions is given. The results obtained provide a theoretical basis for empirical evidence indicating that the phenotypic properties of tumour cells in vascularised tumours vary with the distance from the blood vessels and establish a relation between the degree of tumour tissue vascularisation and the level of pre-treatment intratumour phenotypic heterogeneity. Moreover, we demonstrate that lower oxygen levels may correlate with higher levels of phenotypic variability, which suggests that the presence of hypoxic regions supports intratumour phenotypic heterogeneity. The results of the analysis put on a solid mathematical basis the idea that hypoxia favours the selection for chemoresistant phenotypic variants prior to treatment, facilitating the development of resistance following chemotherapy. The results of this study are in agreement with previous empirical and theoretical works and lead to various promising research perspectives.

Part II is organised as follows: in Chapter 1 the related biological background is presented, along with an overview of nonlocal PDE models of adaptive dynamics in the current literature; in Chapter 2 a nonlocal PDE model of cancer cell evolutionary dynamics in vascularised tumours is presented together with its analytical and numerical results; in Chapter 3 these results are discussed, together with promising research perspectives.

The contents of Part II are based on the papers Villa et al. (2021b,c).

# Chapter 1

## Biological and modelling background

### 1.1 Intratumour phenotypic heterogeneity in vascularised tumours

First, a brief overview of cancer biology is given in Section 1.1.1. This is followed by a description of popular therapeutic strategies for tumours at different stages of cancer progression and the associated development of resistance often responsible for treatment failure in Section 1.1.2. Finally, in Section 1.1.3 evidence of the emergence of metabolic phenotypic heterogeneity in tumours, deemed to be correlated with higher therapeutic resistance, is presented along with open problems associated with heterogeneity in vascularised tumours.

#### 1.1.1 Cancer overview

Cancer is a disease, or collection of diseases, caused by uncontrolled division of abnormal cells in a part of the body. Cancer research has been continuously expanding over the years, particularly motivated by the high incidence and diversity of cancer (Sung et al., 2021). While it was once thought to be a disease of genes, it is now recognised to be an evolutionary disease (Chisholm et al., 2016a; Greaves and Maley, 2012). In particular, tumours are seen as organ-like ecosystems, dynamically interacting with elements of their surrounding microenvironment and capable of acquiring new malignant properties that favour their survival and invasion of the host organism (Egeblad et al., 2010).

**The Hallmarks of cancer.** Hanahan and Weinberg (2000) identified six characteristics, known as the ‘Hallmarks of cancer’ (see Figure 1.1), that cancer cells can acquire in order to progress through the different stages of cancer. These include the ability to sustain proliferative signalling, evade growth suppressors, resist cell death, enable replicative immortality, induce angiogenesis, and invade the local tissue or other parts of the host (metastasis). Hanahan and Weinberg (2011) later recognised four additional hallmarks, including the cells’ ability to avoid immune destruction, recruit immune cells to cause tumour-promoting inflammation, mutate and alter their metabolic processes to avoid the need for oxygen. The authors particularly highlight the crucial role played by the tumour microenvironment in the acquisition of these hallmarks and, therefore, its impact on tumour progression and development of malignancy.

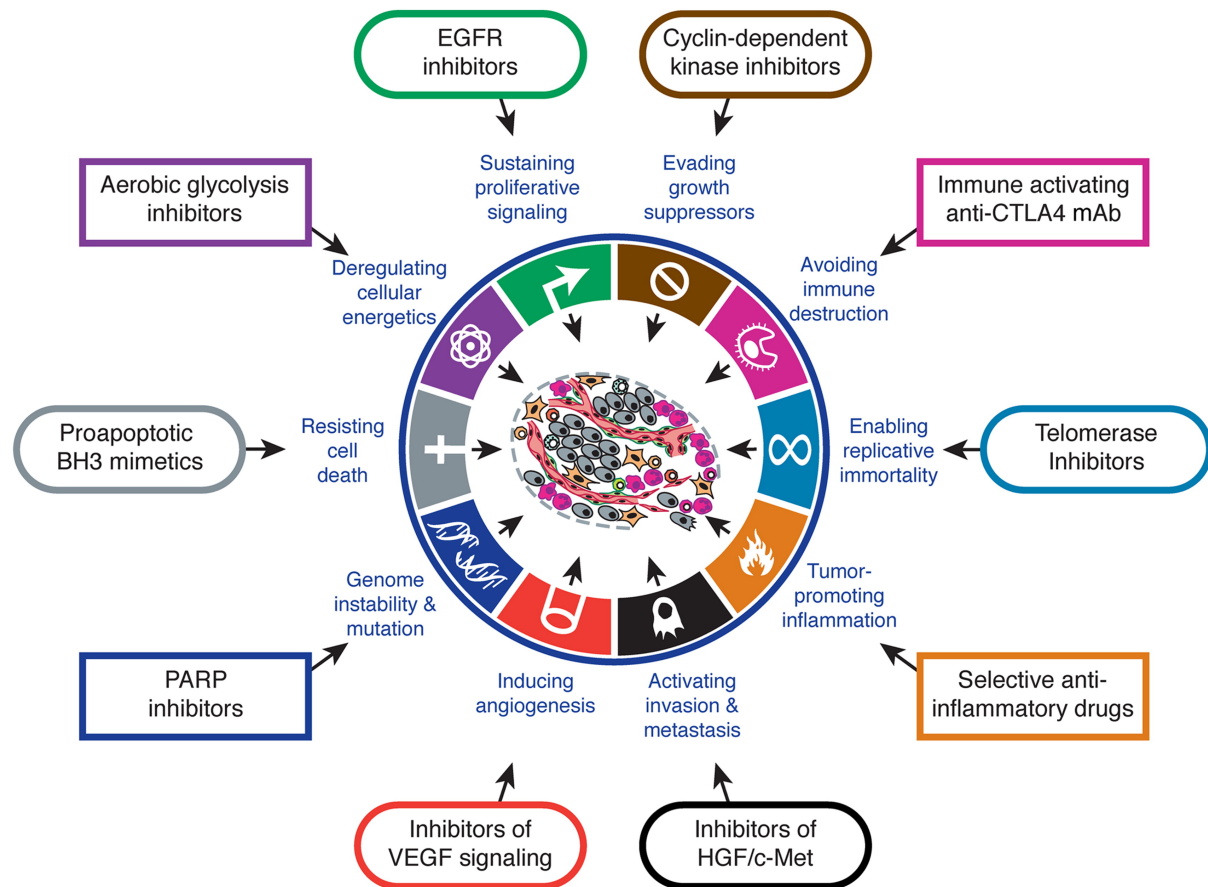


**Figure 1.1: The Hallmarks of cancer.** Summary of the ten Hallmarks of cancer and their potential treatment options. Reprinted from Cell, 144 (5), D. Hanahan, R. A. Weinberg, Hallmarks of Cancer: The Next Generation, 646-674, Copyright (2011), with permission from Elsevier (Hanahan and Weinberg, 2011, Figure 6).

**The stages of cancer.** Tumours form from the uncontrolled proliferation of abnormal cells due to the accumulation of mutations (Hanahan and Weinberg, 2011; Weinberg, 2013). They initially grow as multicellular spheroids up to a size of approximately 1-2 mm<sup>3</sup> above which their metabolic demands are restricted due to the diffusion limit

of oxygen and nutrients (Hillen and Griffioen, 2007). Hypoxia, i.e. decreased oxygen availability, is one of the first environmental stresses that cancer cells experience, and it leads to a variety of cellular changes and biological processes initiated by the cells in response to such stress. Among the cellular changes caused by hypoxia and by other environmental clues are a series of phenotypic changes based on metabolic reprogramming (see Section 1.1.3) and what is known as epithelial-to-mesenchymal<sup>1</sup> transition (EMT) allowing the cancer cells to invade the local tissue (Friedl and Wolf, 2003). We note that the term ‘cancer’ refers to malignant rather than benign tumours, where malignancy is determined by the tumour cells’ potential to spread to other parts of the body. Moreover, among the processes induced by hypoxia is the formation of new vasculature (Hillen and Griffioen, 2007) from pre-existing vessels (angiogenesis) or by recruiting endothelial progenitor cells (see Chapter 4 for a more detailed overview of neovascularisation processes), responsible for the development of vascularised tumours. Due to the new oxygen supply, vascularised tumours can grow further and, because of the abnormal structure of the new blood vessels (Magnussen and Mills, 2021) as well as EMT, cancer cells can intravasate and leave the original site. If they manage to survive within the circulatory system, they may eventually extravasate into a new site, undergo mesenchymal-to-epithelial transition and begin to proliferate uncontrollably again (Lambert et al., 2017). This last step is known as metastatic spread and constitutes the culmination of tumour malignancy. Moreover, cancer cells in metastatic sites may intravasate and create new metastases or may travel back to the primary site and contribute to the further growth of the primary tumour, a phenomenon known as secondary self-seeding (Leung and Brugge, 2009).

### 1.1.2 Therapeutic issues associated with cancer

As cancer progresses, acquiring more malignant traits and spreading to different parts of the host body, it starts to disrupt the essential bodily processes performed by the affected organs. Various therapeutic strategies have been developed over the years, particularly diversified to tackle tumours at different stages.

**Therapeutic strategies.** Benign tumours are generally treated locally via surgery or radiotherapy<sup>2</sup> (Chu and Sartorelli, 2004) or, if they appear stable, they might even be left untouched and simply monitored via regular check ups. On the other hand, malignant tumours are generally treated with a combination of different therapeutic strategies,

<sup>1</sup>Epithelial-like cells are characterised by high E-cadherin expression which translates into static cells collectively embedded via cell-cell adhesion bonds. Mesenchymal-like cells are characterised by a down-regulation of membrane E-cadherin expression, associated with more motile and invasive behaviours.

<sup>2</sup>Radiotherapy is a cancer treatment based on the use of high doses of radiation which damages the DNA of cancerous cells leading to cell death.

the most common one being chemotherapy. This treatment is based on the use of cytotoxic drugs which particularly damage highly proliferative cells by interfering with mitosis (Chu and Sartorelli, 2004; Corrie, 2011). None of these treatments, however, are without drawbacks: surgery can involve highly invasive procedures, radiotherapy may damage healthy cells surrounding the targeted tumour, and chemotherapy tends to damage healthy tissues throughout the whole body leading to many side effects (Corrie, 2011). New targeted therapies are increasingly being tested, aimed at damaging cancer cells while leaving healthy ones unaffected (Tsimberidou, 2015; Wu et al., 2006). Immunotherapy, which aims at contrasting the cancer cell's ability to avoid immune destruction by training the immune system, is becoming more and more popular (Mellman et al., 2011). Various other therapies have been developed to specifically target each hallmark of cancer (Hanahan and Weinberg, 2011), as summarised in Figure 1.1. Moreover, in vascularised tumours, vascular normalisation may be essential for optimal drug delivery or immune response (Magnussen and Mills, 2021). However, as previously mentioned, these less aggressive therapeutic strategies are generally used in combination with more aggressive ones.

**Development of resistance.** Despite the progress made in the formulation of therapeutic strategies for cancer, treatment failure still occurs, particularly due to the development of drug resistance by the surviving cancer cell population. In particular, while various types of therapeutic resistance may be encountered (Lavi et al., 2012), we here focus on drug-induced resistance that may be acquired during treatment. This therapeutic issue is common in most cancers during both chemotherapy and radiotherapy, and even in targeted therapies (Chisholm et al., 2016a; Corrie, 2011; Barker et al., 2015; Gillies et al., 2012). During chemotherapy, for instance, less susceptible cells may still experience DNA damage, yet to a lesser extent than highly susceptible cells and may therefore develop an increased capability to repair DNA lesions (e.g. via reduced drug uptake or up-regulation of DNA repairing enzymes) (Chu and Sartorelli, 2004; Corrie, 2011). After treatment, the surviving cells, possibly owing their survival to the newly acquired resistance capabilities, will resume proliferation and potentially lead to a resistant population. Treatment failure is particularly common in metastatic cancer, not only because of the need to treat multiple tumours at different locations or because of the repopulating effects of secondary self-seeding, but also because therapeutic resistance capabilities acquired by cells in a primary site may spread to metastatic sites (Lambert et al., 2017). The development of resistance in tumours is particularly favoured by pre-treatment intratumour phenotypic heterogeneity.

### 1.1.3 Intratumour phenotypic heterogeneity

A phenotype is the set of observable characteristics of an individual, in this case a cancer cell, resulting from the interaction of its genotype with the surrounding environment. In this work, we focus on the metabolic phenotype of cancer cells as it plays an important role in the development of resistance to chemotherapy.

**Tumour metabolism.** In order to proliferate, as well as to grow and maintain cell homeostasis<sup>3</sup>, cells require energy which they can obtain via the fundamental process of metabolism, during which they convert nutrients into adenosine triphosphate (ATP), the energy-storing molecule. Several metabolic pathways exploiting different energy sources exist, but the primary nutrients converted by cells are oxygen and glucose (Romero-Garcia et al., 2011). Cells first convert glucose into a chemical compound known as pyruvate via glycolysis, producing two ATP molecules and a proton. In anaerobic conditions, that is in the absence of oxygen, pyruvate is turned into lactate and the cells rely only on the energy stored in the ATP produced via anaerobic glycolysis. In aerobic conditions, on the other hand, glycolysis is followed by oxidative phosphorylation, during which oxygen and pyruvate transported to the mitochondria<sup>4</sup> are converted into CO<sub>2</sub>, H<sub>2</sub>O and ATP. This aerobic energy pathway leads to a net production of about 36 ATP molecules per one glucose and five oxygen molecules (Vander Heiden et al., 2009), thus cells can rely on much more energy than with anaerobic glycolysis to boost proliferation.

In normal tissues, hypoxia induces a higher expression of hypoxia-inducible factors<sup>5</sup>, such as HIF-1, which favours a shift towards anaerobic energy pathways<sup>6</sup> (Lee et al., 2004) and inhibits cell proliferation (Huang, 2013a). In tumours, the presence of hypoxic regions also induces a shift towards a glycolytic metabolic phenotype (Denko, 2008; Semenza, 2010) and cancer cells eventually switch to glycolysis even in aerobic conditions, a phenomenon known as the Warburg effect (Vander Heiden et al., 2009). Although this is an inefficient way to produce energy, it is associated with better cancer cell survival and higher malignancy, particularly because lactate production increases acidity levels in the local environment promoting more aggressive phenotypes (Robertson-Tessi et al., 2015; Krtolica and Ludlow, 1996). Nevertheless, heterogeneity with respect to oxidative phosphorylation, aerobic and anaerobic glycolysis is generally found in cancer cell popu-

<sup>3</sup>Homeostasis is the state of steady internal, physical, and chemical conditions necessary for survival of living systems.

<sup>4</sup>Mitochondria are membrane-bound cell organelles responsible for the production of most of the chemical energy, stored in ATP molecules, needed to power the cell's biochemical reactions.

<sup>5</sup>In normoxic conditions, HIF-1 is synthesised and made inactive due to the action of an oxygen-dependent enzyme known as pVHL; in hypoxic conditions, HIF-1 levels increase within minutes as pVHL cannot synthesise it.

<sup>6</sup>HIF-1 promotes glycolysis by activating genes responsible for glucose transport and inhibits oxidative phosphorylation in the mitochondria.

lations (Chisholm et al., 2016a; Denko, 2008). Hypoxia and anaerobic glycolysis – and, more generally, metabolic heterogeneity – in tumours are particularly associated with higher resistance to therapy (Denko, 2008; Shannon et al., 2003; Strese et al., 2013; Zhao et al., 2013). Given that they are associated with inhibition of cell proliferation (Krtolica and Ludlow, 1996; Tannock, 1968), this is consistent with the notion that slowly proliferating cells are less susceptible to chemotherapy and thus more likely to develop resistance, as outlined in Section 1.1.2.

**Spontaneous phenotypic changes.** A shift in the metabolic phenotype of cancer cells can be induced by environmental stress factors such as hypoxia, which can up-regulate the transcription of genes like HIF-1 and induce a glycolytic switch in the span of a few days (Baumann et al., 2007). However, phenotypic changes may also occur spontaneously due to genetic and non-genetic instability. The former is associated with mutations, which may occur on long timescales (Beerenwinkel et al., 2007) and result in irreversible changes in the genome thus affecting the cell phenotype. Nevertheless, even in genetically homogeneous cell populations, great heterogeneity in gene expression levels is observed (Chisholm et al., 2016a). Non-genetic instability is generally associated with noise in gene expression particularly due to epimutations (Levine et al., 2020). These are heritable and reversible phenotypic changes occurring over the lifespan of a tumour cell due to, for instance, DNA methylation<sup>7</sup> and histone<sup>8</sup> modification (Hansen et al., 2011; Sandoval and Esteller, 2012), which are responsible for changes in gene transcription mechanisms (e.g. gene silencing) and are not induced by any selective pressure (Huang, 2013b). It has been hypothesised that epigenetic modifications alone can be responsible for the emergence of phenotypic diversity and drug resistance (Brown et al., 2014; Chisholm et al., 2016a).

**Intratumour phenotypic heterogeneity.** A growing body of experimental and clinical studies demonstrate that tumour cells with different phenotypic properties occupy tumour regions which are characterised by different oxygen levels. In particular, hypoxic parts of the tumour (i.e the inner areas – excluding the necrotic core – in avascular tumours and the regions far from blood vessels in vascularised tumours) are mainly populated by slow-dividing cells, which display higher levels of hypoxia-inducible factors, such as HIF-1 (Carmona-Fontaine et al., 2017; Eales et al., 2016; Giatromanolaki et al., 2001; Padhani et al., 2007; Semenza, 2003; Strese et al., 2013; Tannock, 1968). On the other hand, fast-dividing cells with lower levels of expression of hypoxia-inducible

<sup>7</sup>DNA methylation is a biological process by which methyl groups are added to the DNA molecule, shutting off some genes and activating others.

<sup>8</sup>A histone is a protein providing structural support to a chromosome. In the nucleus, long DNA molecules are wrapped around complexes of histone proteins

factors, which typically correlate with higher levels of resistance to chemotherapy, are primarily detected in well-oxygenated parts of the tumour tissue (i.e the tumour border in avascular tumours and the regions in the vicinity of blood vessels in vascularised tumours) (Carmona-Fontaine et al., 2017; Eales et al., 2016; Dewhirst et al., 2008; Giatromanolaki et al., 2001; Semenza, 2003; Tannock, 1968). This evidence, illustrated in Figure 1.2B, indicates that spatial variability in the intratumoural concentration of oxygen plays a pivotal role in the emergence and development of phenotypic heterogeneity among tumour cells (Alfarouk et al., 2013; Axelson et al., 2005; Gillies et al., 2012; Marusyk et al., 2012; Molavian et al., 2009; Sun and Yu, 2015). This impinges on anti-cancer treatment by making it impossible for single biopsies to exhaustively portray the phenotypic composition of the whole tumour tissue (Burrell and Swanton, 2014; Poleszczuk et al., 2015; Yap et al., 2012). This is particularly the case in vascularised tumours, where the chaotic and abnormal vasculature leads to significant spatial gradients in the oxygen distribution. While continuously improving non-invasive imaging techniques allow for a clear mapping of the blood vessel distribution in vascularised tumours (Upputuri et al., 2015; Schuh et al., 2017), this information is still insufficient to inform treatment design as no precise connection between blood vessel distribution and intratumour phenotypic heterogeneity has yet been established. In fact, despite the progress made in cancer research, we are still far from a systematic understanding of the processes responsible for the emergence of intratumour phenotypic heterogeneity and of the role this has in the development of chemotherapeutic resistance. Mathematical modelling can provide a theoretical framework in which to investigate these open problems in biology and medicine (Lavi et al., 2012).

## 1.2 Mathematical models of phenotypic evolution in cancer

Evolutionary principles at the basis of the theoretical study of intratumour phenotypic heterogeneity and therapeutic resistance are presented in Section 1.2.1. An overview of mathematical models of cancer phenotypic evolution in the current literature is given in Section 1.2.2, followed by a detailed review of nonlocal PDE models of phenotype-structured cancer cell population dynamics in Sections 1.2.3 and 1.2.4.

### 1.2.1 The ecological argument and evolutionary principles

Since first proposed by Nowell (1976), the study of cancer as an eco-evolutionary process has been widely accepted (Aktipis and Nesse, 2013; Basanta and Anderson, 2013; Crespi

and Summers, 2005; Dujon et al., 2021; Gatenby and Gillies, 2008; Gatenby and Brown, 2017; Merlo et al., 2006). In particular, the tumour microenvironment can be viewed as an ecological landscape in which cells evolve in response to the selective pressure of the local environmental conditions. In the case of vascularised tumours, an analogy can be drawn between cancer cells surrounding a blood vessel and riparian habitats within desert landscapes, illustrated in Figure 1.2 as presented by Alfarouk et al. (2013) who proposed the vascular network as a common and primary source of intratumour heterogeneity. Rivers in deserts or semi-arid landscapes bring nutrients and resources to plants and carry away toxic and waste products. Near the stream, the high water and nutrient availability supports the growth of thick vegetation consisting of tall trees and mesic<sup>9</sup> shrubs, which results in intense competitive interactions between plants for space and resources, i.e. a biotically harsh environment. Away from the stream, the level and availability of ground water declines and, together with a rise in minerals and salts, results in the selection of sparse xeric<sup>10</sup> grasses, shrubs and cacti, which are able to survive the harsher abiotic environment whilst experiencing little biotic competition. Analogously, in vascularised tumours, it has been hypothesised that the nonlinear interplay between impaired oxygen delivery caused by structural abnormalities present in the tumour vasculature (Dewhirst et al., 2008; Fukumura et al., 2010; Jain, 1988; Jordan and Sonveaux, 2012; Padhani et al., 2007; Vartanian et al., 2014; Vaupel et al., 1989), limited oxygen diffusion and oxygen consumption by tumour cells may lead to the creation of distinct ecological niches in the tumour landscape, whereby tumour cells with different phenotypic characteristics can be selected (Alfarouk et al., 2013; Casciari et al., 1992; Gatenby et al., 2007; Hockel and Vaupel, 2001; Ibrahim-Hashim et al., 2017; Lloyd et al., 2016). This hypothesis is supported by the growing body of experimental and clinical studies summarised in Section 1.1.3, and it agrees with further empirical and theoretical work also suggesting that spatial variation in oxygen levels can foster the emergence of intratumour phenotypic heterogeneity (Gallagher and Anderson, 2013; Gay et al., 2016; Gillies et al., 2012; Kotler and Brown, 2020; Loeb, 2001; Marusyk et al., 2012; Molavian et al., 2009; Sun and Yu, 2015).

**Evolutionary principles of adaptive dynamics.** The ecological analogy described above relies on the principles of Darwinian selection of the fittest to local environmental conditions following competition for space and resources. In this theoretic framework, new phenotypic traits are generally assumed to emerge due to phenotypic stochasticity, i.e. spontaneous and random phenotypic changes (e.g. in cancer due to mutations and epimutations). We note that this is different to the concept of phenotypic plasticity, that is the ability of an individual to undergo phenotypic changes in response to environ-

<sup>9</sup>A mesic habitat (or plant) is characterised by (or requiring) a moderate amount of moisture.

<sup>10</sup>A xeric habitat (or plant) is characterised by (or requiring only) a small amount of moisture.

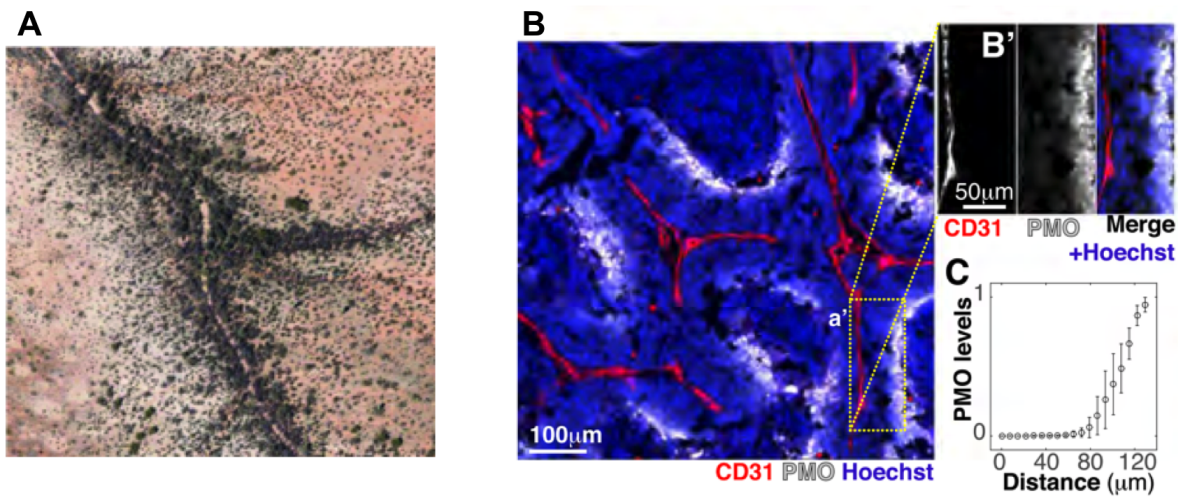


**Figure 1.2: The analogy between riparian habitats and vascularised tumours.** (A) Riparian habitat in the Sonoran Desert of Arizona. Reprinted from Evolutionary Applications, 6(1), K. O. Alfarouk, M. E. Ibrahim, R. E. Gatenby, J. S. Brown, Riparian ecosystems in human cancers, 46–53, 2013, under Creative Commons licence <https://creativecommons.org/licenses/by/3.0/> (Alfarouk et al., 2013, Figure 2). (B-C) Hypoxic (white, PMO = hypoxia) and cellular (blue, Hoechst = cells) spatial gradients in a vascularised tumour (red, CD31 = blood vessels). Reprinted from Proceedings of the National Academy of Sciences, 114(11), C. Carmona-Fontaine, M. Deforet, L. Akkari, C. B. Thompson, J. A. Joyce, J. B. Xavier, Metabolic origins of spatial organisation in the tumour microenvironment, 2934–2939, 2017 (Carmona-Fontaine et al., 2017, Figure 1B-C).

mental stimuli (e.g. in cancer hypoxia-induced up-regulation of HIF-1 and subsequent signalling cascade resulting in a metabolic switch) (Levine et al., 2020). The role of phenotypic stochasticity in cellular and organismal phenotypic evolution was first illustrated by Waddington's well-known epigenetic landscape (Waddington, 1957), reported in Figure 1.3a. In this metaphor, the cell is represented by a ball rolling down a landscape, the shape of which is determined by the complex interaction between the cell's genes and its environment. The resulting landscape, however, is characterised by many bifurcations so that the final trajectory of the ball will be determined by stochastic fluctuations in gene expression (i.e. epimutations). Figures 1.3b-1.3c illustrate how the epigenetic landscape of cancer cells might be expected to vary following treatment (Chisholm et al., 2016a). While evolutionary theories have continuously progressed since then (Levine et al., 2020), the notion that phenotypic fluctuations can lead to the emergence of new traits, which are then subjected to Darwinian competition, has been particularly popular in mathematical models of cancer evolutionary dynamics. Spontaneous phenotypic variation and dispersal, i.e. spatial movement, have been proposed to support phenotypic heterogeneity and thus identified as bet-hedging, i.e. risk-spreading, strategies that allow species to survive temporal changes in their environment (Villa Martín et al., 2019). On top of this, spatial

heterogeneity in environmental conditions and habit selection are indicated as one of the largest sources of biodiversity (Kotler and Brown, 2020).

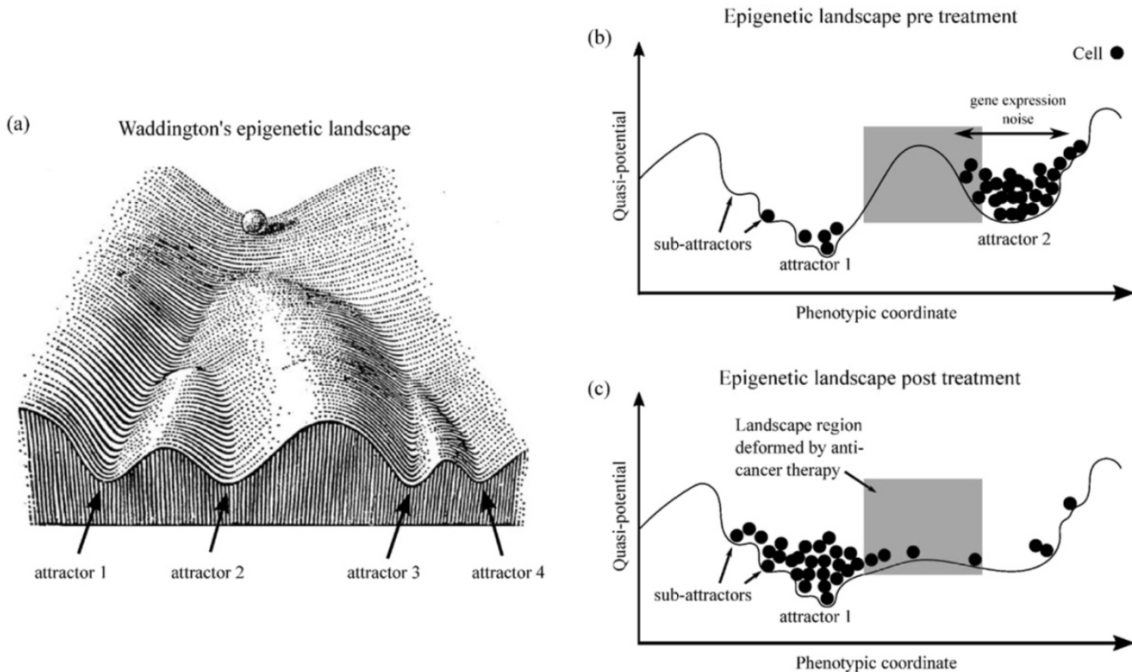


**Figure 1.3: Waddington epigenetic landscape.** (a) Waddington epigenetic landscape (Waddington, 1957), and how this might differ (b) preceding and (c) following treatment. Reprinted from Biochimica et Biophysica Acta (BBA) - General Subjects, 1860 (11), R. H. Chisholm, T. Lorenzi, J. Clairambault, Cell population heterogeneity and evolution towards drug resistance in cancer: Biological and mathematical assessment, theoretical treatment optimisation, 2627-2645, Copyright (2016), with permission from Elsevier (Chisholm et al., 2016a, Figure 3.2).

## 1.2.2 Modelling the evolutionary dynamics of cancer

Various stochastic and deterministic approaches have been used to model phenotypic evolution in cancer and development (Chisholm et al., 2016a).

**Stochastic approaches.** Probabilistic approaches in cancer include branching processes, which capture evolution towards irreversible malignancy (Altrock et al., 2015; Gardner, 2002; Komarova and Wodarz, 2005), IB or hybrid models, where the phenotypic evolution of each single cell is tracked allowing for reversible phenotypic changes. In the latter a finite range of phenotypic states, and therefore of resistance levels, is generally represented (Chisholm et al., 2016b; Stace et al., 2020), although models representing heritable traits with continuous variables have also been proposed (Chisholm et al., 2015; Robertson-Tessi et al., 2015). These works particularly focus on the emergence

of metabolic phenotypic heterogeneity and its impact on treatment outcomes, yielding analogous results to the models discussed in the next sections.

**Evolutionary game theory.** Another popular framework in which to study cancer evolutionary dynamics is that of evolutionary game theory models, in which evolutionary stable strategies are identified and employed in the study of the development of malignancy and resistance (Wölfel et al., 2021). Various works, such as those of Basanta and coworkers (Basanta et al., 2008, 2012a,b), track different populations each characterised by an intrinsic phenotypic state, thus only a finite number of states can be represented, as in deterministic ODE models with similar applications (Page and Nowak, 2002; Stiehl et al., 2014). On the other hand, many studies consider the evolution in time of sensitive and resistant populations, the latter depending on a continuous variable modelling what is referred to as resistance strategy which satisfies its own evolution equation (Brown et al., 2016; Gatenby and Vincent, 2003b,a; Gatenby and Gillies, 2008; Pressley et al., 2021; Zhang et al., 2017). These frameworks have been used to investigate different strategies in adaptive and evolutionary therapy, taking into account the cost of resistance, using optimal control methods (Cunningham et al., 2018, 2020; Staňková et al., 2019).

**The structured-population approach.** Bürger (2000) first proposed a nonlocal PDE model of mutation-selection dynamics of populations in which the phenotypic state of each individual is described by a continuous structuring variable under fixed environmental conditions, the more complex problems of which can be analysed using the Hamilton–Jacobi formalism advocated by Diekmann et al. (2005). In this framework, an evolution equation of the fittest phenotypic state can be analytically derived, rather than be imposed as in evolutionary game theory models. These works started a new branch of adaptive dynamics investigating nonlocal PDE models of the evolutionary dynamics of phenotype-structured populations, that has attracted the attention of the mathematical community, as demonstrated by the reviews in Sections 1.2.3 and 1.2.4, for well-mixed and spatially-structured populations, respectively. The possibility to capture phenotypic variants on a continuum, together with the mathematical progress made in characterising the solutions to these equations, have made these models particularly suited for the study of cancer phenotypic evolution and the development of therapeutic resistance (Chisholm et al., 2016a; Clairambault and Pouchol, 2019; Kuznetsov et al., 2021).

### 1.2.3 Nonlocal PDE models of well-mixed phenotype-structured populations

These models consider well-mixed populations  $n(t, \mathbf{y})$ , where  $t \geq 0$  indicates time, structured by some continuous trait  $\mathbf{y} \in \mathbb{R}^d$  ( $d \in \mathbb{N}$ ). The evolutionary dynamics of a population with phenotypic distribution  $n(t, \mathbf{y})$  can be modelled by a nonlocal version of the classic Lotka-Volterra equation<sup>11</sup> (cf. Clairambault and Pouchol (2019) and references therein), where the growth dynamics of individuals in each subpopulation depend on their phenotypic state  $\mathbf{y}$  and their death is determined by nonlocal interactions. In the field of adaptive dynamics, particular attention has been given to diffusive nonlocal Lotka-Volterra equations (Barles et al., 2009; Lorz et al., 2011; Perthame and Barles, 2008) in the form

$$\begin{cases} \partial_t n - \beta \Delta_{\mathbf{y}} n = R(\mathbf{y}, \rho(t))n & \mathbf{y} \in \mathbb{R}^d, \quad t \geq 0 \\ \rho(t) = \int_{\mathbb{R}^d} \psi(\mathbf{y}) n(t, \mathbf{y}) d\mathbf{y} \\ n(0, \mathbf{y}) = n^0(\mathbf{y}) \in L^1(\mathbb{R}^d), \quad n^0 \geq 0 \end{cases} \quad (1.1)$$

where the function  $\psi(\mathbf{y})$  can be seen, in analogy with the classic Lotka-Volterra equation, as the ‘predation’ of individuals of trait  $\mathbf{y}$  (Perthame and Barles, 2008), although it is often set to  $\psi(\mathbf{y}) \equiv 1$  to capture death due to intrapopulation competition for space and resources within the fitness function  $R$ . The diffusion term models spontaneous phenotypic variation at a rate  $\beta > 0$ , although more complex terms have been considered for alternative forms of phenotypic changes – e.g. nonlocal terms modelling mutations at birth (Carrillo et al., 2007; Desvillettes et al., 2008; Diekmann et al., 2005; Jabin and Schram, 2016; Perthame, 2006), and advection terms modelling stress-induced epimutations (Chisholm et al., 2015, 2016c[b]). These initial-value problems are often dealt with by introducing an  $\varepsilon$  parameterisation and time scaling. In the case of system (1.1), this

---

<sup>11</sup> The classic Lotka-Volterra equations, also known as predator-prey equations, model the evolution of population  $n_1(t)$  (prey) and  $n_2(t)$  (predator) as

$$\begin{cases} \dot{n}_1 = (r_1 - d_1 n_2)n_1 \\ \dot{n}_2 = (r_2 n_1 - d_2)n_2. \end{cases}$$

When considering infinitely many subpopulations, each characterised by a trait  $y \in \mathcal{Y} \subset \mathbb{R}$ , the dynamics of  $n(t, y)$  will mirror those of the prey  $n_1$ , where death can be induced by interactions with all other subpopulations, resulting in a nonlocal term. The equation may, for instance, be given by

$$\partial_t n = (r(y) - d(y) \int_{\mathcal{Y}} n dy) n,$$

although it may take many alternative forms.

results in

$$\begin{cases} \varepsilon \partial_t n_\varepsilon - \varepsilon^2 \Delta_{\mathbf{y}} n_\varepsilon = R(\mathbf{y}, \rho_\varepsilon(t)) n_\varepsilon & \mathbf{y} \in \mathbb{R}^d, \quad t \geq 0 \\ \rho_\varepsilon(t) = \int_{\mathbb{R}^d} \psi(\mathbf{y}) n_\varepsilon(t, \mathbf{y}) d\mathbf{y} \\ n_\varepsilon(0, \mathbf{y}) = n_\varepsilon^0(\mathbf{y}) \in L^1(\mathbb{R}^d), \quad n_\varepsilon^0 \geq 0 \end{cases} \quad (1.2)$$

which takes a form which allows the study of the asymptotic behaviour of the solution in the limit of rare phenotypic variation and long times, generally ideal to study evolution, as  $\varepsilon \rightarrow 0$ . In such limit one may obtain weak-\* convergence

$$n_\varepsilon(t, \mathbf{y}) \xrightarrow[\varepsilon \rightarrow 0]{*} \rho(t) \delta(\mathbf{y} - \bar{\mathbf{y}}(t)), \quad (1.3)$$

in the sense of measures<sup>12</sup>, where  $\bar{\mathbf{y}}(t)$  and  $\rho(t)$  are obtained from a constrained Hamilton-Jacobi equation (Barles et al., 2009; Lorz et al., 2011; Perthame and Barles, 2008). The monomorphism result exemplified by (1.3) is dependent on the assumption of a unique maximum of  $R$  such that  $R(\bar{\mathbf{y}}(t), \rho(t)) = 0$  for  $\rho(t)$  in (1.3), and  $R < 0$  otherwise, while polymorphism results may be obtained under alternative assumptions. Similar results can be obtained in the absence of diffusion, although in this case a uniform strict positivity assumption on  $n_\varepsilon^0$  is required otherwise extinction might occur (Clairambault and Pouchol, 2019; Lorz et al., 2011; Perthame, 2006; Pouchol et al., 2018). On the other hand, exact solutions to problems considering non-trivial diffusion, i.e. problems in the form (1.1), have also been constructed and take the form of Gaussian-like functions (Alfaro and Carles, 2014; Alfaro and Veruete, 2019; Chisholm et al., 2016b; Lorenzi et al., 2015). These models can be obtained in the continuum limit of stochastic IB models – see for instance Champagnat et al. (2006, 2008); Champagnat and Méléard (2011). Nonlocal PDE models of well-mixed phenotype-structured populations of cancer cells have been used to elucidate a series of evolutionary mechanisms responsible for the emergence of intratumour phenotypic heterogeneity and the development of therapeutic resistance.

**Insights into the emergence of intratumour phenotypic heterogeneity.** The work of Lavi et al. (2013) indicates that levels of intratumour phenotypic heterogeneity increase under higher rates of phenotypic variation (e.g. epimutations), suggesting that reducing the alteration rate as a first step in treatment may improve targeted therapy. This motivated further studies which confirmed the correlation between intratumour phenotypic heterogeneity levels and phenotypic variation rates (Cho and Levy, 2018b; Greene et al., 2014; Lorenzi et al., 2015, 2016, 2019), further indicating that phenotypic

---

<sup>12</sup> Consider  $n(y) \in L^1(\mathcal{Y})$  as a sequence of functions  $n_\varepsilon(y) \in L^1(\mathcal{Y})$ , and these as elements of the bigger space of Radon measures  $\mathcal{M}^1(\bar{\mathcal{Y}})$ . Then  $n$  is the weak-\* limit of  $n_\varepsilon$  if

$$\int_{\mathcal{Y}} n_\varepsilon \varphi(y) dy \xrightarrow[\varepsilon \rightarrow 0]{} \int_{\mathcal{Y}} n \varphi(y) dy \quad \forall \varphi(y) \in C(\bar{\mathcal{Y}}).$$

heterogeneity levels decrease under stronger environmental selective pressures. Moreover, harsher environments may lead the population to extinction, while in the case of survival, in constant environments, the cell population size at equilibrium depends on the maximum fitness and rate of death due to intrapopulation competition. On the other hand, in temporally fluctuating environments, e.g. cycling hypoxia, we observe temporal oscillations in the population size (Ardaševa et al., 2020b,c; Lorenzi et al., 2015). In the framework of competing populations characterised by different rates of spontaneous phenotypic variation, higher rates of phenotypic variation have been shown to provide a competitive advantage in periodically fluctuating environments, while lower rates are favourable in constant environments (Ardaševa et al., 2020b,c; Pouchol et al., 2018). Ardaševa et al. (2020c) highlight this might be particularly significant in vascularised tumours, where the environment transitions from normoxia to cycling and chronic hypoxia as the distance from blood vessels increases.

**Insights into the development of therapeutic resistance.** The first works modelling the evolutionary dynamics of cancer cells under therapy using a continuous variable to capture the level of therapeutic resistance of the cells indicate that treatment acts as a selective process and phenotypic variation as a diffusive one (Greene et al., 2014; Lavi et al., 2013; Lorz et al., 2013). In particular it has been shown, under constant concentrations of cytotoxic drugs until equilibrium, that higher doses of cytotoxic drugs promote a selective sweep towards weakly proliferating cells characterised by higher therapeutic resistance, lowering the level of intratumoural phenotypic heterogeneity (Chisholm et al., 2015; Lorenzi et al., 2016). However, harsher environments in combination with higher rates of phenotypic variability may lead to population extinction and more effective chemotherapy (Lorenzi et al., 2016; Stace et al., 2020). Stace et al. (2020), in particular, employ this result in the study of a combination therapeutic strategy relying on chemotherapy and epigenetic treatment. Previous works, on the other hand, theoretically assess the efficacy of different therapeutic strategies, considering various multidrug approaches and drug delivery schedules (Almeida et al., 2019; Cho and Levy, 2018b; Lorenzi et al., 2016; Lorz et al., 2013; Pouchol et al., 2018) – e.g. cytotoxic and cytostatic combination therapy, or continuous vs. on/off drug delivery – some even including healthy cells as a competing population to consider chemotherapeutic damage to healthy tissue (Lorz et al., 2013; Pouchol et al., 2018). Optimal therapeutic control strategies can be designed by applying optimal control methods to nonlocal PDEs of adaptive dynamics, and used to predict the qualitative behaviour of cancer cell populations under different strategies (Chisholm et al., 2016a; Clairambault and Pouchol, 2019; Kuznetsov et al., 2021). In this regard, the work of Almeida et al. (2019) indicates that continuous administration of a relatively low dose of the chemotherapy performs more closely to the

optimal dosing regimen to minimise the average number of tumour cells during the course of treatment.

### 1.2.4 Nonlocal PDE models of space- and phenotype-structured populations

Spatially explicit nonlocal PDE models of adaptive dynamics generally consider space- and phenotype-structured populations  $n(t, \mathbf{x}, \mathbf{y})$ , where  $\mathbf{x} \in \mathcal{X} \subseteq \mathbb{R}^d$  indicates the position in the  $d$ -dimensional spatial domain. The evolutionary dynamics of populations undergoing explicit spatial movement can be modelled by nonlocal versions of the Fisher-KPP model<sup>13</sup>. In this framework, individuals are assumed to undergo undirected random movement which translates mathematically into a Fickian diffusion term, as in the classic Fisher-KPP model (Fisher, 1937), and die due to competition for space and resources against all other individuals present at their position resulting in a nonlocal reaction term similarly to the nonlocal Fisher-KPP model (Berestycki et al., 2009).

**Heterogeneous motility and homogeneous reaction terms.** Particular attention has been given to models in which the structuring variable indicates individual mobility in order to investigate the mechanisms underlying the spatial spread and phenotypic evolution of populations with heterogeneous motility (Arnold et al., 2012; Benichou et al., 2012; Bouin and Calvez, 2014; Bouin et al., 2012), such as cane toad populations. These models comprise variations of nonlocal Fisher-KKP equations where the diffusion coefficient is given as a function of the structuring variable, and phenotypic changes are modelled via differential or integral operators. Analytical investigations of these models – which at times rely on an  $\varepsilon$  parameterisation and appropriate asymptotic limit – have led to travelling front solutions, with the most motile individuals selected at the edge of the invasion front in the case of bounded motility, and front acceleration in the case of unbounded motility. Similar results have been obtained in the case of a nonlocal advection-reaction-diffusion equation where, instead of Fickian diffusion, random movement towards less crowded regions results in a nonlocal advection term with velocity

---

<sup>13</sup> The classic 1D Fisher equation models the reaction-diffusion dynamics of a population of density  $n(t, x)$  as

$$\partial_t n - D \partial_{xx}^2 n = rn(1 - n),$$

and it is also known as the Fisher-KPP equation since the KPP equation, published in the same year by mathematicians Kolmogorov, Petrovsky and Piskunov, takes a similar form with a more generic reaction term  $F(n)$ . In the case of a population  $n(t, x, y)$ , structured also by a phenotypic variable  $y \in \mathcal{Y}$ , we retrieve the nonlocal Fisher-KPP equation

$$\partial_t n - D \partial_{xx}^2 n = rn(1 - \int_{\mathcal{Y}} n dy). .$$

field given as a function of the local number density of individuals (Lorenzi et al., 2021). The study of Lorenzi et al. (2021) also considers a heterogeneous reaction term, usually included in models with homogeneous motility.

**Homogeneous motility and heterogeneous reaction terms.** Models with a constant spatial diffusion coefficient and more complex reaction terms, defined as functions of the spatial and phenotypic variables, have also been considered. Alfaro and coworkers constructed travelling wave solutions under specific assumptions on the reaction term modelling an environmental cline, in order to study species adaptation to climate change (Alfaro et al., 2013, 2017). Bouin and Mirrahimi (2015) generalised the method developed for well-mixed populations (Barles et al., 2009; Lorz et al., 2011; Perthame and Barles, 2008) by considering the asymptotic limit of small spatial diffusion and rare phenotypic changes of a spatially explicit diffusive nonlocal Lotka-Volterra equation, retrieving population monomorphism under strict concavity assumptions of the reaction term. Existence of solutions in the case of non-trivial spatial diffusion and mutations, modelled nonlocally, has been shown by Arnold et al. (2012) whose numerical solutions indicate population polymorphism can arise for high enough spatial diffusion. The role spatial movement plays in the emergence of a polymorphic population has also been demonstrated by the work of Mirrahimi who studied the evolutionary dynamics of well-mixed populations in separate sites undergoing habitat-specific selection and transition between the sites, both in the rare phenotypic variation limit (Mirrahimi, 2017) and under non-trivial phenotypic variation (Mirrahimi and Gandon, 2020). Other nonlocal PDE models of space- and phenotype-structured populations have been proposed in the study of cell migration incorporating bound and available membrane receptor densities as structuring variables (Domschke et al., 2017; Hodgkinson et al., 2018).

**Nonlocal PDE models of space- and phenotype-structured cancer cell populations.** Lorz et al. (2015) proposed the first spatially explicit nonlocal PDE model of cancer phenotypic evolution with continuous phenotypic structure. Their model comprises a nonlocal Lotka-Volterra equation similar to previous non-diffusive ones proposed for well-mixed populations (Clairambault and Pouchol, 2019; Lorz et al., 2011; Perthame, 2006; Pouchol et al., 2018), coupled with elliptic equations describing the dynamics of abiotic factors. While their work solely relied on numerical solutions, it inspired further analytical works in which the balance equation for the phenotypic distribution  $n$  is coupled, through the reaction term, with elliptic equations describing the dynamics of abiotic factors (Jabin and Schram, 2016; Mirrahimi and Perthame, 2015). The abiotic factors, taken at the quasi-stationary equilibrium, are assumed to undergo diffusion and consumption by the cells at rates dictated by the cell phenotypic state. Cho and

---

Levy (2017) further included cell density-dependent drug permeability. Moreover, Cho and Levy (2018a) include cell density-dependent pressure-driven movement of cells and consider asymmetric tumour growth in a heterogeneous environment under combination therapy, including competition with healthy cells in a later study (Cho and Levy, 2020). On the other hand, Lorenzi et al. (2018) included an influx term in the abiotic factor concentration equation in order to model nutrient and drug inflow from either the boundary of an avascular tumour or from the blood vessels of a vascularised one. In particular, Lorenzi et al. (2018) perform numerical simulations on the 3D geometry of an *in vivo* human hepatic tumour imaged using computerised tomography, on which they subsequently construct artificial blood vessels.

These works indicate that the presence of spatial gradients in the concentration of abiotic factors, which can result from the nonlinear interplay with cancer cells, leads to the selection of cells in different phenotypic states in different parts of the spatial domain. This fosters the emergence of intratumour phenotypic heterogeneity, and it supports the presence of resistant cells prior to treatment. Moreover, numerical simulations point towards the advantage of combination therapy (Cho and Levy, 2017, 2020; Lorz et al., 2015), in agreement with studies conducted for well-mixed populations. The work presented in Chapter 2 builds on the model of Lorenzi et al. (2018) including spatial diffusion and phenotypic variation in the PDE describing cell evolutionary dynamics, and systematically assessing the impact of tissue vascularisation on the level of intratumour phenotypic heterogeneity. Fiandaca et al. (2021b) extended our modelling framework to numerically investigate the emergence of resistance to both hypoxia and acidity at various distances from a blood vessel, by including two phenotypic traits and multiple abiotic factors, i.e. oxygen, glucose and lactate. Their work indicates, coherently with empirical evidence, that cancer resistance to hypoxia may be developed first and resistance to acidity later.

## Chapter 2

# A space- and phenotype-structured PDE model of the emergence of intratumour phenotypic heterogeneity in vascularised tumours

The empirical and theoretical work presented in Section 1.1 points towards a key role played by spatial variability in the intratumoural concentration of oxygen in the emergence of intratumour metabolic phenotypic heterogeneity. This affects anti-cancer therapy, on one hand because it supports the emergence of chemotherapeutic resistant phenotypes, and on the other by making it impossible to exhaustively portray the phenotypic composition of the whole tumour tissue from single biopsies. This issue is particularly crucial in vascularised tumours, where the presence of intratumoural blood vessels results in highly heterogeneous oxygen distributions. Moreover, it has been proposed that intratumour phenotypic heterogeneity is fostered by higher rates of phenotypic variation, e.g. due to non-genetic instability, and spatial dispersal.

In this chapter, we use a spatially explicit phenotype-structured model to elucidate the eco-evolutionary dynamics that underpin the emergence of phenotypic heterogeneity in vascularised tumours, and the development of resistance to chemotherapeutic agents. Building upon the modelling framework developed by Lorenzi et al. (2018) and Lorz et al. (2015), the model comprises a nonlocal PDE that governs the local phenotypic distribution of cells within the tumour tissue, similar to equations that have received increasing attention from the mathematical community as seen in Section 1.2. This equation is coupled with a parabolic PDE that governs the local concentration of oxygen

and one for the chemotherapeutic agent, whereby a spatially heterogeneous source term captures the presence of intratumoural blood vessels which bring oxygen and the drug into the tumour tissue. Compared to previous related studies (Lorenzi et al., 2018; Lorz et al., 2015), the main novelties of the work here presented are the following:

- The model takes into account the effect of movement and phenotypic variation of tumour cells and, in addition, it does not rely on a quasi-stationary equilibrium assumption for the oxygen concentration;
- In the first instance, in the absence of spatial movement, no smallness assumptions are imposed on the rate at which phenotypic changes occur. In this more general scenario, building upon a method of proof presented for well-mixed populations (Almeida et al., 2019; Ardaševa et al., 2020b; Chisholm et al., 2016b; Lorenzi et al., 2015), an analytical study of evolutionary dynamics is carried out. In particular, explicit solutions to the equation for the phenotypic distribution of tumour cells are constructed and, considering the case where the concentrations of oxygen and chemotherapeutic agent are stationary, a detailed quantitative characterisation of the long-time asymptotic behaviour of such solutions is given;
- Next, the model including both phenotypic variation and spatial movement is addressed. Building upon previous asymptotic methods proposed for simpler models (Bouin and Mirrahimi, 2015; Jabin and Schram, 2016; Mirrahimi and Perthame, 2015), a formal asymptotic analysis is conducted on the equation for the phenotypic distribution of tumour cells, in the asymptotic limit of rare phenotypic changes, low diffusion and many cell generations, considering again the case where the concentrations of oxygen and chemotherapeutic agent are stationary, and the solutions are compared with those obtained in the previous case;
- While previous studies are mainly focused on avascular tumours, in this chapter we consider vascularised tumours. The analytical results obtained are integrated with numerical simulations of a calibrated version of the model based on biologically consistent parameter values, in order to further assess the impact of the dynamics of oxygen and chemotherapeutic agent on the phenotypic evolution of tumour cells in vascularised tumours;
- Different possible definitions of the source term in the PDEs governing the abiotic factors are considered, including definitions that are derived from clinical images obtained using dynamic optical coherence tomography (D-OCT) (Schuh et al., 2017) – i.e. a non-invasive imaging technique that enables the visualisation of cutaneous microvasculature in 2D tissue sections with a width of, and at a depth of, up to several millimetres (Olsen et al., 2018);
- The numerical solutions are employed to systematically assess the impact of the degree of tumour tissue vascularisation on the level of pre-treatment phenotypic heterogeneity of tumour cells, which is mathematically quantified through suitable

diversity indices.

Taken together, these elements of novelty widen considerably the range of application of the results of this study, as will be discussed in Chapter 3, and support a more in-depth theoretical understanding of the eco-evolutionary process which leads to the emergence of phenotypic heterogeneity and the development of chemotherapeutic resistance in vascularised tumours.

This chapter is organised as follows. In Section 2.1, the equations of the model and the underlying modelling assumptions are introduced. In Section 2.2, the analytical results of the study of evolutionary dynamics in the absence of spatial diffusion are presented, followed by those of the formal asymptotic analysis. In Section 2.3, numerical solutions that confirm and extend the analytical results obtained are reported. A discussion of these results, together with possible research perspectives, is given in Chapter 3.

## 2.1 The mathematical model

We model the evolution of tumour cells within a region of a vascularised tumour along with the dynamical interactions that occur between tumour cells and both oxygen and a chemotherapeutic agent, which are released from the intratumoural vascular network.

The tumour region is approximated as a bounded set  $\Omega \subset \mathbb{R}^d$ , with smooth boundary  $\partial\Omega$ , where  $d = 1, 2, 3$  depending on the biological scenario under study. The spatial position of tumour cells is described by a vector  $\mathbf{x} \in \overline{\Omega}$  and the phenotypic state of every cell is modelled by a scalar variable  $y \in \mathbb{R}$ , which represents the rescaled level of a hypoxia-inducible factor. Building upon the ideas presented in Lorenzi et al. (2016) and Pisco and Huang (2015), we assume that there is a sufficiently high level of expression of the hypoxia-inducible factor  $y^H$  conferring both the highest rate of cellular division via anaerobic energy pathways and the highest level of resistance to chemotherapy, while there is a sufficiently low level of expression of the hypoxia-inducible factor  $y^L < y^H$  providing the highest rate of cellular division via aerobic energy pathways. Without loss of generality, we define  $y^H := 1$  and  $y^L := 0$ , so that values of  $y \rightarrow 1$  correspond to phenotypic variants with higher rates of cellular division via anaerobic energy pathways and higher levels of chemoresistance (i.e. anaerobic and chemoresistant phenotypic variants), whereas values of  $y \rightarrow 0$  correspond to phenotypic variants with higher rates of cellular division via aerobic energy pathways (i.e. aerobic phenotypic variants) – see Figure 2.1.

The phenotypic distribution of tumour cells at time  $t \geq 0$  and position  $\mathbf{x}$  is described by the function  $n(t, \mathbf{x}, y)$ , while the functions  $s(t, \mathbf{x})$  and  $c(t, \mathbf{x})$  describe, respectively, the oxygen concentration and the concentration of the chemotherapeutic agent at time  $t$  and position  $\mathbf{x}$ . Moreover, at each time  $t$ , we define the density of tumour cells at position  $\mathbf{x}$

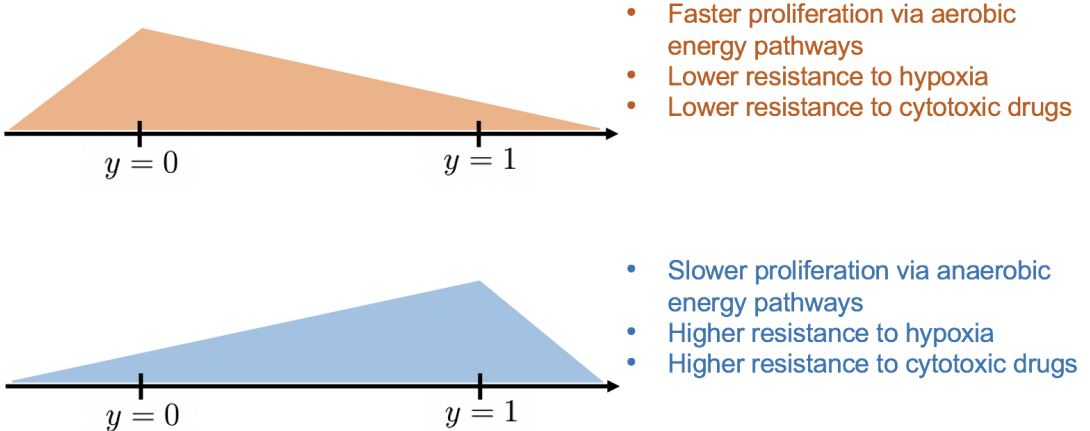


**Figure 2.1: Assumptions on the phenotypic state.** Summary of the modelling assumptions on the phenotypic state  $y \in \mathbb{R}$  of each cancer cell.

as

$$\rho(t, \mathbf{x}) := \int_{\mathbb{R}} n(t, \mathbf{x}, y) dy, \quad (2.1)$$

the local mean phenotypic state as

$$\mu(t, \mathbf{x}) := \frac{1}{\rho(t, \mathbf{x})} \int_{\mathbb{R}} y n(t, \mathbf{x}, y) dy \quad (2.2)$$

and the related variance as

$$\sigma^2(t, \mathbf{x}) := \frac{1}{\rho(t, \mathbf{x})} \int_{\mathbb{R}} y^2 n(t, \mathbf{x}, y) dy - \mu^2(t, \mathbf{x}). \quad (2.3)$$

We additionally define the total cell mass<sup>1</sup> and the fraction of cells in the phenotypic state  $y$  within the tumour, respectively, as

$$N(t) := \int_{\Omega} \rho(t, \mathbf{x}) d\mathbf{x} \quad \text{and} \quad F(t, y) := \frac{1}{N(t)} \int_{\Omega} n(t, \mathbf{x}, y) d\mathbf{x}. \quad (2.4)$$

### 2.1.1 Dynamics of tumour cells

Tumour cells divide, die, move randomly (i.e. undergo undirected, spontaneous migration) and undergo spontaneous phenotypic changes, that is, heritable phenotypic changes that occur randomly due to non-genetic instability and are not induced by any selective pressure (Huang, 2013b). The dynamic of the local cell phenotypic distribution of tumour cells  $n(t, \mathbf{x}, y)$  is governed by the following boundary value problem subject to a suitable

---

<sup>1</sup>In the proposed framework, the cell mass  $N(t)$  is given in units of ‘cells’ so that it may be understood as an approximate total cell number.

initial condition

$$\begin{cases} \partial_t n - \beta \partial_{yy}^2 n - D_n \Delta_{\mathbf{x}} n = R(y, \rho(t, \mathbf{x}), s(t, \mathbf{x}), c(t, \mathbf{x}))n & \text{in } \Omega, \\ \rho(t, \mathbf{x}) := \int_{\mathbb{R}} n(t, \mathbf{x}, y) dy, \\ \nabla_{\mathbf{x}} n \cdot \hat{\mathbf{u}} = 0 & \text{on } \partial\Omega, \end{cases} \quad (2.5)$$

where  $\hat{\mathbf{u}}$  is the unit normal to  $\partial\Omega$  that points outward from  $\Omega$ . The first diffusion term on the left-hand side of the nonlocal parabolic equation (2.5) describes the effect of heritable spontaneous phenotypic changes that occur randomly due to non-genetic instability and are not induced by any selective pressure, which occur at rate  $\beta > 0$ . The second diffusion term models the effect of cell random movement and the parameter  $D_n \geq 0$  represents the cell motility. The function  $R(y, \rho(t, \mathbf{x}), s(t, \mathbf{x}), c(t, \mathbf{x}))$  represents the fitness of tumour cells in the phenotypic state  $y$  at position  $\mathbf{x}$  and time  $t$  under the local environmental conditions given by the cell density  $\rho(t, \mathbf{x})$ , the oxygen concentration  $s(t, \mathbf{x})$  and the concentration of chemotherapeutic agent  $c(t, \mathbf{x})$  (i.e. the phenotypic fitness landscape of the tumour at position  $\mathbf{x}$  and time  $t$ ). In particular, we consider

$$R(y, \rho, s, c) := p(y, s) - \zeta \rho - k(y, c) \quad (2.6)$$

with

$$p(y, s) := f(y) + g(y, s). \quad (2.7)$$

Here,  $f(y)$  is a  $C^2$ -function such that

$$\arg \max_{y \in \mathbb{R}} f(y) = 1, \quad f(1) > 0, \quad \partial_{yy}^2 f < 0, \quad (2.8)$$

$g(y, s)$  is a  $C^2$ -function of  $y$  and a  $C^1$ -function of  $s$  that satisfies the following assumptions

$$\begin{aligned} \arg \max_{y \in \mathbb{R}} g(y, s) &= 0, \quad g(0, s) > 0, \quad \partial_{yy}^2 g(\cdot, s) < 0 \quad \forall s \in (0, \infty) \\ \text{and} \quad \lim_{s \rightarrow \infty} g(0, s) &> f(1), \end{aligned} \quad (2.9)$$

$$g(\cdot, 0) = 0, \quad \partial_s |g(\cdot, s)| \geq 0 \quad \forall s \in (0, \infty), \quad (2.10)$$

and  $k(y, c)$  is a  $C^2$ -function of  $y$  and a  $C^1$ -function of  $c$  that satisfies the following assumptions

$$\arg \min_{y \in \mathbb{R}} k(y, c) = 1, \quad k(1, c) = 0, \quad \partial_{yy}^2 k(\cdot, c) > 0 \quad \forall c \in (0, \infty), \quad (2.11)$$

$$k(\cdot, 0) = 0, \quad \partial_c k(\cdot, c) \geq 0 \quad \forall c \in (0, \infty). \quad (2.12)$$

Definition (2.6) along with assumptions (2.11) and (2.12) models a biological scenario whereby the background fitness of tumour cells in the phenotypic state  $y$  at position  $\mathbf{x}$  and time  $t$  is given by a function  $p(y, s(t, \mathbf{x}))$ , the value of which is reduced:

- Due to competition for limited space, by a certain amount which is the same for all phenotypic variants and is proportional to  $\rho(t, \mathbf{x})$ , with a proportionality constant  $\zeta > 0$  that is related to the local carrying capacity of the tumour;
- Due to the cytotoxic action of the chemotherapeutic agent, by a certain amount  $k(y, c)$  which increases monotonically with the concentration of the chemotherapeutic agent  $c$  and is smaller for phenotypic variants with  $y \rightarrow 1$ , which are characterised by higher levels of chemoresistance, and is null for the phenotypic variant corresponding to  $y = 1$ , since such a phenotypic variant is assumed to be completely resistant to the chemotherapeutic agent.

Definition (2.7) corresponds to the case where the background fitness  $p(y, s)$  is defined as a linear combination of the background fitness associated with anaerobic energy pathways  $f(y)$  and that associated with aerobic energy pathways  $g(y, s)$ . In particular, assumptions (2.8)-(2.10) translate into mathematical terms the following biological ideas:

- The state  $y = 1$  corresponds to the phenotypic variant with the maximal background fitness associated with anaerobic energy pathways, whereas the state  $y = 0$  corresponds to the phenotypic variant with the maximal background fitness associated with aerobic energy pathways.
- Due to the fact that less fit phenotypic variants are driven to extinction by natural selection, the background fitness associated with anaerobic (or aerobic) energy pathways can be negative for phenotypic variants with values of  $y$  sufficiently far from 1 (or 0).
- Because of the fitness cost associated with a less efficient anaerobic metabolism (Basant et al., 2008), the maximal background fitness of aerobic phenotypic variants in well-oxygenated environments is larger than the maximal background fitness of anaerobic phenotypic variants.
- The larger is the oxygen concentration, the stronger is the impact of the background fitness associated with aerobic energy pathways  $g(y, s)$  on the background fitness  $p(y, s)$ .

In particular, following the modelling strategies presented by Lorenzi et al. (2018), here we use the definitions

$$f(y) := \varphi \left[ 1 - (1 - y)^2 \right], \quad g(y, s) := \gamma_s \frac{s}{\alpha_s + s} (1 - y^2) \quad (2.13)$$

and

$$k(y, c) := \gamma_c \frac{c}{\alpha_c + c} (1 - y)^2, \quad (2.14)$$

where  $\varphi > 0$  is the maximal background fitness of anaerobic phenotypic variants,  $\gamma_s > \varphi$  is the maximal background fitness of aerobic phenotypic variants,  $\alpha_s > 0$  and  $\alpha_c > 0$  are the Michaelis-Menten constants of oxygen and of chemotherapeutic agent respectively, and  $\gamma_c > 0$  is the maximal reduction of the background fitness due to the cytotoxic action of the chemotherapeutic agent. Definitions (2.13) and (2.14) satisfy assumptions (2.8)-(2.12), ensure analytical tractability of the model and lead to a fitness function  $R(y, \rho, s, c)$  that is close to the approximate fitness landscapes which can be inferred from experimental data through regression techniques – see, for instance, equation (1) in Otwinowski and Plotkin (2014). In fact, with these definitions, after a little algebra, the difference  $p(y, s) - k(y, c)$  in (2.6) can be rewritten as

$$p(y, s) - k(y, c) = a(s, c) - b(s, c) (y - h(s, c))^2 \quad (2.15)$$

where

$$a(s, c) := \gamma_s \frac{s}{\alpha_s + s} - \gamma_c \frac{c}{\alpha_c + c} + \frac{\left( \varphi + \gamma_c \frac{c}{\alpha_c + c} \right)^2}{\varphi + \gamma_s \frac{s}{\alpha_s + s} + \gamma_c \frac{c}{\alpha_c + c}}, \quad (2.16)$$

$$b(s, c) := \varphi + \gamma_s \frac{s}{\alpha_s + s} + \gamma_c \frac{c}{\alpha_c + c} \quad (2.17)$$

and

$$h(s, c) := \frac{\varphi + \gamma_c \frac{c}{\alpha_c + c}}{\varphi + \gamma_s \frac{s}{\alpha_s + s} + \gamma_c \frac{c}{\alpha_c + c}}. \quad (2.18)$$

Here,  $a(s, c)$  is the maximum fitness,  $h(s, c)$  is the fittest phenotypic state and  $b(s, c)$  is the selection gradient under the environmental conditions corresponding to the oxygen concentration  $s(t, \mathbf{x})$  and the concentration of chemotherapeutic agent  $c(t, \mathbf{x})$ . We remark that  $b(s, c)$  is a selection gradient in that it provides a measure of the strength of the selective pressure exerted on tumour cells by oxygen and the chemotherapeutic agent (Lande and Arnold, 1983). Notice that,

$$h : [0, \infty) \times [0, \infty) \rightarrow [0, 1], \quad \lim_{s \rightarrow 0} h(s, \cdot) = 1, \quad \lim_{s \rightarrow \infty} h(s, 0) = \frac{1}{1 + \frac{\gamma_s}{\varphi}},$$

and

$$\lim_{c \rightarrow \infty} h(s, c) = \frac{1}{1 + \frac{\gamma_s}{\varphi + \gamma_c} \frac{s}{\alpha_s + s}} \quad \forall s \in [0, \infty).$$

Hence, consistent with our modelling assumptions,

- For any concentrations of oxygen and chemotherapeutic agent, the fittest phenotypic state is between  $y = 0$  (i.e. the state corresponding to the phenotypic variant with the highest rate of cellular division via aerobic energy pathways) and  $y = 1$

(i.e. the state corresponding to the phenotypic variant with the highest rate of cellular division via anaerobic energy pathways and the highest level of resistance to chemotherapy);

- In hypoxic conditions (i.e. when  $s \rightarrow 0$ ), the fittest phenotypic state is  $y = 1$ ;
- When there is no chemotherapeutic agent (i.e. when  $c \equiv 0$ ), in well-oxygenated environments (i.e. when  $s \rightarrow \infty$ ) the larger is the ratio between the maximal background fitness of aerobic phenotypic variants  $\gamma_s$  and the maximal background fitness of anaerobic phenotypic variants  $\varphi$ , the closer the fittest phenotypic state will be to  $y = 0$ ;
- Under high-dose chemotherapy, the smaller is the ratio between the maximal background fitness of aerobic phenotypic variants  $\gamma_s$  and the maximal reduction of the background fitness of aerobic phenotypic variants due to the cytotoxic action of the chemotherapeutic agent  $\gamma_c$ , the closer the fittest phenotypic state will be to  $y = 1$ .

### 2.1.2 Dynamics of abiotic factors

We let the oxygen and the chemotherapeutic agent enter the tumour through intratumoural blood vessels, diffuse in space, decay over time and be consumed by tumour cells which divide via aerobic pathways. In this scenario, the dynamic of the oxygen concentration  $s(t, \mathbf{x})$  is governed by the following boundary value problem

$$\begin{cases} \partial_t s - D_s \Delta_{\mathbf{x}} s = - \int_{\mathbb{R}} r_s(y, s) n(t, \mathbf{x}, y) dy - \lambda_s s + q_s(t, \mathbf{x}) & \text{in } \Omega, \\ \nabla_{\mathbf{x}} s \cdot \hat{\mathbf{u}} = 0 & \text{on } \partial\Omega, \end{cases} \quad (2.19)$$

while the dynamic of the chemotherapeutic agent concentration  $c(t, \mathbf{x})$  is governed by the boundary value problem

$$\begin{cases} \partial_t c - D_c \Delta_{\mathbf{x}} c = - \int_{\mathbb{R}} r_c(y, c) n(t, \mathbf{x}, y) dy - \lambda_c c + q_c(t, \mathbf{x}) & \text{in } \Omega, \\ \nabla_{\mathbf{x}} c \cdot \hat{\mathbf{u}} = 0 & \text{on } \partial\Omega, \end{cases} \quad (2.20)$$

both subject to a suitable initial condition and coupled to the nonlocal parabolic equation (2.5). In (2.19)<sub>1</sub> and (2.20)<sub>1</sub>, the parameters  $D_s > 0$  and  $D_c > 0$  are the diffusion coefficients of oxygen and of chemotherapeutic agent, the functions  $r_s(y, s)$  and  $r_c(y, c)$  are the consumption rates of oxygen and of chemotherapeutic agent by tumour cells in the phenotypic state  $y$ , the parameters  $\lambda_s > 0$  and  $\lambda_c > 0$  are the natural decay rates of oxygen and of chemotherapeutic agent, and the source terms  $q_s(t, \mathbf{x})$  and  $q_c(t, \mathbf{x})$  model

the influx of oxygen and of chemotherapeutic agent from the intratumoural blood vessels at position  $\mathbf{x} \in \Omega$  and at time  $t$ .

We assume that oxygen is consumed only by phenotypic variants corresponding to values of  $y$  for which the fitness associated with aerobic energy pathways  $g(y, s)$  is positive and we let oxygen consumption occur at a rate proportional to  $g(y, s)$ . Moreover, we assume that the chemotherapeutic agent is consumed by phenotypic variants corresponding to different  $y$  at different rates proportional to the amount  $k(y, c)$  by which their background fitness is reduced due to the cytotoxic action of the chemotherapeutic agent. In accordance with these assumptions, we use the following definitions

$$r_s(y, s) := \eta_s (g(y, s))_+ \quad \text{and} \quad r_c(y, s) := \eta_c k(y, c), \quad (2.21)$$

where  $\eta_s > 0$  and  $\eta_c > 0$  are constants of proportionality and  $(\cdot)_+$  denotes the positive part of  $(\cdot)$ . We let  $\omega \subset \Omega$  be the set of points within the tumour tissue which are occupied by blood vessels and, since we do not consider the formation of new blood vessels, we assume  $\omega$  to be given and remain constant in time. Therefore, we define the source terms  $q_s$  and  $q_c$  as

$$q_s(t, \mathbf{x}) := i_s(t, \mathbf{x}) \mathbf{1}_\omega(\mathbf{x}) \quad \text{and} \quad q_c(t, \mathbf{x}) := i_c(t, \mathbf{x}) \mathbf{1}_\omega(\mathbf{x}), \quad (2.22)$$

where  $\mathbf{1}_\omega$  is the indicator function of the set  $\omega$ , and  $i_s(t, \mathbf{x})$  and  $i_c(t, \mathbf{x})$  are the rates of inflow of oxygen and of chemotherapeutic agent through intratumoural blood vessels at position  $\mathbf{x} \in \omega$  and time  $t$ . In particular, we assume the rate of inflow of oxygen and chemotherapeutic agent through intratumour blood vessels be constant in time and the same for all vessels, i.e. we define the functions  $i_s(t, \mathbf{x})$  and  $i_c(t, \mathbf{x})$  in (2.22) as

$$i_s(t, \mathbf{x}) \equiv I_s \quad \text{and} \quad i_c(t, \mathbf{x}) \equiv I_c, \quad (2.23)$$

for given inflow rates  $I_s > 0$  and  $I_c > 0$ .

**Remark 1.** *In this chapter, we do not take into account the effect of mechanical interactions between tumour cells and blood vessels and we do not allow tumour cells to extravasate. Therefore, focussing on the case of intratumoural blood vessels of small size, we implicitly make the following simplifying assumptions: (i) a point  $\mathbf{x}$  can be simultaneously occupied by blood vessels and tumour cells; (ii) cell movement is not affected by the presence of blood vessels. Therefore, we do not impose any condition on  $n(t, \mathbf{x}, y)$  in  $\omega$ .*

## 2.2 Analytical investigations

In order to disentangle and quantify the impact of different evolutionary parameters on the emergence and development of intratumour phenotypic heterogeneity, in Section 2.2.1 we construct explicit solutions of (2.5) in the absence of spatial diffusion and study the long-time asymptotic behaviour of such solutions in the case where the concentrations of oxygen and of chemotherapeutic agent are stationary, i.e. when, instead of being solutions of (2.19) and (2.20), the functions  $s(t, \mathbf{x})$  and  $c(t, \mathbf{x})$  are given and satisfy the following assumptions

$$s(t, \mathbf{x}) \equiv S(\mathbf{x}) \quad \text{and} \quad c(t, \mathbf{x}) \equiv C(\mathbf{x}), \quad (2.24)$$

with  $S(\mathbf{x})$  and  $C(\mathbf{x})$  being given functions such that

$$S \in C(\bar{\Omega}) \quad \text{with} \quad S : \bar{\Omega} \rightarrow \mathbb{R}_{\geq 0} \quad \text{and} \quad C \in C(\bar{\Omega}) \quad \text{with} \quad C : \bar{\Omega} \rightarrow \mathbb{R}_{\geq 0}. \quad (2.25)$$

In Section 2.2.2 we consider system (2.5) in the presence of spatial diffusion and consider the following: typical values of the epimutation rate  $\beta$  are one or two orders of magnitude larger than the rate of somatic DNA mutation (Doerfler and Böhm, 2006, p.45), which is about  $10^{-12} \text{ s}^{-1}$  (Duesberg et al., 2000), and typical values of the cell diffusivity  $D_n$  are about  $10^{-12} \text{ cm}^2 \text{s}^{-1}$  (Smith et al., 2004; Wang et al., 2009). Hence, spontaneous phenotypic changes and cell random movement occur on slower time scales compared to cell division and death. To capture this fact, in Section 2.2.2 we introduce a small parameter  $\varepsilon > 0$ , assume both  $\beta := \varepsilon^2$  and  $D_n := \varepsilon^2$ , and formally analyse the long-time asymptotic behaviour of the solution to (2.5) in the asymptotic limit  $\varepsilon \rightarrow 0$ , again in the case where the concentrations of oxygen and of chemotherapeutic agent are stationary, i.e. under assumptions (2.24) and (2.25).

Under assumptions (2.24) and (2.25), we introduce the abridged notation

$$a \equiv a(S(\mathbf{x}), C(\mathbf{x})), \quad b \equiv b(S(\mathbf{x}), C(\mathbf{x})), \quad h \equiv h(S(\mathbf{x}), C(\mathbf{x})).$$

### 2.2.1 Analytical results in the absence of spatial diffusion

We first focus on the case without spatial diffusion of cells, i.e. the case in which  $D_n = 0$ . Note that in this case equation (2.5)<sub>1</sub> is posed on  $\bar{\Omega}$  and we do not require boundary conditions (2.5)<sub>3</sub>. Under these assumptions, the system (2.5) reduces to

$$\begin{cases} \partial_t n - \beta \partial_{yy}^2 n = R(y, \rho(t, \mathbf{x}), s(t, \mathbf{x}), c(t, \mathbf{x}))n & \text{in } \bar{\Omega}, \\ \rho(t, \mathbf{x}) := \int_{\mathbb{R}} n(t, \mathbf{x}, y) dy. \end{cases} \quad (2.26)$$

In this scenario, under assumptions (2.24) and (2.25), we construct explicit solutions of (2.26) (*cf.* Proposition 1) and we study the asymptotic behaviour of such solutions for  $t \rightarrow \infty$  (*cf.* Theorem 1).

**Initial conditions.** In agreement with much of the previous work on the mathematical analysis of the evolutionary dynamics of continuously-structured populations (Perthame, 2006; Rice, 2004), we consider the case where at time  $t = 0$  the local phenotypic distribution of tumour cells is of the following Gaussian form

$$n(0, \mathbf{x}, y) = \frac{\rho_0(\mathbf{x})}{\sqrt{2\pi\sigma_0^2(\mathbf{x})}} \exp\left[-\frac{1}{2\sigma_0^2(\mathbf{x})}(y - \mu_0(\mathbf{x}))^2\right], \quad \forall \mathbf{x} \in \overline{\Omega} \quad (2.27)$$

where

$$\begin{aligned} \rho_0 &\in C(\overline{\Omega}) \text{ with } \rho_0 : \overline{\Omega} \rightarrow \mathbb{R}_{>0}, & \sigma_0^2 &\in C(\overline{\Omega}) \text{ with } \sigma_0^2 : \overline{\Omega} \rightarrow \mathbb{R}_{>0}, \\ \mu_0 &\in C(\overline{\Omega}) \text{ with } \mu_0 : \overline{\Omega} \rightarrow \mathbb{R}. \end{aligned} \quad (2.28)$$

**Proposition 1.** *Let assumptions (2.6), (2.15)-(2.18), (2.24) and (2.25) hold. Then, (2.26) subject to (2.27) and (2.28) admits the exact solution*

$$n(t, \mathbf{x}, y) = \rho(t, \mathbf{x}) \sqrt{\frac{v(t, \mathbf{x})}{2\pi}} \exp\left[-\frac{v(t, \mathbf{x})}{2}(y - \mu(t, \mathbf{x}))^2\right], \quad \forall \mathbf{x} \in \overline{\Omega}, \quad (2.29)$$

with  $\rho(t, \mathbf{x})$ ,  $\mu(t, \mathbf{x})$  and  $v(t, \mathbf{x}) := 1/\sigma^2(t, \mathbf{x})$  being solutions of the Cauchy problem

$$\left\{ \begin{array}{l} \partial_t v = 2(b - \beta v^2), \quad v \equiv v(t, \mathbf{x}), \\ \partial_t \mu = \frac{2}{v} b(h - \mu), \quad \mu \equiv \mu(t, \mathbf{x}), \\ \partial_t \rho = \left[ \left( a - \frac{b}{v} - b(\mu - h)^2 \right) - \zeta \rho \right] \rho, \quad \rho \equiv \rho(t, \mathbf{x}), \\ v(0, \mathbf{x}) = 1/\sigma_0^2(\mathbf{x}), \quad \mu(0, \mathbf{x}) = \mu_0(\mathbf{x}), \quad \rho(0, \mathbf{x}) = \rho_0(\mathbf{x}), \end{array} \right. \quad \text{in } \overline{\Omega}. \quad (2.30)$$

**Theorem 1.** *Let assumptions (2.6), (2.15)-(2.18), (2.24) and (2.25) hold. Then, the solution of (2.26) subject to (2.27) and (2.28) is such that*

$$\rho(t, \cdot) \rightarrow \rho_\infty(S, C), \quad \mu(t, \cdot) \rightarrow \mu_\infty(S, C), \quad \sigma^2(t, \cdot) \rightarrow \sigma_\infty^2(S, C) \quad \text{as } t \rightarrow \infty, \quad (2.31)$$

with

$$\begin{aligned}\rho_\infty(S, C) &= \max \left( 0, \frac{a(S, C) - \sqrt{\beta b(S, C)}}{\zeta} \right), \quad \mu_\infty(S, C) = h(S, C), \\ \sigma_\infty^2(S, C) &= \sqrt{\frac{\beta}{b(S, C)}}.\end{aligned}\tag{2.32}$$

**Proof sketch.** The proofs of Proposition 1 and Theorem 1 are reported in Appendix A.1 and Appendix A.2, respectively. Reported below are the key steps of these proofs.

- *Proposition 1:* Consider the nonlocal PDE (2.26) complemented with (2.27) and (2.28) under assumptions (2.6) and (2.15)-(2.18). Substituting the Gaussian ansatz (2.29), together with definitions (2.6) and (2.15), into (2.26) and equating terms of equal order of  $y$ , one can retrieve the Cauchy problem (2.30). Note that this can be obtained even if assumptions (2.24) and (2.25) are not satisfied, i.e. even for time-dependent concentrations of abiotic factors.
- *Theorem 1:* Under assumptions (2.24) and (2.25), equation (2.30)<sub>1</sub> can be solved for  $v(t, \mathbf{x})$  and the asymptotic limit  $v_\infty(\mathbf{x})$  as  $t \rightarrow \infty$  can be obtained. Similarly, equations (2.30)<sub>2</sub> and (2.30)<sub>3</sub> can be respectively solved for  $\mu(t, \mathbf{x})$  and  $\rho(t, \mathbf{x})$ , as functions of  $v(t, \mathbf{x})$ , and the corresponding asymptotic limit as  $t \rightarrow \infty$  can be thus obtained exploiting  $v_\infty(\mathbf{x})$ . Using  $\sigma_\infty^2(\mathbf{x}) = 1/v_\infty(\mathbf{x})$ , we retrieve results (2.31) and (2.32).

The asymptotic results established by Theorem 1 provide a mathematical formalisation of the idea that, when the concentrations of oxygen and of chemotherapeutic agent are stationary (i.e.  $s(t, \mathbf{x}) \equiv S(\mathbf{x})$  and  $c(t, \mathbf{x}) \equiv C(\mathbf{x})$ ), the tumour cell density  $\rho(t, \mathbf{x})$ , the local mean phenotypic state  $\mu(t, \mathbf{x})$  and the related variance  $\sigma^2(t, \mathbf{x})$  converge to some equilibrium values  $\rho_\infty(\mathbf{x})$ ,  $\mu_\infty(\mathbf{x})$  and  $\sigma_\infty^2(\mathbf{x})$ , respectively, which are determined by the concentration of oxygen and the concentration of chemotherapeutic agent – i.e.  $\rho_\infty(\mathbf{x}) \equiv \rho_\infty(S(\mathbf{x}), C(\mathbf{x}))$ ,  $\mu_\infty(\mathbf{x}) \equiv \mu_\infty(S(\mathbf{x}), C(\mathbf{x}))$  and  $\sigma_\infty^2(\mathbf{x}) \equiv \sigma_\infty^2(S(\mathbf{x}), C(\mathbf{x}))$ . The biological meaning behind the results of Theorem 1 are discussed in Section 2.2.3.

**Remark 2.** Under the assumptions of Theorem 1, in the case where (2.19)-(2.23) coupled with (2.26) admits classical solutions  $s(t, \mathbf{x})$  and  $c(t, \mathbf{x})$  that converge, respectively, to some limits  $s_\infty(\mathbf{x})$  and  $c_\infty(\mathbf{x})$  as  $t \rightarrow \infty$ , we expect the long-time asymptotic limit of the local phenotypic distribution of tumour cells  $n(t, \mathbf{x}, y)$  to be of the Gaussian form

$$n_\infty(\mathbf{x}, y) = \frac{\rho_\infty(\mathbf{x})}{\sqrt{2\pi\sigma_\infty^2(\mathbf{x})}} \exp \left[ -\frac{1}{2\sigma_\infty^2(\mathbf{x})} (y - \mu_\infty(\mathbf{x}))^2 \right]\tag{2.33}$$

where

$$\rho_\infty(\mathbf{x}) \equiv \rho_\infty(s_\infty(\mathbf{x}), c_\infty(\mathbf{x})) = \max \left( 0, \frac{a(s_\infty(\mathbf{x}), c_\infty(\mathbf{x})) - \sqrt{\beta b(s_\infty(\mathbf{x}), c_\infty(\mathbf{x}))}}{\zeta} \right), \quad (2.34)$$

$$\mu_\infty(\mathbf{x}) \equiv \mu_\infty(s_\infty(\mathbf{x}), c_\infty(\mathbf{x})) = h(s_\infty(\mathbf{x}), c_\infty(\mathbf{x})) \quad (2.35)$$

and

$$\sigma_\infty^2(\mathbf{x}) \equiv \sigma_\infty^2(s_\infty(\mathbf{x}), c_\infty(\mathbf{x})) = \sqrt{\frac{\beta}{b(s_\infty(\mathbf{x}), c_\infty(\mathbf{x}))}}. \quad (2.36)$$

### 2.2.2 Formal results in the limit of small spatial diffusion and rare phenotypic changes

We now focus on the case with spatial diffusion, under the simplifying assumptions introduced at the beginning of Section 2.2. That is, motivated by the small order of magnitude of parameter values estimated in the literature for  $\beta$  and  $D_n$  (Doerfler and Böhm, 2006; Duesberg et al., 2000; Smith et al., 2004; Wang et al., 2009), we introduce a small parameter  $\varepsilon > 0$  and assume both  $\beta := \varepsilon^2$  and  $D_n := \varepsilon^2$ .

Following previous studies on the long-time behaviour of nonlocal PDEs and integro-differential equations modelling the dynamics of continuously structured populations (Barles et al., 2009; Chisholm et al., 2016c; Desvillettes et al., 2008; Diekmann et al., 2005; Jabin and Schraml, 2016; Lorz et al., 2011; Mirrahimi and Perthame, 2015; Perthame and Barles, 2008), we use the time scaling  $t \mapsto \frac{t}{\varepsilon}$  in the balance equation (2.5)<sub>1</sub>. This gives the following nonlocal PDE for the local cell phenotypic distribution  $n\left(\frac{t}{\varepsilon}, \mathbf{x}, y\right) = n_\varepsilon(t, \mathbf{x}, y)$

$$\begin{cases} \varepsilon \partial_t n_\varepsilon - \varepsilon^2 \partial_{yy}^2 n_\varepsilon - \varepsilon^2 \Delta_{\mathbf{x}} n_\varepsilon = R(y, \rho_\varepsilon(t, \mathbf{x}), s(t, \mathbf{x}), c(t, \mathbf{x})) n_\varepsilon & \text{in } \Omega, \\ \rho_\varepsilon(t, \mathbf{x}) := \int_{\mathbb{R}} n_\varepsilon(t, \mathbf{x}, y) dy, \\ \nabla_{\mathbf{x}} n_\varepsilon \cdot \hat{\mathbf{u}} = 0 & \text{on } \partial\Omega, \end{cases} \quad (2.37)$$

In this scenario, under assumptions (2.24) and (2.25), we formally derive weak solutions to (2.37) by considering the asymptotic regime  $\varepsilon \rightarrow 0$ , which is equivalent to studying the behaviour of  $n_\varepsilon(t, \mathbf{x}, y)$  over many cell generations and in the case where spontaneous phenotypic changes and random cell movement induce small changes in the local phenotypic distribution.

**Initial conditions.** In agreement with much of the previous work on the mathematical analysis of the evolutionary dynamics of continuously-structured populations (Perthame, 2006), we consider the case where at time  $t = 0$  tumour cells that occupy the same position are mainly in the same phenotypic state, that is, at every position  $\mathbf{x}$  the initial local cell phenotypic distribution  $n_\varepsilon(0, \mathbf{x}, y)$  is a sharp Gaussian-like function with mean value  $\bar{y}^0(\mathbf{x}) \in C(\Omega)$ , where  $\bar{y}^0 : \Omega \rightarrow \mathbb{R}$ , and integral  $\rho_\varepsilon(0, \mathbf{x}) \in C(\Omega)$ , where  $\rho_\varepsilon(0, \cdot) : \Omega \rightarrow \mathbb{R}_{>0}$ . Hence, we assume

$$n_\varepsilon(0, \mathbf{x}, y) = \exp \left[ \frac{u_\varepsilon^0(\mathbf{x}, y)}{\varepsilon} \right] \quad (2.38)$$

with  $u_\varepsilon^0(\mathbf{x}, y)$  being a smooth, uniformly concave function of  $y$  for every  $\mathbf{x} \in \Omega$  such that  $0 < \rho_\varepsilon(0, \mathbf{x}) < \infty$  and

$$\exp \left[ \frac{u_\varepsilon^0(\mathbf{x}, y)}{\varepsilon} \right] \xrightarrow[\varepsilon \rightarrow 0]{*} \rho(0, \mathbf{x}) \delta(y - \bar{y}^0(\mathbf{x})) \quad \text{for all } \mathbf{x} \in \Omega \quad (2.39)$$

in the sense of measures, where  $\delta(y - \bar{y}^0(\mathbf{x}))$  is the Dirac delta distribution centred at  $\bar{y}^0(\mathbf{x})$ . We assume the bounds on  $\rho_\varepsilon$  still hold in the limit  $\varepsilon \rightarrow 0$ , i.e. we assume

$$0 < \rho(0, \mathbf{x}) < \infty. \quad (2.40)$$

**Formal analysis results.** Building upon the method presented by Barles et al. (2009); Diekmann et al. (2005); Lorz et al. (2011); Perthame (2006); Perthame and Barles (2008), we make the real phase WKB<sup>2</sup> ansatz (Barles et al., 1989; Evans and Souganidis, 1989; Fleming and Souganidis, 1986)

$$n_\varepsilon(t, \mathbf{x}, y) = \exp \left[ \frac{u_\varepsilon(t, \mathbf{x}, y)}{\varepsilon} \right]. \quad (2.41)$$

Formal calculations, reported in Appendix A.3, lead to the following constrained Hamilton-Jacobi equation for  $u(t, \mathbf{x}, y)$ , the leading order term of the asymptotic expansion of  $u_\varepsilon(t, \mathbf{x}, y)$ , in the asymptotic regime  $\varepsilon \rightarrow 0$

$$\begin{cases} \partial_t u = R(y, \rho(t, \mathbf{x}), S(\mathbf{x}), C(\mathbf{x})) + (\partial_y u)^2 + |\nabla_{\mathbf{x}} u|^2 & \mathbf{x} \in \Omega \\ \max_{y \in \mathbb{R}} u(t, \mathbf{x}, y) = 0 & \mathbf{x} \in \text{supp}(\rho) \subseteq \Omega \end{cases} \quad (2.42)$$

where  $\rho(t, \mathbf{x})$  is the leading order term of the asymptotic expansion of  $\rho_\varepsilon(t, \mathbf{x})$ . A canonical equation for the time evolution of a nondegenerate maximum point of  $u$ , i.e. a point  $\bar{y}(t, \mathbf{x}) = \arg \max_{y \in \mathbb{R}} u(t, \mathbf{x}, y)$ , can be obtained for  $\mathbf{x} \in \text{supp}(\rho)$ . Studying the steady state solution of such equation, we obtain equilibrium values of  $\rho$  and  $\bar{y}$ , say  $\rho_\infty(\mathbf{x})$  and  $\bar{y}_\infty(\mathbf{x})$ .

---

<sup>2</sup>The WKB ansatz takes its name from physicists Wentzel–Kramers–Brillouin and it is sometimes referred to as Hopf–Cole transformation.

Moreover, under definitions (2.6), (2.13) and (2.14) we have a unique solution for  $\bar{y}_\infty(\mathbf{x})$  at each  $\mathbf{x} \in \Omega$ .

Taken together, these formal results indicate that, in the framework of the assumptions considered in this section, we can expect the local cell phenotypic distribution at steady-state  $n_\infty(\mathbf{x}, y)$  to be of the form

$$n_\infty(\mathbf{x}, y) = \rho_\infty(\mathbf{x}) \delta(y - \bar{y}_\infty(\mathbf{x})), \quad (2.43)$$

with the local cell density  $\rho_\infty(\mathbf{x})$  and the locally dominant phenotypic state  $\bar{y}_\infty(\mathbf{x})$  given by

$$\begin{cases} \rho_\infty(\mathbf{x}) \equiv \rho_\infty(S, C) = \max \left( 0, \frac{a(S, C)}{\zeta} \right) & \mathbf{x} \in \Omega, \\ \bar{y}_\infty(\mathbf{x}) \equiv \bar{y}_\infty(S, C) = h(S, C) & \mathbf{x} \in \text{supp}(\rho_\infty). \end{cases} \quad (2.44)$$

This also implies that the local mean phenotypic state of the tumour cells at steady-state, say  $\mu_\infty(\mathbf{x})$ , coincides with  $\bar{y}_\infty(\mathbf{x})$ , that is,

$$\mu_\infty(\mathbf{x}) := \frac{1}{\rho_\infty(\mathbf{x})} \int_{\mathbb{R}} y n_\infty(\mathbf{x}, y) dy = \bar{y}_\infty(\mathbf{x}). \quad (2.45)$$

**Remark 3.** In analogy with Remark 2, under the assumptions introduced in Section 2.2.2, in the case where (2.19)-(2.23) coupled with (2.37) admits classical solutions  $s(t, \mathbf{x})$  and  $c(t, \mathbf{x})$  that converge to some limits  $s_\infty(\mathbf{x})$  and  $c_\infty(\mathbf{x})$  as  $t \rightarrow \infty$ , we expect that, in the asymptotic limit of low motility, rare phenotypic changes and long times, the local phenotypic distribution of tumour cells  $n(t, \mathbf{x}, y)$  will be of the weak form

$$n_\infty(\mathbf{x}, y) = \rho_\infty(\mathbf{x}) \delta(y - \mu_\infty(\mathbf{x})), \quad (2.46)$$

where

$$\rho_\infty(\mathbf{x}) \equiv \rho_\infty(s_\infty(\mathbf{x}), c_\infty(\mathbf{x})) = \max \left( 0, \frac{a(s_\infty(\mathbf{x}), c_\infty(\mathbf{x}))}{\zeta} \right), \quad (2.47)$$

and

$$\mu_\infty(\mathbf{x}) \equiv \mu_\infty(s_\infty(\mathbf{x}), c_\infty(\mathbf{x})) = h(s_\infty(\mathbf{x}), c_\infty(\mathbf{x})). \quad (2.48)$$

**Remark 4.** The formal results obtained as  $t \rightarrow \infty$  in the asymptotic regime  $D_n \rightarrow 0$  and  $\beta \rightarrow 0$ , presented in Section 2.2.2, are consistent with the strong solutions obtained as  $t \rightarrow \infty$  for  $D_n = 0$  and  $\beta > 0$ , presented in Section 2.2.1. This can be observed, for instance, by considering the limit of solution (2.33)-(2.36) as  $\beta \rightarrow 0$  and comparing this

limit to (2.46)-(2.48). As  $\beta \rightarrow 0$ : the local cell density  $\rho_\infty(\mathbf{x})$  in (2.34) converges to

$$\rho_\infty(\mathbf{x}) = \max \left( 0, \frac{a(\mathbf{x}) - \sqrt{\beta b(\mathbf{x})}}{\zeta} \right) \xrightarrow{\beta \rightarrow 0} \max \left( 0, \frac{a(\mathbf{x})}{\zeta} \right),$$

which corresponds to (2.47); the mean phenotypic state  $\mu_\infty(\mathbf{x})$  in (2.35) does not depend on  $\beta$ , thus remains unchanged in the limit and corresponds to (2.48); the variance  $\sigma_\infty^2(\mathbf{x})$  in (2.36) converges to

$$\sigma_\infty^2(\mathbf{x}) = \sqrt{\frac{\beta}{b(\mathbf{x})}} \xrightarrow{\beta \rightarrow 0} 0,$$

which is consistent with the fact that, in this limit, the local phenotypic distribution at equilibrium  $n_\infty(\mathbf{x}, y)$  takes the form of a Dirac delta distribution (2.46) instead of a Gaussian-like function (2.33).

**Remark 5.** While the results of the analysis of evolutionary dynamics presented in Section 2.2.1 only hold for  $y \in \mathbb{R}$ , the results of the formal asymptotic analysis presented in Section 2.2.2 still hold in the finite domain  $y \in [0, 1]$ , as we detailed in Villa et al. (2021c).

### 2.2.3 Biological interpretation of analytical results

The analytical results presented in Sections 2.2.1 and 2.2.2 allow us to extrapolate qualitative and quantitative information about the expected phenotypic distribution of tumour cells in the idealised biological scenario of a closed system, comprising tumour cells and abiotic factors such as oxygen and a chemotherapeutic agent, reaching an equilibrium. They provide a mathematical formalisation of the idea that, when the concentrations of oxygen and of chemotherapeutic agent are stationary, the local phenotypic distribution of tumour cells at equilibrium can be fully characterised by its moments, which are in turn determined by the local concentration of oxygen and chemotherapeutic agent, according to the specific scenario under study. In particular:

- In the absence of spatial movement, we expect the cell population at equilibrium to have a Gaussian-like phenotypic distribution at each point in space, with the most prevalent phenotypic state corresponding to the fittest one dictated by local environmental conditions (Section 2.2.1);
- In the case of low cell mobility and rare phenotypic changes, we expect the cell population at equilibrium to be monomorphic at each point in space, where the dominant phenotypic state is the fittest one dictated by local environmental conditions (Section 2.2.2).

Let us now further consider the quantitative information that can be extrapolated from

the analytical results presented in Section 2.2.1, i.e. the case in which the cells do not undergo spatial movement. Note that similar biological interpretations can be drawn from the formal results presented in Section 2.2.2, in view of the consistency of solutions highlighted in Remark 4.

**The moments of  $n_\infty$ .** According to the asymptotic results established by Theorem 1 under stationary concentrations of oxygen  $S(\mathbf{x})$  and of chemotherapeutic agent  $C(\mathbf{x})$ , we expect the equilibrium values of the tumour cell density  $\rho_\infty(\mathbf{x})$ , the local mean phenotypic state  $\mu_\infty(\mathbf{x})$  and the related variance  $\sigma^2(t, \mathbf{x})$  to be determined by said stationary concentrations  $S(\mathbf{x})$  and  $C(\mathbf{x})$ . This is illustrated by the heat maps in Figure 2.2, which show how, for the biologically consistent parameter values listed in Table 2.1 ( $D_n = 0$ ,  $\beta = 10^{-6}$ ), the values of  $\rho_\infty$ ,  $\mu_\infty$  and  $\sigma_\infty^2$  given by (2.34)-(2.36) vary as functions of  $S$  and  $C$ . Notice that the parameter values in Table 2.1 are such that  $\rho_\infty > 0$ .

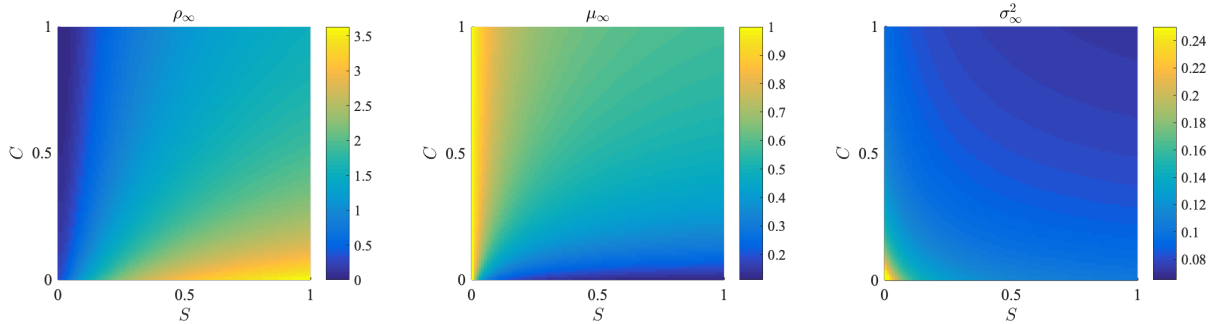


**Figure 2.2: Plots of  $\rho_\infty(S, C)$ ,  $\mu_\infty(S, C)$  and  $\sigma_\infty^2(S, C)$ .** Plots of the equilibrium cell density  $\rho_\infty$ , the equilibrium local mean phenotypic state  $\mu_\infty$  and the related variance  $\sigma_\infty^2$  given by (2.32) as functions of the stationary concentrations of oxygen  $S$  and of chemotherapeutic agent  $C$ . The plots refer to the parameter values listed in Table 2.1 ( $D_n = 0$ ,  $\beta = 10^{-6}$ ). The cell density is in units of  $10^8$  and the concentrations of oxygen and of chemotherapeutic agent are scaled by the reference values  $S_0$  and  $C_0$  given in Table 2.1, respectively.

These results demonstrate that spatial variation of the oxygen concentration determines spatial variation of the tumour cell density, of the local mean phenotypic state and of the related variance. Specifically, under the parameter values listed in Table 2.1 ( $D_n = 0$ ,  $\beta = 10^{-6}$ ), the tumour cell density  $\rho_\infty$  is an increasing function of the oxygen concentration. Moreover, the local mean phenotypic state  $\mu_\infty$  decreases from values close to  $y = 1$  (i.e. the state corresponding to the phenotypic variant with the highest rate of cellular division via anaerobic energy pathways) to values close to  $y = 0$  (i.e. the state corresponding to the phenotypic variant with the highest rate of cellular division via aerobic energy pathways) for increasing values of the oxygen concentration. This suggests that aerobic phenotypic variants are to be expected to colonise oxygenated regions of the tumour, while anaerobic phenotypic variants are likely to populate poorly-oxygenated regions. Finally,

the local phenotypic variance  $\sigma_\infty^2$  is a decreasing function of the oxygen concentration, which supports the idea that higher levels of phenotypic variability may occur in hypoxic regions of the tumour.

On the other hand, larger values of the concentration of chemotherapeutic agent bring about smaller values of the tumour cell density  $\rho_\infty$ , a shift of the local mean phenotypic state  $\mu_\infty$  from values closer to  $y = 0$  to values closer to  $y = 1$  (i.e. the state corresponding to the anaerobic phenotypic variant with the highest level of resistance to chemotherapy), and smaller values of the local phenotypic variance  $\sigma_\infty^2$ . This indicates that the selective pressure exerted by the chemotherapeutic agent causes a population bottleneck in tumour cells leading to a reduction in cell density coming along with the selection of more chemoresistant phenotypic variants and lower levels of phenotypic variability.

## 2.3 Numerical investigations

In this section we construct numerical solutions to the problem given by (2.5), (2.19) and (2.20), subject to suitable initial conditions. All simulations are carried out using the parameter values listed in Table 2.1, which are chosen to be consistent with the existing literature – see Appendix C.1 for details. In Section 2.3.1, we describe the set-up of numerical simulations and the methods employed to construct numerical solutions. In Section 2.3.2, we consider the case of a 1D spatial domain whereby the concentrations of oxygen and of chemotherapeutic agent are stationary. In Section 2.3.3, we focus on the case of a 2D spatial domain and let the dynamics of oxygen and of chemotherapeutic agent be governed by (2.19) and (2.20). In particular, in these two sections we consider the problem in the absence of spatial diffusion and compare our results to the analytic ones reported in Section 2.2.1. In Section 2.3.4, we first consider the case where the blood vessel distribution is reconstructed from clinical images obtained via D-OCT, and then assess the impact of tissue vascularisation on intratumour phenotypic heterogeneity in the absence of a chemotherapeutic agent. There, we consider the problem under small values of spatial diffusion and phenotypic variability, briefly verifying consistency with the results in Section 2.2.2. This choice was made in view of the monotonicity results in Section 2.2.2, in order to avoid the global level of phenotypic heterogeneity being affected by local phenotypic variability.

### 2.3.1 Set-up of numerical simulations and numerical methods

**Set-up of numerical simulations of Section 2.3.2.** For the numerical simulations we present in Section 2.3.2, we define  $\Omega := (0, 0.05)$  and assume that increasing values of

**Table 2.1:** Parameter values used in numerical simulations. Two variations of this parameter set are considered: (A) with  $\beta = 10^{-6} \text{ s}^{-1}$  and  $D_n = 0 \text{ cm}^2 \text{ s}^{-1}$  to match assumptions made in Section 2.2.1 and (B) with  $\beta = 10^{-13} \text{ s}^{-1}$  and  $D_n = 10^{-13} \text{ cm}^2 \text{ s}^{-1}$  to match assumptions made in Section 2.2.2

Parameter	Biological meaning	Value	Reference
$\alpha_c$	Michaelis-Menten constant of chemotherapeutic agent	$2 \times 10^{-6} \text{ g cm}^{-3}$	Norris et al. (2006)
$\alpha_s$	Michaelis-Menten constant of oxygen	$1.5 \times 10^{-7} \text{ g cm}^{-3}$	Casciaro et al. (1992)
$\beta$	Rate of spontaneous phenotypic changes	(A) $10^{-6} \text{ s}^{-1}$ (B) $10^{-13} \text{ s}^{-1}$	Chisholm et al. (2015) Doerfler and Böhm (2006)
$D_n$	Cell motility	(A) $0 \text{ cm}^2 \text{s}^{-1}$ (B) $10^{-13} \text{ cm}^2 \text{s}^{-1}$	Section 2.2.1 Wang et al. (2009)
$D_c$	Diffusivity of chemotherapeutic agent	$4.4 \times 10^{-6} \text{ cm}^2 \text{s}^{-1}$	Powathil et al. (2012b)
$D_s$	Diffusivity of oxygen	$2 \times 10^{-5} \text{ cm}^2 \text{s}^{-1}$	Hlatky and Alpen (1985)
$\gamma_c$	Maximal reduction of the background fitness due to chemotherapy	$1.8 \times 10^{-4} \text{ s}^{-1}$	Ward and King (1997)
$\gamma_s$	Maximal background fitness of aerobic phenotypic variants	$1 \times 10^{-4} \text{ s}^{-1}$	Gordan et al. (2007)
$\zeta$	Rate of cell death due to competition for space	$2 \times 10^{-13} \text{ cm}^3 \text{s}^{-1} \text{cells}^{-1}$	Lorenzini et al. (2018)
$\eta_c$	Conversion factor for cell consumption of chemotherapeutic agent	$4 \times 10^{-11} \text{ g cells}^{-1}$	Lorenzini et al. (2018)
$\eta_s$	Conversion factor for cell consumption of oxygen	$2 \times 10^{-11} \text{ g cells}^{-1}$	Lorenzini et al. (2018)
$\lambda_c$	Rate of natural decay of chemotherapeutic agent	$2.3 \times 10^{-4} \text{ s}^{-1}$	Powathil et al. (2012b)
$\lambda_s$	Rate of natural decay of oxygen	$2.78 \times 10^{-6} \text{ s}^{-1}$	Cumsille et al. (2015)
$\varphi$	Maximal background fitness of anaerobic phenotypic variants	$1 \times 10^{-5} \text{ s}^{-1}$	Gordan et al. (2007)
$I_c$	Constant rate of inflow of chemotherapeutic agent through blood vessels	$2.5 \times 10^{-6} \text{ g cm}^{-3} \text{s}^{-1}$	Norris et al. (2006)
$I_s$	Constant rate of inflow of oxygen through blood vessels	$6.3996 \times 10^{-7} \text{ g cm}^{-3} \text{s}^{-1}$	Kumosa et al. (2014)
$C_0$	Reference value for the concentration of chemotherapeutic agent	$2.5 \times 10^{-6} \text{ g cm}^{-3}$	Norris et al. (2006)
$S_0$	Reference value for the concentration of oxygen	$6.3996 \times 10^{-7} \text{ g cm}^{-3}$	Kumosa et al. (2014)

$\mathbf{x} \equiv x$  correspond to increasing values of the distance from a blood vessel located in  $x = 0$ . Under the parameter values listed in Table 2.1 ( $D_n = 0$ ,  $\beta = 10^{-6}$ ), the values of  $x$  are in units of cm. Coherently with assumptions (2.24) and (2.25), we let the concentrations of oxygen and of chemotherapeutic agent be stationary and given by

$$s(t, x) \equiv S(x) \quad \text{and} \quad c(t, x) \equiv C(x),$$

with the functions  $S(x)$  and  $C(x)$  defined as shown by the plots in Figure 2.3. Here, the oxygen concentration  $S(x)$  is defined in such a way as to match the experimental oxygen distribution presented in (Helmlinger et al., 1997, Fig. 3). Furthermore, the concentration of chemotherapeutic agent  $C(x)$  is defined in such a way as to have a behaviour qualitatively similar to that of  $S(x)$  and the value of  $C(0)$  is chosen in agreement with experimental data presented by Helmlinger et al. (1997). We complement (2.26) with

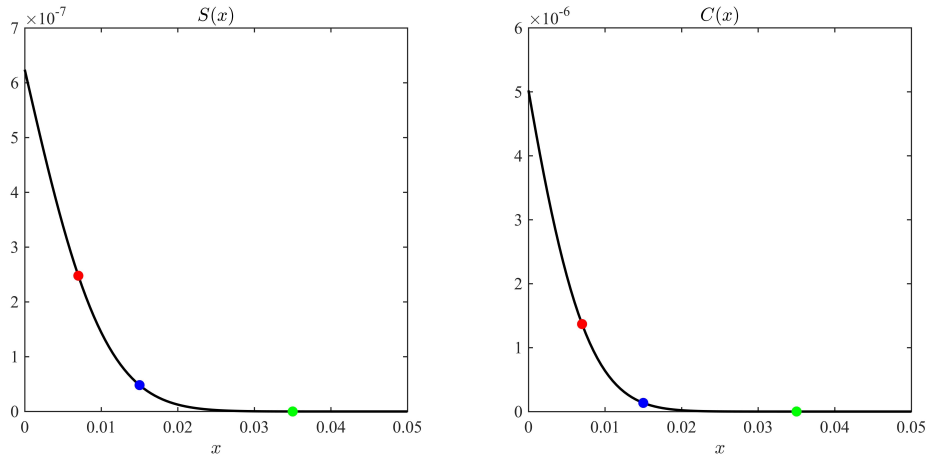


**Figure 2.3: Stationary concentrations of oxygen and of chemotherapeutic agent considered in Section 2.3.2.** Plots of the oxygen concentration  $S(x)$  and of the concentration of chemotherapeutic agent  $C(x)$  used to obtain the numerical results of Figure 2.4 and Figure 2.5. The coloured dots highlight the values of  $S(x)$  and  $C(x)$  corresponding to the lines of the same colours in Figure 2.4 and Figure 2.5 – i.e.  $S(x)$  and  $C(x)$  at  $x = 0.007$  (red),  $x = 0.015$  (blue) and  $x = 0.035$  (green). The space variable  $x$  is in units of cm, while both  $S(x)$  and  $C(x)$  are in units of  $\text{g cm}^{-3}$ . The oxygen concentration  $S(x)$  is defined in such a way as to match the experimental  $\text{pO}_2$  profile presented in (Helmlinger et al., 1997, Fig. 3). The conversion from mmHg of  $\text{pO}_2$  to  $\text{g cm}^{-3}$  of oxygen concentration was performed using the conversion factor  $1 \text{ mmHg} = 4.6 \times 10^{-8} \text{ g cm}^{-3}$ , which was estimated using the ideal gas law. The concentration of chemotherapeutic agent  $C(x)$  is defined in such a way as to have a behaviour which is qualitatively similar to that of  $S(x)$  and the value of  $C(0)$  is chosen in agreement with experimental data presented in Helmlinger et al. (1997).

the initial condition (2.27) and assume

$$\sigma^2(0, \mathbf{x}) \equiv \sigma_0^2 = 1, \quad \mu(0, \mathbf{x}) \equiv \mu_0 = 0.5 \quad \text{and} \quad \rho(0, \mathbf{x}) \equiv \rho_0 \approx 10^8. \quad (2.49)$$

Assumptions (2.49) correspond to a biological scenario whereby at the initial time  $t = 0$  tumour cells are uniformly distributed across the spatial domain  $\Omega$  and are mainly found in the phenotypic state  $y = 0.5$ .

**Set-up of numerical simulations of Section 2.3.3.** For the numerical simulations we present in Section 2.3.3, we define  $\Omega := (0, 0.5) \times (0, 0.5)$  in order to model the cross-section of a vascularised tumour tissue. Under the parameter values listed in Table 2.1 ( $D_n = 0$ ,  $\beta = 10^{-6}$ ), the values of  $\mathbf{x} \in \Omega$  are in units of cm. We let the dynamics of oxygen and of chemotherapeutic agent be governed by (2.19) and (2.20), together with definitions (2.21)-(2.23). We complement (2.26) with the initial condition defined via (2.27) and (2.49), while (2.19) and (2.20) are complemented with the following initial conditions

$$s(0, \mathbf{x}) = S_0 \mathbf{1}_\omega(\mathbf{x}) \quad \text{and} \quad c(0, \mathbf{x}) = C_0 \mathbf{1}_\omega(\mathbf{x}), \quad (2.50)$$

with the values of  $S_0$  and  $C_0$  being those given in Table 2.1. These initial conditions correspond to a biological scenario whereby at the initial time  $t = 0$  tumour cells are uniformly distributed across the spatial domain  $\Omega$  and are mainly found in the phenotypic state  $y = 0.5$ , while the oxygen and the chemotherapeutic agent are solely present in the blood vessels.

**Set-up of numerical simulations of Section 2.3.4.** For the numerical simulations we present in Section 2.3.4, we again consider  $\Omega := (0, 0.5) \times (0, 0.5)$  in order to model the cross-section of a vascularised tumour tissue. Under the parameter values listed in Table 2.1 ( $D_n = \beta = 10^{-13}$ ), the values of  $\mathbf{x} \in \Omega$  are in units of cm. We let the dynamics of oxygen be governed by (2.19), together with definitions (2.21)-(2.23), and initial condition (2.50). On the other hand, we let the concentration of chemotherapeutic agent be stationary and given by  $c(t, \mathbf{x}) \equiv 0$ . We complement (2.5) with the initial condition (2.27) and assume

$$\sigma^2(0, \mathbf{x}) \equiv \sigma_0^2 = 0.05, \quad \mu(0, \mathbf{x}) \equiv \mu_0 = 0.5 \quad \text{and} \quad \rho(0, \mathbf{x}) \equiv \rho_0 \approx 10^8. \quad (2.51)$$

Assumptions (2.51) are similar to (2.49), with the exception of  $\sigma_0^2$  which is much smaller in (2.51). This choice is consistent with the initial conditions of Section 2.2.2 and helps to numerically portray the biological scenario in which at each point in space the population is monomorphic. For the numerical results presented in Section 2.3.4, we make use of the indices of intratumour phenotypic heterogeneity defined at the end of this section.

**Numerical methods.** Numerical solutions are constructed using a uniform discretisation of the interval  $[0, 0.05]$  or the square  $[0, 0.5] \times [0, 0.5]$  as the computational domain of

the independent variable  $\mathbf{x}$ . Moreover, a uniform discretisation of the set  $[-L, L]$  is used as the computational domain of the independent variable  $y$ , with  $L = 7$ . We consider  $t \in [0, T]$ , with  $T > 0$  being the final time of simulations. The final time  $T$  is chosen sufficiently large so as to ensure that the numerical solutions are sufficiently close to equilibrium at the end of simulations (the exact values of  $T$  are reported in the figure captions). We discretise the interval  $[0, T]$  with a uniform step. The method for solving (2.5) numerically, as well as (2.26), subject to the zero-flux boundary conditions

$$\partial_y n(\cdot, \cdot, -L) = 0 \quad \text{and} \quad \partial_y n(\cdot, \cdot, L) = 0, \quad (2.52)$$

as well as equations (2.19) and (2.20), is based on an explicit finite difference scheme using second order central difference approximations for the second order derivatives, the composite trapezoidal rule for the nonlocal terms and first order forward difference approximations for the time derivatives (LeVeque, 2007). Finally, numerical solutions to the Cauchy problem (2.30) are constructed using the explicit Euler method. All numerical computations are performed in MATLAB. Details of the numerical schemes are given in Appendix B.1.

**Indices of intratumour phenotypic heterogeneity.** In order to systematically assess the impact of tumour tissue vascularisation on the level of intratumour phenotypic heterogeneity in Section 2.3.4, we require a metric of vascular density and appropriate indices of intratumour phenotypic heterogeneity. We define the vascular density  $\varrho$  as

$$\varrho := \frac{|\omega|}{|\Omega|}. \quad (2.53)$$

We quantify the level of intratumour phenotypic heterogeneity through the following continuum versions of the equitability index  $E(t)$  (defined as a rescaled Shannon diversity index) and the Simpson diversity index  $D(t)$  (Shannon, 1948; Simpson, 1949)

$$E(t) := - \int_{\mathbb{R}} \frac{F(t, y) \log F(t, y)}{\log N(t)} dy \quad \text{and} \quad D(t) := \left( \int_{\mathbb{R}} F^2(t, y) dy \right)^{-1}, \quad (2.54)$$

where the total cell mass  $N(t)$  and the fraction  $F(t, y)$  of cells in the phenotypic state  $y$  within the tumour are defined according to (2.4).

### 2.3.2 1D numerical results under stationary concentrations of oxygen and chemotherapeutic agent

The sample of numerical results presented in Figure 2.4 refer to the case where the oxygen concentration  $s(t, x) \equiv S(x)$  and the concentration of cytotoxic agent  $c(t, x) \equiv 0$ , while

the results presented in Figure 2.5 refer to the case where  $s(t, x) \equiv S(x)$  and  $c(t, x) \equiv C(x)$ , with  $S(x)$  and  $C(x)$  being defined as illustrated by the plots in Figure 2.3.

**Agreement between analytical and numerical results.** In agreement with the results established by Proposition 1, the numerical results displayed in the top rows of Figure 2.4 and Figure 2.5 show that there is a perfect match between the cell density  $\rho(t, x)$ , the local mean phenotypic state  $\mu(t, x)$  and the related variance  $\sigma^2(t, x)$  computed via numerical integration of the local cell phenotypic distribution  $n(t, x, y)$ , which is obtained by solving numerically (2.26) subject to the initial condition defined via (2.27) and (2.49), and the corresponding quantities obtained by solving numerically the Cauchy problem (2.30) complemented with (2.49). Similarly, the sample of numerical results presented in the bottom rows of Figure 2.4 and Figure 2.5 show that the local cell phenotypic distribution  $n(t, x, y)$  matches the exact local cell phenotypic distribution (2.29). Moreover, in accordance with the asymptotic results established by Theorem 1, the cell density, the local mean phenotypic state and the related variance converge, respectively, to the equilibrium values  $\rho_\infty(\mathbf{x})$ ,  $\mu_\infty(\mathbf{x})$  and  $\sigma_\infty^2(\mathbf{x})$  given by (2.32).

**Tumour cell dynamics in the absence of chemotherapeutic agent.** The numerical results of Figure 2.4 show that, in the absence of chemotherapeutic agent, since the stationary oxygen concentration  $S(x)$  decreases monotonically with the distance from the blood vessel located at  $x = 0$  (*vid. Figure 2.3*), the cell density  $\rho(t, x)$  at equilibrium is maximal in the vicinity of the blood vessel (*cf. red line*), where the oxygen concentration is higher, and decreases monotonically as the distance from the vessel increases (*cf. blue and green lines*). Accordingly, the local mean phenotypic state at equilibrium increases from values closer to  $y = 0$  (i.e. the state corresponding to the phenotypic variant with the highest rate of cellular division via aerobic energy pathways) to values closer to  $y = 1$  (i.e. the state corresponding to the phenotypic variant with the highest rate of cellular division via anaerobic energy pathways) moving away from the blood vessel. Moreover, the local phenotypic variance  $\sigma^2(t, x)$  at equilibrium is a monotonically increasing function of the distance from the blood vessel (i.e. local phenotypic variability increases with the distance from the blood vessel).

**Tumour cell dynamics in the presence of chemotherapeutic agent.** A comparison of the numerical results of Figure 2.4 and Figure 2.5 reveals that in the regions in close proximity of the blood vessel (*cf. red lines*), where its concentration is higher, the chemotherapeutic agent leads to the occurrence of a population bottleneck in tumour cells, which results in: a reduction of the equilibrium value of the cell density  $\rho(t, x)$ ; a selective sweep toward more resistant phenotypic variants, as demonstrated by the fact

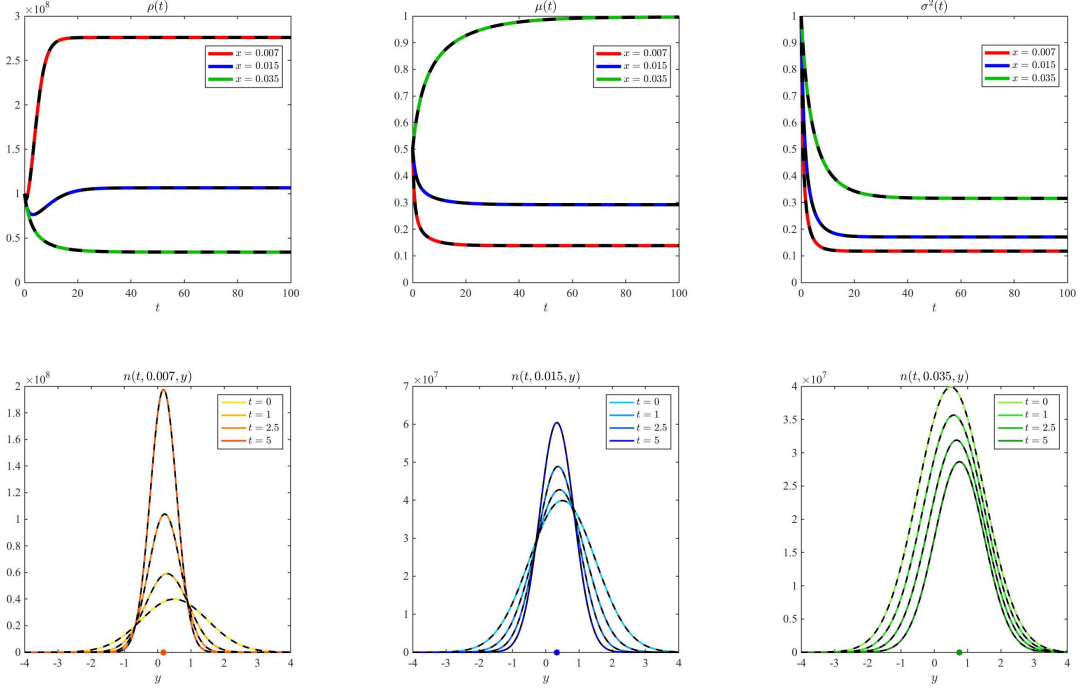


**Figure 2.4: 1D numerical results under stationary concentration of oxygen and in the absence of chemotherapeutic agent.** First row: Plots of the cell density  $\rho(t, x)$  (left panel), the local mean phenotypic state  $\mu(t, x)$  (central panel) and the related variance  $\sigma^2(t, x)$  (right panel) at  $x = 0.007$  (red, solid lines),  $x = 0.015$  (blue, solid lines) and  $x = 0.035$  (green, solid lines) obtained by solving numerically (2.26) subject to the initial condition defined via (2.27) and (2.49), under the stationary concentration of oxygen  $s(t, x) \equiv S(x)$  displayed in Figure 2.3 and the stationary concentration of chemotherapeutic agent  $c(t, x) \equiv 0$  (i.e. in the absence of chemotherapeutic agent). The black, dashed lines highlight the corresponding quantities obtained by solving numerically the Cauchy problem (2.30) complemented with (2.49). Second row: Plots of the local cell phenotypic distribution  $n(t, x, y)$  obtained by solving numerically (2.26) subject to the initial condition defined via (2.27) and (2.49), under the stationary concentration of oxygen  $s(t, x) \equiv S(x)$  displayed in Figure 2.3 and the stationary concentration of chemotherapeutic agent  $c(t, x) \equiv 0$  (i.e. in the absence of chemotherapeutic agent), at  $x = 0.007$  (left panel),  $x = 0.015$  (central panel) and  $x = 0.035$  (right panel). Different solid, coloured lines correspond to different time instants  $t$  and the dashed lines highlight the exact solution (2.29) with  $\sigma^2(t, x)$ ,  $\mu(t, x)$  and  $\rho(t, x)$  given by numerical solutions of the Cauchy problem (2.30) complemented with (2.49). The bullets on the axis of abscissas highlight the value of the mean phenotypic state  $\mu(t, x)$  at  $t = 5$ . The time variable  $t$  is in units of  $10^4$  s, the space variable  $x$  is in units of cm and the parameters values used are those listed in Table 2.1 ( $D_n = 0$ ,  $\beta = 10^{-6}$ ).

that the equilibrium value of the local mean phenotypic state  $\mu(t, x)$  shifts from values closer to  $y = 0$  (i.e. the state corresponding to the phenotypic variant with the highest rate of cellular division via aerobic energy pathways) to values closer to  $y = 1$  (i.e. the state corresponding to the anaerobic phenotypic variant with the highest level of resistance to chemotherapy); a reduction of the equilibrium value of the local phenotypic variance  $\sigma^2(t, x)$ . Moreover, moving away from the blood vessel, since its concentration

decreases, the chemotherapeutic agent has a weaker impact on the dynamics of tumour cells (*cf.* blue lines). As a result, the evolution of tumour cells in regions distal to the blood vessel is hardly affected by the chemotherapeutic agent (*cf.* green lines).

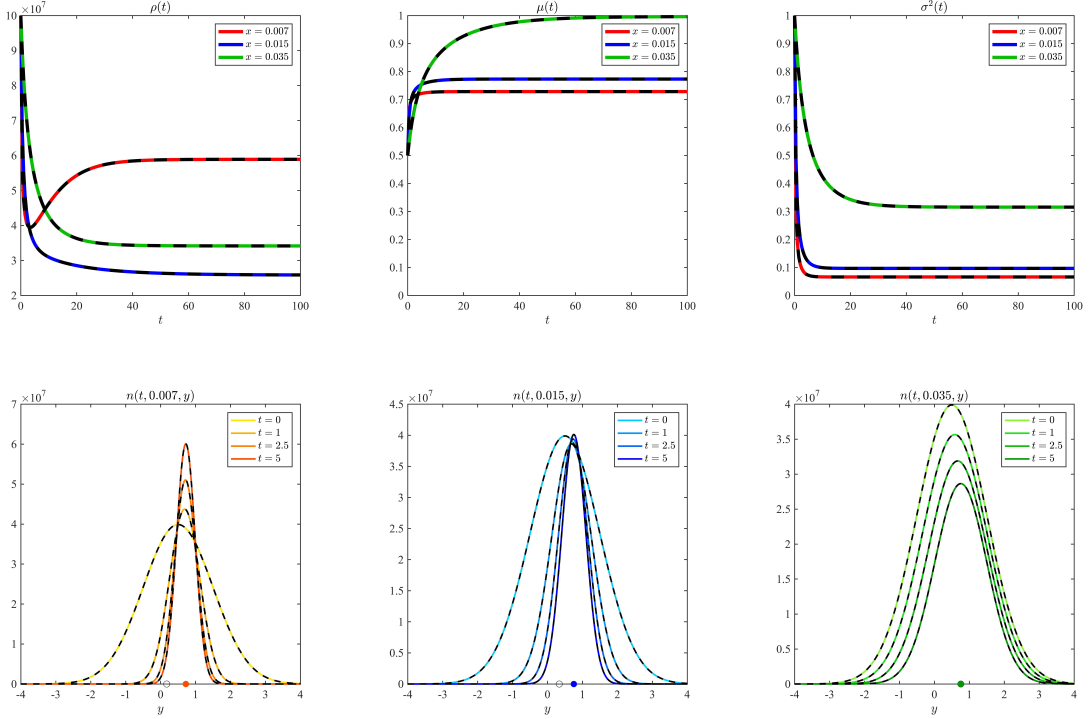


**Figure 2.5: 1D numerical results under stationary concentrations of oxygen and chemotherapeutic agent.** *First row:* Plots of the cell density  $\rho(t, x)$  (left panel), the local mean phenotypic state  $\mu(t, x)$  (central panel) and the related variance  $\sigma^2(t, x)$  (right panel) at  $x = 0.007$  (red, solid lines),  $x = 0.015$  (blue, solid lines) and  $x = 0.035$  (green, solid lines) obtained by solving numerically (2.26) subject to the initial condition defined via (2.27) and (2.49), and under the stationary concentrations of oxygen  $s(t, x) \equiv S(x)$  and chemotherapeutic agent  $c(t, x) \equiv C(x)$  displayed in Figure 2.3. The black, dashed lines highlight the corresponding quantities obtained by solving numerically the Cauchy problem (2.30) complemented with (2.49). *Second row:* Plots of the local cell phenotypic distribution  $n(t, x, y)$  obtained by solving numerically (2.26) subject to the initial condition defined via (2.27) and (2.49), and under the stationary concentrations of oxygen  $S(x)$  and chemotherapeutic agent  $C(x)$  displayed in Figure 2.3, at  $x = 0.007$  (left panel),  $x = 0.015$  (central panel) and  $x = 0.035$  (right panel). Different solid, coloured lines correspond to different time instants  $t$  and the dashed lines highlight the exact solution (2.29) with  $\sigma^2(t, x)$ ,  $\mu(t, x)$  and  $\rho(t, x)$  given by numerical solutions of the Cauchy problem (2.30) complemented with (2.49). The filled bullets on the axis of abscissas highlight the value of the mean phenotypic state  $\mu(t, x)$  at  $t = 5$ , while the empty bullets highlight the corresponding values obtained in the case where  $c(t, x) \equiv 0$  (i.e. in the absence of chemotherapeutic agent). The time variable  $t$  is in units of  $10^4$  s, the space variable  $x$  is in units of cm and the parameters values used are those listed in Table 2.1 ( $D_n = 0$ ,  $\beta = 10^{-6}$ ).

**Tumour cell dynamics for different delivered doses of chemotherapeutic agent.** The numerical results of Figure 2.6 reproduce a realistic scenario whereby variation in the delivered dose of the chemotherapeutic agent leads to pronounced changes in the agent concentration in close proximity of the blood vessel while leaving the concentration far from the blood vessel almost unchanged (*vid.* the stationary distributions of chemotherapeutic agent displayed in the first panel of Figure 2.6). These results indicate that increasing the value of the delivered dose leads to a reduction in the number of tumour cells at the cost of promoting a selective sweep toward more resistant phenotypic variants in the vicinity of the blood vessel – i.e. for values of  $x$  sufficiently close to 0, the area under the curve of the equilibrium local cell phenotypic distribution shrinks (*vid.* the plots in the second and third panel of Figure 2.6) and the equilibrium value of the local mean phenotypic state progressively shifts from values closer to  $y = 0$  to values closer to  $y = 1$  (*vid.* the insets in the second and third panel of Figure 2.6). This supports the idea that higher doses of chemotherapeutic agent removes the selective barrier limiting the growth of less proliferative and more resistant phenotypic variants in vascularised areas of the tumour.

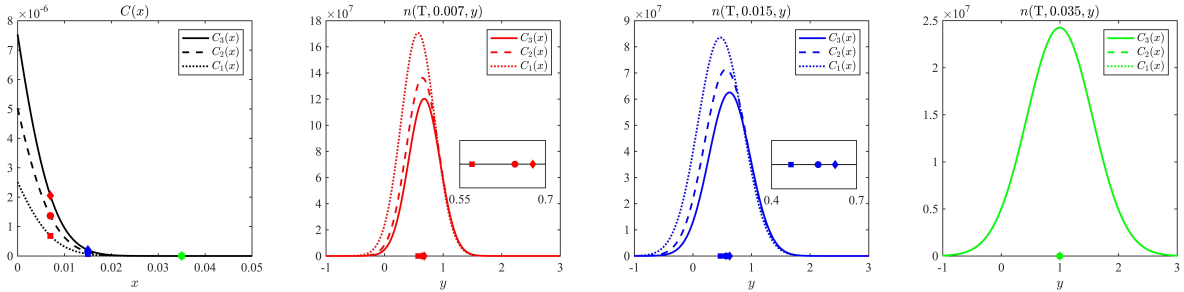


**Figure 2.6: 1D numerical results for different delivered doses of chemotherapeutic agent.** Plots of the local cell phenotypic distributions  $n(T, x, y)$  at  $x = 0.007$  (second panel),  $x = 0.015$  (third panel) and  $x = 0.035$  (fourth panel) obtained by solving numerically (2.26) subject to the initial condition defined via (2.27) and (2.49), under the stationary concentration of oxygen  $S(x)$  displayed in Figure 2.3 and different stationary concentrations of chemotherapeutic agent. In particular, the three stationary concentrations of chemotherapeutic agent displayed in the first panel are used, that is,  $C_1(x) = 0.5 C(x)$  (dotted line),  $C_2(x) = C(x)$  (dashed line) and  $C_3(x) = 1.5 C(x)$  (solid line), where  $C(x)$  is the reference concentration of chemotherapeutic agent displayed in Figure 2.3. In the second, third and fourth panels, the local cell phenotypic distributions at  $t = T$  corresponding to  $C_1$  (dotted lines),  $C_2$  (dashed lines) and  $C_3$  (solid lines) are displayed, and the markers on the axis of abscissas highlight the value of the mean phenotypic state  $\mu(T, x)$  corresponding to  $C_1$  (square),  $C_2$  (bullet) and  $C_3$  (diamond). The insets in the second and third panel display a close-up of the axis of abscissas. The space variable  $x$  is in units of cm,  $T = 10^6$  s and the parameters values used are those listed in Table 2.1 ( $D_n = 0$ ,  $\beta = 10^{-6}$ ).

### 2.3.3 2D numerical results under dynamical concentrations of oxygen and chemotherapeutic agent

The sample of numerical results presented in Figure 2.7 and Figure 2.8 refer to the case where the oxygen concentration  $s(t, \mathbf{x})$  is governed by (2.19), subject to the initial condition (2.50), while the concentration of chemotherapeutic agent  $c(t, \mathbf{x}) \equiv 0$ . On the other hand, the results presented in Figure 2.9 and Figure 2.10 refer to the case where  $s(t, \mathbf{x})$  and  $c(t, \mathbf{x})$  are governed by (2.19) and (2.20), respectively, subject to the initial conditions (2.50). In both cases, the set of points within the tumour tissue which are occupied by blood vessels (i.e. the set  $\omega$ ) is defined as illustrated by the plots in the first panels of Figure 2.7 and Figure 2.9.

**Agreement between analytical and numerical results.** The sample of numerical results presented in Figure 2.7 and Figure 2.9 show that, in the case of constant influx from intratumoural blood vessels, the concentration of oxygen  $s(t, \mathbf{x})$  and the concentration of chemotherapeutic agent  $c(t, \mathbf{x})$  obtained by solving numerically (2.19) and (2.20), subject to the initial conditions (2.50), converge to some equilibria  $s_\infty(\mathbf{x})$  and  $c_\infty(\mathbf{x})$ . As a result, in agreement with our expectation based on the results established by Theorem 1 (*cf.* Remark 2), the cell density  $\rho(t, \mathbf{x})$  and the local mean phenotypic state  $\mu(t, \mathbf{x})$  computed via numerical integration of the local cell phenotypic distribution  $n(t, \mathbf{x}, y)$ , which is obtained by solving numerically (2.5) subject to the initial condition defined via (2.27) and (2.49), converge to the equilibrium values  $\rho_\infty(\mathbf{x})$  and  $\mu_\infty(\mathbf{x})$  given by (2.34) and (2.35). Moreover, the sample of numerical results presented in Figure 2.8 and Figure 2.10 show that the local phenotypic distribution of tumour cells  $n(t, \mathbf{x}, y)$  converges to the equilibrium phenotypic distribution  $n_\infty(\mathbf{x}, y)$  given by (2.33).

**Emergence of spatial gradients of oxygen and chemotherapeutic agent.** The numerical results of Figure 2.7 and Figure 2.9 show that, as one would expect based on the experimental results presented by Helmlinger et al. (1997), the equilibrium concentration of oxygen  $s(T, \mathbf{x})$  and the equilibrium concentration of chemotherapeutic agent  $c(T, \mathbf{x})$  are maximal in the vicinity of the blood vessels and decrease monotonically with the distance from the blood vessels. Moreover, these results demonstrate that the nonlinear interplay between the spatial distribution of the blood vessels, the reaction-diffusion dynamics of oxygen and chemotherapeutic agent, and their consumption by tumour cells leads naturally to the emergence of spatial inhomogeneities in the equilibrium concentrations of such abiotic factors.

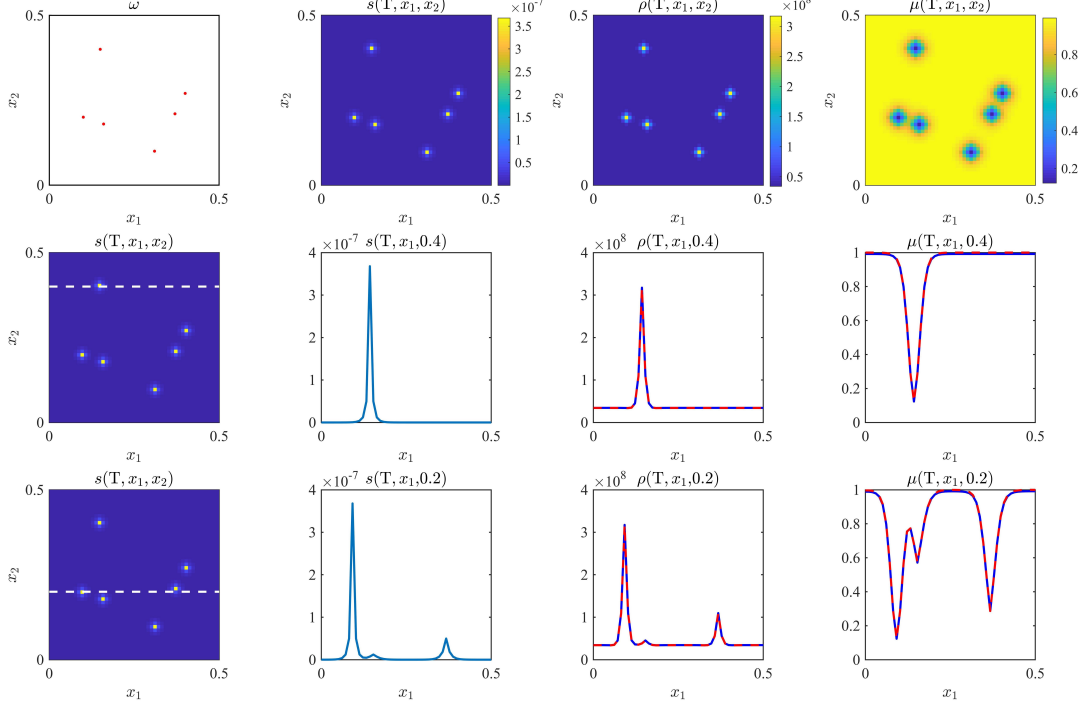


**Figure 2.7: 2D numerical results under dynamical concentration of oxygen and in the absence of chemotherapeutic agent.** *First row:* Plots of the oxygen concentration  $s(T, \mathbf{x})$  (second panel), the cell density  $\rho(T, \mathbf{x})$  (third panel) and the local mean phenotypic state  $\mu(T, \mathbf{x})$  (fourth panel), with  $T = 5 \times 10^5$  s, obtained by solving numerically (2.26) and (2.19) imposing the initial conditions defined via (2.27), (2.49) and (2.50), and assuming  $c(t, \mathbf{x}) \equiv 0$  (i.e. in the absence of chemotherapeutic agent). The set  $\omega$  in (2.22) consists of the parts of  $\Omega$  highlighted in red in the first panel. *Second row:* Plots of the oxygen concentration  $s(T, x_1, 0.4)$  (second panel), the cell density  $\rho(T, x_1, 0.4)$  (third panel, blue line) and the local mean phenotypic state  $\mu(T, x_1, 0.4)$  (fourth panel, blue line). The plot of the oxygen concentration  $s(T, \mathbf{x})$  is displayed in the first panel, where the white, dashed line highlights the 1D cross-section corresponding to  $x_2 = 0.4$ . The red lines in the third and fourth panels highlight  $\rho_\infty(x_1, 0.4)$  and  $\mu_\infty(x_1, 0.4)$  computed through (2.34) and (2.35) with  $s_\infty(x_1, 0.4) := s(T, x_1, 0.4)$  and  $c_\infty \equiv 0$ . *Third row:* Same as the second row but for  $x_2 = 0.2$ . The space variables  $x_1$  and  $x_2$  are in units of cm, and the parameters values used are those listed in Table 2.1 ( $D_n = 0$ ,  $\beta = 10^{-6}$ ).

**Tumour cell dynamics.** The plots in Figures 2.7–2.10 demonstrate that the qualitative behaviour of the numerical results obtained under stationary concentrations of oxygen and chemotherapeutic agents displayed in Figure 2.4 and Figure 2.5 remains unchanged when dynamical concentrations of oxygen and chemotherapeutic agent are considered. Specifically, in the absence of chemotherapy, when moving away from the blood vessels, the equilibrium value of the cell density  $\rho(t, \mathbf{x})$  decreases, the local mean phenotypic state  $\mu(t, \mathbf{x})$  at equilibrium increases from values close to  $y = 0$  to values close to  $y = 1$ , and the equilibrium value of the related variance  $\sigma^2(t, \mathbf{x})$  increases (vid. Figure 2.7 and Figure 2.8). When chemotherapy is administered, its effect is more pronounced in the prox-

imity of the blood vessels and consists in a reduction of the equilibrium value of  $\rho(t, \mathbf{x})$ , a shift of the equilibrium value of  $\mu(t, \mathbf{x})$  toward  $y = 1$  and a reduction of the equilibrium value of  $\sigma^2(t, \mathbf{x})$  compared to the case where the chemotherapeutic agent is not present. Moreover, the evolutionary dynamics of tumour cells is weakly affected by chemotherapy in regions far from the blood vessels, where the concentration of chemotherapeutic agent is lower (*vid.* Figure 2.9 and Figure 2.10).

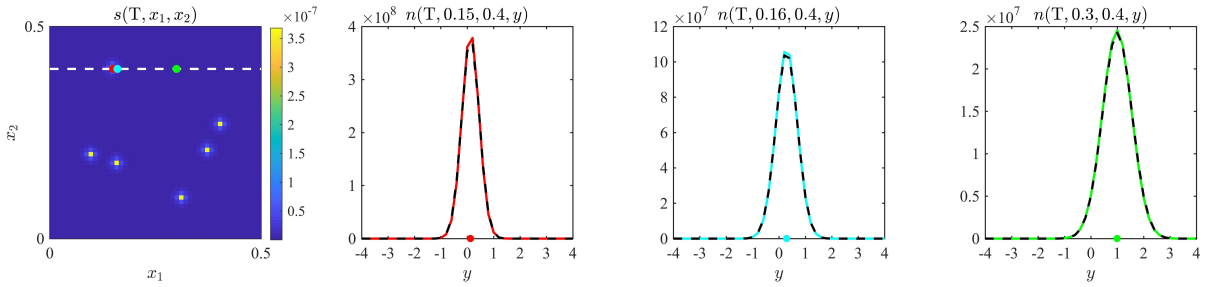


**Figure 2.8: 2D numerical results under dynamical concentration of oxygen and in the absence of chemotherapeutic agent.** Plots of the oxygen concentration  $s(T, \mathbf{x})$  (first panel) and the local cell phenotypic distribution  $n(T, \mathbf{x}, y)$  at  $\mathbf{x} = (0.15, 0.4)$  (second panel),  $\mathbf{x} = (0.16, 0.4)$  (third panel) and  $\mathbf{x} = (0.3, 0.4)$  (fourth panel), with  $T = 5 \times 10^5$  s, obtained by solving numerically (2.26) and (2.19) imposing the initial conditions defined via (2.27), (2.49) and (2.50), and assuming  $c(t, \mathbf{x}) \equiv 0$  (i.e. in the absence of chemotherapeutic agent). The set  $\omega$  in (2.22) consists of the parts of  $\Omega$  highlighted in red in the first panel of Figure 2.7. The white, dashed line in the first panel highlights the 1D cross-section corresponding to  $x_2 = 0.4$  and the bullets highlight the points  $(0.15, 0.4)$ ,  $(0.16, 0.4)$  and  $(0.3, 0.4)$ . In the second, third and fourth panels, the bullets on the axis of abscissas highlight the value of the local mean phenotypic state  $\mu(T, \mathbf{x})$  and the black, dashed lines highlight the asymptotic limit (2.33) with  $\rho_\infty(\mathbf{x})$ ,  $\mu_\infty(\mathbf{x})$  and  $\sigma_\infty^2(\mathbf{x})$  computed through (2.34) and (2.35) with  $s_\infty(x_1, 0.4) := s(T, x_1, 0.4)$  and  $c_\infty \equiv 0$ . The space variables  $x_1$  and  $x_2$  are in units of cm, and the parameters values used are those listed in Table 2.1 ( $D_n = 0$ ,  $\beta = 10^{-6}$ ).

### 2.3.4 Numerical results assessing the impact of tumour tissue vascularisation on intratumour phenotypic heterogeneity

In this section, we first comment on the consistency of the numerical and analytical solutions at equilibrium in the case of  $D_n = \beta = 10^{-13}$ . Then, we illustrate how blood vessel distributions from clinical images may be used along with our modelling framework in order to recreate an *in silico* phenotypic landscape of a vascularised tumour. Finally, we systematically assess the impact of tumour tissue vascularisation on the level of intratumour phenotypic heterogeneity, with numerical simulations considering first increasing numbers of regularly distributed blood vessels, which correspond to increasing values of the vascular density  $\varrho$  defined in (2.53), and then different random distributions

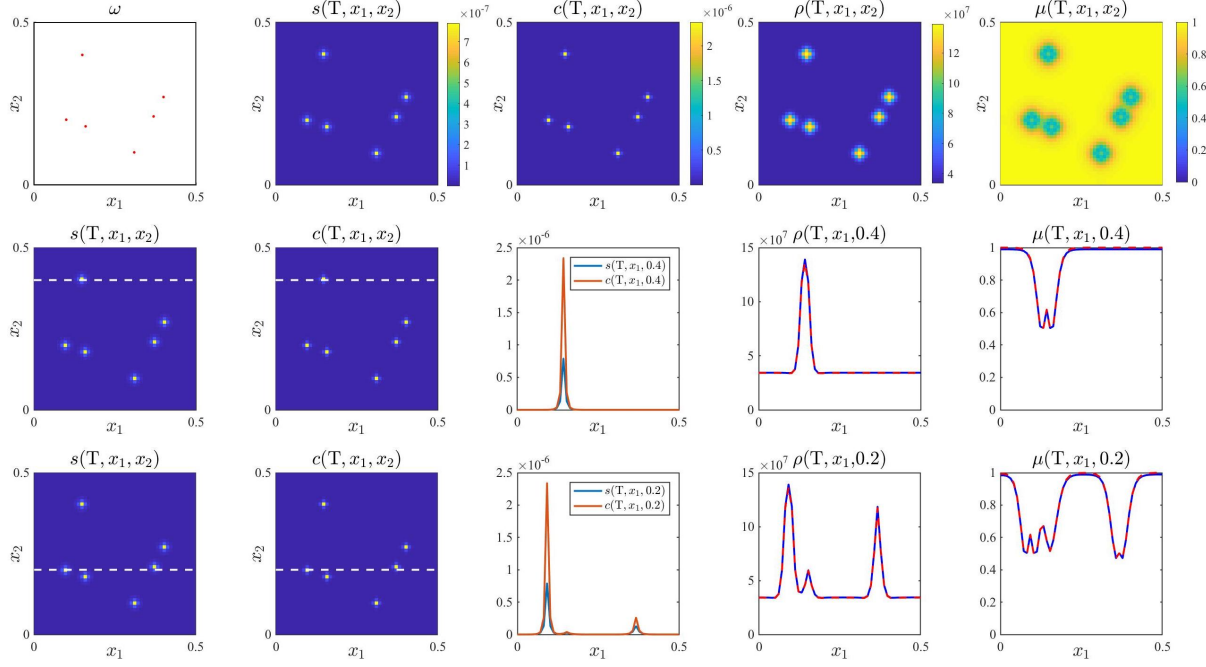


**Figure 2.9: 2D numerical results under dynamical concentrations of oxygen and chemotherapeutic agent.** *First row:* Plots of the oxygen concentration  $s(T, \mathbf{x})$  (second panel), the concentration of chemotherapeutic agent  $c(T, \mathbf{x})$  (third panel), the cell density  $\rho(T, \mathbf{x})$  (fourth panel) and the local mean phenotypic state  $\mu(T, \mathbf{x})$  (fifth panel), with  $T = 5 \times 10^5$  s, obtained by solving numerically (2.26), (2.19) and (2.20) imposing the initial conditions defined via (2.27), (2.49) and (2.50). The set  $\omega$  in (2.22) consists of the parts of  $\Omega$  highlighted in red in the first panel. *Second row:* Plots of the oxygen concentration  $s(T, x_1, 0.4)$  (third panel, blue line), the concentration of chemotherapeutic agent  $c(T, x_1, 0.4)$  (third panel, orange line), the cell density  $\rho(T, x_1, 0.4)$  (fourth panel, blue line) and the local mean phenotypic state  $\mu(T, x_1, 0.4)$  (fifth panel, blue line). The plots of the oxygen concentration  $s(T, \mathbf{x})$  and the concentration of chemotherapeutic agent  $c(T, \mathbf{x})$  are displayed in the first and second panels, where the white, dashed lines highlight the 1D cross-section corresponding to  $x_2 = 0.4$ . The red lines in the fourth and fifth panels highlight  $\rho_\infty(x_1, 0.4)$  and  $\mu_\infty(x_1, 0.4)$  computed through (2.34) and (2.35) with  $s_\infty(x_1, 0.4) := s(T, x_1, 0.4)$  and  $c_\infty(x_1, 0.4) := c(T, x_1, 0.4)$ . *Third row:* Same as the second row but for  $x_2 = 0.2$ . The space variables  $x_1$  and  $x_2$  are in units of cm, and the parameters values used are those listed in Table 2.1 ( $D_n = 0$ ,  $\beta = 10^{-6}$ ).

of blood vessels characterised by increasing levels of vessel clustering for a fixed vascular density. We quantify the level of intratumour phenotypic heterogeneity through the equitability index  $E(t)$  and the Simpson diversity index  $D(t)$  defined in (2.54). We ignore the chemotherapeutic agent to focus on the assessment of pre-treatment intratumour heterogeneity, thus in the following we always consider  $c(t, \mathbf{x}) \equiv 0$ .

**Agreement between analytical and numerical results.** Solving numerically (2.5) and (2.19), subject to initial conditions (2.27), (2.49) and (2.50) under the parameter set reported in Table 2.1 ( $D_n = \beta = 10^{-13}$ ), for an arbitrary distribution of blood vessels,

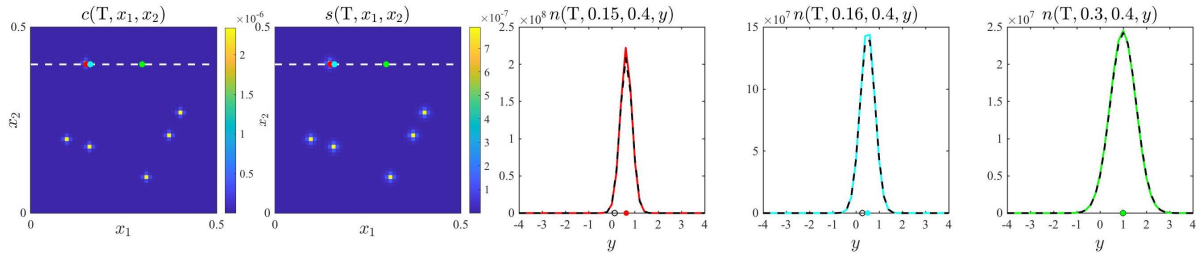


**Figure 2.10: 2D numerical results under dynamical concentrations of oxygen and chemotherapeutic agent.** Plots of the oxygen concentration  $s(T, \mathbf{x})$  (first panel), the concentration of chemotherapeutic agent  $c(T, \mathbf{x})$  (second panel) and the local phenotypic cell distribution  $n(T, \mathbf{x}, y)$  at  $\mathbf{x} \equiv (x_1, x_2) = (0.15, 0.4)$  (third panel),  $\mathbf{x} \equiv (x_1, x_2) = (0.16, 0.4)$  (fourth panel) and  $\mathbf{x} \equiv (x_1, x_2) = (0.3, 0.4)$  (fifth panel), with  $T = 5 \times 10^5$  s, obtained by solving numerically (2.26), (2.19) and (2.20) imposing the initial conditions defined via (2.27), (2.49) and (2.50). The set  $\omega$  in (2.22) consists of the parts of  $\Omega$  highlighted in red in the first panel of Figure 2.9. The white, dashed lines in the first and second panels highlight the 1D cross-section corresponding to  $x_2 = 0.4$  and the bullets highlight the points  $(0.15, 0.4)$ ,  $(0.16, 0.4)$  and  $(0.3, 0.4)$ . In the third, fourth and fifth panels, the filled bullets on the axis of abscissas highlight the value of the mean phenotypic state  $\mu(T, \mathbf{x})$ , while the empty bullets highlight the corresponding values obtained in the case where  $c(t, \mathbf{x}) \equiv 0$  (i.e. in the absence of chemotherapeutic agent). Moreover, the black, dashed lines highlight the asymptotic limit (2.33) with  $\rho_\infty(\mathbf{x})$ ,  $\mu_\infty(\mathbf{x})$  and  $\sigma_\infty^2(\mathbf{x})$  computed through (2.34) and (2.35) with  $s_\infty(x_1, 0.4) := s(T, x_1, 0.4)$  and  $c_\infty(x_1, 0.4) := c(T, x_1, 0.4)$ . The space variables  $x_1$  and  $x_2$  are in units of cm, and the parameters values used are those listed in Table 2.1 ( $D_n = 0$ ,  $\beta = 10^{-6}$ ).

yields similar results to those displayed in Figure 2.7 (vid. supplementary Figure D.1). This is in agreement with the analytic results of Section 2.2.2, in particular with the equilibrium solutions (2.47) and (2.48). Moreover, we verified that the mean phenotypic state  $\mu(T, \mathbf{x})$  and of the maximum point of  $n(T, \mathbf{x}, y)$  at equilibrium correspond, thus verifying numerically the results (2.44) and (2.45) of our formal analysis (cf. insets in the fourth panels of supplementary Figure D.1).

**Reconstruction of blood vessel distributions from clinical images.** The plots in Figure 2.11 demonstrate that the qualitative behaviour of the numerical results in Figure D.1 remains unchanged when spatial distributions of the intratumour blood vessels reconstructed from clinical images are considered. These are the plots of the oxygen concentration  $s(T, \mathbf{x})$ , the cell density  $\rho(T, \mathbf{x})$  and the mean phenotypic state  $\mu(T, \mathbf{x})$  obtained by solving numerically the problem given by (2.5) and (2.19) subject to the initial conditions (2.27), (2.51) and (2.50), with  $\omega$  defined according to the distributions of blood vessels provided by the clinical images displayed in the first column of the figure, which were obtained via D-OCT and correspond to three cross-sections of a malignant melanoma at a depth of 0.02 cm (top panel), 0.03 cm (central panel) and 0.04 cm (bottom panel) from the surface of the epidermis (Schuh et al., 2017, Fig. 5). These results also

indicate that increasing levels of tumour vascularisation (from top to bottom panel in the first column) lead to a more homogeneous spatial distribution of oxygen (second column), which correlates with a more uniform cell density (third column) and a less diverse mean phenotypic state (fourth column). This suggests the existence of a relationship between the level of tumour tissue vascularisation and the level of intratumour phenotypic heterogeneity, which is systematically investigated in the next subsection.

**The impact of blood vessel density.** The results obtained varying the vascular density  $\varrho$  are summarised by the plots in Figure 2.12, which display the equitability index and the Simpson diversity index at the end of numerical simulations as functions of  $\varrho$ . Both diversity indices are relatively low for small values of the vascular density, increase and reach a maximum value for intermediate values of the vascular density – notice that both  $E(T)$  and  $D(T)$  attain their maximum at the same value of  $\varrho$  – and then decrease again for high values of the vascular density. This is due to the fact that, as shown by the insets in Figure 2.12, for low blood vessel densities the oxygen concentration  $s(T, \mathbf{x})$  is uniformly low throughout  $\Omega$  and, therefore, the mean phenotypic state  $\mu(T, \mathbf{x})$  is uniformly close to  $y = 1$  (*cf.* the insets related to  $\varrho = 0.4 \times 10^{-3}$ ); for intermediate blood vessel densities the oxygen concentration is more heterogeneously distributed and, as a consequence, the mean phenotypic state is more diverse (*cf.* the insets related to  $\varrho = 2.5 \times 10^{-3}$ ); for high blood vessel densities the oxygen concentration is relatively high throughout the tumour tissue and the mean phenotypic state is on average close to  $y = 0$  (*cf.* the insets related to  $\varrho = 8.1 \times 10^{-3}$ ).

**The impact of blood vessel clusterisation.** The results obtained varying the level of blood vessel clustering for a fixed vascular density  $\varrho$  are summarised by the plots in Figure 2.13, which display the oxygen distribution  $s(T, \mathbf{x})$  and the mean phenotypic state  $\mu(T, \mathbf{x})$ , along with the corresponding fraction of cells in each phenotypic state  $F(T, y)$  and diversity indices  $E(T)$  and  $D(T)$ . These results refer to an intermediate value of  $\varrho$  that corresponds to the maximum of the equitability index and the Simpson diversity index displayed in Figure 2.12 (i.e.  $\varrho = 25 \times 10^{-4}$ ). Both diversity indices decrease as the level of blood vessel clustering increases (*cf.* the values of  $E(T)$  and  $D(T)$  in the insets of the panels in the third column of Figure 2.13). In fact, for lower levels of blood vessel clustering the oxygen concentration  $s(T, \mathbf{x})$  is more heterogeneously distributed and, as a consequence, the mean phenotypic state  $\mu(T, \mathbf{x})$  is more diverse and the cell phenotypic distribution across  $\Omega$  given by  $F(T, y)$  is rather uniform (*cf.* the plots in the first row of Figure 2.13). On the other hand, for higher levels of blood vessel clustering, the oxygen concentration is relatively high in the regions in close proximity to the clusters of blood vessels and relatively low throughout the rest of tumour tissue. As a result, the mean

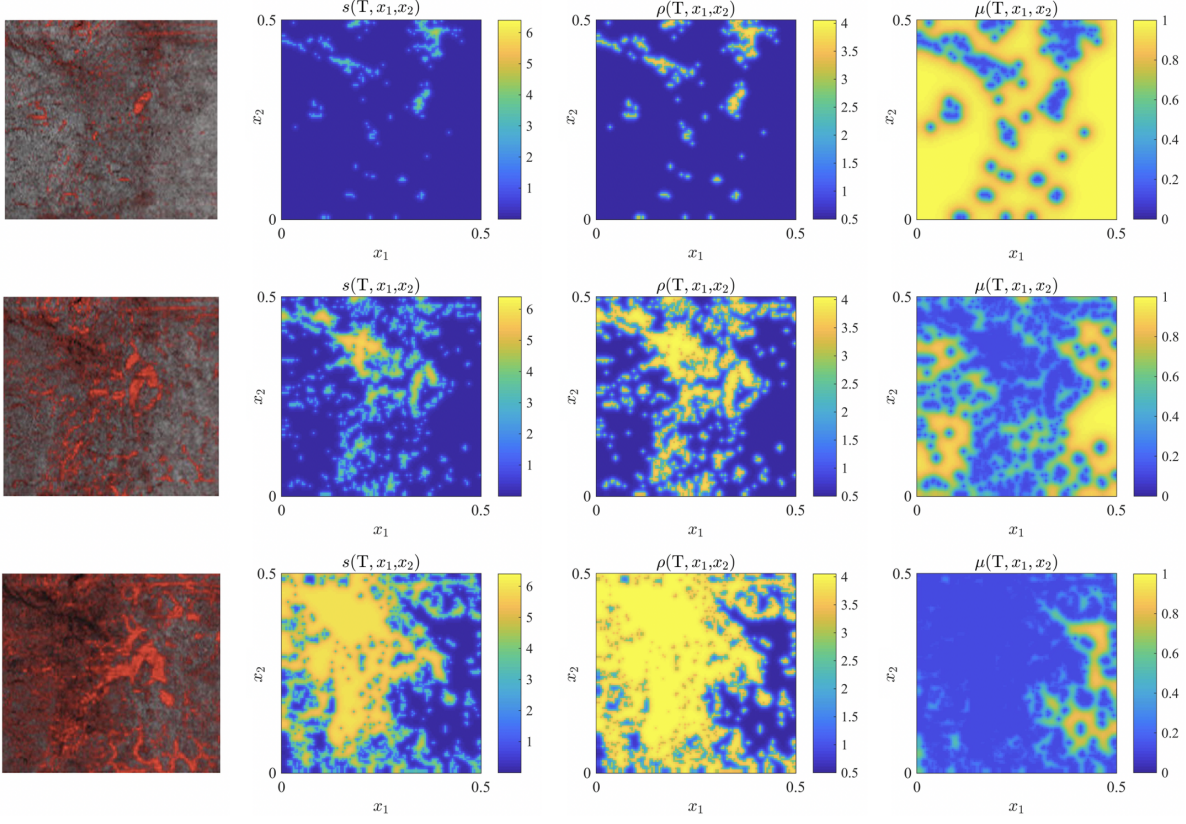


**Figure 2.11: Numerical results for blood vessel distributions reconstructed from clinical images.** *First row:* Plots of the oxygen concentration  $s(T, \mathbf{x})$  (second panel), the cell density  $\rho(T, \mathbf{x})$  (third panel) and the mean phenotypic state  $\mu(T, \mathbf{x})$  (fourth panel), with  $T = 5 \times 10^5$  s, obtained by solving numerically the problem given by (2.5) and (2.19) subject to the initial conditions defined via (2.27), (2.51) and (2.50). The set  $\omega$  is reconstructed from the blood vessel distribution provided by the clinical image displayed in the first panel, where the intratumoural vascular network is highlighted in red. *Second and third row:* Same as the first row but for a different clinical image. Clinical images are taken from Dermatology and Therapy 7(2), S. Schuh, J. Holmes, M. Ulrich, L. Themstrup, G. B. Jemec, N. De Carvalho, G. Pellecani, J. Welzel, Imaging blood vessel morphology in skin: dynamics optical coherence tomography as a novel potential diagnostic tool in dermatology, 187-202, 2017, under Creative Commons licence <https://creativecommons.org/licenses/by-nc/4.0/> (Schuh et al., 2017, Fig. 5(d-f)). These images correspond to three cross sections of a malignant melanoma at a depth of 0.02 cm (first row), 0.03 cm (second row) and 0.04 cm (third row) from the surface of the epidermis. The oxygen concentration  $s(T, \mathbf{x})$  is in units of  $10^{-7} \text{ g cm}^{-2}$ , the cell density  $\rho(T, \mathbf{x})$  is in units of  $10^8 \text{ cells cm}^{-2}$ , and the spatial variables  $x_1$  and  $x_2$  are in units of cm. The parameter values listed in Table 2.1 ( $D_n = \beta = 10^{-13}$ ) except for  $\eta_s = 2 \times 10^{-10} \text{ g cell}^{-1}$ .

phenotypic state is mostly close to  $y = 1$  with the exception of the regions near the clusters of blood vessels where it is close to  $y = 0$ , and the cell phenotypic distribution across the whole tumour is approximatively bimodal, with a high peak at  $y = 1$  and a low peak at  $y = 0$  (*cf.* the plots in the third row of Figure 2.13).

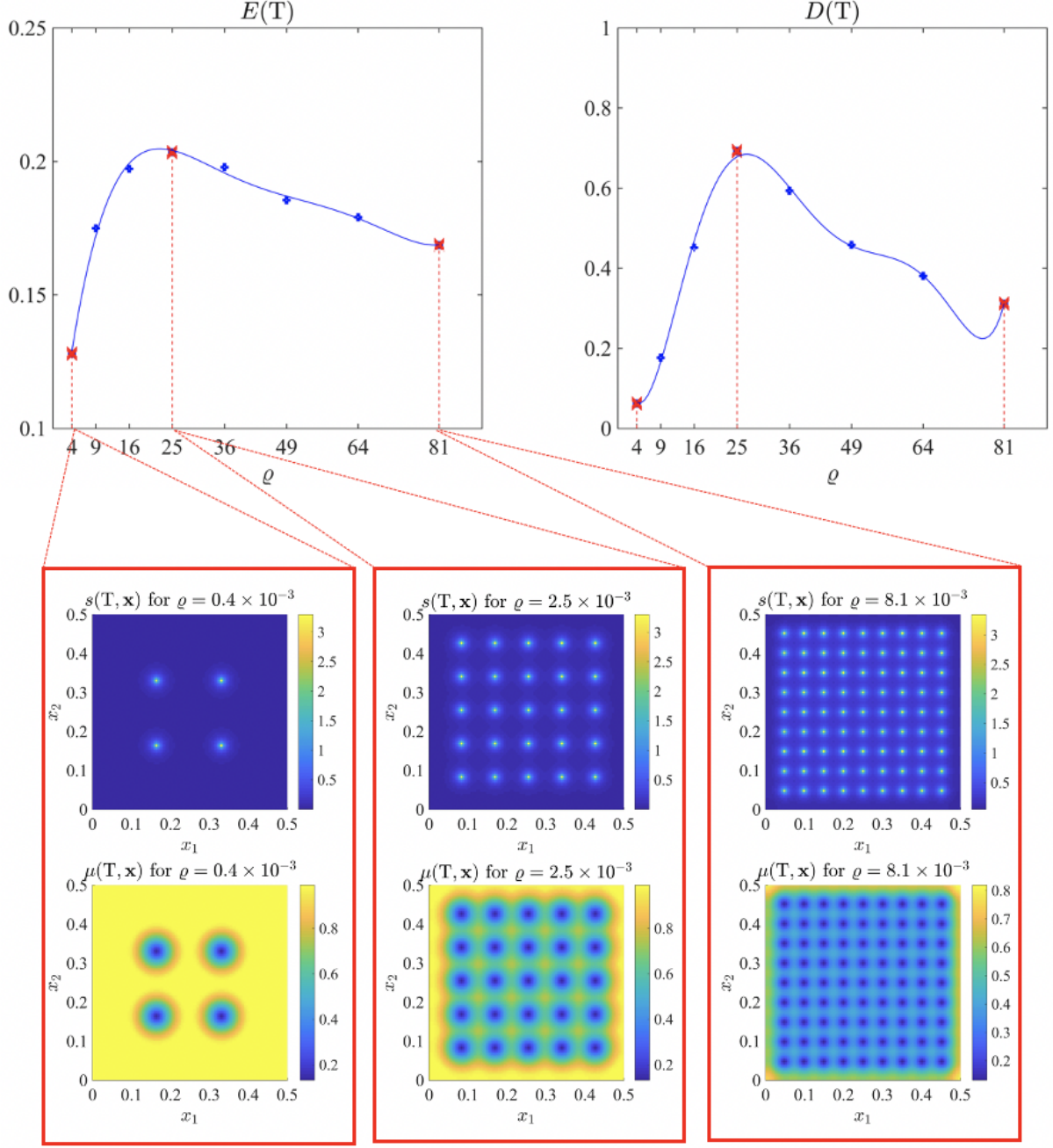


**Figure 2.12: Effect of varying blood vessel density on the level of intratumour phenotypic heterogeneity.** Plots of the equitability index  $E(T)$  and the Simpson diversity index  $D(T)$ , with  $T = 5 \times 10^5$  s, for different definitions of the set  $\omega$  characterised by different values of the vascular density  $\varrho$  defined according to (2.53). The equitability index and the Simpson diversity index are computed numerically through formulas (2.54) using the numerical solutions of the problem given by (2.5) and (2.19) subject to the initial conditions defined via (2.27), (2.51) and (2.50). The insets display sample plots of the oxygen distributions  $s(T, \mathbf{x})$  (top panel) and the mean phenotypic state  $\mu(T, \mathbf{x})$  (bottom panel) corresponding to different values of  $\varrho$ . The Simpson diversity index  $D(T)$  is in units of  $10^4$ , the vascular density  $\varrho$  is in units of  $10^{-4}$ , the oxygen concentration  $s(T, \mathbf{x})$  is in units of  $10^{-7} \text{ g cm}^{-2}$ , the spatial variables  $x_1$  and  $x_2$  are in units of cm, and the parameter values used are those listed in Table 2.1 ( $D_n = \beta = 10^{-13}$ ).

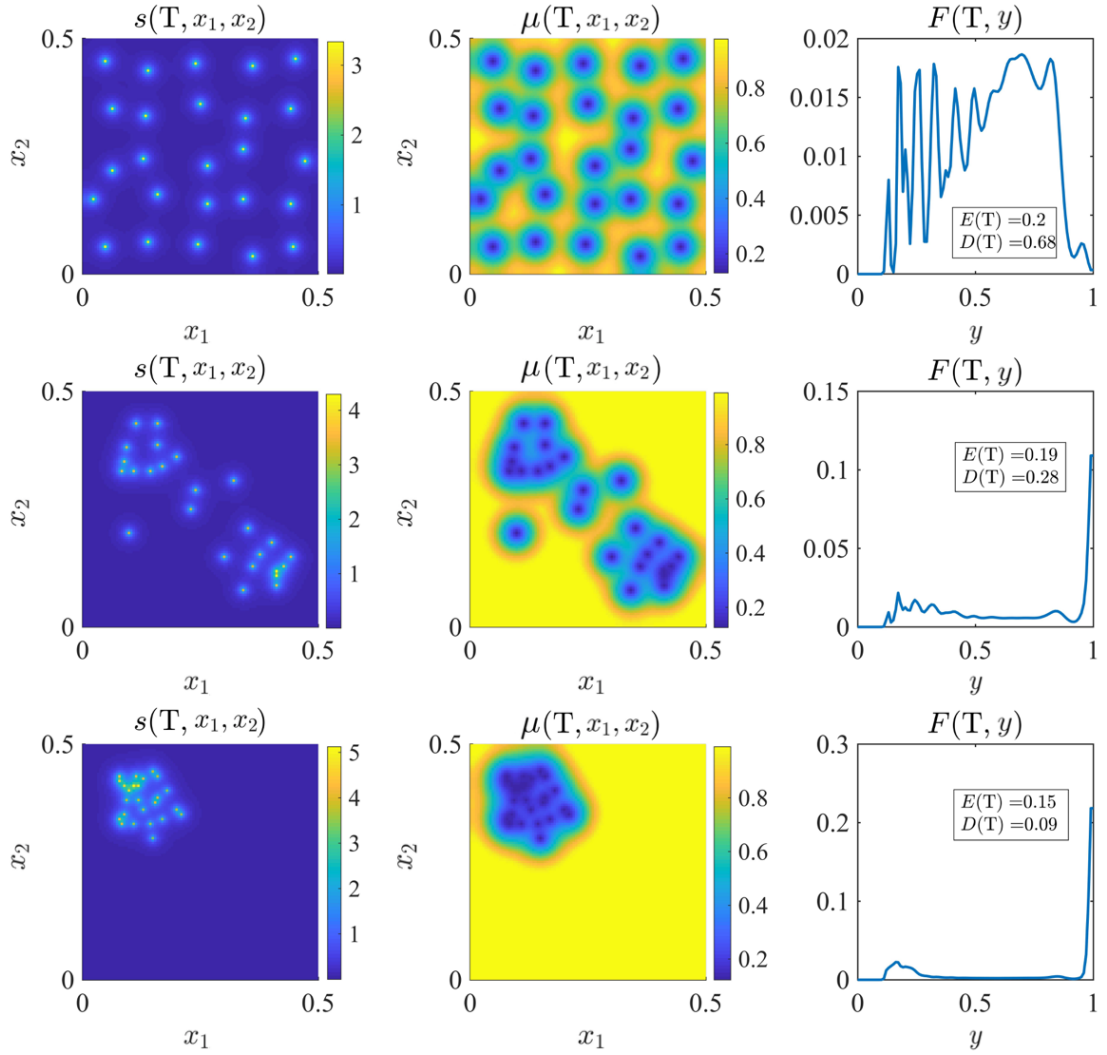


**Figure 2.13: Effect of varying blood vessel clusterisation on the level of intratumour phenotypic heterogeneity.** First row: Plots of the oxygen distribution  $s(T, \mathbf{x})$  (first panel), mean phenotypic state  $\mu(T, \mathbf{x})$  (second panel) and fraction of cells in each phenotypic state  $F(T, y)$  defined via (2.4) (third panel), with  $T = 5 \times 10^5$  s, obtained by solving numerically the problem given by (2.5) and (2.19) subject to the initial conditions defined via (2.27), (2.49) and (2.50). The set  $\omega$  is defined according to a random distribution of blood vessels characterised by vascular density  $\varrho = 25 \times 10^{-4}$  and a low level of blood vessel clustering. The values of the corresponding equitability index  $E(T)$  and Simpson diversity index  $D(T)$ , which are computed numerically through formulas (2.54), are provided in the inset of the third panel. Second and third row: Same as the first row but for a definition of the set  $\omega$  corresponding to an intermediate level (second row) and a high level (third row) of blood vessel clustering. The oxygen concentration  $s(T, \mathbf{x})$  is in units of  $10^{-7} \text{ g cm}^{-2}$ , the spatial variables  $x_1$  and  $x_2$  are in units of cm, the Simpson diversity index  $D(T)$  is in units of  $10^4$ , and the parameter values used are those listed in Table 2.1 ( $D_n = \beta = 10^{-13}$ ).

# Chapter 3

## Discussion and research perspectives

### 3.1 Summary and discussion

The theoretical works and empirical data presented in Chapter 1 demonstrate how intratumour phenotypic heterogeneity supports the emergence of therapeutic resistance and therefore poses a major obstacle to anti-cancer therapy (Burrell and Swanton, 2014; Chisholm et al., 2015; Gillies et al., 2012; Lipinski et al., 2016; Michor and Polyak, 2010; Shah and Schwartz, 2001). It has been hypothesised that the emergence of phenotypic heterogeneity among cancer cells within malignant tumours is an eco-evolutionary process driven by spatial variability in the distribution of abiotic factors, which supports the creation of distinct ecological niches whereby cells with different phenotypic characteristics can be selected (Alfarouk et al., 2013; Kaznatcheev et al., 2017; Marusyk et al., 2012; Sun and Yu, 2015). In particular, oxygen is one of the key abiotic components of the tumour microenvironment that are implicated in the emergence of intratumour phenotypic heterogeneity (Gillies et al., 2012; Lorenzi et al., 2018; Sun and Yu, 2015).

In Chapter 2, we have undertaken a mathematical study of the eco-evolutionary dynamics of tumour cells within vascularised tumours both pre-treatment and under chemotherapy. The study is based on analysis and numerical simulations of a nonlocal PDE model that describes the phenotypic evolution of tumour cells and their nonlinear dynamic interactions with the oxygen and chemotherapeutic drug, which are released from the intratumoural vascular network. In particular, following previous works in the growing literature of mathematical models of adaptive dynamics of populations structured by a continuous trait (*cf.* Chapter 1), the model relies on a nonlocal reaction-diffusion equation describing the spatiotemporal evolution of a space- and phenotype-structured population. Under stationary concentrations of oxygen and chemotherapeutic agent and in the absence of spatial diffusion, exact solutions to system (2.5) have been obtained and

verified numerically. In the presence of spatial diffusion, under analogous assumptions on the abiotic factor concentrations, formal asymptotic analysis has been employed to obtain weak solutions which are consistent with the exact solution obtained in the previous case. The analytical and numerical results elucidate the adaptive processes that underpin the emergence of intratumour phenotypic heterogeneity and development of resistance to chemotherapeutic agents.

### 3.1.1 The emergence of intratumour phenotypic heterogeneity and the development of chemotherapeutic resistance

The results of the analysis of evolutionary dynamics recapitulate previous theoretical results (Alfarouk et al., 2013; Anderson et al., 2006; Ardaševa et al., 2020c; Gallaher and Anderson, 2013; Gillies et al., 2012; Ibrahim-Hashim et al., 2017; Kaznatcheev et al., 2017; Lorenzi et al., 2018; Lorz et al., 2015; Marusyk et al., 2012; Sun and Yu, 2015) and experimental data (Padhani et al., 2007; Semenza, 2003; Sun and Yu, 2015; Tannock, 1968) by demonstrating that spatial inhomogeneities in the concentration of oxygen promote the selection of different phenotypic variants at different positions within the tumour. More specifically, the analytical results indicate that the tumour tissue in the vicinity of blood vessels is to be expected to be densely populated by aerobic phenotypic variants, while poorly oxygenated regions of the tumour are more likely to be sparsely populated by anaerobic phenotypic variants. Furthermore, the analytical results obtained in the absence of spatial diffusion support the idea that higher levels of phenotypic variability may occur in hypoxic regions of the tumour, which provides a theoretical basis for experimental results such as those presented by Axelson et al. (2005).

Coherently with observations made in previous theoretical and experimental studies (Adamski et al., 2013; Brown and Giaccia, 1998; Powathil et al., 2012b; Sullivan et al., 2008; Wartenberg et al., 2003), the analytical results also suggest that hypoxia favours the selection for chemoresistant phenotypic variants prior to treatment, which facilitates the development of resistance following chemotherapy. Moreover, these results put on a rigorous mathematical basis the idea, previously suggested by formal analysis and numerical simulations (Lorenzi et al., 2018; Robertson-Tessi et al., 2015), that chemotherapy removes the selective barrier limiting the growth of chemoresistant phenotypic variants by killing aerobic phenotypic variants in well-oxygenated regions of the tumour.

The analytical results are corroborated by the numerical simulations. The numerical results also indicate that gradients of oxygen and chemotherapeutic agents, which are released from the intratumoural vascular network, naturally emerge in vascularised tumours due to the nonlinear interplay between the spatial distribution of the blood vessels, the reaction-diffusion dynamics of oxygen and chemotherapeutic agents, and their con-

sumption by tumour cells.

### 3.1.2 Vascularisation and phenotypic heterogeneity

The results of numerical simulations of the model further establish a relation between the degree of tissue vascularisation and the level of intratumour phenotypic heterogeneity, measured either as the equitability index or the Simpson diversity index, which may be affected by the level of clusterisation of blood vessels. This supports the idea that maps of the intratumour vascular network, which can be reconstructed from clinical images obtained via non-invasive imagine techniques, such as D-OCT (Lavinia, 2016; Schuh et al., 2017) and many others (Anderson et al., 2001; Fukumura et al., 2010; Grimes et al., 2016; Nobre et al., 2018; Padhani et al., 2007), could be clinically relevant, as they could be used to inform targeted anticancer therapy (Marusyk et al., 2012; Powathil et al., 2012a,b; Vaupel, 2004). In view of the simplifying assumptions on blood vessel morphology and inflow rates of abiotic factors from the vasculature made in Chapter 2, the aforementioned results would be of particular clinical relevance in combination with vascular normalisation treatments (Jain et al., 2007; Magnussen and Mills, 2021). Whilst numerical simulations were carried out considering a region of tumour tissue of area  $2.5 \times 10^{-3} \text{ cm}^2$ , which was chosen in agreement with clinical images provided by Schuh et al. (2017), and using parameter values that are derived from specific cancer datasets, given the robustness and structural stability of the results of analysis presented here, we expect the conclusions of this study about the emergence of substantial intratumour phenotypic heterogeneity driven by eco-evolutionary processes at the cellular scale to hold when larger tumour regions and different cancer datasets are considered.

### 3.1.3 The role of spatial diffusion

The results of the formal asymptotic analysis presented in Section 2.2.2, in the case where cell movement is modelled through Fick's first law, indicate that the qualitative behaviour of the results obtained in the absence of spatial diffusion remain unchanged in the asymptotic regime where the rate of spontaneous phenotypic variation and the cell diffusivity tend to zero. In order to disentangle and quantify the impact of spatial movement on the emergence and development of intratumour phenotypic heterogeneity, it would be useful to have exact solutions of (2.5). However, further developments of the method of proof employed here are required in order to carry out a similar analysis of evolutionary dynamics in more general scenarios. In fact, some works suggest that more significant spatial movement may result in the emergence of a polymorphic population (Arnold et al., 2012; Mirrahimi, 2017; Mirrahimi and Gandon, 2020).

## 3.2 Research perspectives

### 3.2.1 Alternative temporal scales and stochasticity

In order to further assess the clinical relevance of intratumoural phenotypic landscapes that could be drawn from clinical images discussed in Section 3.1.2, the model should be validated experimentally. The results presented in Chapter 2 rely on the assumption of a fixed vasculature in order to obtain a steady state solution and the intratumoural blood vessel maps that can be obtained from clinical images illustrate only a snapshot of a complex biological system undergoing spatiotemporal changes. Despite the long-time asymptotics considered to characterise the phenotypic landscapes discussed in Section 2.3.4, we expect the drawn conclusions to be comparable with empirical observations in evolving vascularised tumours, given the agreement between the model results presented in Section 2.3.3 and the empirical observations on intratumour phenotypic heterogeneity reported in Section 1.1.3. Moreover, the realistic time-scale at which chemoresistant phenotypic variants are selected in hypoxic regions may be shorter in view of the hypoxia-induced up-regulation of HIF-1 (Denko, 2008; Lee et al., 2004; Semenza, 2010) and related glycolytic switch (Baumann et al., 2007). This could be tested by extending the model here presented to include a phenotypic drift induced by environmental stress, i.e. hypoxia, similarly to the one proposed by Chisholm and coworkers (Chisholm et al., 2016b, 2015; Lorenzi et al., 2015).

Furthermore, although well suited to modelling the dynamics of large cell populations, PDE models like that considered here cannot capture adaptive phenomena that are driven by stochasticity in the evolutionary paths of single cells, particularly relevant in the comparison with empirical data. Therefore, it would also be interesting to complement the results of our study with numerical simulations of corresponding IB models which track the evolutionary trajectories of single cells across a space of discrete phenotypic states, as similarly done by Ardaševa et al. (2020a); Chisholm et al. (2016b, 2015); Stace et al. (2020). In such case, the dynamics of tumour cells would be described in terms of a branching random walk, while the concentrations of oxygen and chemotherapeutic agent would be governed by discrete balance equations. This would make it possible to have a more precise description of the phenotypic evolution of tumour cells in cases where cell numbers are relatively low and, therefore, stochastic fluctuations in single-cell phenotypic properties will have a stronger impact on intratumour phenotypic heterogeneity. This may, for instance, be the case for highly vascularised tumours, where distances between capillaries may be so small that only few cells reside in the space between them.

### 3.2.2 Environmental fluctuations and additional abiotic factors

Further investigations on a possible link between the tumour blood vessel distribution and the level of intratumour phenotypic heterogeneity could be undertaken, along the lines of Scott et al. (2016), and extended to post-treatment scenarios. It would also be interesting to include the effect of temporal variation in the spatial distribution of intratumoural blood vessels, which would make it possible to explore the influence of angiogenesis on the evolutionary dynamics of tumour cells in vascularised tumours. More complex models would need to be formulated in order to include explicit vascular dynamics, as indicated by the extensive literature addressing the experimental and theoretical study of neovascularisation processes – see Part III. Moreover, building upon the ideas presented by Ardaševa and coworkers (Ardaševa et al., 2020b,c), it would be interesting to study the effect on the evolutionary dynamics of tumour cells of fluctuations in the rate of oxygen inflow, which are known to influence intratumour phenotypic heterogeneity (Gillies et al., 2018; Marusyk et al., 2012; Robertson-Tessi et al., 2015). Finally, while the focus of this work has been on the impact of spatial variability in the oxygen and chemotherapeutic agent concentrations on the emergence of intratumour phenotypic heterogeneity, building on Fiandaca et al. (2021b), it would be interesting to extend the modelling framework used here to incorporate the effect of nonlinear dynamic interactions between tumour cells and other abiotic factors, such as glucose and lactate, that are known to influence the levels of intratumour phenotypic heterogeneity (Gatenby et al., 2007; Gatenby and Gillies, 2007; Gillies and Gatenby, 2007; Kaznatcheev et al., 2017; Manem et al., 2015; Molavian et al., 2009; Robertson-Tessi et al., 2015; Zhao et al., 2013).

### 3.2.3 Optimal therapeutic strategies

As similarly done in Almeida et al. (2019) and Pouchol et al. (2018), it would be relevant to address numerical optimal control of the model equations in order to identify possible delivery schedules of the chemotherapeutic agent that make it possible to minimise the number of tumour cells at the end of the treatment or the average number of tumour cells during the course of treatment (Chisholm et al., 2016a; Clairambault and Pouchol, 2019). In particular, it would be relevant to verify whether the results presented by Almeida et al. (2019) for a spatially homogeneous model carry through when spatial reaction-diffusion dynamics of the chemotherapeutic agent are incorporated into the model. In this regard, it would be interesting to assess the impact of molecular properties of the chemotherapeutic agent (e.g. decay, diffusion and cellular uptake rates) and structural properties of the intratumoural vascular network (e.g. vascular density and blood vessels distribution) on the optimal chemotherapy schedule.

### 3.2.4 A nonlocal PDE model of metastatic spread

Finally, the model considered here could be extended to carry out a mathematical study of the eco-evolutionary dynamics of tumour cells in metastatic tumours. In this respect, a modelling approach analogous to the one presented by Franssen et al. (2019), whereby different metastatic sites are represented as distinct compartments and the metastatisation process is modelled by allowing tumour cells to transition from one site to another through the intratumour blood vessels seen as entry/exit locations, may prove useful.

Building on Mirrahimi (2017) and Mirrahimi and Gandon (2020), insights on the eco-evolutionary dynamics of metastatic cancers could first be gained considering a simpler modelling framework. Consider the evolutionary dynamics of  $N \in \mathbb{N}$  cancer cell populations residing in  $N$  different sites of the body, each characterised by its local environment, some of which may be connected. In particular, we label the primary tumour site as site  $i = 1$ , while sites  $i = 2, \dots, N$  represent the  $N - 1$  metastatic ones, as illustrated in Figure 3.1A. Proliferation, death and spontaneous phenotypic changes of population  $n_i(t, y)$  ( $i = 1, \dots, N$ ) is determined locally as in the model presented in Chapter 2. Moreover, cells can transition between sites at a rate  $\nu_{ij}(y)$  which depends on site connectivity and the cell phenotypic state, i.e. we have

$$\begin{cases} \partial_t n_i = R_i(y, \rho_i) n_i + \beta_i \partial_y^2 n_i + \sum_{\substack{j=1 \\ j \neq i}}^N [\nu_{ji}(y) n_j - \nu_{ij}(y) n_i] \\ \rho_i(t) := \int_0^1 n_i(t, y) dy \end{cases} \quad i = 1, \dots, N \quad (3.1)$$

subject to suitable initial conditions. This model could be employed to disentangle the evolutionary determinants of metastatic spread (e.g. the seed-and-soil hypothesis, secondary seeding), by investigating the conditions under which different solutions are observed (cf. Figure 3.1B).

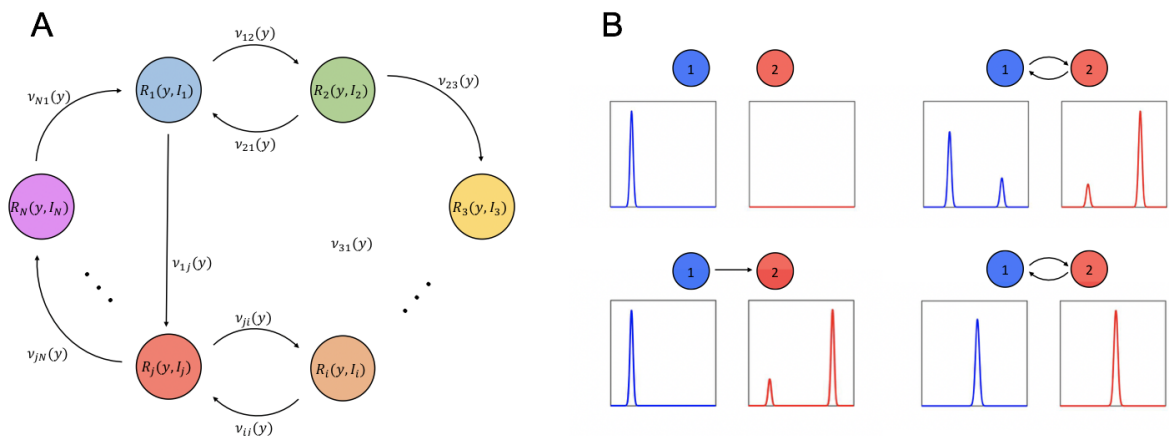


**Figure 3.1: Modelling metastatic spread.** (A) Schematic illustration of interconnected metastatic sites modelled by system (3.1). (B) Example solutions of system (3.1).

## **Part III**

# **Modelling cluster formation in vasculogenesis**

This part focusses on modelling the formation of clusters during the early stages of vasculogenesis. The formation of new vascular networks is essential for tissue development and regeneration, in addition to playing a key role in pathological settings such as ischemia and tumour development. Experimental findings in the past two decades have led to the identification of a new mechanism of neovascularisation, known as cluster-based vasculogenesis, during which endothelial progenitor cells (EPCs) mobilised from the bone marrow are capable of bridging distant vascular beds in a variety of hypoxic settings *in vivo*. This process is characterised by the formation of EPC clusters during its early stages and, while much progress has been made in identifying various mechanisms underlying cluster formation, we are still far from a comprehensive description of such spatiotemporal dynamics. In addition, a systematic mathematical description of the determinants of cluster formation and size may help unlock its full therapeutic potential. In order to achieve this, we propose a novel mathematical model of the early stages of cluster-based vasculogenesis, comprising a system of PDEs including key mechanisms such as endogenous chemotaxis, matrix degradation, cell proliferation and nonlocal cell-to-cell adhesion. We conduct a LSA on the system and solve the equations numerically, employing the numerical solutions to investigate the determinants of cluster formation and cluster size. The results, which qualitatively compare with data from *in vitro* experiments, elucidate the complementary role played by endogenous chemotaxis and matrix degradation in the formation of clusters, suggesting chemotaxis is responsible for the clusters' structure while matrix degradation is responsible for the speed of cluster formation. Our results also indicate that the nonlocal cell-to-cell adhesion term in our model, even though it initially causes cells to aggregate, is not sufficient to ensure clusters are stable over long time periods. Consequently, new modelling strategies for cell-to-cell adhesion are required to stabilise *in silico* clusters. The results of the proposed model are compared with related findings in the extant literature and various promising future research perspectives are identified.

Part III is organised as follows: in Chapter 4 the biological background leading to relevant *in vitro* studies of cluster-based vasculogenesis is presented together with an overview of the mathematical models of vasculogenesis proposed in the literature; in Chapter 5 a nonlocal PDE model of EPC cluster formation during the early stages of vasculogenesis is presented together with its analytical and numerical results; in Chapter 6 a thorough discussion of the results is given together with promising research perspectives.

The contents of Part III are based on the paper Villa et al. (2022).

# Chapter 4

## Biological and modelling background

### 4.1 Endothelial progenitor cell cluster-based vasculogenesis

Blood vessels are tubular structures of various sizes – with diameters varying between  $5\mu\text{m}$  (capillaries) and 2cm (aorta) – which carry blood throughout the body and they are part of the circulatory system (Gartner, 2020). Capillaries, the smallest type of blood vessel, are composed of a layer of mature endothelial cells (ECs), called endothelium, covered by what is known as the basement membrane, separating it from the surrounding connective tissue<sup>1</sup>. Arteries and veins have a more laminated structure, composed of a thick outer layer (tunica externa or adventina) made up of connective tissue, an even thicker middle layer (tunica media) made up of circularly arranged elastic fibers and smooth muscle cells, and a thin inner layer (tunica intima) of endothelium supported by a subendothelial layer. The void area in which the blood flows is known as the lumen.

The formation of new vascular networks is essential for tissue development and regeneration, since a functional vasculature is critical for tissue homeostasis. It is responsible for the delivery of oxygen and nutrients as well as the disposal of waste products. In addition, neovascularisation of local tissue is critical in a variety of pathological processes, among which are retinopathy, wound healing, soft-tissue ischemia<sup>2</sup> and tumour growth (Ramos et al., 2018). As seen in Section 1.1.1, the development of a vascular network in localised solid tumours is particularly well-known to promote further tumour growth and metas-

<sup>1</sup>Connective tissue supports, protects, and gives structure to other tissues and organs in the body; it is made up of cells, fibers and a gel-like substance (interstitial matrix).

<sup>2</sup>Ischemia is a restriction in blood supply, causing a shortage of oxygen and nutrients needed for cellular metabolism and inadequate removal of metabolic waste, resulting in tissue damage or dysfunction.

tases. Therefore a better understanding of the mechanisms governing neovascularisation can help improve current therapeutic strategies, as well as identify new ones.

New blood vessels may form from pre-existing ones through the neovascularisation process known as angiogenesis. Vasculogenesis, on the other hand, is the *de novo* formation of blood vessels, during which endothelial progenitor cells (EPCs) reorganise into networks and subsequently differentiate into mature ECs, as summarised in Figure 4.1. This is an important distinction since EPCs are highly proliferative cells, unlike mature ECs (Asahara et al., 1997; Blatchley et al., 2019; Kukumberg et al., 2021; Vajkoczy et al., 2003; Zhang et al., 2014). Once a new network-like pattern of mature ECs has formed, lumen formation occurs along EC cords due to a series of complex molecular mechanisms involving cell shape changes (Lammert and Axnick, 2012). Different biological, chemical and mechanical processes are at the basis of EC and EPC reorganisation into networks, and they involve a variety of homotypic and heterotypic interactions<sup>3</sup>.

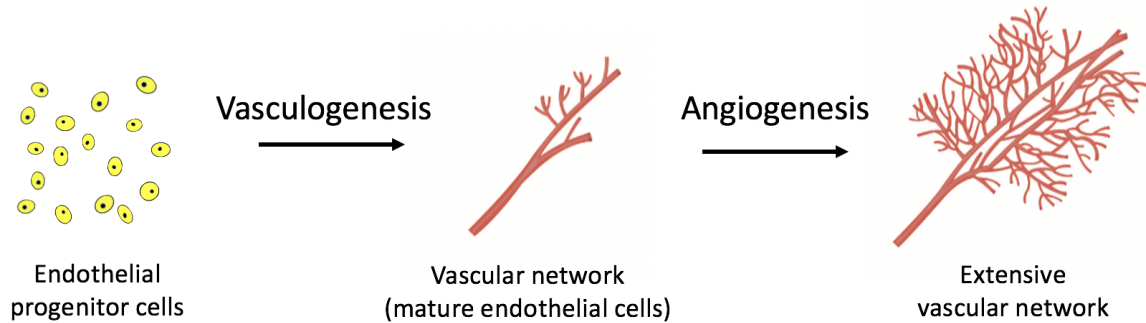


**Figure 4.1: Neovascularisation processes.** Visual summary of vascular network formation via vasculogenesis (EPCs, *de novo*) and angiogenesis (mature ECs, from pre-existing vessels). Figure produced by editing illustrations by L. Govi, with permission from the artist.

#### 4.1.1 Homotypic and heterotypic interactions

Cells are equipped with membrane receptors, usually transmembrane proteins, which mediate signal transduction for cellular responses to extracellular stimuli (Yeagle, 2016). The receptors can bind to extracellular molecules – e.g. nutrients, growth factors, cell adhesion molecules (CAM) – on one side of the membrane and the binding induces a cascade of chemical changes thus transmitting information to the other side of it.

**Chemotaxis.** A key growth factor for blood vessel formation is the Vascular Endothelial Growth Factor (VEGF), which may stimulate EC proliferation during angiogenesis

---

<sup>3</sup>Cell interactions with cells of the same type are called homotypic, while those with other cell types or extracellular components are called heterotypic.

and EPC differentiation into mature ECs (Heloterä and Alitalo, 2007; Weinberg, 2013). VEGF is also a well-known chemoattractant, inducing cell migration towards areas of high VEGF densities. When the chemoattractant's source is external, we refer to this type of migration as exogenous chemotaxis, while we use the term endogenous chemotaxis when the chemoattractant is being secreted by cells within the same population. In fact, ECs and EPCs can themselves secrete VEGF (Heloterä and Alitalo, 2007).

**Adhesion.** Cells may adhere to other cells or extracellular components due to CAMs (Roberts et al., 2002), which provide anchorage, cues for migration, and signals for growth and differentiation. In particular, ECs and EPCs are the only cell types expressing vascular endothelial cadherin (VE-cadherin), which allows them to create cell-to-cell adhesion bonds (Blatchley et al., 2019; Vestweber et al., 2009). On the other hand, cells may also adhere to components of what is known as the extracellular matrix (ECM) due to a family of CAMs called integrins (Bachmann et al., 2019; Ruoslahti et al., 1991).

**Extracellular matrix.** The ECM is the non-cellular component of tissues and organs in which the cells are embedded, providing essential scaffolding for the cells as well as a series of biochemical and biomechanical cues required for tissue morphogenesis, differentiation and homeostasis (Frantz et al., 2010; Ingber, 2003; Khalilgharibi and Mao, 2021; Kular et al., 2014; Wolf and Friedl, 2011). It is made up of fibrous proteins and macromolecules, partly produced by the cells embedded in it, generally made of polymer chains<sup>4</sup> or long filaments, which are interconnected via cross-linkers<sup>5</sup>, while the remaining space is occupied by interstitial fluid<sup>6</sup>. The most abundant structural proteins in the ECM are collagen and elastin. Collagen is arranged into fibrils, structures which confer to connective tissues the tensile strength required to withstand mechanical stresses (e.g. tension, shear stresses, pressure), while elastin confers to the ECM the ability to recover from continuous stretching. Non-structural proteins of the ECM, such as fibronectin and laminin, are linked to integrins and therefore play a key role in cell adhesion. We can distinguish between two forms of ECM:

1. The basement membrane: a thin and dense ECM layer between epithelial cells<sup>7</sup> and other cell types which can be found in blood vessels and epithelial and endothelial tissues, mostly made up of collagen, laminin and fibronectin;

<sup>4</sup>Polymer chains are macromolecules formed by the chemical bonding of large numbers of smaller molecules, or repeating units, called monomers.

<sup>5</sup>A cross-link is a bond or short sequence of bonds linking one polymer chain to another.

<sup>6</sup>The interstitial fluid is mostly made up of water and proteoglycans (extremely hydrophylic molecules), with space-filling and lubricating functions.

<sup>7</sup>Epithelial cells are a type of cell that covers internal and external body surfaces; endothelial cells are a specialised type of epithelial cells that only line the internal surfaces of the components of the circulatory system.

2. The interstitial matrix: the porous 3D ECM lattice found in connective tissue, mostly made up of collagen, elastin and fibronectin, with the latter being responsible for the organisation of the matrix structure.

During *in vitro* studies for tissue engineering applications different types of ECM scaffolds can be used, such as natural ECM (e.g. collagen), other biomaterials (e.g. fibrin), *ex vivo* decellularised ECM (e.g. Matrigel) or synthetic ECM (e.g. hydrogels) (Brafman, 2013; Hoshiba and Yamaoka, 2019; Kular et al., 2014; Wolf and Friedl, 2011).

**Cell-matrix interactions.** Cellular adhesion to the ECM via integrins leads to a great variety of heterotypic interactions (Espina et al., 2021; Harris Jr, 1984; Khalilgharibi and Mao, 2021; Kular et al., 2014; Rauff et al., 2019; Wolf and Friedl, 2011). First of all cells can exploit such adhesion bonds to move within the extracellular environment, which they can sense and scout using thin membrane protrusions called filopodia. In this regard, cells have a tendency to move towards areas of higher ECM density (haptotaxis) or higher ECM stiffness (durotaxis), as these areas provide, respectively, more and more solid structural support for the cells. The ECM stiffness is a mechanical property quantifying its resistance to deform under stress, and it is generally linked with the number of cross-links between collagen fibers. Via transduction and mechanotransduction (respectively, the transmission of chemical signals and mechanical forces via cell adhesion bonds), ECM stiffness can affect the cell cytoskeletal structure<sup>8</sup> and stiffness, with important consequences on cell morphology and movement. On the other hand, cells adhering to the ECM and pulling on it in order to migrate may generate considerable traction forces capable of deforming the ECM. In addition, high ECM density may impose serious physical limits of cell migration, which can be overcome by the cells secreting matrix degrading enzymes such as matrix-metalloproteases (MMPs), which may be membrane-bound or diffusible, and are responsible for proteolytic degradation of the ECM.

#### 4.1.2 *In vivo* processes of vascular network formation

**Embryonic vasculogenesis.** The first occurrence of formation of new vasculature in living organisms is embryonic vasculogenesis, as the cardiovascular system is the first functional organ system to develop in the embryo. This process takes place in the mesoderm<sup>9</sup>, in which reside EPCs called angioblasts. These assemble into a vascular pattern by cell migration and cohesion (Poole et al., 2001). In particular, together with hematopoietic precursor cells<sup>10</sup>, they aggregate to form blood islands. After aggregation, angioblasts

<sup>8</sup>The cytoskeleton is a cellular structure made up of filamentous proteins, from microtubules to actin microfilaments, responsible for structural support, substance transport and movement of the cell.

<sup>9</sup>The mesoderm is the middle of the three embryonic germ layers (between ectoderm and endoderm).

<sup>10</sup>Hematopoietic precursor cells are stem cells capable of differentiating into blood cells.

differentiation into ECs occurs, an event followed by lumen formation and basal lamina<sup>11</sup> production. The growth and fusion of multiple blood islands results in a primitive capillary network (Kolte et al., 2016; Risau and Flamme, 1995), from which an extended vascular network can form via angiogenesis.

**Angiogenesis.** New blood vessels may form from pre-existing ones through two types of angiogenesis (Adair and Montani, 2010):

- (i) Intussusceptive angiogenesis, or splitting angiogenesis, during which elements of interstitial tissues invade existing vessels due to the extension of the vessel wall into the lumen causing a single vessel to split in two;
- (ii) Sprouting angiogenesis, during which new sprouts composed of ECs grow from existing blood vessels towards areas devoid of blood vessels.

In the embryo, as often in local tissue of the adult organism, angiogenesis is driven by angiogenic stimuli activated by hypoxia. Low oxygen levels stimulate HIF- $\alpha$ -mediated gene expression of pro-angiogenic factors, such as VEGF, in parenchymal<sup>12</sup> cells (Rahimi, 2012). In sprouting angiogenesis, the pro-angiogenic factors induce blood vessel' basement membrane degradation, proliferation of ECs and migration towards the origin of the angiogenic stimuli, i.e. exogenous chemotaxis. This is followed by tube formation and remodelling before maturation of the new blood vessels (Kolte et al., 2016), and in order for blood to circulate in the new vasculature anastomosis may need to occur, that is, the fusion of vessel segments to eliminate dead ends (Diaz-Santana et al., 2015).

**Postnatal vasculogenesis.** The distinction between blood vessels that originated by cell differentiation *in situ* (vasculogenesis) and those which developed from pre-existing vessels (angiogenesis) has been clear since the early days of the field of study of early vascular development (Sabin, 1917). On the other hand, for a long time the term vasculogenesis has only been associated with the early embryonic vasculogenesis described above, while blood vessel formation in adult organisms was believed to be formed predominantly, if not exclusively, via angiogenesis (Risau and Flamme, 1995). This understanding of neovascularisation, constraining vasculogenesis to only occur during embryonic development, has quickly changed over the past two decades. Asahara et al. (1997) first isolated putative EPCs from human peripheral blood, which were shown to differentiate *in vitro* into ECs and be incorporated in active angiogenic sites in ischemic tissue. These circulating EPCs were then found to be recruited from the bone marrow and mobilised to the peripheral circulation to reach angiogenic sites *in vivo* (Asahara et al., 1999; Shi et al., 1998).

<sup>11</sup>The basal lamina is a layer of ECM secreted by the epithelial cells, on which the epithelium sits; it constitutes a portion of the basement membrane.

<sup>12</sup>Parenchymal cells are those contributing to the functional parts (the parenchyma) of organs or structures such as tumours, as opposed to the structural parts (the stroma, e.g. connective tissue).

Since these discoveries, much progress has been made in recognising the origin and role of EPCs – both in animals and humans – in neovascularisation of developing tumours, wound healing, ischemia and physiological neovascularisation (Asahara and Kawamoto, 2004; Asahara et al., 1999) introducing the notion of postnatal vasculogenesis.

#### 4.1.3 *In vitro* single-cell vasculogenesis

We have seen that mature ECs reside in the endothelium of blood vessels and thus only participate in *in vivo* neovascularisation through angiogenesis. Despite this, many *in vitro* studies of vasculogenesis actually investigate the direct reorganisation into a vascular network of sparse single ECs. Different types of ECs have been considered, the most popular one being human umbilical vein endothelial cells (HUVECs), and cultured mostly in fibrin gels and Matrigel (Ambrosi et al., 2005; Morin and Tranquillo, 2013; Sasaki et al., 2017; Serini et al., 2003). We will henceforth refer to this process as “single-cell” vasculogenesis. The work of Serini et al. (2003) has particularly caught the attention of the mathematical community – see Section 4.2.1.

Serini et al. (2003) investigated single-cell vasculogenesis in Matrigel. During the early stages of this process, ECs were observed to undergo rapid motion, during which they maintained a round shape, until collision with their closest neighbours (3-6 hours). They then proceeded to reorganise into a continuous multicellular network, which can be represented as a collection of nodes connected by capillary cords (of mean length  $\ell \approx 200\mu\text{m}$ ), exhibiting a more elongated morphology, until network stabilisation (9-15 hours). The authors observed that EC trajectories have a high degree of directional persistence and undergo endogenous chemotaxis following VEGF-A. Moreover, they observed the formation of groups of disconnected structures, instead of a single connected network, below a critical density of 100 cells/mm<sup>2</sup>. Increasing the cell density above 200 cells/mm<sup>2</sup> resulted in increased cord thickness eventually leading to a cell monolayer with void areas called lacunae, that is, a “Swiss-cheese” pattern.

Investigation of single-cell vasculogenesis in fibrin gels indicated that vessel formation is inhibited by low cell numbers, similarly to what is observed in Matrigel, and a high gel density, while it is fostered by exogenous chemotaxis (Morin and Tranquillo, 2013).

#### 4.1.4 *In vivo* and *in vitro* cluster-based vasculogenesis

With increased attention being given to circulating EPCs and postnatal vasculogenesis came a deeper understanding of the mechanisms behind *de novo* vascularisation. In particular, a new vasculogenic mechanism has been identified, characterised by EPC

cluster formation during the early-stages of this process and thus referred to as cluster-based vasculogenesis. This neovascularisation process has been documented in animal models, specifically in hypoxic settings *in vivo*, such as in ischemia and tumour vascularisation (Blatchley et al., 2019; Tepper et al., 2005; Vajkoczy et al., 2003). As indicated by Tepper et al. (2005), prior to these experiments there had not been any direct evidence for true *in situ* vasculogenesis in adult physiology. Nevertheless, as described in Section 4.1.2, previous embryonic vasculogenesis studies anticipated the ability of EPCs to organise into clusters – specifically blood islands – from which to extend projections and form vascular networks. Cluster-based vasculogenesis has also been observed in embryos, such as during cranial vasculature formation in zebrafish embryos (Proulx et al., 2010), in a later stage than that of the formation of the primary vascular plexus. Recall that, as anticipated in Section 4.1.2, prior to the discovery of circulating EPCs and cluster-based vasculogenesis, the term vasculogenesis was used to indicate embryonic vasculogenesis – i.e. the formation of the primary vascular plexus. Many works in the literature still consider this definition, such as Vajkoczy et al. (2003) who have proposed the term “angiomorphosis” (from the Greek words “angio” for blood vessel and “morphosis” to give shape, to form) for the neovascularisation process under study, to distinguish it from angiogenesis and vasculogenesis. Nowadays, the term vasculogenesis is more often used to indicate any *de novo* vascular formation that does not originate from pre-existing blood vessels. For this reason, we here choose to use the term “cluster-based” vasculogenesis, first introduced by Blatchley et al. (2019), for the process under study as it quickly summarises its key difference with single-cell vasculogenesis. Below we report the main findings of *in vivo* studies in which this mechanisms was first described.

**In vivo cluster-based vasculogenesis.** Vajkoczy et al. (2003) conducted an animal model study of the contribution of *ex vivo*-expanded embryonic EPCs (eEPCs) to tumour-induced blood vessel growth in the adult, and mention similar experiments on tissue ischemia models. Tepper et al. (2005) and Blatchley et al. (2019) also studied postnatal vasculogenesis in ischemic tissue *in vivo*. All of these authors observed cluster-based vasculogenesis, occurring through the following steps:

- (i) Circulating EPCs are mobilised and home into hypoxic and ischemic sites (e.g. through growth factors and oxygen gradients);
- (ii) Recruited EPCs attach to the local endothelium (via integrins and intercellular adhesion molecules);
- (iii) EPCs extravasate to the interstitial tissue, actively proliferate and form clusters;
- (iv) EPC clusters undergo sprouting and anastomose with existing blood vessels, revascularising the local microenvironment.

The final network formed was reported to be larger than previously observed ones formed via angiogenesis or single-cell vasculogenesis (Blatchley et al., 2019). In fact, EPC clus-

ters form in regions far from pre-existing blood vessels and, after sprouting, function as a bridge for distant vascular beds, allowing for neovascularisation in physiological and pathological settings in which angiogenesis alone would not have sufficed. Vajkoczy et al. (2003) specifically report that recruitment, extravasation, survival and incorporation into functional tumour blood vessels of eEPCs within a few days ( $\sim$  4 days) was tumour-specific, by comparison with control experiments. Interestingly, they detected no significant effect of eEPC incorporation in the local vasculature on the total vessel density and tumour size. This suggests that eEPCs may be used to regulate tumour vasculature and hence optimise drug delivery to treat tumours without stimulating tumour growth. In tissue ischemia models, recruitment, adhesion to the local endothelium, localised migration and proliferation of recruited EPCs were significantly increased in severe hypoxia ( $\sim$  0.5% O<sub>2</sub> tension). Tepper et al. (2005) report that, by day 14, cord-like structures along ischemic gradients had formed – i.e. blood vessels entirely made of EPCs – which canalised and connected with existing vasculature. Contrary to observations in tumour vascularisation, in ischemic tissues this process resulted in increased vessel density, blood flow levels and tissue function.

**In vitro cluster-based vasculogenesis.** Akita et al. (2003) reported that EPC differentiation, secretion of pro-angiogenic factors, such as VEGF, and migration were enhanced by hypoxic conditioning (i.e. exposition to hypoxia for an extended period of time), resulting in increased EPC cluster formation in hypoxia *in vitro*. While the recruitment of circulating EPCs to regions of hypoxia and ischemia has been well defined, it is not yet understood how clusters form and what drives subsequent vascular sprouting. This was further investigated by Blatchley et al. (2019) who, thanks to oxygen controllable hydrogels, reproduced hypoxic gradients *in vitro* (hypoxia defined by <5% O<sub>2</sub> tension), see Figure 4.2A, in which they deposited a high concentration of a subtype of EPCs, known as endothelial colony-forming cells (ECFCs). Cluster formation was eventually observed in highly hypoxic conditions ( $\sim$  1% O<sub>2</sub>), while not in non-hypoxic ones – see Figure 4.2B. In particular, cluster formation started 6-12 hours after encapsulation, by which time an oxygen gradient was present. Cluster sizes increased up to 24 hours, while the number of single cells decreased, and stayed at a consistent level up to 48 hours, suggesting clusters reached their maximum natural size at the 24 hour mark, with diameters in the range 100-400  $\mu$ m. After 24 hours increased cell-to-matrix interactions were observed with extensive sprouting from the clusters taking place after 48 hours. Within 72 hours a network up to 500  $\mu$ m in length had formed, much larger than single-cell vasculogenesis derived networks. In the course of the experiment, high matrix-degrading activity was recorded in hypoxic regions, starting at the 6 hour mark with a significant increase

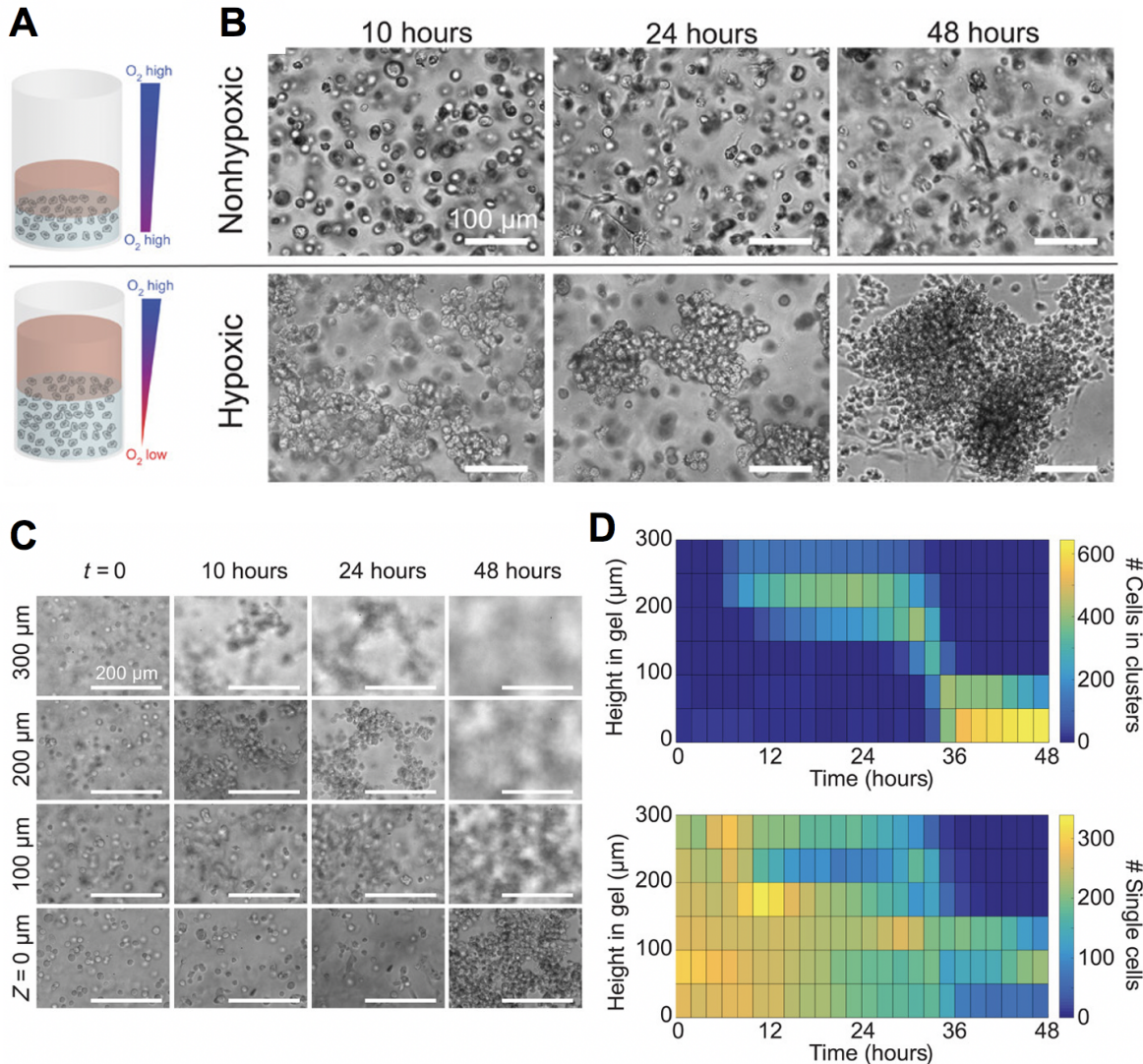


**Figure 4.2: *In vitro* cluster-based vasculogenesis.** (A) Illustration summarising the 3D *in vitro* experimental set ups considered by Blatchley et al. (2019) to study EPC cluster formation in hypoxic gradients (bottom) and in control nonhypoxic environments (top). (B) Corresponding experimental images displaying cluster formation after 48 hours in hypoxic environments (bottom), while no clusters formed in nonhypoxic conditions (top). (C) Time-lapse microscopy and (E) subsequent quantification of number of cells in clusters (top) and single cells (bottom) observed over time at different heights in the 3D hypoxic hydrogel. Figures reproduced from (Blatchley et al., 2019, Figure 1) under Creative Commons licence <https://creativecommons.org/licenses/by-nc/4.0/>.

by 18 and 24 hours, thanks to the employment of DQ-gelatin<sup>13</sup>. This suggests protease-mediated matrix degradation, up-regulated in hypoxic conditions, may be responsible for cluster formation. This was supported by further experimental observations indicating MMP-1 was significantly more prevalent under hypoxic conditions than non-hypoxic ones, and that a high concentration of MMP inhibitor hindered cluster formation. Upon

<sup>13</sup>DQ-gelatin is a fluorogenic substrate that can be used to detect protease activity *in vitro*.

cluster formation, clusters are stabilised by CAM, such as VE-cadherin, and cells at the cluster periphery extend filopodia towards the outside ready to sprout. The increased cell-ECM interaction plays a big role in the extensive sprouting from clusters and network formation. In particular, vascular networks extended below the clusters, suggesting the extensive matrix degradation needed for cluster formation may inhibit vascular network formation. In addition, an increase in matrix stiffness was observed to speed up sprouting and lead to extensive vascular network formation. Figure 4.3 provides a summary of the cluster-based vasculogenesis mechanism proposed by Blatchley et al. (2019).

While the findings reported in this section are significant steps forward in the understanding of cluster-based vasculogenesis, much further work is required to reach an exhaustive comprehension of the process, as well as to unlock its full potential in therapeutic interventions in a variety of pathological conditions. In this regard, mathematical modelling can help elucidate the mechanisms behind cluster and network formation, as demonstrated by previous works investigating single-cell vasculogenesis, discussed in Section 4.2.

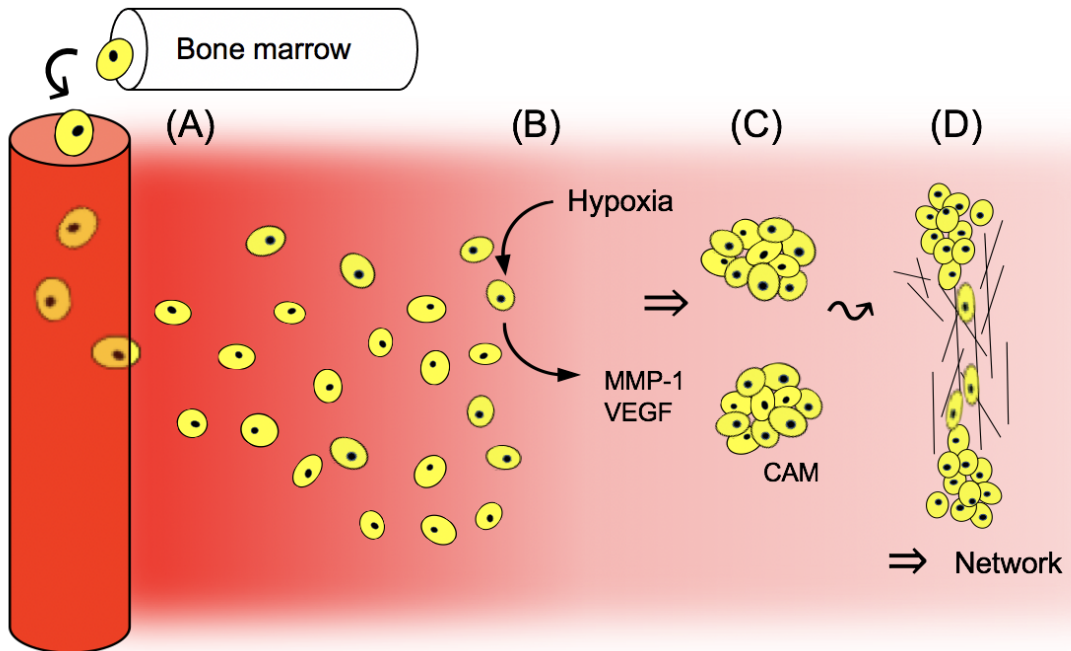


**Figure 4.3: Cluster-based vasculogenesis steps.** Summary of the steps of cluster-based vasculogenesis: (A) EPCs in the bone-marrow enter the circulation and reach the hypoxic site; (B) local hypoxia fosters EPC production of matrix degrading enzymes (MMP-1) and chemotactic agents (VEGF); (C) clusters form and are stabilised by cell-adhesion molecules (CAM); (D) cell-matrix interactions increase, sprouting from clusters occurs and a vascular network forms.

## 4.2 Mathematical models of vasculogenesis

While the mathematical model we will present in Chapter 5 is the first one formulated to study cluster-based vasculogenesis, many have been proposed to investigate *in vitro* single-cell vasculogenesis. With the exception of Sasaki et al. (2017), whose model of EC network formation in fibrin gels showed that random searching of ECs and cell-to-cell adhesion were sufficient to generate a network in such a medium, most models in the literature refer back to the work of Serini et al. (2003), presented in Section 4.1.3, who investigated single-cell vasculogenesis in Matrigel. We first review key single-cell vasculogenesis models in the literature, referring the interested reader to detailed reviews by Ambrosi et al. (2005); Boas et al. (2018); Czirok (2013); Scianna et al. (2013), and then discuss model requirements to study cluster-based vasculogenesis.

### 4.2.1 PDE models of single-cell vasculogenesis

Continuum deterministic models in the extant literature can be categorised as Persistence and Endogenous Chemotaxis (PEC) models (Ambrosi et al., 2004; Coniglio et al., 2004; Gamba et al., 2003; Kowalczyk et al., 2004; Liu et al., 2021; Serini et al., 2003), modelling the early stages of single-cell vasculogenesis, and mechanochemical models (Manoussaki, 2003; Murray, 1993, 2003; Namy et al., 2004), better suited to describe the late stages of the process, with the exception of the work by Tosin et al. (2006) who proposed a comprehensive model.

**PEC models of single-cell vasculogenesis.** First introduced by Serini and coworkers (Gamba et al., 2003; Serini et al., 2003), PEC models consist of a conservation equation for the EC density, a momentum equation describing changes in the EC velocity and a reaction-diffusion equation describing VEGF dynamics. In particular ECs are assumed to undergo persistent motion, that is movement characterised by inertia in the velocity field, and this movement is modulated by friction between cells and substrate, density-dependent pressure and chemotaxis, with the VEGF being secreted by the cells themselves. Ambrosi et al. (2004) also considered network formation in anisotropic conditions, by including a constant velocity field in the transport equation for the VEGF concentration. The solution of PEC models in 3D was recently analysed (Liu et al., 2021), and various interesting analytical insights for the 2D model have been presented over the years. Such models have so far helped to extrapolate information underlying the origin and structure of newly formed vascular networks, for instance relating the characteristic cord length  $\ell$  to the VEGF diffusion coefficient  $D_c$  and decay rate  $\lambda_c$  with the formula  $\ell = \sqrt{D_c(\lambda_c)^{-1}}$  (Ambrosi et al., 2004, 2005; Gamba et al., 2003; Serini et al., 2003), or

investigating the minimum – and maximum – initial cell density required for network assembly (Ambrosi et al., 2005; Coniglio et al., 2004; Gamba et al., 2003; Kowalczyk et al., 2004; Serini et al., 2003). In particular, Gamba et al. (2003) and Coniglio et al. (2004) analysed in detail the transition from a phase in which several disconnected structures appear to one in which a single connected structure appears, a phenomenon known as percolative transition, as the initial cell density increases, identifying the critical EC density at which we observe this phenomenon to be around 100 cells/mm<sup>2</sup>, in agreement with the work of Serini et al. (2003). PEC models have also been used to investigate the mechanisms at the basis of the Swiss-cheese transition, leading to the formation of lacunae as cell density increases. Studying the linear stability properties of PEC models, chemotaxis was found to be the key destabilising force for lacunae fomation and pressure to be the main stabilising one, and suitable conditions on the density-dependent pressure function to avoid blow up of the solution in finite time were derived (Kowalczyk, 2005; Kowalczyk et al., 2004). As a result of the presence of the pressure term, the Swiss-cheese transition can be predicted by PEC models to occur about the critical initial cell density of 300 cells/mm<sup>2</sup> (Ambrosi et al., 2005).

**Mechanochemical models of single-cell vasculogenesis.** Mechanochemical models of vasculogenesis, on the other hand, placed special emphasis on the role played by cell traction forces, and are therefore particularly suited for the later stages of vasculogenesis during which the mechanical interaction between the ECs and the ECM cannot be neglected. Mechanical models of vasculogenesis, following the work of Murray et al. (1983), consist of a conservation equation for the EC density and one for the ECM density, a force-balance equation to describe changes in the cell-ECM displacement as cells pull on the ECM and, in the case of mechanochemical models, additional reaction-diffusion equations for chemical factors, such as the VEGF concentration (Ambrosi et al., 2005). Both ECs and ECM are assumed to be advected according to changes in the cell-ECM displacement, and ECs are also assumed to undergo strain-dependent movement (Manoussaki, 2003; Murray, 2003; Namy et al., 2004), haptotaxis (Namy et al., 2004) and chemotaxis (Manoussaki, 2003). Note that while sometimes these models include reaction terms, modelling EC proliferation (Holmes and Sleeman, 2000; Manousaki, 2003) and ECM degradation (Holmes and Sleeman, 2000; Tranqui and Tracqui, 2000), such cases are considered in relation to angiogenesis rather than *de novo* vasculogenesis. In the force-balance equation ECs and ECM, itself modelled as linear elastic or viscoelastic material, are assumed to be connected in parallel and the overall stress of the system is in equilibrium with external restoring forces, such as viscous drag or elastic forces depending on the assumed external substratum. Cell traction is assumed to grow linearly at low cell densities and go to zero for large densities, with the exception

of [Namy et al., 2004] and [Tranqui and Tracqui, 2000] whose cell traction term becomes negative at large densities, thus modelling the effect of density-dependent pressure. LSA predicts instability of the homogeneous steady state, and in general lacunae formation, if the cell traction coefficient is high enough or the ECM Young modulus is low enough, and if the initial cell density is below a threshold value, dependent on the way cell traction is modelled ([Ambrosi et al., 2005]). Haptotaxis was also indicated to have a destabilising effect ([Namy et al., 2004]; [Tranqui and Tracqui, 2000]), while the restoring forces and long range effects have a stabilising effect ([Ambrosi et al., 2005]). Note that while these models may predict cluster formation in the case of very high cell traction or very low ECM stiffness, such modelling frameworks are not compatible with the application here considered as they do not include any of the key mechanisms of early-stage cluster-based vasculogenesis.

**A comprehensive model of single-cell vasculogenesis.** The only model considering both early-stages dynamics and cell-ECM mechanical interactions was proposed by [Tosin et al. (2006)]. Their model resembles those proposed for PEC, with the addition of an external drag force in the momentum equation, which models the fact that EC movement is slowed down by cell adhesion to the ECM as they move over it. The same drag force appears as an external restoring force in the force-balance equation for the ECM, where the ECM is modelled as a linear elastic material. In this framework, cells and ECM are modelled as separate layers influencing each other by generating external forces at their interface, and we only keep track of the ECM displacement, not the ECM density itself. The model indicated that cell adhesiveness to the substratum plays a key role in network formation, with excessive adhesiveness resulting in no network and insufficient adhesiveness affecting the stability of cords so that cells would eventually clusterise due to chemotaxis.

#### 4.2.2 Cellular Potts models of single-cell vasculogenesis

Despite their lower analytical tractability, Cellular Potts (CP) models have been widely used to study single-cell vasculogenesis over the years ([Boas et al., 2018]; [Scianna et al., 2013]). These are lattice-based models, with simulations obtained via a Monte-Carlo method following energy minimisation principles, which track cell and ECM dynamics at the mesoscale. They are therefore particularly suited to investigate mechanisms occurring at the cell level, such as cell shape and cell-to-cell adhesion, which are difficult to describe with continuum models of macroscale dynamics and which may be crucial for single-cell vasculogenesis as the process involves few cells ([Merks et al., 2006]). In fact, it is standard to omit cell proliferation and death when considering *in vitro* dynamics of mature ECs

on a relatively short timescale (9-15 hours).

**CP models ignoring active cell traction.** Palm and Merks (2013) showed that elongated, adhesive cells can self-organise into vascular structures. Extending the model to include endogenous chemotaxis results in a faster pattern formation process and the stabilisation of the network (Merks et al., 2006). This framework confirmed a correlation between the characteristic cord length, and thus size of lacunae, and the VEGF diffusion rate, as previously predicted with PEC models. In the absence of elongation, network formation is compromised and cells form islands, whether elongation is imposed as a constraint (Merks et al., 2006) or is a consequence of strong cell-to-cell adhesion (Merks et al., 2004). Similar results were obtained when considering cell adhesion-mediated saturation of chemotaxis instead of cell elongation, as this motility inhibition still led to cell polarisation and, in the absence of such an effect, clusters were observed (Merks and Glazier, 2005; Merks et al., 2008; Singh et al., 2015). Overall the work of Merks and coworkers pointed towards cell elongation, or polarisation, and endogenous chemotaxis being essential for network formation, just like persistence of motion and endogenous chemotaxis in PEC models. In fact, we might expect cell elongation to result in more persistent motion at the macroscale. Alternatively, Szabo and coworkers suggested that a preferential attraction of cells to elongated structure is sufficient for vascular network formation (Szabo et al., 2007), particularly highlighting the role this plays in cell sprouting from clusters which would otherwise remain stable due to cell-to-cell adhesion (Szabo et al., 2008; Szabó and Czirók, 2010).

**CP models investigating active cell traction.** Cell elongation has also been proposed to result from the mechanical interaction of ECs with the ECM (van Oers et al., 2014; Ramos et al., 2018). Van Oers et al. (2014) proposed a CP model which included cell-to-cell adhesion, active cell traction on the ECM and durotaxis, the preferential movement of cells up ECM stiffness gradients. They further assumed that the ECM would stiffen under strain, generated by the ECs' pulling action which, in combination with durotaxis, resulted in EC elongation. Note that these dynamics may result in cell traction and strain-dependent movement at the macroscale, which are key factors of mechanochemical models. The model was further analysed by Ramos et al. (2018), who predicted network formation for high enough cell traction compared to the ECM Young modulus, just like in mechanochemical models, with cell alignment and polarisation still playing an important role, while cell-to-cell adhesion was indicated to be responsible for network configuration.

### 4.2.3 Modelling the early stages cluster-based vasculogenesis

We are interested in investigating the determinants of cluster formation and cluster size with a model of the early stages cluster-based vasculogenesis. While much work has been conducted in order to better understand the mechanisms at the basis of single-cell vasculogenesis, many of which are relevant to cluster-based vasculogenesis, recent experimental observations (Blatchley et al., 2019) suggest that other processes need to be considered when studying EPC cluster formation. While CP models may be preferred when studying a system comprising a few cells, EPCs actively proliferate and we therefore choose to study this process through the lense of a continuum deterministic model. The model should include endogenous chemotaxis, MMP-mediated ECM degradation, cell-to-cell adhesion, EPC random movement, proliferation and death, together with annexed ECM, VEGF and MMP dynamics. Note that while cell proliferation and ECM degradation have been included in previous models of vascular network formation (Boas et al., 2018; Daub and Merks, 2013; Holmes and Sleeman, 2000; Manoussaki, 2003; Tranqui and Tracqui, 2000), these have been formulated to study angiogenesis rather than vasculogenesis, which require different initial conditions and exogenous, rather than endogenous, chemotaxis.

**Modelling chemotaxis.** PEC models included chemotaxis in the momentum equation, but this implies that cells accelerate in chemical gradients, an assumption that might be unrealistic given the highly viscous, non-inertial environment of the ECM (Merks et al., 2006, 2008). We thus choose to follow standard modelling of chemotaxis in the flux term of the EPC density mass-balance equation, as done in mechanochemical models (Ambrosi et al., 2005; Manoussaki, 2003), following the classic Patlak–Keller–Segel model of diffusion and chemotaxis (Keller and Segel, 1970; Painter, 2019). As the PKS model is well-known for having solutions that blow up in finite time, a number of variations have been proposed in the literature (Bubba et al., 2019; Kowalczyk, 2005; Painter, 2019), and we will hereby consider a modified version of the forms proposed by Hillen and Painter (Hillen and Painter, 2001; Painter and Hillen, 2002) whereby chemotaxis is saturated in a tightly packed environment. While this results in a local description of chemotaxis, various nonlocal ones have also been proposed over the years, reviewed for instance by Chen et al. (2020); Hillen and Painter (2009); Painter et al. (2015).

**Modelling cell-to-cell adhesion.** While CP models allowed for a mesoscopic description of cell-to-cell adhesion, during the development of PEC and mechanochemical models this biological process had not yet been explicitly modelled at the macroscopic scale. Armstrong et al. (2006) proposed, in their seminal paper, a continuum nonlocal description

of intrapopulation and interpopulation cell adhesion. This was later adapted by Gerisch and Chaplain (2008) to account for cell-to-cell and cell-to-matrix adhesion. The model relies on the presence of an advective flux of the cell density at position  $\mathbf{x}$ , calculated nonlocally by scouting for availability of adhesion sites in a sensing region centered in  $\mathbf{x}$ . This has become a popular continuum description of cell adhesion, with a number of variations proposed to study tumour invasion and cell movement across the ECM (Betsouni et al., 2017; Buttenschön et al., 2018; Chaplain et al., 2011; Domschke et al., 2014; Gerisch and Painter, 2010; Painter et al., 2010; Sherratt et al., 2009), development and cell-sorting dynamics (Armstrong et al., 2009; Carrillo et al., 2019; Gerisch and Painter, 2010; Painter et al., 2015). Attention has also been given over the years to variations of the nonlocal modelling of adhesion by considering different ways to enforce limits on the cell density and to include nonlinear cross diffusion, that is substituting linear diffusion modelling random movement with nonlinear diffusion modelling movement of cells down a density-dependent pressure gradient, into the overall model (Burger et al., 2020; Carrillo et al., 2019; Madzvamuse et al., 2017; Murakawa and Togashi, 2015). These modifications principally lead to sharper interfaces between the densities of different cell types, or the ECM, or can even lead to strict segregation of them. Since such effects are not part of the primary dynamics which we will focus on in our model of the early stages of cluster-based vasculogenesis, we will not include these variations here.

# Chapter 5

## A novel nonlocal PDE model of endothelial progenitor cell cluster formation

We present a continuum deterministic model of EPC cluster formation during the early stages of cluster-based vasculogenesis, during which mechanical interactions between EPCs and the ECM can be neglected. The model comprises a system of PDEs modelling dynamics such as endogenous chemotaxis, MMP-mediated ECM degradation, nonlocal cell-to-cell and cell-to-matrix adhesion, EPC random movement, proliferation and death, together with annexed ECM, VEGF and MMP dynamics. The model provides a theoretical basis for a comprehensive description of the mechanisms underlying cluster formation. In this study we seek to clarify the role played by different dynamics and elucidate the determinants of cluster size, by introducing appropriate metrics for cluster width and compactness. We investigate this *in primis* by means of a LSA and numerical simulations relying on a baseline parameter set drawn from the literature. We then proceed to provide a first overview of potential model behaviour to gain insight into the importance of various parameters or processes in the pattern formation potential of the system. We do this by simulating the model using the baseline parameter set as well as by varying parameters, one at a time, with values in a suitable range identified from existing literature (parametric analysis). The mathematical model is described in detail in Section 5.1. The key results of a LSA are summarised in Section 5.2, followed by numerical results in Section 5.3. In particular, the numerical investigations on the determinants of cluster formation and cluster size are presented for the 1D and 2D problems, and the results are qualitatively compared with the experimental findings of Blatchley et al. (2019) presented in Section 4.1.4.

## 5.1 The mathematical model

Let  $t \geq 0$  indicate time and  $\mathbf{x} \in \mathbb{R}^2$  a position in space. We will consider the dynamics in a 2D spatial domain  $\Omega \subset \mathbb{R}^2$ , as well as the corresponding 1D problem, for which we make use of the notation  $x \in \mathbb{R}$  to indicate space. Unless indicated otherwise, all definitions introduced in this section for the 2D problem hold for the corresponding 1D one. The density of EPCs at time  $t$  and position  $\mathbf{x}$  is given by  $n(t, \mathbf{x})$ , in units of  $\text{cell cm}^{-3}$ <sup>1</sup>, and the ECM density by  $\rho(t, \mathbf{x})$ , in units of  $\text{nM}$ . Similarly we indicate the concentration of a matrix-degrading enzyme, such as MMP-1, by  $m(t, \mathbf{x})$ , in units of  $\mu\text{g cm}^{-3}$ , and that of a chemotactic agent, such as VEGF-A, by  $c(t, \mathbf{x})$ , in units of  $\text{ng cm}^{-3}$ . We also introduce the vector of dependent variables  $\mathbf{v}(t, \mathbf{x}) := (n(t, \mathbf{x}), \rho(t, \mathbf{x}), m(t, \mathbf{x}), c(t, \mathbf{x}))^\top$ . Our model then consists of a system of mass-balance equations, one for each dependent variable introduced.

### 5.1.1 Dynamics of endothelial progenitor cells

The mass-balance equation for the density of EPCs is of the form:

$$\partial_t n + \nabla \cdot [\mathbf{J}_d(n) + \mathbf{J}_c(n, c) + \mathbf{J}_a(\mathbf{v})] = pn(1 - \vartheta_1 n - \vartheta_2 \rho), \quad (5.1)$$

where  $\mathbf{J}_d(n)$  models spatial diffusion to account for random movement of cells,  $\mathbf{J}_c(n, c)$  indicates the chemotactic flux in response to VEGF gradients and  $\mathbf{J}_a(\mathbf{v})$  the advective flux due to cell-to-cell and cell-to-matrix adhesion, while the term on the right-hand side of the equation models cell proliferation and death. In particular, we consider a modified version of the standard logistic growth, as proposed by Gerisch and Chaplain (2008), in which EPCs proliferate at rate  $p \geq 0$  and die due to competition for space – occupied by both cells and ECM – and resources. Parameters  $\vartheta_1 > 0$  and  $\vartheta_2 > 0$  indicate the fraction of one unit volume of physical space occupied by EPCs at unit density and by ECM at unit density respectively, such that  $(\vartheta_1 n + \vartheta_2 \rho)$  indicates the total fraction of locally occupied space.

**Spatial diffusion and chemotaxis.** Following the motivations introduced in Section 4.2.3, we make use of the following definitions for the diffusive and chemotactic flux terms:

$$\mathbf{J}_d(n) = -D_n \nabla n, \quad \mathbf{J}_c(n, c) = \chi f(n, \rho) n \nabla c. \quad (5.2)$$

In definitions (5.2) spatial diffusion follows Fick's law, with diffusivity  $D_n \geq 0$ , while

---

<sup>1</sup>The proposed modelling framework is meant to provide a 2D approximation of a 3D problem, and the units of measurement for the dependent variables are chosen accordingly.

chemotaxis is modelled as an advective flux of cells up the gradient of the chemotactic agent concentration  $c$ , modulated by the chemotactic sensitivity of cells. This is proportional to the chemotactic sensitivity coefficient  $\chi \geq 0$  and the function  $f(n, \rho)$ , which accounts for volume exclusion. This is given by

$$f(n, \rho) = (1 - \vartheta_1 n - \vartheta_2 \rho)_+ \quad (5.3)$$

where we have used  $(\cdot)_+ := \max(0, \cdot)$  – see also [Gerisch and Chaplain (2008); Hillen and Painter (2001); Painter and Hillen (2002)]. According to definition (5.3), the chemotactic sensitivity of the cells is proportional to the locally available space. If the local space is overcrowded, cells will struggle to sense the chemotactic gradient, to the extent that if the space is locally full no chemotaxis can occur.

**Cell-to-cell and cell-to-matrix adhesion.** Following the motivations introduced in Section 4.2.3, we model cell-to-cell and cell-to-matrix adhesion in the continuous form proposed by [Gerisch and Chaplain (2008)]. The advective flux of the EPC density  $n$  due to cell-to-cell and cell-to-matrix adhesion in (5.1) is therefore given by

$$\mathbf{J}_a(\mathbf{v}) = n \mathcal{A}[\mathbf{v}(t, \cdot)] \quad (5.4)$$

where  $\mathcal{A}[\mathbf{v}(t, \cdot)]$  is the adhesion velocity at some point  $\mathbf{x}$ , that is the velocity of cells at  $\mathbf{x}$  due to adhesive interactions with their environment, which is an operator acting on  $\mathbf{v}(t, \cdot)$  defined as a function of  $\mathbf{x}$ . For problems in 1D this is defined as

$$\mathcal{A}[\mathbf{v}(t, \cdot)](x) := \frac{1}{R} \int_0^R \sum_{j=0}^1 \eta(j) \Gamma(r) g(\mathbf{v}(t, x + r\eta(j))) dr , \quad (5.5)$$

while for problems in 2D it is defined as

$$\mathcal{A}[\mathbf{v}(t, \cdot)](\mathbf{x}) := \frac{1}{R} \int_0^R r \int_0^{2\pi} \boldsymbol{\eta}(\theta) \Gamma(r) g(\mathbf{v}(t, \mathbf{x} + r\boldsymbol{\eta}(\theta))) d\theta dr . \quad (5.6)$$

In equation (5.5)  $\eta(j) = (-1)^j$  with  $j = 0, 1$  indicates the 1D right and left unit outer normal vector, while in equation (5.6) the 2D unit outer normal vector corresponding to angle  $\theta$  is given by  $\boldsymbol{\eta}(\theta) = (\cos \theta, \sin \theta)^\top$ . In definitions (5.5) and (5.6), we have that the sensing region of cells at position  $\mathbf{x} \in \mathbb{R}^d$  ( $d = 1, 2$ ) is the  $d$ -dimensional ball centred in  $\mathbf{x}$  with radius  $R > 0$ , called the sensing radius. Then  $\Gamma(r)$  is the radial dependency function, indicating how strongly the adhesion velocity at a point  $\mathbf{x}$  is influenced by points at a distance  $r \leq R$  from the centre  $\mathbf{x}$  of the sensing region. Since this should not alter the

magnitude itself of the adhesion velocity,  $\Gamma(r)$  must satisfy

$$\int_0^R 2\Gamma(r) dr = 1 \quad \text{and} \quad \int_0^R 2\pi r \Gamma(r) dr = 1 \quad (5.7)$$

in the 1D and 2D problems respectively, i.e. in equations (5.5) and (5.6) respectively. Assuming  $\Gamma(r)$  decays linearly with  $r$  to be zero at the boundary of the sensing region, we here make use of the forms proposed by Gerisch and Chaplain (2008)

$$\Gamma(r) = \frac{1}{R} \left(1 - \frac{r}{R}\right) \quad \text{and} \quad \Gamma(r) = \frac{3}{\pi R^2} \left(1 - \frac{r}{R}\right) \quad (5.8)$$

in the 1D and 2D problems respectively, chosen so that (5.7) is satisfied. Finally, in both (5.5) and (5.6) the term  $g(\mathbf{v}(t, \cdot))$  represents the nonlocal impact of the system's state at some point within the sensing region at  $\mathbf{x}$  on the velocity of the cells at  $\mathbf{x}$  due to adhesion to other cells or the ECM in the sensing region at  $\mathbf{x}$ . This is given by

$$g(\mathbf{v}) := g(n, \rho) = (S_{nn}n + S_{n\rho}\rho) f(n, \rho), \quad (5.9)$$

in which  $S_{nn} \geq 0$  and  $S_{n\rho} \geq 0$  are the cell-to-cell and cell-to-matrix adhesion coefficients respectively, while the function  $f(n, \rho)$  is defined in (5.3). Under definition (5.9), the velocity of cells at position  $\mathbf{x}$  in the direction of a point – say –  $\mathbf{y}$  in the sensing region of  $\mathbf{x}$  due to cell-to-cell adhesion is directly proportional to the cell density  $n$  at  $\mathbf{y}$ , and that due to cell-to-matrix adhesion is directly proportional to the ECM density  $\rho$  at  $\mathbf{y}$ . This is because a higher cell or ECM density correlates with a higher number of adhesion sites. Meanwhile, under definitions (5.9) and (5.3), the velocity is also proportional to the available space at position  $\mathbf{y}$ . This accounts for volume exclusion, as cells will be unable to sense adhesive sites at spatial locations with high densities of EPCs and/or ECM and, hence, will not migrate in those directions.

### 5.1.2 Dynamics of extracellular factors

**Dynamics of ECM.** We let the ECM be degraded by matrix-degrading enzymes at a rate  $\gamma \geq 0$  and account for ECM remodelling at a rate  $\mu \geq 0$ , resulting in the following mass-balance equation for the ECM density:

$$\partial_t \rho = -\gamma \rho m + \mu(1 - \vartheta_1 n - \vartheta_2 \rho)_+, \quad (5.10)$$

where the parameters  $\vartheta_1$  and  $\vartheta_2$  have already been introduced in Section 5.1.1, indicating ECM remodelling is here understood as a restructuring phenomenon that only occurs if space is available (Domschke et al., 2014). This is assumed to be independent of the cell

density  $n$  as ECM remodelling *in vivo* is generally mediated by other cell types present in the tissue, such as mesenchymal stem cells, fibrocytes and fibroblast (Bellini and Mattoli, 2007; Bianchetti et al., 2012; Diaz-Flores et al., 2014; McAnulty, 2007; Stenmark et al., 2002), which we do not include in our modelling framework.

**Dynamics of MMPs.** We let the matrix-degrading enzyme (MMP) be produced by the EPCs at a rate  $\alpha_m \geq 0$ , undergo Fickian diffusion with diffusivity  $D_m \geq 0$ , and decay at rate  $\lambda_m \geq 0$ . Then the MMP concentration  $m(t, \mathbf{x})$  satisfies:

$$\partial_t m - D_m \Delta m = \alpha_m n - \lambda_m m. \quad (5.11)$$

**Dynamics of VEGFs.** Similarly to the matrix-degrading enzyme, we let the chemo-tactic agent (VEGF) be produced by the EPCs at a rate  $\alpha_c \geq 0$ , undergo Fickian diffusion with diffusivity  $D_c \geq 0$ , and decay at rate  $\lambda_c \geq 0$ . This results in the following mass-balance equation for the VEGF concentration  $c(t, \mathbf{x})$ :

$$\partial_t c - D_c \Delta c = \alpha_c n - \lambda_c c. \quad (5.12)$$

### 5.1.3 Boundary and initial conditions

**Boundary conditions.** While equation (5.10) describes the dynamics of the ECM in the closed spatial domain  $\bar{\Omega} = \Omega \cup \partial\Omega$ , equations (5.1), (5.11) and (5.12) are posed on the open set  $\Omega$ , and are complemented with zero-flux boundary conditions. These boundary conditions imply that no mass is exchanged with the outside of the spatial domain, i.e. we have a closed system. For the nonlocal terms (5.5) and (5.6) this means that they cannot sense the system's state outside of the spatial domain  $\Omega$ . We thus impose that in these terms the function  $g(\mathbf{v}(t, \cdot))$  equals zero if it is to be evaluated for a point outside of  $\Omega$  (Domschke et al., 2014) and thus obtain well-defined nonlocal terms (5.5) and (5.6) throughout the spatial domain.

**Initial conditions.** As proposed by Serini et al. (2003), we construct the initial conditions to mimic sparsely distributed cells on the ECM. In particular, the initial cell density is given by the sum of  $K \in \mathbb{N}$  randomly distributed bell-shaped bumps. In particular, we construct these bumps as Gaussian-like functions with maximum height and full width at half maximum (FWHM) both equal to the size of an average cell diameter  $a > 0$ . We let the initial ECM density be constant and the initial MMP and VEGF concentrations

be null. Thus we have

$$n(t, \mathbf{x}) = \sum_{i=1}^K G_i(\mathbf{x}; a), \quad \rho(0, \mathbf{x}) = \rho_0 > 0, \quad m(0, \mathbf{x}) = c(0, \mathbf{x}) = 0, \quad (5.13)$$

where  $G_i(\mathbf{x}; a)$  indicates the Gaussian-like function centered at the (randomly selected)  $\mathbf{x}^{(i)} \in \Omega$  and is given by

$$G_i(\mathbf{x}; a) := a \exp \left[ -\frac{4 \ln 2}{a^2} |\mathbf{x} - \mathbf{x}^{(i)}|^2 \right]. \quad (5.14)$$

In equation (5.14) we have used the formula  $\text{FWHM} = 2\sqrt{2 \ln 2}\sigma$  where  $\sigma$  is the standard deviation of the Gaussian.

### 5.1.4 Nondimensional model

We nondimensionalise the system of equations (5.1) and (5.10)-(5.12), together with definitions (5.2)-(5.9), (5.13) and (5.14), by letting

$$\hat{t} = \frac{t}{\tau}, \quad \hat{\mathbf{x}} = \frac{\mathbf{x}}{L}, \quad \hat{n} = \frac{n}{N}, \quad \hat{\rho} = \frac{\rho}{P}, \quad \hat{m} = \frac{m}{M}, \quad \hat{c} = \frac{c}{C}.$$

We use  $L = 0.1$  cm as characteristic length scale, in accordance with previous vasculogenesis works (Manoussaki, 2003; Serini et al., 2003) and for easy visual comparison with the experimental results reported by Blatchley et al. (2019). We then take reference time scale  $\tau := L^2/D$ , where  $D$  is a characteristic cell diffusion coefficient  $D \sim 10^{-6}$  cm<sup>2</sup>s<sup>-1</sup> (Bray, 2000), resulting in a reference time scale  $\tau = 10^4$ s. The reference cell density is chosen to be  $N := n_M = \vartheta_1^{-1}$  and we take  $\vartheta_1 = 10^{-9}$  cm<sup>3</sup>/cell, the average volume occupied by an endothelial cell (Rubin et al., 1989). We use a reference ECM density of  $P = 10^{-1}$  nM (Anderson, 2005; Anderson et al., 2000; Terranova et al., 1985) and define the parameter  $\vartheta_2 := P^{-1}$ . We take the reference VEGF density to be  $C = 20$  ng cm<sup>-3</sup>, in the range of values generally considered in *in vitro* set ups (Hanjaya-Putra and Gerecht, 2009; Lee et al., 2007; Serini et al., 2003). Finally, Blatchley et al. (2019) reported concentrations of MMP-1 in the range  $1 - 100$  µg ml<sup>-1</sup>, so we take the intermediate concentration as reference MMP density, i.e.  $M = 10$  µg cm<sup>-3</sup>. Let us introduce the following nondimensional parameters:

$$\begin{aligned} \hat{D}_n &= \frac{D_n}{D}, \quad \hat{\chi} = \frac{\chi C}{D}, \quad \hat{R} = \frac{R}{L}, \quad \hat{S}_{nn} = \frac{S_{nn}}{D\vartheta_1}, \quad \hat{S}_{n\rho} = \frac{S_{n\rho}}{D\vartheta_2}, \quad \hat{p} = p\tau, \quad \hat{\gamma} = \gamma M\tau, \quad \hat{\mu} = \mu\tau\vartheta_2, \\ \hat{D}_m &= \frac{D_m}{D}, \quad \hat{\alpha}_m = \frac{\alpha_m\tau}{M\vartheta_1}, \quad \hat{\lambda}_m = \lambda_m\tau, \quad \hat{D}_c = \frac{D_c}{D}, \quad \hat{\alpha}_c = \frac{\alpha_c\tau}{C\vartheta_1}, \quad \hat{\lambda}_c = \lambda_c\tau, \quad \hat{a} = \frac{a}{L}, \quad \hat{\rho}_0 = \frac{\rho_0}{P}. \end{aligned}$$

Then the overall nondimensionalised system becomes, dropping hats for convenience,

$$\left\{ \begin{array}{l} \partial_t n = D_n \Delta n - \chi \nabla \cdot (n f(n, \rho) \nabla c) - \nabla \cdot (n \mathcal{A}[\mathbf{v}(t, \cdot)]) + pn(1 - n - \rho) \\ \partial_t \rho = -\gamma \rho m + \mu(1 - n - \rho)_+ \\ \partial_t m = D_m \Delta m + \alpha_m n - \lambda_m m \\ \partial_t c = D_c \Delta c + \alpha_c n - \lambda_c c \end{array} \right. \quad (5.15)$$

where (5.15)<sub>1</sub>, (5.15)<sub>3</sub> and (5.15)<sub>4</sub> are posed on  $(t, \mathbf{x}) \in (0, \infty) \times \Omega$  and are complemented by zero-flux boundary conditions on  $\partial\Omega$ , while (5.15)<sub>3</sub> is posed on  $(t, \mathbf{x}) \in (0, \infty) \times \bar{\Omega}$ . In equation (5.15)<sub>1</sub> the operator  $\mathcal{A}[\mathbf{v}(t, \cdot)]$  takes the form (5.5) in 1D and (5.6) in 2D, with  $\Gamma(r)$  still defined as in (5.8), and  $g(\mathbf{v})$  is given as in (5.9) with  $f(n, \rho)$  now given by

$$f(n, \rho) = (1 - n - \rho)_+. \quad (5.16)$$

The parameters  $R$ ,  $S_{nn}$  and  $S_{n\rho}$  are the nondimensional ones introduced above, and the system (5.15) is complemented with initial conditions (5.13)-(5.14), in which the parameters  $a$  and  $\rho_0$  now corresponds to the nondimensional ones introduced above.

## 5.2 Linear stability analysis results

**Linear stability analysis steps.** We perform a LSA on the spatially homogeneous steady states, say,  $\bar{\mathbf{v}}$  of the nondimensional system (5.15)-(5.16), together with the relevant definitions for the 1D and 2D problems, in order to gain insights into the destabilising processes that might lead to cluster formation. During the LSA we first introduce a small spatially homogeneous perturbation  $\mathbf{v} = \bar{\mathbf{v}} + \tilde{\mathbf{v}}(t)$ , with  $|\tilde{\mathbf{v}}| \ll 1$ , in (5.15) and linearise. By assuming the small perturbation is proportional to  $\exp(\psi t)$ , we derive a characteristic equation for  $\psi$ , analogous to that satisfied by the eigenvalues  $\psi_i$  ( $i = 1, \dots, 4$ ) of the Jacobian matrix of the spatially homogeneous system. We distinguish between the following options:

- (i) If all eigenvalues (solutions to the characteristic equation)  $\psi_i$  ( $i = 1, \dots, 4$ ) are such that  $\text{Re}(\psi_i) < 0$ , the steady state is stable under spatially homogeneous perturbations;
- (ii) If at least one eigenvalue  $\psi_i$  (for some  $i \in \{1, 2, 3, 4\}$ ) is such that  $\text{Re}(\psi_i) > 0$ , the steady state is unstable under spatially homogeneous perturbations;
- (iii) If all eigenvalues  $\psi_i$  ( $i = 1, \dots, 4$ ) are such that  $\text{Re}(\psi_i) \leq 0$  with at least one zero eigenvalue, the LSA is inconclusive and the steady state is said to be ‘degenerate’.

In the latter case, the linear stability of the spatially homogeneous steady state under spatially homogeneous perturbations is investigated numerically. We then repeat these steps under a small spatially inhomogeneous perturbation  $\mathbf{v} = \bar{\mathbf{v}} + \tilde{\mathbf{v}}(t, \mathbf{x})$ , with  $|\tilde{\mathbf{v}}| \ll 1$ , assuming it is proportional to  $\tilde{\mathbf{v}}(t, \mathbf{x}) \propto \exp(\psi t + i \mathbf{k} \cdot \mathbf{x})$ . Once we obtain a dispersion relation  $\psi(k^2)$ , where  $k^2 = |\mathbf{k}|^2$ , we study the conditions under which  $\text{Re}(\psi(k^2)) > 0$  for some  $k^2$ , as in such regimes we expect spatially inhomogeneous perturbations to grow in time and patterns to arise. We conduct this analysis both in 1D and 2D for the model (5.15)-(5.16), as well as for the corresponding problem in the absence of volume exclusion, i.e. substituting definition (5.16) for  $f(n, \rho)$  with

$$f(n, \rho) = 1. \quad (5.17)$$

The analytical details are reported in Appendix A.4.

**Linear stability analysis results.** The two spatially homogeneous steady states  $\bar{\mathbf{v}}$  of system (5.15) are such that either the whole domain is solely occupied by cells ( $\bar{n} = 1$  and  $\bar{\rho} = 0$ , the ‘cell-full’ steady state) or solely occupied by ECM ( $\bar{n} = 0$  and  $\bar{\rho} = 1$ , the ‘cell-free’ steady state). The cell-full steady state is the biologically relevant one and LSA indicates that:

- The cell-full steady state is stable under spatially homogeneous perturbations;
- In the presence of volume exclusion saturating effects, i.e. under definition (5.16), it is also stable under spatially inhomogeneous perturbations;
- In the absence of volume exclusion saturating effects, i.e. under definition (5.17), chemotaxis and cell-to-cell adhesion may drive it unstable under spatially inhomogeneous perturbations.

These results suggest that patterns may arise when cell-to-cell adhesions and chemotactic mechanisms dominate the dynamics. This may occur, for instance, when the domain is not too densely packed with cells and ECM.

**Remark 6.** *LSA indicated that the cell-free steady state, which is not biologically relevant per se, is a degenerate steady state. However, while LSA is inconclusive on the linear stability of the cell-free steady state under spatially homogeneous perturbations, numerical simulations indicate instability in the case of perturbations with  $\tilde{n} > 0$  (i.e. if some cells appear in the system), in which case the solution eventually converges to the cell-full steady state. Moreover, further observations indicate cell proliferation and matrix degradation by the cells play important roles in its instability under small spatially homogeneous perturbations. These results suggest that cell proliferation and matrix degradation might have an important destabilising effect when the initial conditions with low cell density satisfy volume filling conditions.*

## 5.3 Numerical investigations

In this section we construct numerical solutions of the nondimensional system (5.15)-(5.16), together with the appropriate definitions in 1D and 2D, with zero-flux boundary conditions and initial conditions (5.13)-(5.14). We use these numerical solutions to provide an overview of potential model behaviours under one-at-a-time perturbations from the baseline parameter set. This, together with the corresponding nondimensional (ND) parameter values according to the choices presented in Section 5.1.4, is reported in Table 5.1 – see Appendix C.2 for details. In Section 5.3.1, we describe the set-up of numerical simulations and the methods employed to construct numerical solutions. In Section 5.3.2 we report the results of the 1D model under the baseline parameter set and qualitatively investigate the determinants of cluster formation in Section 5.3.3. In Section 5.3.4 we report the results of the parametric analysis conducted to elucidate the determinants of cluster size in 1D. In Section 5.3.5 we report the results of the 2D model.

### 5.3.1 Set-up of numerical simulations and numerical methods

**Set-up of numerical simulations of Sections 5.3.2-5.3.5.** For the numerical simulations we present in Sections 5.3.2-5.3.4, we define  $\Omega = (0, 1)$  and solve system (5.15)-(5.16) under definition (5.5) and the 1D version of definitions (5.8) and (5.9), i.e. for  $\mathbf{x} \equiv x$ , with zero-flux boundary conditions and the 1D version of initial conditions (5.13)-(5.14). For the parametric analysis reported in Section 5.3.4 we make use of the metrics of cluster size defined at the end of this section. For the numerical simulations we present in Section 5.3.5, we define  $\Omega = (0, 1) \times (0, 1)$  in order to model a (nondimensional) horizontal cross-section of a 3D *in vitro* vasculogenesis assay. We solve system (5.15)-(5.16) under definition (5.6) and the 2D version of definitions (5.8) and (5.9), with zero-flux boundary conditions and the 2D version of initial conditions (5.13)-(5.14).

**Numerical method.** Numerical solutions are constructed via a numerical scheme that follows the method of lines by first discretising the nonlocal model in space (with 1000 grid cells in 1D and  $100 \times 100$  grid cells in 2D), yielding an initial value problem for a large system of ODEs. This system is then solved using the time integration scheme ROWMAP (Weiner et al., 1997), implemented in a Fortran subroutine and called from MATLAB. For the discretisation in space a second-order finite volume approach which makes use of flux-limiting for an accurate discretisation of the taxis and adhesion terms is employed. All numerical simulations have been performed in MATLAB. See Appendix B.2 for more details on the numerical scheme.

**Table 5.1:** Baseline parameter set (ND = Nondimensional value) used in the numerical simulations reported in Section 5.3

Parameter	Biological meaning	Value	ND	Reference
$\vartheta_1^{-1}$	Average cell volume	$10^{-9} \text{ cm}^3/\text{cell}$		Rubin et al. (1989)
$\vartheta_2^{-1}$	Reference ECM density	$10^{-1} \text{ nM}$		Anderson et al. (2005)
$D$	Reference diffusion rate	$10^{-6} \text{ cm}^2\text{s}^{-1}$		Bray (2000)
$D_n$	EPC diffusion coefficient	$10^{-9} \text{ cm}^2\text{s}^{-1}$	$10^{-3}$	Ambrosi et al. (2005)
$\chi$	Chemotactic coefficient	$1.4 \times 10^{-7} \text{ cm}^5 \text{ ng}^{-1} \text{s}^{-1}$	2.8	Terranova et al. (1985)
$R$	Cell sensing radius	$5 \times 10^{-3} \text{ cm}$	0.05	Jain and Jackson (2013)
$S_{nn}$	Cell-to-cell adhesion coefficient	$10^{-16} \text{ cm}^5 \text{ s}^{-1}$	0.1	Sen et al. (2009)
$S_{np}$	Cell-to-matrix adhesion coefficient	$10^{-6} \text{ cm}^2 \text{ nM}^{-1} \text{ s}^{-1}$	0.1	Gerisch and Chaplain (2008)
$p$	Cell proliferation rate	$10^{-5} \text{ s}^{-1}$	1	Gerisch and Chaplain (2008)
$a$	Average cell diameter ( $\sqrt[3]{\vartheta_1}$ )	$10^{-3} \text{ cm}$	$10^{-2}$	Kinev et al. (2013)
$\gamma$	ECM degradation rate	$9 \times 10^5 \text{ cm}^3 \text{ g}^{-1} \text{s}^{-1}$	0.2	Rubin et al. (1989)
$\mu$	Rate of ECM remodelling	$0.2 \times 10^{-5} \text{ nM s}^{-1}$	0.2	Kim and Friedman (2010)
				Deakin and Chaplain (2013)
				Domschke et al. (2014)
				Gerisch and Chaplain (2008)
$\rho_0$	Initial ECM density	$0.5 \times 10^{-1} \text{ nM}$	0.5	Anderson et al. (2000)
$D_m$	MMP diffusion coefficient	$8 \times 10^{-9} \text{ cm}^2\text{s}^{-1}$	$8 \times 10^{-3}$	Saffarian et al. (2004)
$\alpha_m$	MMP production rate	$0.5 \times 10^{-12} \mu\text{g s}^{-1}$	0.5	Anderson et al. (2000)
				Deakin and Chaplain (2013)
				Domschke et al. (2014)
				Gerisch and Chaplain (2008)
$\lambda_m$	MMP decay rate	$5 \times 10^{-5} \text{ s}^{-1}$	0.5	Kim and Friedman (2010)
$D_c$	VEGF diffusion coefficient	$10^{-7} \text{ cm}^2\text{s}^{-1}$	0.1	Ambrosi et al. (2005)
				Gamba et al. (2003)
				Miura and Tanaka (2009)
				Serini et al. (2003)
				Yen et al. (2011)
$\alpha_c$	VEGF production rate	$5 \times 10^{-12} \text{ ng s}^{-1}$	2.5	Serini et al. (2003)
	VEGF decay rate	$\lambda_c = 2.7 \times 10^{-4} \text{ s}^{-1}$	2.7	Singh et al. (2015)

**Cluster size metrics.** In order to gain insight into the role played by different biological, chemical and mechanical factors in dictating the cluster size, we define two different measures of cluster size with complementary information, as similarly done in Palmer et al. (2003). We define these for the nondimensional 1D problem, but analogous definitions can be considered for the 2D problem. Assume that  $Q \in \mathbb{N}$  clusters have formed at time  $t = T$  and let  $\omega \subset \Omega$  be the subdomain supporting these clusters, i.e.

$$\omega := \text{supp } n(T, x). \quad (5.18)$$

Then  $\omega$  can be partitioned into  $Q$  subdomains  $\omega_1, \dots, \omega_Q$ , i.e. we have

$$\bigcup_{i=1}^Q \omega_i = \omega \quad \text{and} \quad \omega_i \cap \omega_j = \emptyset \quad \text{for } i, j = 1, \dots, Q, \quad i \neq j, \quad (5.19)$$

where each  $\omega_i$  ( $i = 1, \dots, Q$ ) corresponds to the support of a cluster. We let the average cluster *width*  $W$  and average cluster *compactness*  $C$  be defined by

$$W := \frac{1}{Q} \sum_{i=1}^Q W_i, \quad \text{where} \quad W_i := |\omega_i| \quad i = 1, \dots, Q, \quad (5.20)$$

$$C := \frac{1}{Q} \sum_{i=1}^Q C_i, \quad \text{where} \quad C_i = \frac{\int_{\omega_i} n(T, x) dx}{W_i} \quad i = 1, \dots, Q. \quad (5.21)$$

Under definitions (5.18)-(5.20), the width  $W_i$  ( $i = 1, \dots, Q$ ) of each cluster is a measure of the length of its support, which may be understood as an indicator of the diameter of the cluster assuming the 1D case is reflective of the corresponding 2D problem. Note that the analogous 2D definition to (5.20) would inform us on the area covered by each cluster, from which the average cluster diameter could be calculated. However, this would need to be complemented with an additional metric for cluster elongation (e.g. the ratio between the diameter of the circle circumscribing  $\omega_i$  and that of the one inscribed in  $\omega_i$ ), in order to obtain an exhaustive description of the clusters structure. Under definition (5.21), in which  $n(T, x)$  is the nondimensional cell density, the compactness  $C_i$  ( $i = 1, \dots, Q$ ) of each cluster is a measure of the average cell density within cluster  $i$ . Cluster compactness allows us to distinguish between simple cell aggregates and well-defined clusters, identified as such only if  $C$  is higher than 0.5, corresponding to at least half the local volume being occupied by cells. Under the choices of nondimensionalisation and of spatial domain for the numerical simulations, we expect  $0 \leq W_i \leq 1$  and – under cell incompressibility assumptions –  $0 \leq C_i \leq 1$  for all  $i = 1, \dots, Q$ . Figure 5.1 summarises the biological interpretation of possible combinations of  $W$  and  $C$ . In practice, the cluster domains  $\omega_i$

used to calculate  $W$  and  $C$  are identified via image segmentation by thresholding, with a threshold value for the cell density set to be  $10^{-4}$  – though smaller values have also been considered which do not remarkably affect the results presented henceforth – below which  $n(t, x)$  is approximated to zero.

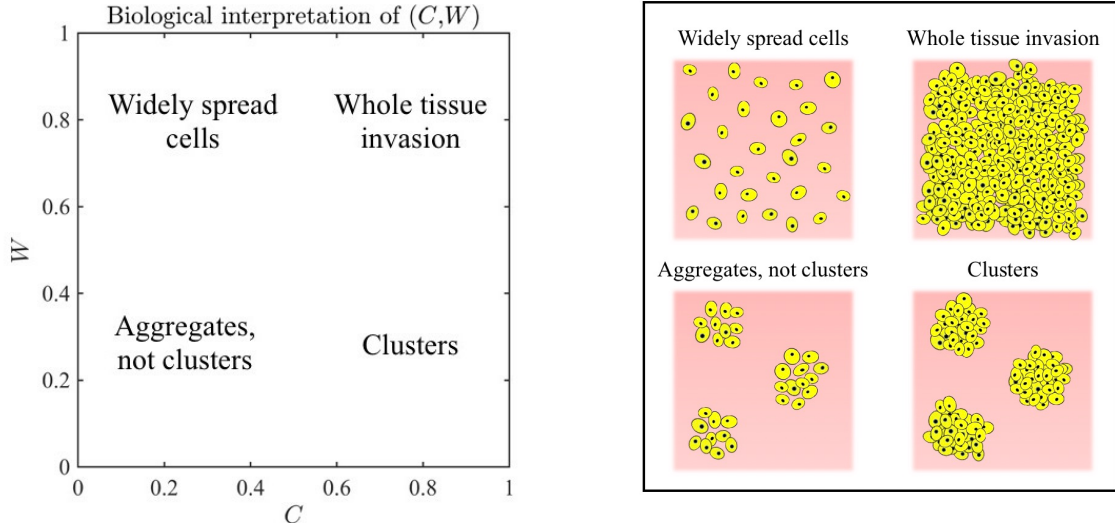


**Figure 5.1: Biological interpretation of cluster width and compactness.** Biological interpretation of possible combinations of cluster width  $W$  (5.20) and cluster compactness  $C$  (5.21): high  $W$  and low  $C$  capture the scenario in which few cells are widely spread across the domain (top left region of the  $C$ - $W$  plane); low  $W$  and low  $C$  capture the presence of loose cell aggregates, (bottom left region); low  $W$  and high  $C$  capture the presence of clusters (bottom right region); high  $W$  and high  $C$  capture the scenario in which many cells are widely spread across the domain, corresponding to the case of tissue invasion in which no clusters can be identified (top right region).

### 5.3.2 Cluster formation under the baseline parameter set

We report in Figure 5.2 the cell density  $n(t, x)$  obtained from numerical simulations of the 1D model under the baseline parameter set and in Figure 5.3 the corresponding cluster width  $W$  and compactness  $C$  measured. The plots displayed in these figures indicate that our model predicts three stages of cluster formation in 1D. First EPCs form aggregates which reach a minimum cluster width of about  $W = 0.2$  around  $t = 17$  (*cf.* left panel in Figure 5.2 and Figure 5.3). Then the cells in these aggregates continue to proliferate, increasing their compactness, while keeping the cluster width unchanged up to about  $t = 50$  (*cf.* central panel in Figure 5.2 and Figure 5.3). Finally, the cells continue to proliferate until the whole domain is occupied by cells (*cf.* right panel in Figure 5.2 and Figure 5.3).

The simulated dynamics of cluster formation nicely match the experimentally observed ones by Blatchley et al. (2019), see Figure 4.2, although in our simulations they occur on

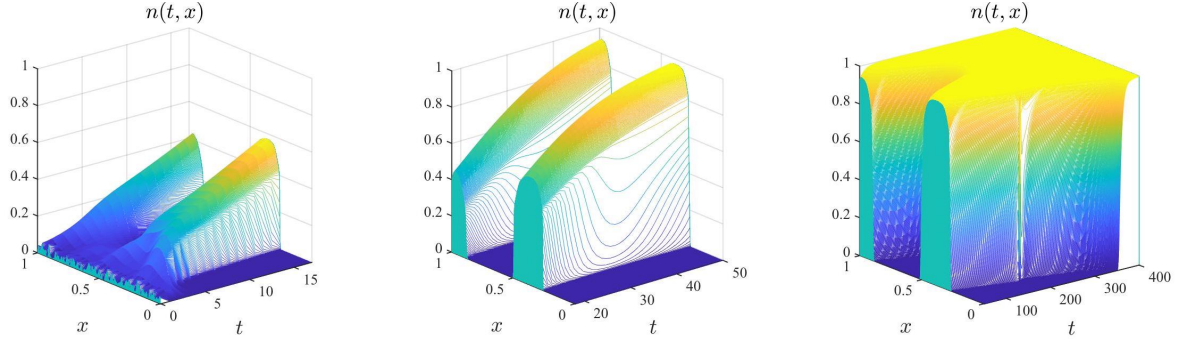


**Figure 5.2: 1D numerical results under the baseline parameter set.** Plots of the cell density  $n(t, x)$  obtained solving the system (5.15), together with definitions (5.5), (5.8) and (5.16), initial conditions (5.13) and (5.14)<sub>1</sub>, complemented with zero-flux boundary conditions, under the baseline parameter set in Table 5.1. The solution is plotted in the time intervals  $t = [0, 17]$  (left panel),  $t = [17, 50]$  (central panel) and  $t = [50, 400]$  (right panel).

a slightly slower timescale. In fact in Blatchley et al. (2019) the minimum cluster size was reached around 24 hours (about nondimensional time  $t = 8.7$ ) and kept unchanged while clusters increased compactness up to 48 hours ( $t = 17.3$ ) before late stage dynamics kick in. The numerically obtained cluster width corresponds to about  $200 \mu\text{m}$ , which is within the range of cluster diameters observed by Blatchley et al. (2019). Finally, after  $t = 50$  we observe the equivalent of whole tissue invasion, suggesting our modelling framework cannot properly capture cluster stabilisation in the long run, at least in the 1D case.

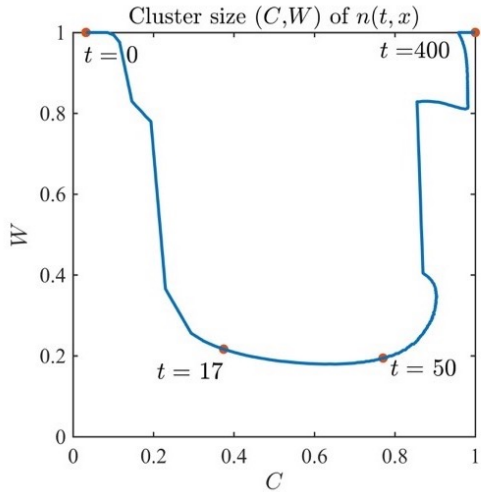


**Figure 5.3: Cluster width and compactness of 1D numerical results under the baseline parameter set.** Average cluster width  $W$  (5.20) and cluster compactness  $C$  (5.21) (left panel) measured over time on the cell density  $n(t, x)$  (right panel) obtained solving the system (5.15), together with definitions (5.5), (5.8) and (5.16), initial conditions (5.13) and (5.14)<sub>1</sub>, complemented with zero-flux boundary conditions, under the baseline parameter set in Table 5.1, reported in Figure 5.2.

### 5.3.3 Numerical investigation of cluster formation

In view of the results reported in Section 5.3.2, we now investigate the role played by chemotaxis, ECM degradation and cell-to-cell adhesion in cluster formation by varying the relevant parameter values and observing changes in the solution up until  $t = 50$ , starting from the same initial conditions considered in the previous section. The long-time dynamics (up to  $t = 400$ ) of the solutions plot in Figure 5.4 are reported in the supplementary Figure D.2.

**The primary role of chemotaxis and ECM degradation** The plots reported in the second row of Figure 5.4 reveal the role of chemotaxis and ECM degradation in cluster formation, according to the dynamics described in Section 5.1. Under the baseline parameter set we observe cluster formation (*cf.* first plot in second row of Figure 5.4), as discussed in the previous paragraph and summarised in Figure 5.2. In the absence of ECM degradation, even though cell aggregates of the same width form, the maximum cell density remains below 0.3 (*cf.* second plot in second row of Figure 5.4) and actually decays over longer periods of time (see supplementary Figure D.2). On the other hand, in the absence of chemotaxis, no cell aggregation occurs and we either observe total invasion of the domain by the cells (*cf.* third plot in second row of Figure 5.4) or, in the absence of ECM degradation, a simple spatial redistribution of the cells (*cf.* fourth plot in second row of Figure 5.4). These results indicate that chemotaxis and ECM degradation are both crucial to cluster formation, with chemotaxis playing a key role in cell aggregation, and ECM degradation being responsible for these aggregates growing into well-defined and compact clusters.

**The secondary role of cell-to-cell adhesion** Let us now compare the plots in the second row of Figure 5.4 with those in the rest of the figure, which have been obtained by varying the cell-to-cell adhesion coefficient  $S_{nn}$ , the value of which was chosen *a priori* due to lack of proper estimates in the current literature. We immediately observe that for small values  $S_{nn} \leq 0.1$ , under the baseline parameter set, cell-to-cell adhesion does not play any particular role in cluster formation, as demonstrated by the fact that the simulations in the absence of cell-to-cell adhesion closely resembles those with  $S_{nn} = 0.1$  (*cf.* first and second row of Figure 5.4). On the other hand, increasing the order of magnitude of the cell-to-cell adhesion coefficient results in the initial formation of small-scale aggregates. Moreover, the maximum density reached by these aggregates increases as  $S_{nn}$  increases (*cf.* third and fourth row of Figure 5.4). This, however, does not seem to affect the long-time dynamics of the solution, which remain analogous to those described in the previous paragraph. For instance, under the baseline parameter set except for

$S_{nn} = 1$ , the initial aggregates merge – likely due to chemotaxis – into wider clusters and then proceed to invade the whole tissue (*cf.* first plot in third row of Figure 5.4 and of Figure D.2). For  $S_{nn} = 10$  we do not yet observe small aggregates merging into larger clusters at  $t = 50$  – likely due to cell-to-cell adhesion overpowering chemotaxis – and tissue invasion is simply delayed (*cf.* first plot in fourth row of Figure 5.4 and of Figure D.2). Overall these results suggest that the continuum nonlocal description of cell-to-cell adhesion considered in our model, while it may capture the aggregating effect of cell-to-cell adhesion for  $S_{nn}$  high enough, does not capture the stabilising effect that we are seeking in this modelling framework.

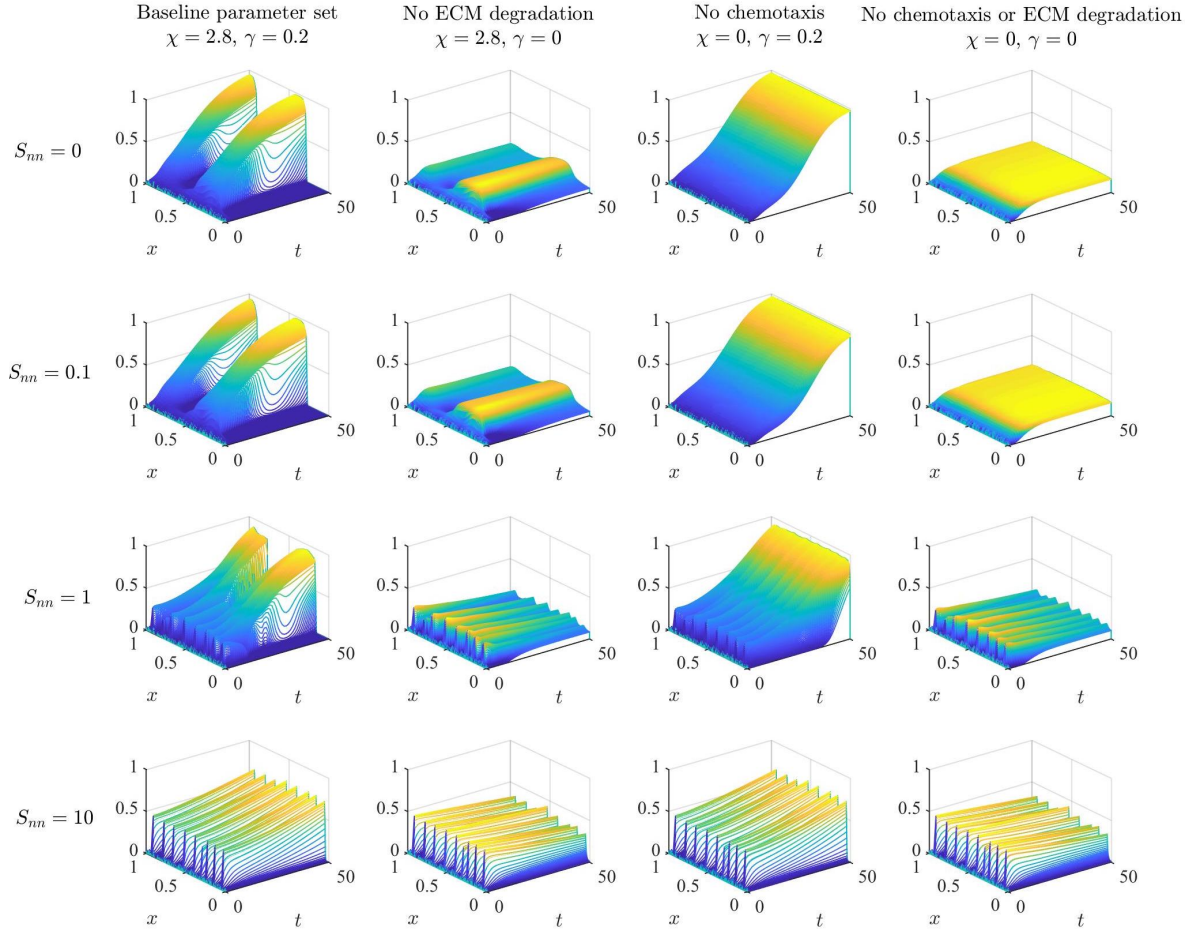


**Figure 5.4:** 1D numerical results under the baseline parameter set with changes to parameters  $S_{nn}$ ,  $\chi$  and  $\gamma$  as detailed. First row: Plots of the cell density  $n(t, x)$  up to  $t = 50$  obtained solving the system (5.15), together with definitions (5.5), (5.8) and (5.16), initial conditions (5.13) and (5.14)<sub>1</sub>, complemented with zero-flux boundary conditions, in the absence of cell-to-cell adhesion, *i.e.* for  $S_{nn} = 0$ : under the baseline parameter set (first column), in the absence of ECM degradation, *i.e.* for  $\gamma = 0$  (second column), in the absence of chemotaxis, *i.e.*  $\chi = 0$  (third column), and in the absence of both chemotaxis and ECM degradation, *i.e.*  $\chi = \gamma = 0$  (fourth column). Second, third and fourth rows: Same as first row but in the presence of cell-to-cell adhesion, with  $S_{nn} = 0.1$  (second row),  $S_{nn} = 1$  (third row) and  $S_{nn} = 10$  (fourth row) respectively.

### 5.3.4 Numerical investigation of cluster size

We study changes in the measures  $W$  and  $C$ , defined according to (5.20) and (5.21), at  $t = 50$  under alternative values of each parameter in the baseline parameter set. In particular, we consider the effect of halving and doubling the magnitude of each parameter in equations (5.15)<sub>1</sub> and (5.15)<sub>2</sub> in Figure 5.5, and those in equations (5.15)<sub>3</sub> and (5.15)<sub>4</sub> in Figure 5.6. Each boxplot had been obtained using data from 100 simulations under the same parameter set, starting from randomised initial conditions as in (5.13) and (5.14)<sub>1</sub>. The cluster width  $W$  measured over 100 simulations under the baseline parameter width ranges between 0.15 and 0.41 with median (and mean) around 0.23, as portrayed in Figures 5.5 and 5.6 (central boxplot in each  $W$  plot). This nondimensional width corresponds to a diameter in the range  $150 - 410\mu\text{m}$ , which is consistent with the experimentally observed cluster size in Blatchley et al. (2019) (*cf.* Figure 4.2).

**The role of chemotaxis** Boxplots of the width  $W$  and compactness  $C$  of clusters for different values of the chemotactic sensitivity  $\chi$  are displayed in Figure 5.5b. While higher values of  $\chi$  correlate with slightly smaller clusters, yet maintaining a mean width around 0.2, lowering the magnitude of  $\chi$  seems to result in a wider range of values of  $W$  with much higher median, as well as higher compactness  $C$ . This supports the notion that lowering the chemotactic sensitivity of the cells hinders cluster formation and – assuming all other dynamics are present – fosters tissue invasion, which is in line with the results presented in Section 5.3.3.

**The role of ECM degradation** Boxplots of the width  $W$  and compactness  $C$  of clusters for different values of the ECM degradation rate  $\gamma$  are displayed in Figure 5.5f. Notice that, while the median width  $W$  is maintained around 0.2, increasing the magnitude of  $\gamma$  results in a smaller range of values measured for both  $W$  and  $C$ , as well as higher values of cluster compactness. In addition, this trend suggests that further decreasing  $\gamma$  will lead to higher values of  $W$  and lower values of  $C$  (see supplementary Figure D.3c), which is in line with the observed dynamics in the absence of ECM degradation in Section 5.3.3 (*cf.* Figure 5.4, second and fourth columns). Overall, this highlights the key role ECM degradation has in cluster formation, establishing a relation between the rate  $\gamma$  and the cluster compactness  $C$ .

**The role of matrix remodelling** We see in Figure 5.5g that increasing the magnitude of the matrix remodelling rate  $\mu$  yields opposing effects to those obtained increasing its degradation rate  $\gamma$  (*vid.* Figure 5.5f), which is coherent with the opposite nature of these dynamics.

**The role of cell-to-cell adhesion** The plots in Figure 5.5c confirm that small changes in the cell-to-cell adhesion coefficient  $S_{nn}$  do not influence the size of clusters, as expected from the results in Section 5.3.3. Additional numerical tests considering different orders of magnitude of  $S_{nn}$  (see supplementary Figure D.3b) revealed a slight increase in the median  $W$ , probably due to the initial presence of smaller clusters (*cf.* Figure 5.4, third row) which at  $t = 50$  may still be in the process of merging depending on their spatial distribution. These results suggest that cell-to-cell adhesion is not a key mechanism in determining cluster structure.

**The role of cell diffusion and cell-matrix interactions** The boxplots of  $W$  and  $C$  of clusters for different values of the cell diffusion coefficient  $D_n$ , displayed in Figure 5.5a, show that changing the magnitude of  $D_n$  has very little effect on the cluster compactness  $C$  and median width  $W$ . There is, however, an increasing range of values of  $W$  measured as  $D_n$  increases, indicating that low diffusivity correlates with more precisely defined clusters, while high diffusivity results in more variability in cluster size. Moreover, this variability allows for larger values of  $W$  to be measured, suggesting that much higher diffusivity may result in tissue invasion (see supplementary Figure D.3a). The same observations can be conducted on the boxplots in Figure 5.5d, obtained by varying the magnitude of the cell-to-matrix adhesion coefficient. This is in line with the notion that lower cell-matrix interactions facilitate cluster formation, while much higher cell-matrix interactions promote tissue invasion.

**The role of cell proliferation** In Figure 5.5e we see that slower proliferation – i.e. lower  $p$  – correlates with a wide range of lower values of cluster compactness  $C$ , while the median width is maintained around 0.2. On the other hand, faster proliferation – i.e. higher  $p$  – results in a wide range of higher values of cluster width  $W$  and a small range of high values of compactness  $C$ . Note that these data portray different stages of the cluster formation process, as demonstrated in Figure 5.3 (central panel): initially aggregates form without being very condensed (low-to-medium  $W$  and  $C$ ), then they increase their compactness while keeping steady width (low  $W$  and high  $C$ ), and eventually grow further invading the surrounding space (medium-to-high  $W$  and high  $C$ ). This suggests that the rate of proliferation of EPCs might play a key role in determining the speed of the cluster formation process.

**The role of initial ECM density** The plots in Figure 5.5h indicate that changes in the initial ECM density  $\rho_0$  do not affect the long-time spatiotemporal dynamics. In fact, while different values of  $\rho_0$  results in slightly different values of the median width and

compactness of clusters observed at  $t = 50$ , these values still capture the same biological scenario (i.e. cluster are recognisable at  $t = 50$ ).

**The role of VEGF dynamics** Figure 5.6e displays changes in cluster width  $W$  and compactness  $C$  as the rate production of VEGF,  $\alpha_c$ , varies. Note that these results well mirror those obtained by varying chemotactic sensitivity (*cf.* Figures 5.5b and 5.6e), which is coherent with the notion that higher VEGF production rates correlate with stronger chemotactic dynamics, already established to play a key role in cluster formation. In addition, the size of clusters seems to be proportional to the VEGF diffusion coefficient  $D_c$ , as demonstrated by the plots in Figure 5.6d in which we see that increasing the magnitude of  $D_c$  results in higher  $W$  and  $C$ . This trend, however, suggests that much higher values of  $D_c$  may result in tissue invasion, rather than cluster formation (see supplementary Figure D.3e). Finally, as suggested by Figure 5.6f, changes in the VEGF decay rate  $\lambda_c$  do not seem to particularly effect cluster size, over the range of parameter values considered.

**The role of MMP dynamics** Figure 5.6b displays changes in cluster width  $W$  and compactness  $C$  as the rate production of MMP,  $\alpha_m$ , varies. Similarly to what was observed for  $\alpha_c$  in relation to  $\chi$ , we see that these boxplots closely resemble those obtained varying  $\gamma$  (*cf.* Figures 5.5f and 5.6b), which is coherent with the notion that higher MMP production rates correlate with stronger degrading dynamics, already established to be responsible for turning aggregates into clusters – that is, increasing their compactness. In addition, we see in Figure 5.6c that increasing the magnitude of the MMP decay rate  $\lambda_m$  yields opposite effects to those obtained increasing their production  $\alpha_m$ , further confirming the role MMP-mediated ECM degradation has in cluster formation. On the other hand, changes in the MMP diffusivity  $D_m$  do not seem to affect cluster size, as demonstrated in Figure 5.6a – verified under different orders of magnitude of  $D_m$  (see supplementary Figure D.3d). This suggests not much will be gained by distinguishing between membrane-bound and diffusive MMPs, at least in this modelling framework and within the range of parameter values considered.

### 5.3.5 2D clusters

Let us now consider the 2D problem. In this section we focus on the most interesting results obtained in Section 5.3.4 and investigate the role played by chemotaxis, ECM degradation and cell proliferation in the formation of 2D clusters. We also consider the results in the absence of ECM remodelling, discussing its biological interpretation in relation to *in vitro* and *in vivo* assays.

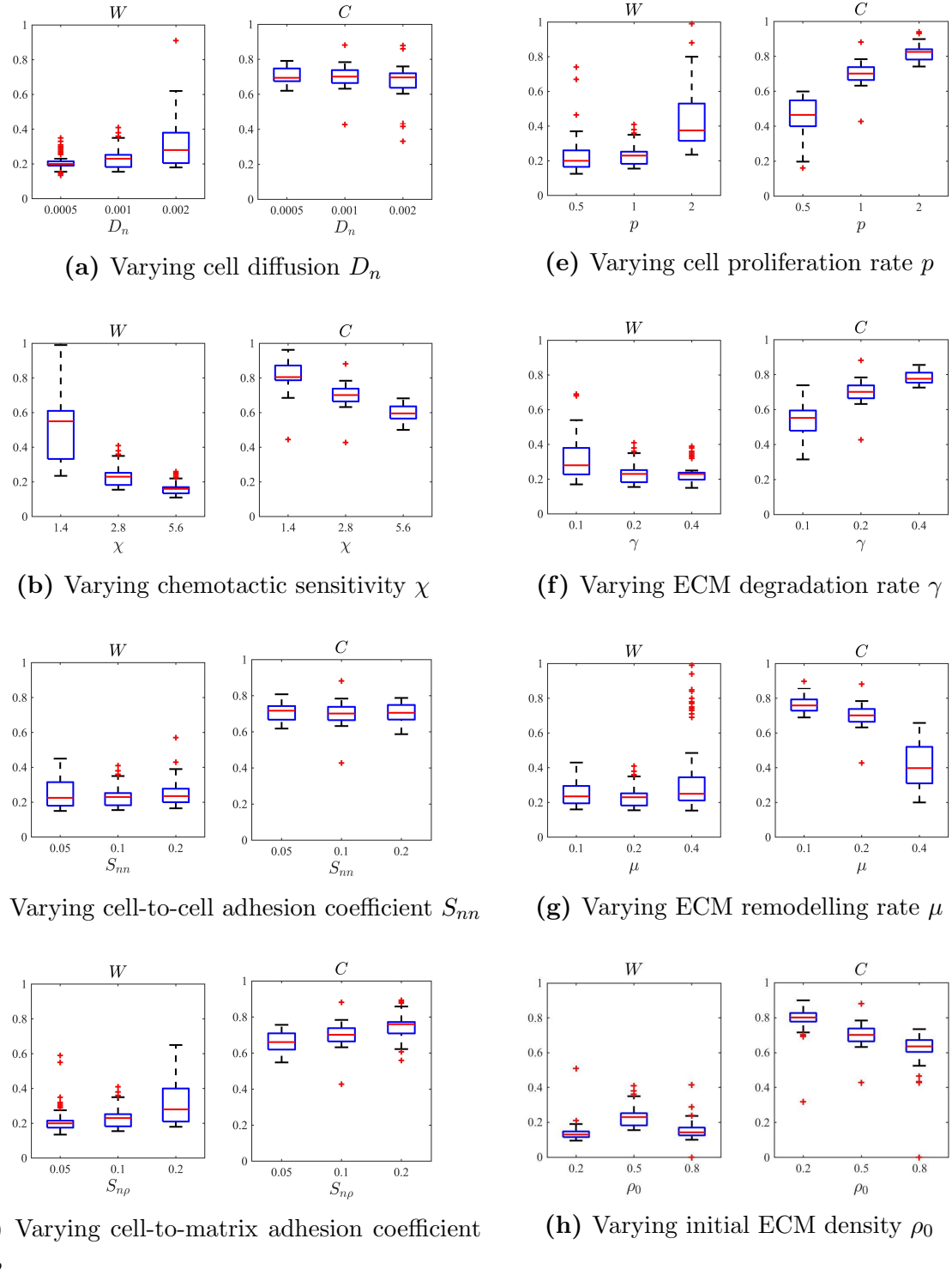


**Figure 5.5: Parametric analysis of cluster width and compactness (part 1).** Cluster width  $W$  and compactness  $C$ , defined in (5.20) and (5.21), under deviations from the baseline parameter set (BPS), in Table 5.1, of each parameter in equations (5.15)<sub>1</sub> and (5.15)<sub>2</sub>. In (a) we have boxplots of  $W$  and  $C$  measured on the numerical solution of the system (5.15) at  $t = 50$ , for  $D_n$  taking its value in the BPS (center), half (left) and double (right) its value in the BPS. Each boxplot collects data from 100 simulations under randomised initial conditions (5.13)-(5.14)<sub>1</sub>. In (b)-(g) we have the same as in (a) but varying parameters  $\chi$  (b),  $S_{nn}$  (c),  $S_{n\rho}$  (d),  $p$  (e),  $\gamma$  (f),  $\mu$  (g) and  $\rho_0$  (h).

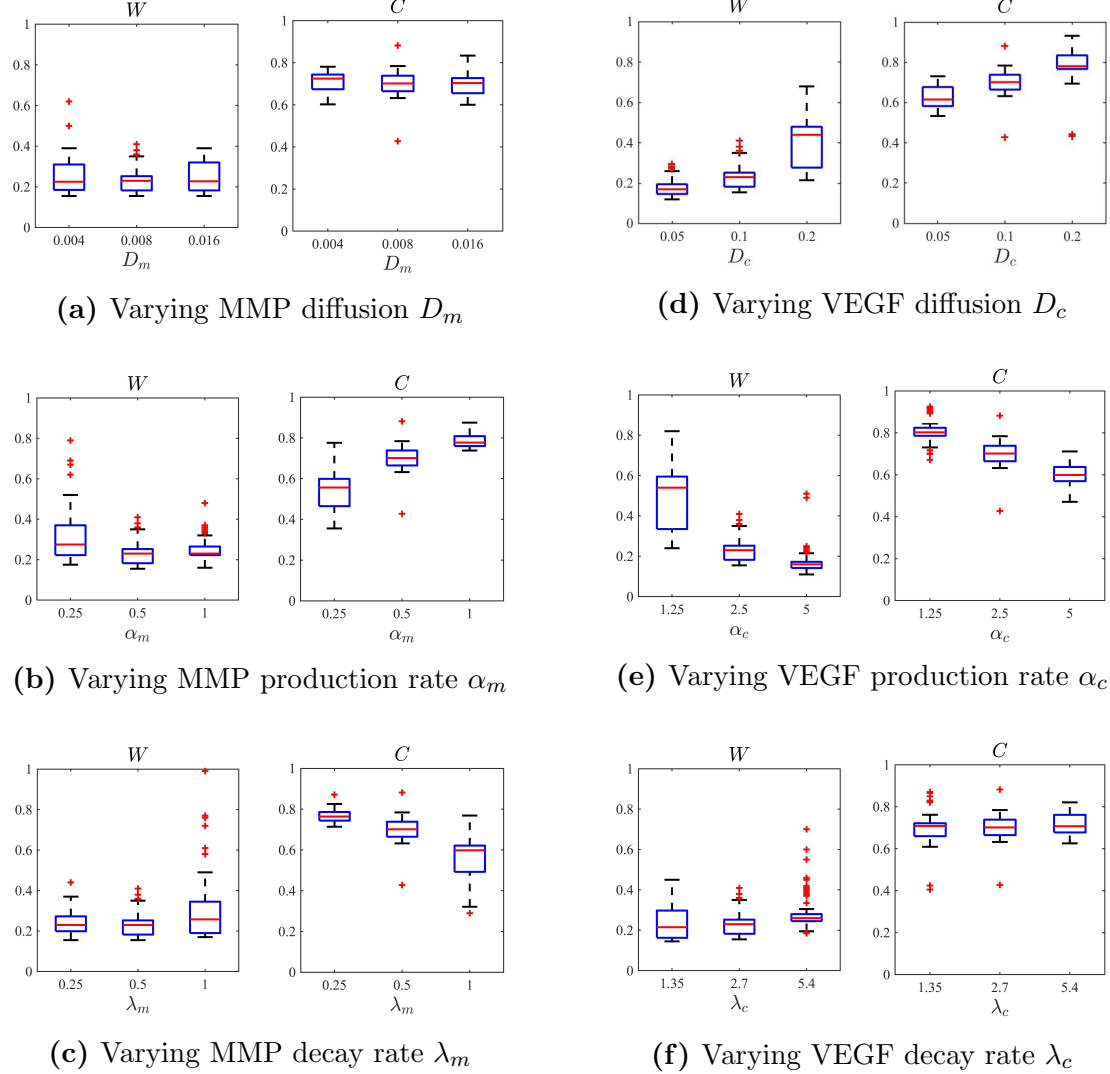


**Figure 5.6: Parametric analysis of cluster width and compactness (part 2).** Cluster width  $W$  and compactness  $C$ , defined in (5.20) and (5.21), under deviations from the baseline parameter set in Table 5.1 of each parameter in equations (5.15)<sub>3</sub> and (5.15)<sub>4</sub>. In (a) we have boxplots of  $W$  and  $C$  measured on the numerical solution of the system (5.15) at  $t = 50$ , for  $D_m$  taking its value in the BPS (center), half (left) and double (right) its value in the BPS. Each boxplot collects data from 100 simulations under randomised initial conditions (5.13)-(5.14)<sub>1</sub>. In (b)-(f) we have the same as in (a) but varying parameters  $\alpha_m$  (b),  $\lambda_m$  (c),  $D_c$  (d),  $\alpha_c$  (e) and  $\lambda_c$  (f).

**2D clusters under the baseline parameter set.** Under the baseline parameter set reported in Table 5.1, 2D cluster formation follows slightly different spatiotemporal dynamics to those observed in the 1D case, as demonstrated by the plots in the second row of Figures 5.7, 5.8 and 5.9. At  $t = 20$ , the cell density has already reached maximum local compactness in some regions, while aggregation dynamics are still at their early stages (*cf.* first panel in second row of Figures 5.7, 5.8 or 5.9), and the minimum cluster size is observed no earlier than  $t = 140$  (*cf.* fourth panel in second row of Figures 5.7, 5.8

or [5.9]). The cluster observed at this stage has a nondimensional diameter of about 0.2, which perfectly agrees with the results in 1D and is also consistent with experimental observations reported by Blatchley et al. (2019). After the cluster has formed, no tissue invasion is observed – see supplementary Figure D.4.

**The role of ECM degradation in 2D.** The plots reported in Figure 5.7 demonstrate that ECM degradation promotes the formation of 2D clusters, as predicted by the results of the 1D model presented in Sections 5.3.3 and 5.3.4. Lower ECM degradation rates correlate with slower aggregation dynamics and lower compactness of such aggregates (*cf.* first row of Figure 5.7) – to the extent that in the absence of ECM degradation no clusters form (see supplementary Figure D.5) – and higher ECM degradation rates correlate with faster cluster formation with well-defined and compact clusters observed at much earlier times (*cf.* third row of Figure 5.7). As for the 1D model, we obtain the same results under analogous changes of the MMP secretion rate  $\alpha_m$  (see supplementary Figure D.6).

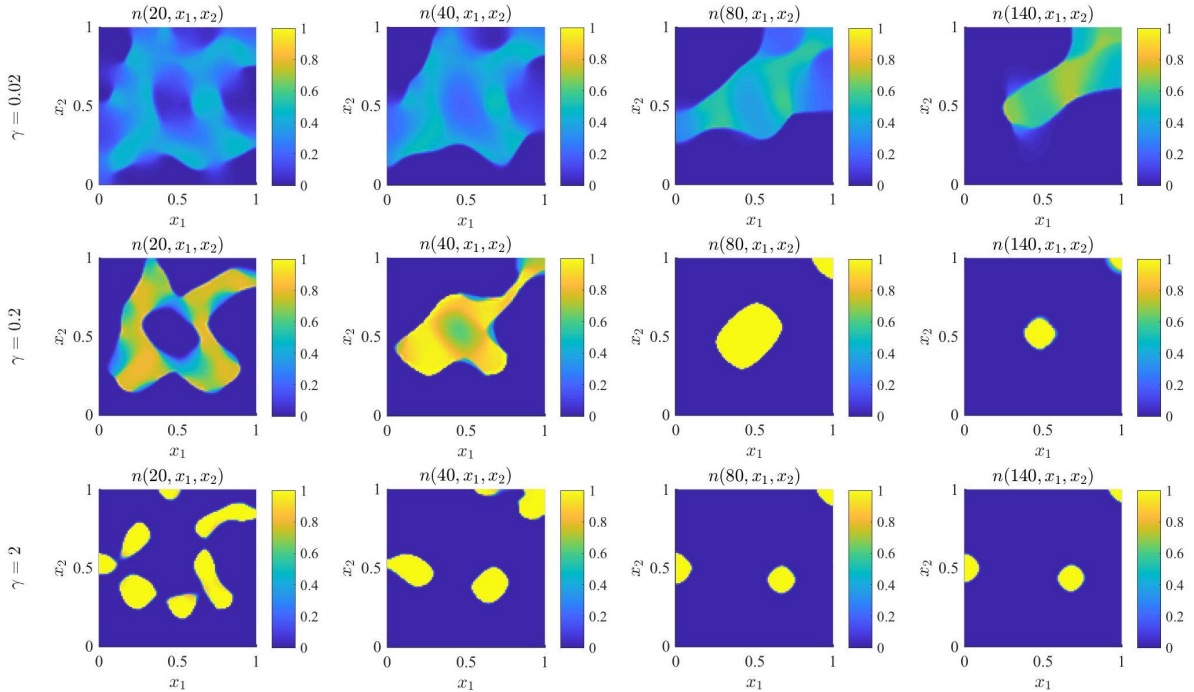


**Figure 5.7: 2D numerical results under different matrix degradation rates.** First row: Plots of the cell density  $n(t, \mathbf{x})$  obtained solving the system (5.15), together with definitions (5.6), (5.8) and (5.16), initial conditions (5.13) and (5.14)<sub>2</sub>, complemented with zero-flux boundary conditions, under the parameter choices reported in Table 5.1, except for  $\gamma = 0.02$ . The solution is plotted at time  $t = 20$  (first panel),  $t = 40$  (second panel),  $t = 80$  (third panel) and  $t = 140$  (fourth panel). Second and third row: Same as first row, except for  $\gamma = 0.2$  (second row) and  $\gamma = 2$  (third row).

**The role of chemotaxis in 2D.** The plots reported in Figure 5.8 demonstrate that endogenous chemotaxis promotes aggregation dynamics, as predicted by the results of the 1D model presented in Sections 5.3.3 and 5.3.4, and reveal that chemotaxis is an important determinant of 2D cluster structure. Lower values of the chemotactic sensitivity  $\chi$  correlate with slower and weaker aggregation dynamics, so that no well-defined clusters can be observed (*cf.* first row of Figure 5.8). Higher values of  $\chi$  correlate with faster and stronger aggregation dynamics, with well-defined clusters observed at earlier times (*cf.* third row of Figure 5.8) and cluster diameter – once the clusters have reached minimum size – smaller than that observed with lower values of  $\chi$  (*cf.* last panel in the second row and last panel in the third row of Figure 5.8). As for the 1D model, we obtain the same results under analogous changes of the VEGF secretion rate  $\alpha_c$  (see supplementary Figure D.7).

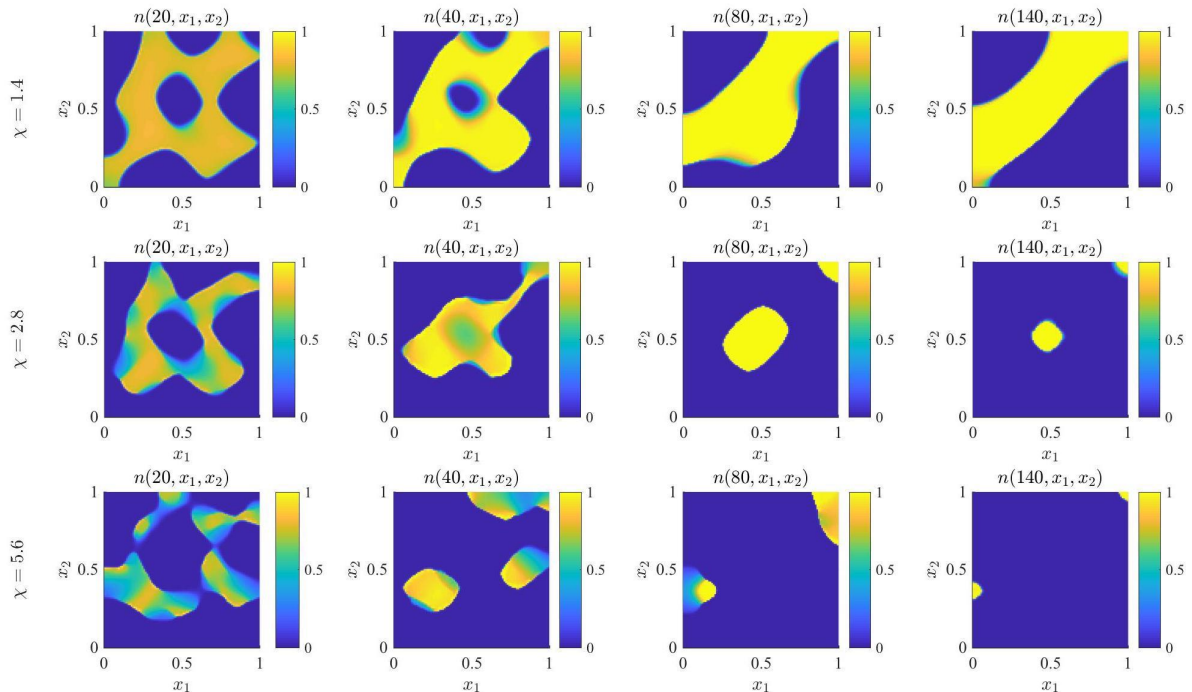


**Figure 5.8: 2D numerical results under different chemotactic coefficients.** First row: Plots of the cell density  $n(t, \mathbf{x})$  obtained solving the system (5.15), together with definitions (5.6), (5.8) and (5.16), initial conditions (5.13) and (5.14)<sub>2</sub>, complemented with zero-flux boundary conditions, under the parameter choices reported in Table 5.1, except for  $\chi = 1.4$ . The solution is plotted at time  $t = 20$  (first panel),  $t = 40$  (second panel),  $t = 80$  (third panel) and  $t = 140$  (fourth panel). Second and third row: Same as first row, except for  $\chi = 2.8$  (second row) and  $\chi = 5.6$  (third row).

**The role of cell proliferation in 2D.** While the results of the 1D model presented in Section 5.3.4 seemed to suggest that the speed of the cluster formation process is proportional to the cell proliferation rate  $p$ , the plots reported in Figure 5.9 in a 2D framework

indicate otherwise. While the rate of cell proliferation may influence how the cells respond to spatial gradients at the beginning of the cluster formation process (*cf.* plots in the second column of Figure 5.9), it does not seem affect the overall spatiotemporal dynamics of 2D cluster formation. Upon these considerations, the results displayed in Figure 5.5e may simply be a 1D projection of the 2D dynamics occurring around the same time – consider for instance a 1D cross-section (e.g.  $x_1 = 0.5$ ) of the plots in the second column of Figure 5.9.

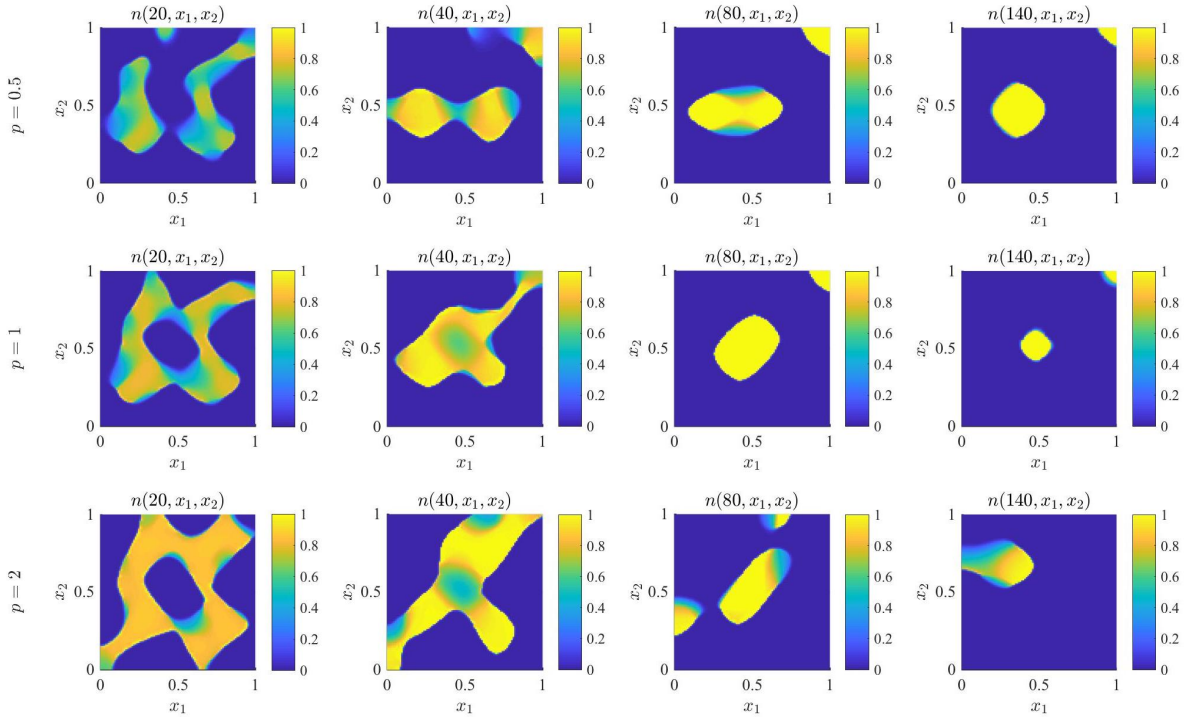


**Figure 5.9: 2D numerical results under different proliferation rates.** *First row:* Plots of the cell density  $n(t, \mathbf{x})$  obtained solving the system (5.15), together with definitions (5.6), (5.8) and (5.16), initial conditions (5.13) and (5.14)<sub>2</sub>, complemented with zero-flux boundary conditions, under the parameter choices reported in Table 5.1, except for  $p = 0.5$ . The solution is plotted at time  $t = 20$  (first panel),  $t = 40$  (second panel),  $t = 80$  (third panel) and  $t = 140$  (fourth panel). *Second and third row:* Same as first row, except for  $p = 1$  (second row) and  $p = 2$  (third row).

**The role of matrix remodelling and its relation to *in vitro* studies.** While matrix remodelling naturally occurs *in vivo* thanks to the presence of other cells in biological tissue, this is not generally observed in *in vitro* assays, which occur in isolated environments. Thus, in order to compare our results with those of *in vitro* studies, we chose to set the ECM remodelling rate  $\mu = 0$ , and present the results in Figure 5.10. We observe that clusters still form in the absence of ECM remodelling, however they are smaller than in the baseline parameter set (*cf.* last panel in the second row of Figures 5.7–5.9 and that of Figure 5.10). The smaller cluster size may result from the more dominant role played

by cell-to-cell adhesion following ECM degradation: in the absence of ECM remodelling, volume exclusion is less likely to affect the cell dynamics and, at the cell boundaries, cell-matrix interactions become negligible compared with cell-cell interactions. We would then expect to observe clusters of a smaller diameter but higher maximum density, but because of death due to competition for space we instead observe a loss of cell mass. While these results are mathematically consistent with our model set up, the observed cluster size under the baseline parameter set was more coherent with *in vitro* experimental observations in Blatchley et al. (2019) than that observed for  $\mu = 0$ . This could be explained by considering that our 2D set up is meant to reflect dynamics occurring in a 2D horizontal cross section of the 3D experimental domain reported in Blatchley et al. (2019), illustrated in Figure 4.2. As the cells degraded the matrix and reorganised into clusters, they also fell towards the bottom of the hydrogel, as illustrated by the experimental data reported in Figure 4.2D, in regions where it was not yet degraded. Thus, following the horizontal plane intersecting the cluster's centre, we would indeed observe cell-independent matrix remodelling.

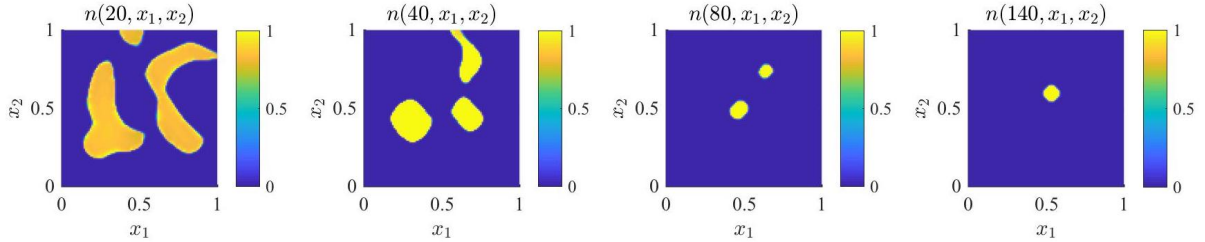


**Figure 5.10: 2D numerical results in the absence of matrix remodelling.** Plots of the cell density  $n(t, \mathbf{x})$  obtained solving the system (5.15), together with definitions (5.6), (5.8) and (5.16), initial conditions (5.13) and (5.14)<sub>2</sub>, complemented with zero-flux boundary conditions, under the parameter choices reported in Table 5.1, except for  $\mu = 0$ . The solution is plotted at time  $t = 20$  (first panel),  $t = 40$  (second panel),  $t = 80$  (third panel) and  $t = 140$  (fourth panel).

# Chapter 6

## Discussion and research perspectives

### 6.1 Summary and discussion

Despite the great progress made in the past 20 years in understanding the mechanisms behind EPC cluster-based vasculogenesis, much more needs to be achieved in order to unlock its full therapeutic potential. Mathematical modelling provides theoretical means to shed light on the otherwise hidden role played by underlying dynamics in the origin and structure of the emergent vascular network, as previously achieved in the study of mature EC vascular network formation (single-cell vasculogenesis). We therefore formulated a nonlocal PDE model of EPC cluster formation during the early stages of vasculogenesis, including mechanisms such as ECM degradation, cell proliferation and cell-to-cell adhesion, which were recently found to distinguish cluster-based vasculogenesis from single-cell vasculogenesis (Blatchley et al., 2019). By introducing appropriate metrics of cluster width and compactness, we investigated the role played by the underlying dynamics in facilitating cluster formation, regulating the speed of the cluster-formation process and the size of clusters – see Table 6.1 for a summary of the results of the parametric analysis of the 1D problem. Furthermore, we verified that most of the key observations from the parametric analysis for the 1D model still hold in a 2D framework.

#### 6.1.1 Chemotaxis, degradation and their link to hypoxia

Our results confirmed the role played by matrix degradation in the formation of EPC clusters in both the 1D and 2D models, providing additional theoretical support to the mechanism of EPC cluster formation proposed by Blatchley et al. (2019). For example, the *in vitro* experiments indicated that no clusters form in the absence of MMPs, which is precisely what we discovered here. In addition, the investigation conducted in Sec-

**Table 6.1:** Summary of the results of the parametric analysis of the 1D problem conducted in Section 5.3.4. The biological meaning of each parameter is summarised in Table 5.1. Cluster width  $W$  and compactness  $C$  are defined in Section 5.3.1. Better defined clusters may correlate with: (i) smaller range of width  $W$  measured; (ii) higher median compactness  $C$  measured. Less well defined clusters correlate with lower median compactness  $C$  measured. Bigger clusters correlate with higher median width  $W$  and compactness  $C$  measured.

Parameter	Main effect of increasing the parameter value on cluster size	Ref. Figure
$D_n$	Little effect favouring tissue invasion	5.5a, D.3a
$\chi$	Better defined clusters (i)	5.5b
$S_{nn}$	Little to no effect	5.5c, D.3b
$S_{np}$	Little effect favouring tissue invasion	5.5d
$p$	Increased cluster formation speed (refuted in 2D)	5.5e
$\gamma$	Better defined clusters (ii)	5.5f, D.3c
$\mu$	Less well defined clusters	5.5g
$\rho_0$	Little to no effect	5.5h
$D_m$	Little to no effect	5.6a, D.3d
$\alpha_m$	Better defined clusters (ii)	5.6b
$\lambda_m$	Less well defined clusters (ii)	5.6c
$D_c$	Bigger clusters	5.6d, D.3e
$\alpha_c$	Better defined clusters (i)	5.6e
$\lambda_c$	Little to no effect	5.6f

tions 5.3.4 and 5.3.5 indicate that the speed of cluster formation is proportional to the rate of matrix degradation – and the rate of MMP secretion by the cells – which nicely agrees with their experimental observations. Our numerical results further highlighted that matrix degradation alone may not suffice to explain the formation of clusters, as endogenous chemotaxis was shown to be responsible for aggregation dynamics, without which the cells would simply invade the whole tissue. In addition, the investigation conducted in Sections 5.3.4 and 5.3.5 suggests that the size of clusters is (inversely) related to the chemotactic sensitivity of the cells – and the rate of VEGF secretion by the cells – indicating chemotaxis may be a key determinant of cluster topology. Note that, in view of the experimental evidence presented by Blatchley et al. (2019) and Akita et al. (2003), the MMP production rate  $\alpha_m$  and the VEGF production rate  $\alpha_c$  may be correlated with the local level of hypoxia. It would therefore be interesting to let these production rates be given as functions of the local oxygen concentration. The results here obtained suggest that our model would then predict cluster formation to be fostered by higher levels of hypoxia, indeed agreeing with the referenced experimental observations (Akita et al., 2003; Blatchley et al., 2019).

### 6.1.2 Cell-to-cell adhesion and cluster stability

Cell-to-cell adhesion, on the other hand, did not seem to play an important role in cluster formation or cluster structure. While this may seem counter-intuitive considering previous single-cell vasculogenesis works (Boas et al., 2018; Merks et al., 2004; Ramos et al., 2018; Scianna et al., 2013), these models did not include both chemotaxis and degradation and thus did not predict cluster formation as an intermediate step in network formation. In view of these works, however, we cannot exclude that the final network configuration (e.g. cord thickness) depends on cell-to-cell adhesion. According to Blatchley et al. (2019), cell-to-cell adhesion is not related to cluster structure, which is consistent with our model predictions, but is responsible for cluster stability. The mathematical study of cluster-based vasculogenesis would therefore benefit from a more suited description of cell-to-cell adhesion, as we have seen in Section 5.3.3 that our modelling choice allows us to capture the aggregative effect of cell-to-cell adhesion, but not its role in cluster stabilisation. This could perhaps be achieved by, instead of modelling cell adhesion nonlocally, modelling diffusion nonlinearly<sup>1</sup> (Carrillo et al., 2019; Murakawa and Togashi, 2015) together with volume exclusion, as done for chemotaxis (*cf.* definitions (5.2) and (5.3)). This would implicitly account for the physical limits of migration imposed by adhesion bonds. Alternatively, one could modify the volume exclusion term (i.e. definition (5.3)) to explicitly model cell adhesion molecules, which would additionally allow for the study of the effect of cell adhesion-mediated saturation of chemotaxis (Merks and Glazier, 2005; Merks et al., 2008; Singh et al., 2015). Otherwise, the stabilising effect of cell-to-cell adhesion could be more easily achieved by adopting an IB or hybrid modelling approach (Anderson, 2005; Singh et al., 2015; Turner and Sherratt, 2002; Turner et al., 2004), as done in previous CP models of single-cell vasculogenesis (Boas et al., 2018; Merks et al., 2004, 2008; Ramos et al., 2018; Scianna et al., 2011, 2013; Szabo et al., 2008).

## 6.2 Research perspectives

### 6.2.1 Model validation

The results reported in Chapter 5 suggest that in order to gain a comprehensive understanding of EPC cluster formation during the early-stages of cluster-based vasculogenesis, it is necessary to consider both ECM degradation and chemotaxis. So far these processes have only been experimentally investigated separately (Akita et al., 2003; Blatchley et al.,

<sup>1</sup>Nonlinear diffusion might also prevent infinite speed of propagation predicted by linear diffusion theory (Andreu et al., 2007), which is *per se* unrealistic when modelling cellular movement. It might therefore also prevent the strict positivity of cell density over the whole domain, which might make the identification of the support of each cluster more straightforward, *cf.* Section 5.3.1.

[\[2019\]](#), but it would be interesting to examine them in both normoxic and hypoxic conditions, in view of our *in silico* results (*cf.* Section [\[6.1.1\]](#)). Model validation would also allow for a more accurate baseline parameter set. In fact, while the role played by matrix degradation and the size of clusters in our numerical simulations well matches the experimental observations reported by [Blatchley et al. \(2019\)](#), this – and future – mathematical models would benefit from the estimation of parameter values by fitting the model to experimental data in order to obtain a better match of the timescale of 2D cluster formation. Note, for instance, that the ten-fold increase in  $\alpha_m$  which results in the observation of well-defined clusters at  $t = 20$  (see supplementary Figure [\[D.6\]](#)) might be justified by the experimental conditions reported in [Blatchley et al. \(2019\)](#) (see Appendix [\[C.2\]](#)). In view of the results reported in Section [\[5.3.5\]](#) in the absence of matrix remodelling, it would also be interesting to further investigate the role ECM remodelling may play in cluster formation and cluster size. This could lead to interesting observations regarding the empirical differences of cluster-based vasculogenesis during *in vitro* and *in vivo* studies, and suggest interesting focus points for therapeutic intervention. In order to achieve this, however, alternative experimental set ups might need to be considered, in order to avoid the remodelling-resembling effects of cells falling towards the bottom of the 3D hydrogel during the cluster-formation process.

### 6.2.2 Further analytical investigations

In Section [\[5.3\]](#) we have conducted a parametric analysis of the model in order to elucidate potential model behaviour. Whereas this already gave meaningful information to discuss the importance of the various processes involved in cluster-based vasculogenesis, there are more advanced mathematical tools available for the analysis of the dependence of the model outcome on the model parameters. In particular, once accurate ranges of parameter values have been estimated from data spanning different levels of hypoxia, it would be of significant interest to conduct a global sensitivity analysis ([Marino et al., 2008](#); [Qian and Mahdi, 2020](#); [Renardy et al., 2019](#)) of the cluster width and compactness to parameter variability. In fact, while the conducted parametric analysis highlighted the role played by each single parameter as it deviates from its baseline value, the global sensitivity analysis would provide a tool to investigate the effect of combined changes in the value of multiple or all parameters over ranges indicative of different levels of hypoxia. This global approach is also significant given the nonlinear nature of the model ([Saltelli and Annoni, 2010](#); [Saltelli et al., 2019](#)). Upon revision of the modelling strategy adopted to describe cell-to-cell adhesion, a global sensitivity analysis could be conducted in 2D in relation to the cluster compactness ( $C$ ), area ( $W$ ) and elongation (see Section [\[5.3.1\]](#)). Moreover, it would be particularly interesting to conduct a weakly nonlinear analysis ([Boonkorkuea](#)

---

et al., 2010; Cross and Greenside, 2009; Han et al., 2017; Hoyle and Hoyle, 2006) of the 2D model for a quantitative description of how chemotaxis is responsible for cluster structure. For instance, considering the results reported in Figure 5.8, there might be a threshold value of the chemotactic sensitivity below which we do not observe 2D clusters.

### 6.2.3 The inclusion of persistence of motion

In addition to the modelling research perspectives discussed in Sections 6.1.1 and 6.1.2, interesting investigations could be conducted by considering the possible interplay between degradation and persistence of motion. Previous CP models of single-cell vasculogenesis predicted cluster formation in the absence of cell elongation (Merks et al., 2006), due to chemotaxis. Despite their exclusion of ECM degradation and proliferation, we expect such result to capture the role of elongation during cluster-based vasculogenesis, given that EPC motion during the early stages of the process is mostly amoeboid-like, and we observe cell polarisation only in the later stages (Blatchley et al., 2019). On the other hand, persistence of motion, indicated to prevent cell clusterisation by PEC models of single-cell vasculogenesis (Tosin et al., 2006), was observed to be enhanced during amoeboid-like migration (Serini et al., 2003). It would therefore be interesting to investigate whether clusters would still form in this modelling framework with the inclusion of persistence of motion. In particular note that Tosin et al. (2006) included in their momentum equation a drag force generated by cells moving on the ECM and observed that lower cell-matrix adhesion resulted in cell clusterisation. We might thus expect ECM degradation to play a key role in lowering cell adhesiveness to the ECM in such modelling framework, thus leading to clusters.

### 6.2.4 Modelling the late-stages of cluster-based vasculogenesis

Future work should focus on the theoretical investigation of cluster-based vasculogenesis at later stages of this process, during which EPCs increase their interaction with the ECM and bridge clusters, forming the vascular network. In these stages the mechanical interaction between the cells and ECM becomes non-trivial and one might therefore consider a mechanochemical model similar to those previously proposed to study the late stages of single-cell vasculogenesis (Manoussaki, 2003; Murray, 2003; Tosin et al., 2006). Various works in the current literature already address the formation of sprouts from existing clusters (Boas et al., 2018; Merks et al., 2008; Szabo et al., 2008; Szabó and Czirók, 2010) and prior single-cell vasculogenesis models investigating the formation of a vascular network, rather than clusters, may still be relevant to these late stages. For instance, while

cell-to-cell adhesion may saturate chemotaxis (Merks et al., 2008), VEGF gradients may still be strongly perceived at the cluster boundaries. This is especially the case if ECM-bound VEGF was the main signalling molecule, and in this case we would indeed expect steep VEGF gradients to form at the cluster boundaries (Merks et al., 2006). Perhaps such a scenario can explain the change in cell morphology. The role cell elongation plays in the formation of a final well-defined network has already been extensively addressed by CP models of single-cell vasculogenesis (Boas et al., 2018; Merks et al., 2004, 2006; van Oers et al., 2014; Palm and Merks, 2013; Ramos et al., 2018; Scianna et al., 2013). Blatchley et al. (2019) indeed reported an elongated cell morphology during sprouting, as well as an increased mechanical interaction with the ECM. The combination of cell traction on the ECM and strain-dependent movement of cells would also suffice in explaining bridging between clusters (Ambrosi et al., 2005; Manoussaki, 2003; Murray, 2003; Namy et al., 2004). Nevertheless mechanochemical models, as well as CP models including cell traction (van Oers et al., 2014; Ramos et al., 2018), generally predict that higher ECM stiffness inhibits network formation, which is in contradiction with the experimental observations presented by Blatchley et al. (2019). Existing single-cell vasculogenesis models of late-stage dynamics, however, do not include ECM degradation, a key element for the study of cluster-based vasculogenesis. On the other hand, ECM degradation has been shown to have an important role during sprouting angiogenesis (Boas et al., 2018; Daub and Merks, 2013; Holmes and Sleeman, 2000; Scianna et al., 2013; Tranqui and Tracqui, 2000), a result which could very well translate into an active role in cluster-based vasculogenesis, although the interplay between ECM degradation and cell-ECM interactions may be particularly complex. Upon formulation of a mathematical model which accurately predicts cluster-based vascular network assembly, this could be used to investigate the determinants of network size and configuration. For instance, one might explore whether the size of clusters or cell-to-cell adhesion (Merks et al., 2008; Ramos et al., 2018) will affect tube diameters, or whether VEGF diffusion and decay rates determine cord length (Ambrosi et al., 2004, 2005; Gamba et al., 2003; Serini et al., 2003), and how these are affected by matrix stiffness.

**Modelling the ECM in mechanochemical models.** During tissue engineering *in vitro* studies different types of ECM scaffolds can be used, see Section 4.1.1. Given the complexity of cell-matrix interactions during many other developmental, physiological and pathological processes, the investigation of the role ECM stiffness plays in the different stages of cluster-based vasculogenesis may benefit from a more precise description of the ECM viscoelastic properties that might differ between *in vivo* and *in vitro* studies. In fact, we will see in Part IV that even simple changes in the ECM linear viscoelasticity assumptions can affect the pattern formation potential of classic mechanical models.

## **Part IV**

# **Modelling the extracellular matrix in mechanical pattern formation**

Mechanical and mechanochemical models of pattern formation in biological tissues have been used to study a variety of biomedical systems, particularly in developmental biology, and describe the physical interactions between cells and their local surroundings. These models, in their original form, consist of a balance equation for the cell density, a balance equation for the density of the extracellular matrix (ECM), and a force-balance equation describing the mechanical equilibrium of the cell-ECM system. Under the assumption that the cell-ECM system can be regarded as an isotropic linear viscoelastic material, the force-balance equation is often defined using the Kelvin-Voigt model of linear viscoelasticity to represent the stress-strain relation of the ECM. However, due to the multifaceted bio-physical nature of the ECM constituents, there are rheological aspects that cannot be effectively captured by this model and, therefore, depending on the pattern formation process and the type of tissue considered, other constitutive models of linear viscoelasticity may be better suited. Here, we systematically assess the pattern formation potential of different stress-strain constitutive equations for the ECM within a mechanical model of pattern formation in biological tissues. The results obtained through LSA and the dispersion relations derived therefrom support the idea that fluid-like constitutive models, such as the Maxwell model and the Jeffrey model, have a pattern formation potential much higher than solid-like models, such as the Kelvin-Voigt model and the standard linear solid model. This is confirmed by the results of numerical simulations, which demonstrate that, all else being equal, spatial patterns emerge in the case where the Maxwell model is used to represent the stress-strain relation of the ECM, while no patterns are observed when the Kelvin-Voigt model is employed. These findings suggest that further empirical work is required to acquire detailed quantitative information on the mechanical properties of components of the ECM in different biological tissues in order to furnish mechanical and mechanochemical models of pattern formation with stress-strain constitutive equations for the ECM that provide a more faithful representation of the underlying tissue rheology.

Part **IV** is organised as follows: in Chapter **7** background on mechanochemical models is presented, along with constitutive models of linear viscoelasticity and the rheological properties that they capture; in Chapter **8** a mechanical model of biological pattern formation is presented, along with its analytical and numerical results; in Chapter **9** the implications of this study are discussed, together with an overview of possible research perspectives.

The contents of Part **IV** are based on the paper [Villa et al. \(2021a\)](#).

# Chapter 7

## Background and linear viscoelasticity models

### 7.1 PDE models of pattern formation

Pattern formation resulting from spatial organisation of cells is at the basis of a broad spectrum of physiological and pathological processes in living tissues (Jernvall et al., 2003). While the first formal exploration of pattern and form from a mathematical (strictly speaking, geometrical) perspective goes back over a century to D'Arcy Thompson's "*On Growth and Form*" (Thompson, 1917), the modern development of mathematical models for this biological phenomenon started halfway through the twentieth century to elucidate the mechanisms that underlie morphogenesis and embryogenesis (Maini, 2005). Since then, a number of mathematical models for the formation of cellular patterns have been developed (Urdy, 2012). Amongst these, particular attention has been given to reaction-diffusion models and mechanochemical models of pattern formation (Murray, 2001).

#### 7.1.1 Reaction-diffusion models

Reaction-diffusion models of pattern formation, first proposed by Turing in his seminal 1952 paper (Turing, 1952) and then further developed by Gierer and Meinhardt (Gierer and Meinhardt, 1972; Meinhardt, 1982), apply to scenarios in which the heterogeneous spatial distribution of some chemicals (i.e. morphogens) acts as a template (i.e. a pre-pattern) according to which cells organise and arrange themselves in different sorts of spatial patterns. These models are formulated as coupled systems of reaction-diffusion equations for the spatiotemporal dynamics of the concentrations of two morphogens, with

different reaction kinetics depending on the biological problem at stake. Such systems exhibit diffusion-driven instability whereby homogeneous steady states are driven unstable by diffusion, resulting in the formation of pre-patterns, provided that the diffusion rate of one of the morphogens is sufficiently higher than the other (Maini et al., 1997; Maini and Woolley, 2019; Maini et al., 2012; Murray, 1981).

### 7.1.2 Mechanochemical models

On the other hand, mechanochemical models of pattern formation, first proposed by Murray, Oster and coauthors in the 1980s (Murray and Oster, 1984a,b; Murray et al., 1983; Oster et al., 1983), describe spatial organisation of cells driven by the mechanochemical interaction between cells and the ECM – i.e. the substratum composed of collagen fibers and various macromolecules, partly produced by the cells themselves, in which cells are embedded (Harris Jr, 1984; Harris et al., 1981). As introduced in Section 4.2.1 for mechanochemical models of vasculogenesis, these models in their original form consist of systems of PDEs comprising a balance equation for the cell density, a balance equation for the ECM density, and a force-balance equation describing the mechanical equilibrium of the cell-ECM system (Murray and Maini, 1989; Murray et al., 1988). When chemical processes are neglected, these models reduce to mechanical models of pattern formation (Byrne and Chaplain, 1996; Murray and Maini, 1989; Murray et al., 1988).

**The role of mechanical forces.** While reaction-diffusion models well explain the emergence and characteristics of patterns arising during chemical reactions (Castets et al., 1990; Maini et al., 1997; Maini and Woolley, 2019), as well as pigmentation patterns found on shells (Meinhardt, 2009) or animal coatings (Kondo and Asai, 1995; Murray, 2001), various observations seem to suggest they may not always be the most suited models to study morphogenic pattern formation (Bard and Lauder, 1974; Brinkmann et al., 2018; Maini and Woolley, 2019). For instance, experiments up to this day seem to fail in the identification of appropriate morphogens and overall molecular interactions predicted by Turing models in order for *de novo* patterns to emerge may be too complex. In addition, unrealistic parameter values would be required in order to reproduce experimentally observable patterns and the models appear to be too sensitive to parameter changes, hence lacking the robustness required to capture precise patterns. These considerations indicate that other mechanisms, driven for instance by significant mechanical forces, should be considered since solely chemical interactions may not suffice in explaining the emergence of patterns during morphogenesis. Hence mechanochemical models may be better suited. Interestingly, this need to change modelling framework sometimes arises within the same biological application as time progresses. For instance, supracellular organisation in the

early stages of embryonic development closely follows morphogenetic chemical patterns, but further tissue-level organisation requires additional cooperation of osmotic pressures and mechanical forces (Petrolli et al., 2019). Similarly, pattern formation during vasculogenesis is generally divided into an early stage highly driven by cell migration following chemical cues, and a later one dominated by mechanical interactions between the cells and the ECM (Ambrosi et al., 2005; Scianna et al., 2013; Tosin et al., 2006). Finally, purely mechanical models are a useful tool for studying the isolated role of mechanical forces and can capture observed phenomena without the inclusion of chemical cues (Petrolli et al., 2019; Serra-Picamal et al., 2012; Tlili et al., 2018).

**Applications of mechanochemical models.** Over the years, mechanochemical and mechanical models of pattern formation in biological tissues have been used to study a variety of biomedical problems, including morphogenesis and embryogenesis (Brinkmann et al., 2018; Cruywagen and Murray, 1992; Maini and Murray, 1988; Murray and Maini, 1986; Murray et al., 1988; Murray and Oster, 1984a,b; Murray et al., 1983; Oster et al., 1983; Perelson et al., 1986), angiogenesis and vasculogenesis (Manoussaki, 2003; Scianna et al., 2013; Tranqui and Tracqui, 2000), cytoskeleton reorganisation (Alonso et al., 2017; Lewis and Murray, 1991), wound healing and contraction (Javierre et al., 2009; Maini et al., 2002; Olsen et al., 1995; Tranquillo and Murray, 1992), and stretch marks (Gilmore et al., 2012). These models have also been used to estimate the values of cell mechanical parameters, with a particular focus on cell traction forces (Barocas et al., 1995; Barocas and Tranquillo, 1994; Bentil and Murray, 1991; Ferrenq et al., 1997; Moon and Tranquillo, 1993; Perelson et al., 1986). The roles that different biological processes play in the formation of cellular patterns can be disentangled via LSA of the homogeneous steady states of the model equations – i.e. investigating what parameters of the model, and thus what biological processes, can drive homogeneous steady states unstable and promote the emergence of cell spatial organisation. Further insight into certain aspects of pattern formation in biological tissues can also be provided by nonlinear stability analysis of the homogeneous steady states (Cruywagen and Murray, 1992; Lewis and Murray, 1991; Maini and Murray, 1988).

### 7.1.3 Linear viscoelasticity assumptions on the ECM

Mechanical and mechanochemical models usually rely on the assumption that the cell-ECM system can be regarded as an isotropic linear viscoelastic material. This is clearly a simplification due to the nonlinear viscoelasticity and anisotropy of soft tissues (Bischoff et al., 2004; Huang et al., 2005; Liu and Bilston, 2000; Nasseri et al., 2002; Snedeker et al., 2005; Valtorta and Mazza, 2005; Verdier, 2003), a simplification that various rheological

tests conducted on biological tissues have nonetheless shown to be justified in the regime of small strains (Bilston et al., 1997; Liu and Bilston, 2000; Nasseri et al., 2002; Valtorta and Mazza, 2005), which is the one usually of interest in the applications of such models. Under this assumption, the force-balance equation for the cell-ECM system is often defined using the Kelvin-Voigt model of linear viscoelasticity to represent the stress-strain relation of the ECM (Byrne and Chaplain, 1996; Murray et al., 1988; Oster et al., 1983). However, due to the multifaceted bio-physical nature of the ECM constituents, introduced in Section 4.1.1, there are rheological aspects that cannot be effectively captured by the Kelvin-Voigt model and, therefore, depending on the pattern formation process and the type of biological tissue considered, other constitutive models of linear viscoelasticity may be better suited (Barocas and Tranquillo, 1994). In this regard, Byrne and Chaplain (1996) demonstrated that, *ceteris paribus*, using the Maxwell model of linear viscoelasticity to describe the stress-strain relation of the ECM in place of the Kelvin-Voigt model can lead to different dispersion relations with a higher pattern formation potential. This suggests that a more thorough investigation of the capability of different stress-strain constitutive equations of producing spatial patterns is required.

## 7.2 Essentials of viscoelastic materials and stress-strain constitutive equations

The main properties of viscoelastic materials are summarised in Section 7.2.1. Then, the 1D stress-strain constitutive equations that are considered in Chapter 8 are briefly presented, together with the main rheological properties of linear viscoelastic materials that they capture, in Section 7.2.2. Finally, in Section 7.2.3 are reported the 2D constitutive equations used in Chapter 8. Most of the contents of this section can be found in standard textbooks, such as Findley et al. (1976) and Mase (1970), and are reported here for the sake of completeness. Further considerations of and applications to living tissues can be found in Fung (1993).

### 7.2.1 Essentials of viscoelastic materials

As the name suggests, viscoelastic materials exhibit both viscous and elastic characteristics, and the interplay between them may result in a wide range of rheological properties that can be examined through creep and stress relaxation tests. During a creep test, a constant stress is first applied to a specimen of material and then removed, and the time dynamic of the correspondent strain is tracked. During a stress relaxation test, a constant strain is imposed on a specimen of material and the evolution in time of the

induced stress is observed (Findley et al., 1976).

Here we list the main properties of viscoelastic materials that may be observed during the first phase of a creep test (see properties 1a-1c), during the recovery phase, that is, when the constant stress is removed from the specimen (see properties 2a-2c), and during a stress relaxation test (see property 3).

- 1a *Instantaneous elasticity.* As soon as a stress is applied, an instantaneous corresponding strain is observed.
- 1b *Delayed elasticity.* While the instantaneous elastic response to a stress is a purely elastic behaviour, due to the viscous nature of the material a delayed elastic response may also be observed. In this case, under constant stress the strain slowly and continuously increases at decreasing rate.
- 1c *Viscous flow.* In some viscoelastic materials, under a constant stress, the strain continues to grow within the viscoelastic regime (i.e. before plastic deformation). In particular, viscous flow occurs when the strain increases linearly with time and stops growing at removal of the stress only.
- 2a *Instantaneous recovery.* When the stress is removed, an instantaneous recovery (i.e. an instantaneous strain decrease) is observed because of the elastic nature of the material.
- 2b *Delayed recovery.* Upon removal of the stress, a delayed recovery (i.e. a continuous decrease of the strain at decreasing rate) occurs.
- 2c *Permanent set.* While elastic strain is reversible, in viscoelastic materials a non-zero strain, known as “permanent set” or “residual strain”, may persist even when the stress is removed.
- 3 *Stress relaxation.* Under constant strain, gradual relaxation of the induced stress occurs. In some cases, this may even culminate in total stress relaxation (i.e. the stress decays to zero).

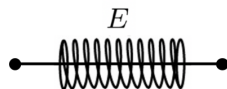
The subset of these properties exhibited by a viscoelastic material will depend on – and hence define – the type of material being tested. Moreover, during each phase of the creep test, more than one of the above properties may be observed. For instance, a Maxwell material under constant stress will exhibit instantaneous elasticity followed by viscous flow – see supplementary Figure A.3.

### 7.2.2 1D stress-strain constitutive equations

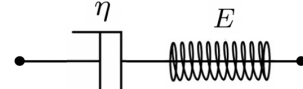
In this section, we briefly describe the different constitutive equations that are used in our study to represent the stress-strain relation of the ECM. In general, these equations can be used to predict how a viscoelastic material will react to different loading conditions,

in one spatial dimension, and rely on the assumption that viscous and elastic characteristics of the material can be modelled, respectively, via linear combinations of dashpots and springs, as illustrated in Figure 7.1. Different stress-strain constitutive equations correspond to different arrangements of these elements and capture different subsets of the rheological properties summarised in the previous section (see Table 7.2). Rules of derivation of the constitutive equations are detailed in Appendix A.5.1. In the remainder of this section, we will denote the stress and the strain at position  $x$  and time  $t$  by  $\sigma(t, x)$  and  $\varepsilon(t, x)$ , respectively.

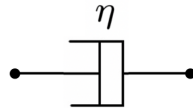
a) Linear elastic model



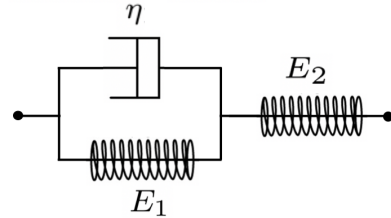
d) Maxwell model



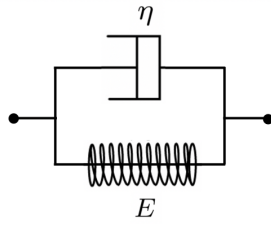
b) Linear viscous model



e) SLS model



c) Kelvin-Voigt model



f) Jeffrey model

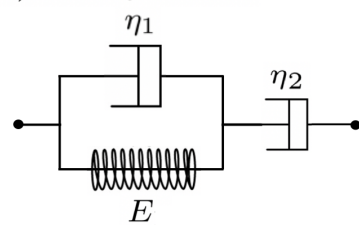


**Figure 7.1: Models of linear viscoelasticity considered in Chapter 8.** Combinations of elastic springs and viscous dampers, together with the associated elastic ( $E$ ,  $E_1$ ,  $E_2$ ) and viscous moduli ( $\eta$ ,  $\eta_1$ ,  $\eta_2$ ), for the models of linear viscoelasticity considered in Chapter 8: the linear elastic model (a), the linear viscous model (b), the Kelvin-Voigt model (c), the Maxwell model (d), the SLS model (e), and the Jeffrey model (f).

**Linear elastic model.** When viscous characteristics are neglected, a linear viscoelastic material can be modelled as a purely elastic spring with elastic modulus (i.e. Young's modulus)  $E > 0$ , as illustrated in Figure 7.1a. In this case, the stress-strain constitutive equation is given by Hooke's spring law for continuous media, that is,

$$\sigma = E\varepsilon. \quad (7.1)$$

**Linear viscous model.** When elastic characteristics are neglected, a linear viscoelastic material can be modelled as a purely viscous damper of viscosity  $\eta > 0$ , as illustrated in Figure 7.1b. In this case, the stress-strain constitutive equation is given by Newton's law of viscosity, that is,

$$\sigma = \eta \partial_t \varepsilon. \quad (7.2)$$

**Kelvin-Voigt model.** The Kelvin-Voigt model, also known as the Voigt model, relies on the assumption that viscous and elastic characteristics of a linear viscoelastic material can simultaneously be captured by considering a purely elastic spring with elastic modulus  $E > 0$  and a purely viscous damper of viscosity  $\eta > 0$  in parallel, as illustrated in Figure 7.1c. The corresponding stress-strain constitutive equation is

$$\sigma = E\varepsilon + \eta \partial_t \varepsilon. \quad (7.3)$$

**Maxwell model.** The Maxwell model relies on the assumption that viscous and elastic characteristics of a linear viscoelastic material can be captured by considering a purely elastic spring with elastic modulus  $E > 0$  and a purely viscous damper of viscosity  $\eta > 0$  in series, as illustrated in Figure 7.1d. The corresponding stress-strain constitutive equation is

$$\frac{1}{E} \partial_t \sigma + \frac{\sigma}{\eta} = \partial_t \varepsilon. \quad (7.4)$$

**Standard linear solid (SLS) model.** The SLS model, also known as the Kelvin model, relies on the assumption that viscous and elastic characteristics of a linear viscoelastic material can be captured by considering a Kelvin arm of elastic modulus  $E_1 > 0$  and viscosity  $\eta > 0$  in series with a purely elastic spring of elastic modulus  $E_2 > 0$ , as illustrated in Figure 7.1e. The corresponding stress-strain constitutive equation is (Mase, 1970)

$$\frac{1}{E_2} \partial_t \sigma + \frac{1}{\eta} \left( 1 + \frac{E_1}{E_2} \right) \sigma = \partial_t \varepsilon + \frac{E_1}{\eta} \varepsilon. \quad (7.5)$$

**Jeffrey model.** The Jeffrey model, also known as the Oldroyd-B or 3-parameter viscous model, relies on the assumption that viscous and elastic characteristics of a linear viscoelastic material can be captured by considering a Kelvin arm of elastic modulus  $E > 0$  and viscosity  $\eta_1 > 0$  in series with a purely viscous damper of viscosity  $\eta_2 > 0$ , as illustrated in Figure 7.1f. The corresponding stress-strain constitutive equation is

$$\left( 1 + \frac{\eta_1}{\eta_2} \right) \partial_t \sigma + \frac{E}{\eta_2} \sigma = \eta_1 \partial_{tt}^2 \varepsilon + E \partial_t \varepsilon. \quad (7.6)$$

**Generic 4-parameter model.** The following stress-strain constitutive equation encompasses all constitutive models of linear viscoelasticity whereby a combination of purely elastic springs and purely viscous dampers, up to a total of four elements, and therefore 4 parameters, is considered

$$a_2 \partial_{tt}^2 \sigma + a_1 \partial_t \sigma + a_0 \sigma = b_2 \partial_{tt}^2 \varepsilon + b_1 \partial_t \varepsilon + b_0 \varepsilon. \quad (7.7)$$

Here the non-negative, real parameters  $a_0, a_1, a_2, b_0, b_1, b_2$  depend on the elastic moduli and the viscosities of the underlying combinations of springs and dampers. For example, a Kelvin-Voigt arm (elasticity  $E_1 > 0$  and viscosity  $\eta_1 > 0$ ) and a Maxwell arm (elasticity  $E_2 > 0$  and viscosity  $\eta_2 > 0$ ) connected in series, representing what is known as the Burger's model, correspond to the constitutive equation

$$\frac{\eta_1 \eta_2}{E_1 E_2} \partial_{tt}^2 \sigma + \left( \frac{\eta_1}{E_1} + \frac{\eta_2}{E_1} + \frac{\eta_2}{E_2} \right) \partial_t \sigma + \sigma = \frac{\eta_1 \eta_2}{E_1} \partial_{tt}^2 \varepsilon + \eta_2 \partial_t \varepsilon.$$

When parameters  $a_0, a_1, a_2, b_0, b_1, b_2$  are defined as in Table 7.1, the generic 4-parameter constitutive model (7.7) reduces to the specific stress-strain constitutive equations (7.1)-(7.6). For convenience of notation, we define the differential operators

$$\mathcal{L}_a := a_2 \partial_{tt}^2 + a_1 \partial_t + a_0 \quad \text{and} \quad \mathcal{L}_b := b_2 \partial_{tt}^2 + b_1 \partial_t + b_0 \quad (7.8)$$

so that the stress-strain constitutive equation (7.7) can be rewritten in the following compact form

$$\mathcal{L}_a[\sigma] = \mathcal{L}_b[\varepsilon]. \quad (7.9)$$

A summary of the rheological properties of linear viscoelastic materials listed in Section 7.2.1 that are captured by the 1D stress-strain constitutive equations (7.1)-(7.6) is provided in Table 7.2. These properties can be examined through mathematical procedures that mimic creep and stress relaxation tests (Findley et al., 1976), of which examples for the Kevin-Voigt and Maxwell models can be found in Appendix A.6. Notice that, for all these constitutive models, instantaneous elasticity correlates with instantaneous recovery, delayed elasticity correlates with delayed recovery, and viscous flow correlates with permanent set. Materials are said to be more solid-like when their elastic response dominates their viscous response, and more fluid-like in the opposite case (Nargess and Yanlan, 2021). For this reason, models of linear viscoelasticity that capture viscous flow and, as a consequence, permanent set – such as the Maxwell model and the Jeffrey model – are classified as “fluid-like models”, while those which do not – such as the Kelvin-Voigt model and the SLS model – are classified as “solid-like models”. In the remainder of the paper we are going to include the linear viscous model in the fluid-like class and the linear elastic model in the solid-like class, as they capture – or do not capture – the relevant properties, even if they are not models of viscoelasticity *per se*.

**Table 7.1:** Relations between the generic 4-parameter model (7.7) and the stress-strain constitutive equations (7.1)-(7.6). \*Burger's model has been included for illustrative purposes (*cf.* Section 9.2.1).

Generic 4-parameters model	$a_2$	$a_1$	$a_0$	$b_2$	$b_1$	$b_0$
Linear elastic model	0	0	1	0	0	$E$
Linear viscous model	0	0	1	0	$\eta$	0
Kelvin-Voigt model	0	0	1	0	$\eta$	$E$
Maxwell model	0	$\frac{1}{E}$	$\frac{1}{\eta}$	0	1	0
SLS model	0	$\frac{1}{E_2}$	$\frac{1}{\eta} \left(1 + \frac{E_1}{E_2}\right)$	0	1	$\frac{E_1}{\eta}$
Jeffrey model	0	$1 + \frac{\eta_1}{\eta_2}$	$\frac{E}{\eta_2}$	$\eta_1$	$E$	0
Burger's model*	$\frac{\eta_1 \eta_2}{E_1 E_2}$	$\left(\frac{\eta_1}{E_1} + \frac{\eta_2}{E_1} + \frac{\eta_2}{E_2}\right)$	1	$\frac{\eta_1 \eta_2}{E_1}$	$\eta_2$	0

**Table 7.2:** Properties of linear viscoelastic materials captured by the stress-strain constitutive equations (7.1)-(7.6). \*Burger's model has been included for illustrative purposes (*cf.* Section 9.2.1). N.A.= not applicable (see Appendix A.6).

Model	Instantaneous elasticity	Delayed elasticity	Viscous flow	Instantaneous recovery	Delayed recovery	Permanent set	Stress relaxation
Linear elastic	✓			✓			
Linear viscous			✓			✓	N. A.
Kelvin-Voigt		✓			✓		
Maxwell	✓		✓	✓		✓	✓
SLS	✓	✓		✓	✓		✓
Jeffrey		✓	✓		✓	✓	✓
Burger's*	✓	✓	✓	✓	✓	✓	✓

### 7.2.3 2D stress-strain constitutive equations

Most of the study presented in Chapter 8 is conducted for the 1D case, but numerical simulations of a 2D model, making use of the Kelvin-Voigt or the Maxwell model of linear viscoelasticity for the ECM, are also considered. In analogy with equation (7.7), we consider the following generic 2D constitutive equation

$$a_1 \partial_t \boldsymbol{\sigma} + a_0 \boldsymbol{\sigma} = b_1 \partial_t \boldsymbol{\varepsilon} + b_0 \boldsymbol{\varepsilon} + c_1 \partial_t \theta \mathbf{I} + c_0 \theta \mathbf{I}. \quad (7.10)$$

This, together with the associated parameter choices reported in Table 7.3, summarises the 2D versions of the 1D Kelvin-Voigt (7.3) and the Maxwell model (7.4) used in Chapter 8, which are derived in Appendix A.5.2.

**Table 7.3:** Relations between the parameters in the generic 2D stress-strain constitutive equation (7.10) and those in the 2D constitutive equations for the Kelvin-Voigt model and the Maxwell model.

Generic 2D model	$\mathbf{a}_1$	$\mathbf{a}_0$	$\mathbf{b}_1$	$\mathbf{b}_0$	$\mathbf{c}_1$	$\mathbf{c}_0$
Kelvin-Voigt model	0	$\frac{1}{\eta}$	1	$\frac{E'}{\eta}$	$\nu'$	$\frac{E'\nu'}{\eta}$
Maxwell model	$\frac{1}{E'}$	$\frac{1}{\eta}$	1	0	$\nu'$	0

In (7.10),  $\boldsymbol{\sigma}(t, \mathbf{x})$  is the stress tensor, while the strain  $\boldsymbol{\varepsilon}(t, \mathbf{x})$  and the dilation  $\theta(t, \mathbf{x})$  are defined in terms of the displacement  $\mathbf{u}(t, \mathbf{x})$  as

$$\boldsymbol{\varepsilon} = \frac{1}{2}(\nabla \mathbf{u} + \nabla \mathbf{u}^\top) \quad \text{and} \quad \theta = \nabla \cdot \mathbf{u}. \quad (7.11)$$

Notice that both  $\boldsymbol{\varepsilon}$  and  $\theta$  reduce to  $\varepsilon = \partial_x u$  in the 1D case. Amongst the parameters in the stress-strain constitutive equation (7.10) reported in Table 7.3 for the 2D Kelvin-Voigt and Maxwell models,  $\eta > 0$  is the shear viscosity,

$$E' := \frac{E}{1 + \nu} \quad \text{and} \quad \nu' := \frac{\nu}{1 - 2\nu}, \quad (7.12)$$

where  $\nu > 0$  is Poisson's ratio and  $E > 0$  is Young's modulus. The 2D Maxwell model in the form (7.10) holds under the simplifying assumption that the quotient between the bulk viscosity and the shear viscosity of the ECM is equal to  $\nu'$  (see Appendix A.5.2). Note that the entries of Table 7.3 rely on this relation, which was assumed to hold for both the Maxwell and the Kelvin Voigt models in our baseline parameter set.

# Chapter 8

## The role of stress-strain constitutive equations in mechanical models of biological pattern formation

Following the problem introduced in Section 7.1.3, here we complement and further develop the results presented in Byrne and Chaplain (1996) by systematically assessing the pattern formation potential of different stress-strain constitutive equations for the ECM within a mechanical model of pattern formation in biological tissues (Byrne and Chaplain, 1996; Murray et al., 1988; Oster et al., 1983). Compared to the work of Byrne and Chaplain (1996) here we consider a wider range of constitutive models, presented in Section 7.2.1, we allow cell traction forces to be reduced by cell-cell contact inhibition, and undertake numerical simulations of the model equations showing the formation of cellular patterns both in 1D and 2D. A related study has been conducted by Alonso et al. (2017), who considered a mathematical model of pattern formation in the cell cytoplasm. The chapter is structured as follows. In Section 8.1, we describe the 1D mechanical model of pattern formation in biological tissues that is used in this study, which follows closely the one considered in Byrne and Chaplain (1996); Murray et al. (1988); Oster et al. (1983), and briefly introduce the corresponding 2D model. In Section 8.2, we carry out a LSA of a biologically relevant homogeneous steady state of the 1D model equations, derive dispersion relations when different stress-strain constitutive equations for the ECM are used, and investigate how the model parameters affect the dispersion relations obtained. In Section 8.3, we verify key results of LSA via numerical simulations of the 1D model equations, complementing these findings with the results of numerical simulations of the 2D version of the mechanical model of pattern formation considered.

## 8.1 A mathematical model of mechanical pattern formation

We consider a 1D region of tissue and represent the normalised densities of cells and ECM at time  $t \geq 0$  and position  $x \in [\ell, L]$  by means of the non-negative functions  $n(t, x)$  and  $\rho(t, x)$ , respectively. We let  $u(t, x)$  model the displacement of a material point of the cell-ECM system originally at position  $x$ , which is induced by mechanical interactions between cells and the ECM – i.e. cells pull on the ECM in which they are embedded, thus inducing ECM compression and densification which in turn cause a passive form of cell repositioning (Van Helvert et al., 2018). In Section 8.1.5, the extension of this modelling framework to the 2D case is addressed.

### 8.1.1 Dynamics of the cells

Following Murray et al. (1988); Oster et al. (1983), we consider a scenario where cells change their position according to a combination of: (i) undirected, random movement, which we describe through Fick’s first law of diffusion with diffusivity (i.e. cell motility)  $D \geq 0$ ; (ii) haptotaxis (i.e. cell movement up the density gradient of the ECM) with haptotactic sensitivity  $\alpha \geq 0$ ; (iii) passive repositioning caused by mechanical interactions between cells and the ECM, which is modelled as an advection with velocity field  $\partial_t u$ . Moreover, we model variation of the normalised cell density caused by cell proliferation and death via logistic growth with intrinsic growth rate  $r \geq 0$  and unitary local carrying capacity. Under these assumptions, we describe cell dynamics through the following balance equation for  $n(t, x)$

$$\partial_t n = \partial_x [D \partial_x n - n (\alpha \partial_x \rho + \partial_t u)] + r n(1 - n) \quad (8.1)$$

subject to suitable initial and boundary conditions.

### 8.1.2 Dynamics of the ECM

As was done for the cell dynamics, in a similar manner we model compression and densification of the ECM induced by cell-ECM interactions as an advection with velocity field  $\partial_t u$ . Furthermore, as in Murray et al. (1988) and Oster et al. (1983), we neglect secretion of ECM components by the cells since this process occurs on a slower time scale compared to mechanical interactions between cells and the ECM. Under these assumptions,

we describe the cell dynamics through the following transport equation for  $\rho(t, x)$

$$\partial_t \rho = -\partial_x (\rho \partial_t u) \quad (8.2)$$

subject to suitable initial and boundary conditions.

### 8.1.3 Force-balance equation for the cell-ECM system

Following Murray et al. (1988); Oster et al. (1983), we represent the cell-ECM system as a linear viscoelastic material with low Reynolds number (i.e. inertial terms are negligible compared to viscous terms) and we assume the cell-ECM system to be in mechanical equilibrium (i.e. traction forces generated by the cells are in mechanical equilibrium with viscoelastic restoring forces developed in the ECM and any other external forces). Under these assumptions, the force-balance equation for the cell-ECM system is of the form

$$\partial_x (\sigma_c + \sigma_m) + \rho F = 0, \quad (8.3)$$

where  $\sigma_m(t, x)$  is the contribution to the stress of the cell-ECM system coming from the ECM,  $\sigma_c(t, x)$  is the contribution to the stress of the cell-ECM system coming from the cells, and  $F(t, x)$  is the external force per unit matrix density, which comes from the surrounding tissue that constitutes the underlying substratum to which the ECM is attached.

The stress  $\sigma_c$  is related to cellular traction forces acting on the ECM and is defined as

$$\sigma_c := \tau f(n) n (\rho + \beta \partial_{xx}^2 \rho) \quad \text{with} \quad f(n) := \frac{1}{1 + \lambda n^2}. \quad (8.4)$$

Definition (8.4) relies on the assumption that the stress generated by cell traction on the ECM is proportional to the cell density  $n$  and – in the short range – the ECM density  $\rho$ , while the term  $\beta \partial_{xx}^2 \rho$  accounts for long-range cell traction effects, with  $\beta > 0$  being the long-range traction proportionality constant. The factor of proportionality is given by a parameter  $\tau \geq 0$ , which measures the average traction force generated by a cell, multiplied by a non-negative and monotonically decreasing function of the cell density,  $f(n)$ , which models the fact that the average traction force generated by a cell is reduced by cell-cell contact inhibition (Murray, 2001). The parameter  $\lambda \geq 0$  measures the level of cell traction force inhibition and assuming  $\lambda = 0$  corresponds to neglecting the reduction in the cell traction forces caused by cellular crowding.

The stress  $\sigma_m$  is given by the stress-strain constitutive equation that is used for the ECM, which we choose to be the general constitutive model (7.9) with the strain  $\varepsilon(t, x)$  being given by the gradient of the displacement  $u(t, x)$ , that is,  $\varepsilon = \partial_x u$ . Therefore, we define

the stress-strain relation of the ECM via the following equation

$$\mathcal{L}_a[\sigma_m] = \mathcal{L}_b[\partial_x u], \quad (8.5)$$

where the differential operators  $\mathcal{L}_a$  and  $\mathcal{L}_b$  are defined according to (7.8).

Assuming the surrounding tissue to which the ECM is attached to be a linear elastic material (Murray, 2001), the external body force  $F$  can be modelled as a restoring force proportional to the cell-ECM displacement, that is,

$$F := -s u. \quad (8.6)$$

Here the parameter  $s \geq 0$  represents the elastic modulus of the surrounding tissue.

In order to obtain a closed equation for the displacement  $u(t, x)$ , we apply the differential operator  $\mathcal{L}_a[\cdot]$  to the force-balance equation (8.3) and then substitute (8.4)-(8.6) into the resulting equation. In so doing, we find

$$\begin{aligned} \mathcal{L}_a[\partial_x(\sigma_m + \sigma_c)] &= -\mathcal{L}_a[\rho F] \\ \Leftrightarrow \mathcal{L}_a[\partial_x \sigma_m] + \mathcal{L}_a[\partial_x \sigma_c] &= \mathcal{L}_a[s\rho u] \\ \Leftrightarrow \partial_x \mathcal{L}_a[\sigma_m] &= \mathcal{L}_a[s\rho u] - \mathcal{L}_a[\partial_x \sigma_c] \\ \Leftrightarrow \partial_x \mathcal{L}_b[\partial_x u] &= \mathcal{L}_a[s\rho u - \partial_x \sigma_c] \\ \Leftrightarrow \mathcal{L}_b[\partial_{xx} u] &= \mathcal{L}_a[s\rho u - \partial_x \sigma_c], \end{aligned}$$

that is,

$$\mathcal{L}_b[\partial_{xx} u] = \mathcal{L}_a \left[ s\rho u - \partial_x \left( \frac{\tau n}{1 + \lambda n^2} (\rho + \beta \partial_{xx} \rho) \right) \right]. \quad (8.7)$$

Finally, to close the system, equation (8.7) needs to be supplied with suitable initial and boundary conditions.

#### 8.1.4 Boundary conditions

We close our mechanical model of pattern formation defined by the system of PDEs (8.1), (8.2) and (8.7) with the following boundary conditions

$$\left\{ \begin{array}{l} n(t, \ell) = n(t, L), \quad \partial_x n(t, \ell) = \partial_x n(t, L), \\ \rho(t, \ell) = \rho(t, L), \quad \partial_{xx} \rho(t, \ell) = \partial_{xx} \rho(t, L), \quad \forall t \geq 0. \\ u(t, \ell) = u(t, L), \quad \partial_x u(t, \ell) = \partial_x u(t, L), \end{array} \right. \quad (8.8)$$

Here, the conditions on the derivatives of  $n$ ,  $\rho$  and  $u$  ensure that the fluxes in equations (8.1) and (8.2), and the overall stress  $(\sigma_m + \sigma_c)$  in equation (8.3), are periodic on the boundary, i.e. they ensure that

$$\left\{ \begin{array}{l} [D \partial_x n - n (\alpha \partial_x \rho + \partial_t u)]_{x=\ell} = [D \partial_x n - n (\alpha \partial_x \rho + \partial_t u)]_{x=L}, \\ [n \partial_t u]_{x=\ell} = [n \partial_t u]_{x=L}, \\ \left[ \tau \frac{n}{(1+\lambda^2)} (\rho + \beta \partial_{xx}^2 \rho) + \sigma_m \right]_{x=\ell} = \left[ \tau \frac{n}{(1+\lambda^2)} (\rho + \beta \partial_{xx}^2 \rho) + \sigma_m \right]_{x=L}, \end{array} \right. \quad \forall t \geq 0,$$

with  $\sigma_m$  given as a function of  $\partial_x u$  in equation (8.5), according to the selected constitutive model. The periodic boundary conditions (8.8) reproduce a biological scenario in which the spatial region considered is part of a larger area of tissue whereby similar dynamics of the cells and the ECM occur.

### 8.1.5 Extension to 2D

The mechanical model of pattern formation defined by the system of PDEs (8.1), (8.2) and (8.3) posed on a 2D spatial domain represented by a bounded set  $\Omega \subset \mathbb{R}^2$  with smooth boundary  $\partial\Omega$  reads as

$$\left\{ \begin{array}{l} \partial_t n = \operatorname{div} [D \nabla n - n (\alpha \nabla \rho + \partial_t \mathbf{u})] + r n (1 - n), \\ \partial_t \rho = -\operatorname{div}(\rho \partial_t \mathbf{u}), \\ \operatorname{div}(\boldsymbol{\sigma}_m + \boldsymbol{\sigma}_c) + \rho \mathbf{F} = 0, \end{array} \right. \quad (8.9)$$

with  $t \geq 0$ ,  $\mathbf{x} = (x_1, x_2)^\top \in \Omega$  and  $\mathbf{u} = (u_1, u_2)^\top$ . We close the system of PDEs (8.9) imposing the 2D version of the periodic boundary conditions (8.8) on  $\partial\Omega$ . Furthermore, we use the following 2D analogues of definitions (8.4) and (8.6)

$$\boldsymbol{\sigma}_c := \frac{\tau n}{1 + \lambda n^2} (\rho + \beta \Delta \rho) \mathbf{I} \quad \text{and} \quad \mathbf{F} := -s \mathbf{u}, \quad (8.10)$$

where  $\mathbf{I}$  is the identity tensor. Moreover, in analogy with the 1D case, we define the stress tensor  $\boldsymbol{\sigma}_m$  via the 2D constitutive model (7.10), together with the parameter choices reported in Table 7.3 for the Kelvin-Voigt and Maxwell models, that is used to represent the stress-strain relation of the ECM. As introduced in Section 7.2.3, the strain  $\boldsymbol{\varepsilon}(t, \mathbf{x})$  and the dilation  $\theta(t, \mathbf{x})$  are defined in terms of the displacement  $\mathbf{u}(t, \mathbf{x})$  according to (7.11).

## 8.2 Linear stability analysis and dispersion relations

In this section, we carry out LSA of a biologically relevant homogeneous steady state of the 1D system of PDEs (8.1), (8.2) and (8.7) in Section 8.2.1, and we compare the dispersion relations obtained when the constitutive models (7.1)-(7.6) are alternatively used to represent the contribution to the overall stress coming from the ECM, in order to explore the pattern formation potential of these stress-strain constitutive equations in Section 8.2.2.

### 8.2.1 Linear stability analysis

**Biologically relevant homogeneous steady state.** All non-trivial homogeneous steady states  $(\bar{n}, \bar{\rho}, \bar{u})^\top$  of the system of PDEs (8.1), (8.2) and (8.7) subject to boundary conditions (8.8) have components  $\bar{n} \equiv 1$  and  $\bar{u} \equiv 0$ , and we consider the arbitrary non-trivial steady state  $\bar{\rho} \equiv \rho_0 > 0$  amongst the infinite number of possible homogeneous steady states of the transport equation (8.2) for the normalised ECM density  $\rho$ . Hence, we focus our attention on the biologically relevant homogeneous steady state  $\bar{\mathbf{v}} = (1, \rho_0, 0)^\top$ .

**Linear stability under spatially homogeneous perturbations.** Similarly to as done in Section 5.2, in order to investigate the linear stability of the steady state  $\bar{\mathbf{v}} = (1, \rho_0, 0)^\top$  under spatially homogeneous perturbations, we make the ansatz  $\mathbf{v}(t, x) \equiv \bar{\mathbf{v}} + \tilde{\mathbf{v}}(t)$ , where the vector  $\tilde{\mathbf{v}}(t) = (\tilde{n}(t), \tilde{\rho}(t), \tilde{u}(t))^\top$  models small spatially homogeneous perturbations, and linearise the system of PDEs (8.1), (8.2) and (8.7) about the steady state  $\bar{\mathbf{v}}$ . Assuming  $\tilde{n}(t)$ ,  $\tilde{\rho}(t)$  and  $\tilde{u}(t)$  to be proportional to  $\exp(\psi t)$ , one can easily verify that  $\psi$  satisfies the algebraic equation  $\psi(\psi + r)(\psi^2 a_2 + \psi a_1 + a_0) = 0$ . Since  $r$  is positive and the parameters  $a_0$ ,  $a_1$  and  $a_2$  are all non-negative, the solution  $\psi$  of such an algebraic equation is either negative, for which the small perturbations  $\tilde{n}(t)$ ,  $\tilde{\rho}(t)$  and  $\tilde{u}(t)$  will decay to zero as  $t \rightarrow \infty$ , or  $\psi = 0$ . However, the zero eigenvalue here does not correlate with instability: small spatially homogeneous perturbations in  $\rho$  simply correspond to a different, nearby, steady states and thus will not grow in time, while small spatially homogeneous perturbations in  $n$  or  $u$  will decay in time (*cf.* spatially homogeneous version of equations (8.1) and (8.7)). This is the case for any choice of the parameter  $a_0$ ,  $a_1$ ,  $a_2$ ,  $b_0$ ,  $b_1$  and  $b_2$  in the stress-strain constitutive equation (8.5) (i.e. for all constitutive models (7.1)-(7.6)).

**Linear instability under spatially inhomogeneous perturbations.** Similarly, in order to investigate conditions under which the steady state  $\bar{\mathbf{v}} = (1, \rho_0, 0)^\top$  is unstable un-

der small spatially inhomogeneous perturbations, we make the ansatz  $\mathbf{v}(t, x) = \bar{\mathbf{v}} + \tilde{\mathbf{v}}(t, x)$ , where the vector  $\tilde{\mathbf{v}}(t, x) = (\tilde{n}(t, x), \tilde{\rho}(t, x), \tilde{u}(t, x))^\top$  models small spatially inhomogeneous perturbations, and linearise the system of PDEs (8.1), (8.2) and (8.7) about the steady state  $\bar{\mathbf{v}}$ . Assuming  $\tilde{n}(t, x)$ ,  $\tilde{\rho}(t, x)$  and  $\tilde{u}(t, x)$  to be proportional to  $\exp(\psi t + ikx)$ , we find that  $\psi$  satisfies the following equation

$$\psi \left[ c_3(k^2)\psi^3 + c_2(k^2)\psi^2 + c_1(k^2)\psi + c_0(k^2) \right] = 0, \quad (8.11)$$

with

$$c_3(k^2) := a_2\tau\lambda_1\beta k^4 + [b_2 - a_2\tau(\lambda_1 + \lambda_2\rho_0)]k^2 + a_2s\rho_0 \quad (8.12)$$

$$\begin{aligned} c_2(k^2) &:= a_2\tau\lambda_1D\beta k^6 + [b_2D - a_2\tau(\lambda_2\rho_0\alpha + D\lambda_1 - r\lambda_1\beta) + a_1\tau\lambda_1\beta]k^4 \\ &\quad + [b_2r + b_1 + a_2(Ds\rho_0 - r\tau\lambda_1) - a_1\tau(\lambda_1 + \lambda_2\rho_0)]k^2 + (a_1 + a_2r)s\rho_0 \end{aligned} \quad (8.13)$$

$$\begin{aligned} c_1(k^2) &:= a_1\tau\lambda_1D\beta k^6 + [b_1D - a_1\tau(\lambda_2\rho_0\alpha + D\lambda_1 - r\lambda_1\beta) + a_0\tau\lambda_1\beta]k^4 \\ &\quad + [b_1r + b_0 + a_1(Ds\rho_0 - r\tau\lambda_1) - a_0\tau(\lambda_1 + \lambda_2\rho_0)]k^2 + (a_0 + a_1r)s\rho_0 \end{aligned} \quad (8.14)$$

and

$$\begin{aligned} c_0(k^2) &:= a_0\tau\lambda_1D\beta k^6 + [b_0D - a_0\tau(\lambda_2\rho_0\alpha + D\lambda_1 - r\lambda_1\beta)]k^4 \\ &\quad + [b_0r + a_0(Ds\rho_0 - r\tau\lambda_1)]k^2 + a_0rs\rho_0 \end{aligned} \quad (8.15)$$

where

$$\lambda_1 := \frac{1}{1+\lambda} \quad \text{and} \quad \lambda_2 := \frac{(1-\lambda)}{(1+\lambda)^2}.$$

Equation (8.11) has multiple solutions  $\psi(k^2)$  for each  $k^2$ , including  $\psi = 0$  which we ignore henceforth in order to focus on positive solutions, and we denote by  $\text{Re}(\cdot)$  the maximum real part of all these solutions. For cell patterns to emerge, we need the non-trivial homogeneous steady state  $\bar{\mathbf{v}}$  to be unstable under spatially inhomogeneous perturbations, that is, we need  $\text{Re}(\psi(k^2)) > 0$  for some  $k^2 > 0$ . Notice that a necessary condition for this to happen is that at least one amongst  $c_0(k^2)$ ,  $c_1(k^2)$ ,  $c_2(k^2)$  and  $c_3(k^2)$  is negative for some  $k^2 > 0$ . Hence, the fact that if  $\tau = 0$  then  $c_0(k^2)$ ,  $c_1(k^2)$ ,  $c_2(k^2)$  and  $c_3(k^2)$  are all non-negative for any value of  $k^2$  allows us to conclude that having  $\tau > 0$  is a necessary condition for pattern formation to occur. This was expected based on the results presented in Murray (2001) and references therein.

In the case where the model parameters are such that  $c_2(k^2) = 0$  and  $c_3(k^2) = 0$ , solving equation (8.11) for  $\psi$  gives the following dispersion relation

$$\psi(k^2) = -\frac{c_0(k^2)}{c_1(k^2)}. \quad (8.16)$$

On the other hand, when the model parameters are such that only  $c_3(k^2) = 0$ , from

equation (8.11) we obtain the following dispersion relations

$$\psi(k^2) = \frac{-c_1(k^2) \pm \sqrt{(c_1(k^2))^2 - 4c_2(k^2)c_0(k^2)}}{2c_2(k^2)}. \quad (8.17)$$

Finally, in the general case where the model parameters are such that  $c_3(k^2) \neq 0$  as well, from equation (8.11) we obtain the following dispersion relation

$$\psi(k^2) = \left\{ q + \left[ q^2 + (m - p^2)^3 \right]^{1/2} \right\}^{1/3} + \left\{ q - \left[ q^2 + (m - p^2)^3 \right]^{1/2} \right\}^{1/3} + p, \quad (8.18)$$

where  $p \equiv p(k^2)$ ,  $q \equiv q(k^2)$  and  $m \equiv m(k^2)$  are defined as

$$p := -\frac{c_2}{3c_3}, \quad q := p^3 + \frac{c_2c_1 - 3c_3c_0}{6c_3^2}, \quad m := \frac{c_1}{3c_3}. \quad (8.19)$$

## 8.2.2 Dispersion relations

Substituting the definitions of  $a_0$ ,  $a_1$ ,  $a_2$ ,  $b_0$ ,  $b_1$  and  $b_2$  corresponding to the stress-strain constitutive equations (7.1)-(7.6), which are reported in Table 7.1, into definitions (8.12)-(8.15) for  $c_0(k^2)$ ,  $c_1(k^2)$ ,  $c_2(k^2)$  and  $c_3(k^2)$ , and then using the dispersion relation given by formula (8.16), (8.17) or (8.18)-(8.19) depending on the values of  $c_2(k^2)$  and  $c_3(k^2)$  so obtained, we derive the dispersion relation for each of the constitutive models (7.1)-(7.6). In particular, we are interested in whether the real part of each dispersion relation is positive, so whenever multiple roots are calculated – for instance using (8.17) – the largest root is considered. In addition, dispersion relations throughout this section are plotted against the quantity  $k/\pi$ , which directly correlates with perturbation modes and can therefore better highlight mode selection during the parametric analysis.

**Base-case dispersion relations.** Figure 8.1 displays the dispersion relations obtained for the stress-strain constitutive equations (7.1)-(7.6) under the following base-case parameter values

$$E = 1, \quad E_1 = E_2 = \frac{1}{2}E = 0.5, \quad \eta = 1, \quad \eta_1 = \eta_2 = \frac{1}{2}\eta = 0.5, \quad D = 0.01, \quad (8.20)$$

$$\rho_0 = 1, \quad \alpha = 0.05, \quad r = 1, \quad s = 10, \quad \lambda = 0.5, \quad \tau = 0.2, \quad \beta = 0.005. \quad (8.21)$$

The parameter values given by (8.20) and (8.21) are chosen for illustrative purposes, in order to highlight the different qualitative behaviour of the dispersion relations obtained using different models, and are comparable with nondimensional parameter values that can be found in the extant literature (see Appendix C.3 for further details). A comparison between the plots in Figure 8.1 reveals that fluid-like models, that is, the linear viscous

model (7.2), the Maxwell model (7.4) and the Jeffrey model (7.6) (*cf.* Table 7.2), have a higher pattern formation potential than solid-like models, since under the same parameter set they exhibit a range – or, more precisely, they exhibit the same range – of unstable modes (i.e.  $\text{Re}(\psi(k^2)) > 0$  for a range of values of  $k/\pi$ ), while the others have no unstable modes.

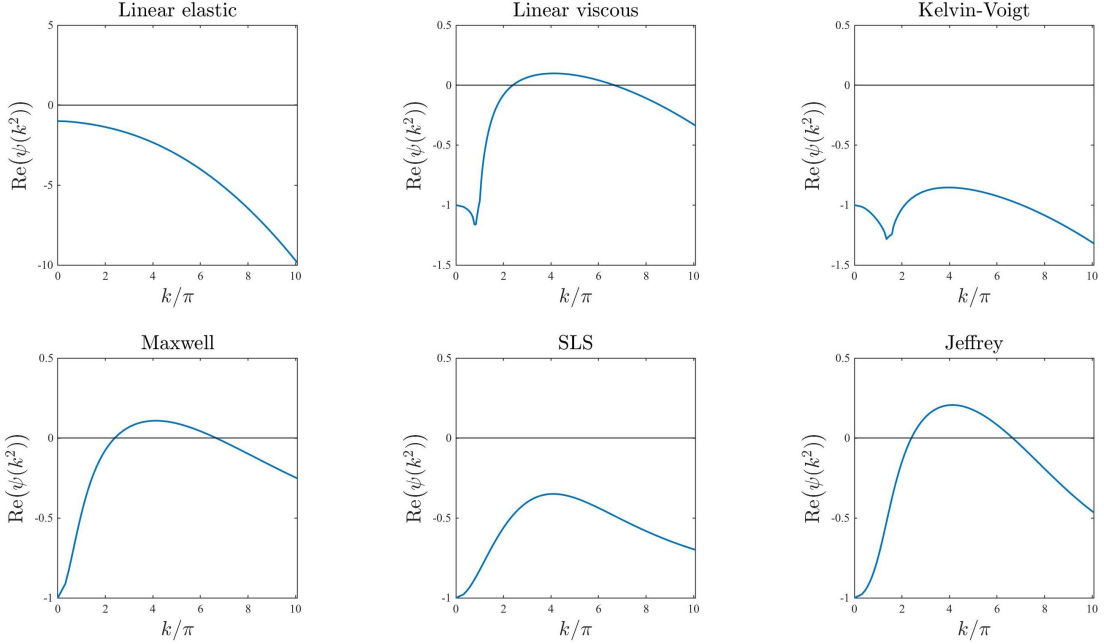


**Figure 8.1: Base-case dispersion relations.** Dispersion relations corresponding to the stress-strain constitutive equations (7.1)–(7.6) for the base-case set of parameter values given by (8.20) and (8.21).

We now undertake a parametric analysis with respect to the different model parameters and discuss key changes that occur in the base-case dispersion relations displayed in Figure 8.1.

**ECM elasticity.** The plots in Figure 8.2 illustrate how the base-case dispersion relations displayed in Figure 8.1 change when different values of the parameter  $E$ , and therefore also  $E_1$  and  $E_2$  (i.e. the parameters modelling ECM elasticity), are considered. These plots show that lower values of these parameters correlate with overall larger values of  $\text{Re}(\psi(k^2))$  for all constitutive models, except for the linear viscous one, which corresponds to speeding up the formation of spatial patterns, when these may form. In addition, sufficiently small values of the parameters  $E$ ,  $E_1$  and  $E_2$  allow the linear elastic model (7.1), the Kelvin-Voigt model (7.3), and the SLS model (7.5) to exhibit unstable modes. However, further lowering the values of these parameters appears to lead to singular dispersion relations (*cf.* the plots for the linear elastic model (7.1), the Maxwell

model (7.4) and the SLS model (7.5) in Figure 8.2), which suggests that linear stability theory may fail in the regime of low ECM elasticity.

**ECM viscosity.** The plots in Figure 8.3 illustrate how the base-case dispersion relations displayed in Figure 8.1 change when different values of the parameter  $\eta$ , and therefore also  $\eta_1$  and  $\eta_2$  (i.e. the parameters modelling ECM viscosity), are considered. These plots show that larger values of these parameters leave the range of modes for which  $\text{Re}(\psi(k^2)) > 0$  unchanged but reduce the values of  $\text{Re}(\psi(k^2))$ . This supports the idea that a higher ECM viscosity may not change the pattern formation potential of the different constitutive models but may slow down the corresponding pattern formation processes.

**Cell motility.** The plots in Figure 8.4 illustrate how the base-case dispersion relations displayed in Figure 8.1 change when different values of the parameter  $D$  (i.e. the parameter modelling cell motility) are considered. These plots show that larger values of this parameter may significantly shrink the range of modes for which  $\text{Re}(\psi(k^2)) > 0$ . In particular, with the exception of the linear elastic model, all constitutive models exhibit: infinitely many unstable modes when  $D \rightarrow 0$ ; a finite number of unstable modes for intermediate values of  $D$ ; no unstable modes for sufficiently large values of  $D$ . This is to be expected due to the stabilising effect of undirected, random cell movement and indicates that higher cell motility may correspond to lower pattern formation potential.

**Intrinsic growth rate of the cell density and elasticity of the surrounding tissue.** The plots in Figures 8.5 and 8.6 illustrate how the base-case dispersion relations displayed in Figure 8.1 change when different values of the parameter  $r$  (i.e. the intrinsic growth rate of the cell density) and the parameter  $s$  (i.e. the elasticity of the surrounding tissue) are, respectively, considered. These plots show that considering larger values of these parameters reduces the values of  $\text{Re}(\psi(k^2))$  for all constitutive models, and in particular it shrinks the range of unstable modes for the linear viscous model (7.2), the Maxwell model (7.4) and the Jeffrey model (7.6), which can become stable for values of  $r$  or  $s$  sufficiently large. This supports the idea that higher growth rates of the cell density (i.e. faster cell proliferation and death), and higher substrate elasticity (i.e. stronger external tethering force) may slow down pattern formation processes and overall reduce the pattern formation potential for all constitutive models. Moreover, the plots in Figure 8.6 indicate that higher values of  $s$  may in particular reduce the pattern formation potential of the different constitutive models by making it more likely that  $\text{Re}(\psi(k^2)) < 0$  for smaller values of  $k/\pi$  (i.e. low-frequency perturbation modes will be more likely to vanish).

**Level of contact inhibition of the cell traction forces and long-range cell traction forces.** The plots in Figures 8.7 and 8.8 illustrate how the base-case dispersion relations displayed in Figure 8.1 change when different values of the parameter  $\lambda$  (i.e. the level of cell-cell contact inhibition of the cell traction forces) and the parameter  $\beta$  (i.e. the long-range cell traction forces) are, respectively, considered. Considerations similar to those previously made about the dispersion relations obtained for increasing values of the parameters  $r$  and  $s$  apply to the case where increasing values of the parameter  $\lambda$  and the parameter  $\beta$  are considered. In addition to these considerations, the plots in Figures 8.7 and 8.8 indicate that for small enough values of  $\lambda$  or  $\beta$  the SLS model (7.5) can exhibit unstable modes, which further suggests that weaker contact inhibition of cell traction forces and lower long-range cell traction forces foster pattern formation. Moreover, the plots in Figure 8.8 indicate that in the asymptotic regime  $\beta \rightarrow 0$  we may observe infinitely many unstable modes (i.e.  $\text{Re}(\psi(k^2)) > 0$  for arbitrarily large wavenumbers), exiting the regime of physically meaningful pattern forming instabilities (Moreo et al., 2010; Perelson et al., 1986).

**Cell haptotactic sensitivity and cell traction forces.** The plots in Figures 8.9 and 8.10 illustrate how the base-case dispersion relations displayed in Figure 8.1 change when different values of the parameter  $\alpha$  (i.e. the cell haptotactic sensitivity) and the parameter  $\tau$  (i.e. the cell traction force) are, respectively, considered. As expected (Murphy, 2001), larger values of these parameters overall increase the value of  $\text{Re}(\psi(k^2))$  and broaden the range of modes for which  $\text{Re}(\psi(k^2)) > 0$ , so that for large enough values of these parameters the linear viscous model (7.2), the Kelvin-Voigt model (7.3) and the SLS model (7.5) can exhibit unstable modes. However, sufficiently large values of  $\tau$  appear to lead to singular dispersion relations (*cf.* the plots for the linear elastic model (7.1), the Maxwell model (7.4) and the SLS model (7.5) in Figure 8.10), which suggests that linear stability theory may fail in the regime of high cell traction for certain constitutive models, as previously observed in (Byrne and Chaplain, 1996).

**Initial ECM density.** The plots in Figure 8.11 illustrate how the base-case dispersion relations displayed in Figure 8.1 change when different values of the parameter  $\rho_0$  (i.e. the initial ECM density) are considered. Considerations similar to those previously made about the dispersion relations obtained for increasing values of the parameter  $\alpha$  apply to the case where increasing values of the parameter  $\rho_0$  are considered. In addition to these considerations, the plots in Figure 8.11 indicate that smaller values of the parameter  $\rho_0$ , specifically  $\rho_0 < 1$ , correlate with a shift in mode selection toward lower modes (*cf.* the plots for the linear viscous model (7.2), the Maxwell model (7.4) and the Jeffrey model (7.6) in Figure 8.11).

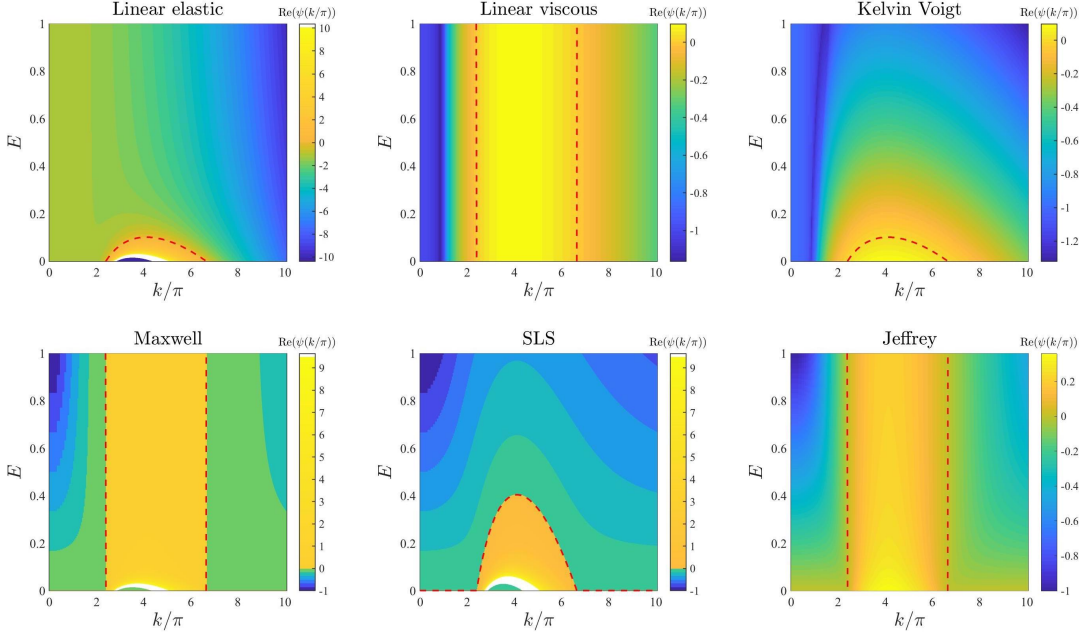


**Figure 8.2: Effects of varying the ECM elasticity.** Dispersion relations corresponding to the stress-strain constitutive equations (7.1)-(7.6) for increasing values of the ECM elasticity, that is for  $E \in [0, 1]$ . The values of the other parameters are given by (8.20) and (8.21). White regions in the plots related to the linear elastic model, the Maxwell model and the SLS model correspond to  $\text{Re}(\psi(k^2)) > 10$  (i.e. a vertical asymptote is present in the dispersion relation). Red dashed lines mark contour lines where  $\text{Re}(\psi(k^2)) = 0$ .

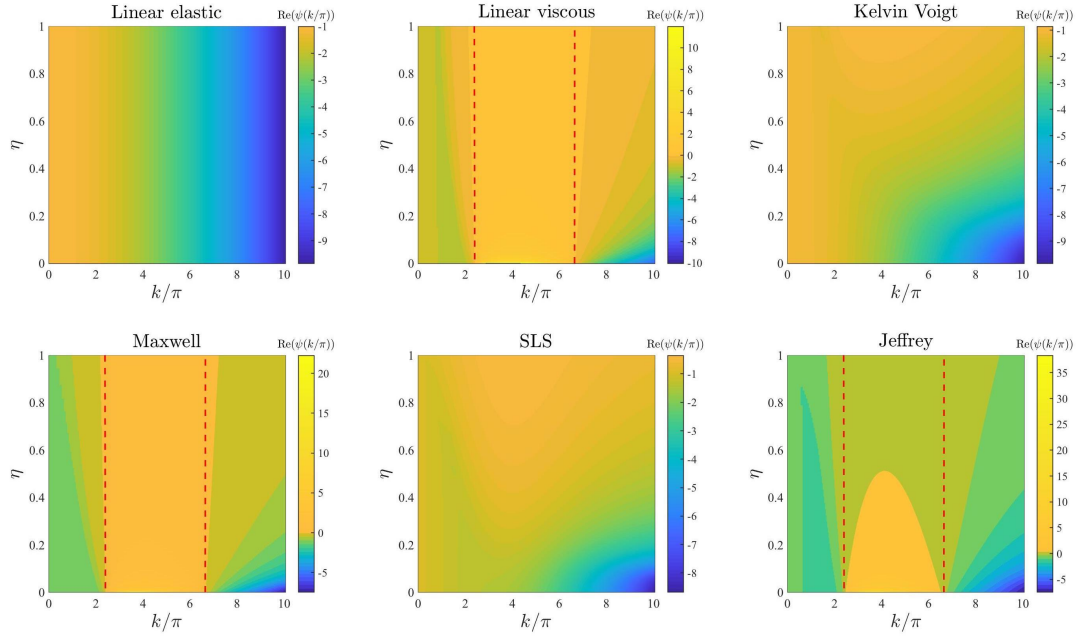


**Figure 8.3: Effects of varying the ECM viscosity.** Dispersion relations corresponding to the stress-strain constitutive equations (7.1)-(7.6) for increasing values of the ECM viscosity, that is for  $\eta \in [0, 1]$ . The values of the other parameters are given by (8.20) and (8.21). Red dashed lines mark contour lines where  $\text{Re}(\psi(k^2)) = 0$ .

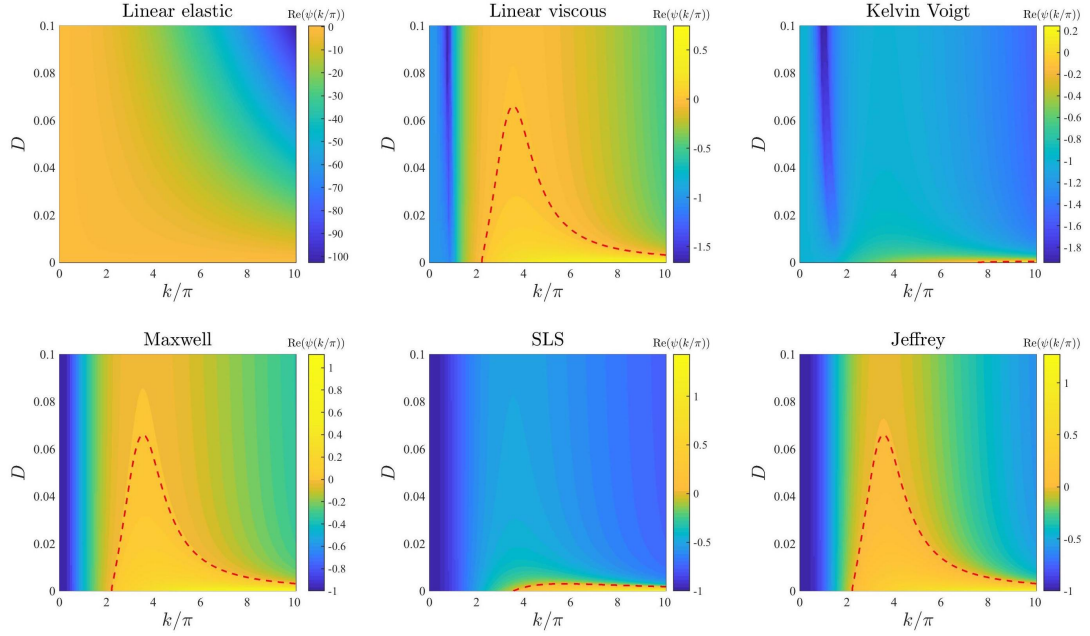


**Figure 8.4: Effects of varying the cell motility.** Dispersion relations corresponding to the stress-strain constitutive equations (7.1)-(7.6) for increasing values of the cell motility, that is for  $D \in [0, 0.1]$ . The values of the other parameters are given by (8.20) and (8.21). Red dashed lines mark contour lines where  $\text{Re}(\psi(k^2)) = 0$ .

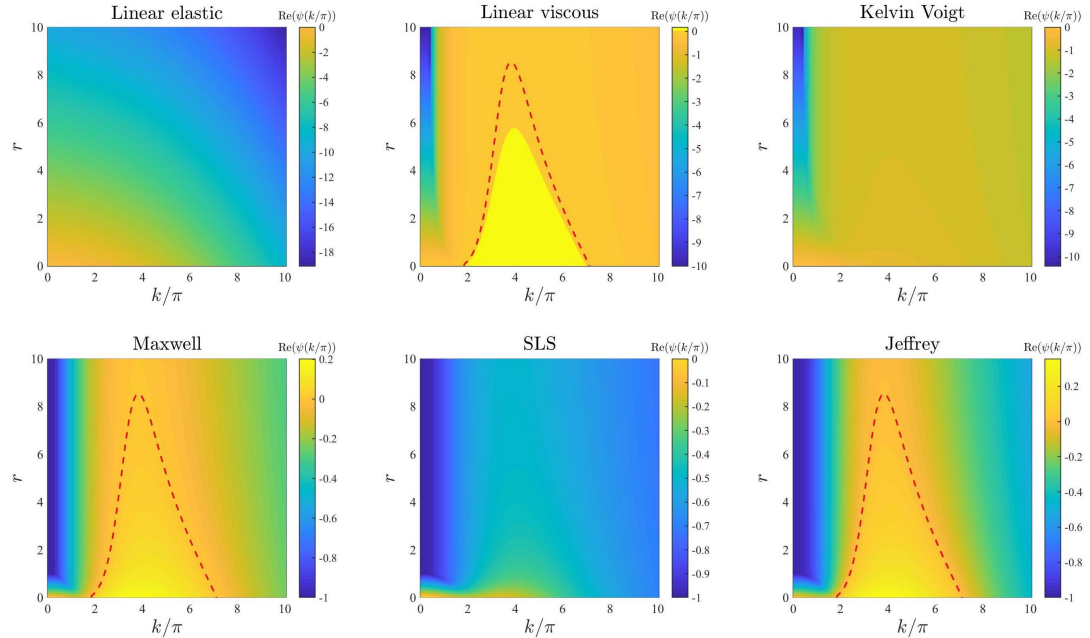


**Figure 8.5: Effects of varying the intrinsic growth rate of the cell density.** Dispersion relations corresponding to the stress-strain constitutive equations (7.1)-(7.6) for increasing values of the intrinsic growth rate of the cell density, that is for  $r \in [0, 10]$ . The values of the other parameters are given by (8.20) and (8.21). Red dashed lines mark contour lines where  $\text{Re}(\psi(k^2)) = 0$ .

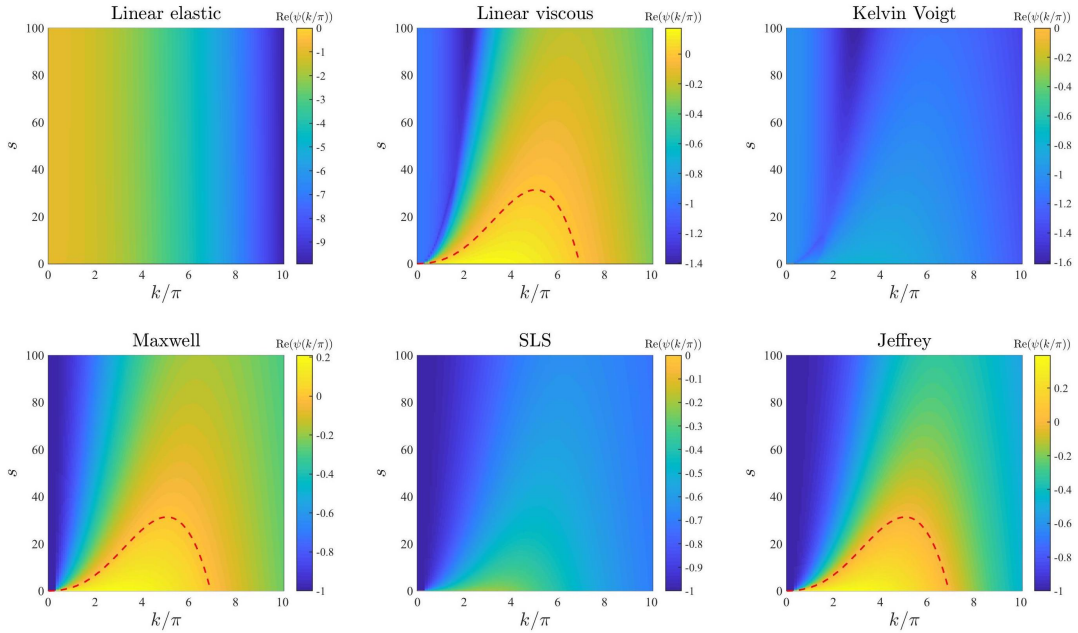


**Figure 8.6: Effects of varying the elasticity of the surrounding tissue.** Dispersion relations corresponding to the stress-strain constitutive equations (7.1)-(7.6) for increasing values of the elasticity of the surrounding tissue, that is for  $s \in [0, 100]$ . The values of the other parameters are given by (8.20) and (8.21). Red dashed lines mark contour lines where  $\text{Re}(\psi(k^2)) = 0$ .

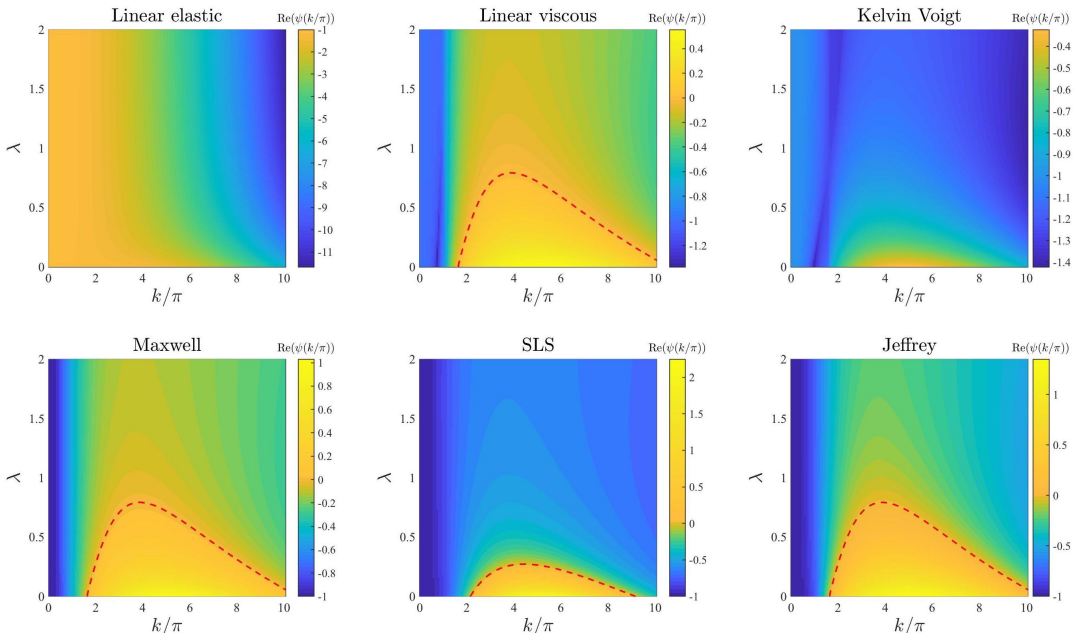


**Figure 8.7: Effects of varying the level of cell-cell contact inhibition of the cell traction forces.** Dispersion relations corresponding to the stress-strain constitutive equations (7.1)-(7.6) for increasing levels of cell-cell contact inhibition of the cell traction forces, that is for  $\lambda \in [0, 2]$ . The values of the other parameters are given by (8.20) and (8.21). Red dashed lines mark contour lines where  $\text{Re}(\psi(k^2)) = 0$ .

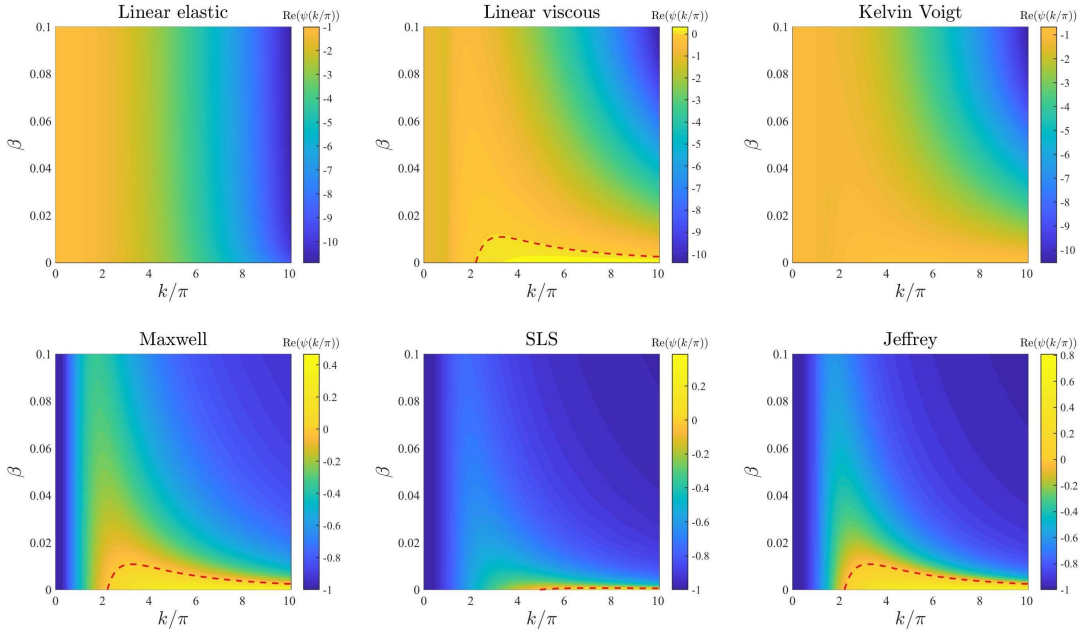


**Figure 8.8: Effects of varying the long-range cell traction forces.** Dispersion relations corresponding to the stress-strain constitutive equations (7.1)-(7.6) for increasing long-range cell traction forces, that is for  $\beta \in [0, 0.1]$ . The values of the other parameters are given by (8.20) and (8.21). Red dashed lines mark contour lines where  $\text{Re}(\psi(k^2)) = 0$ .

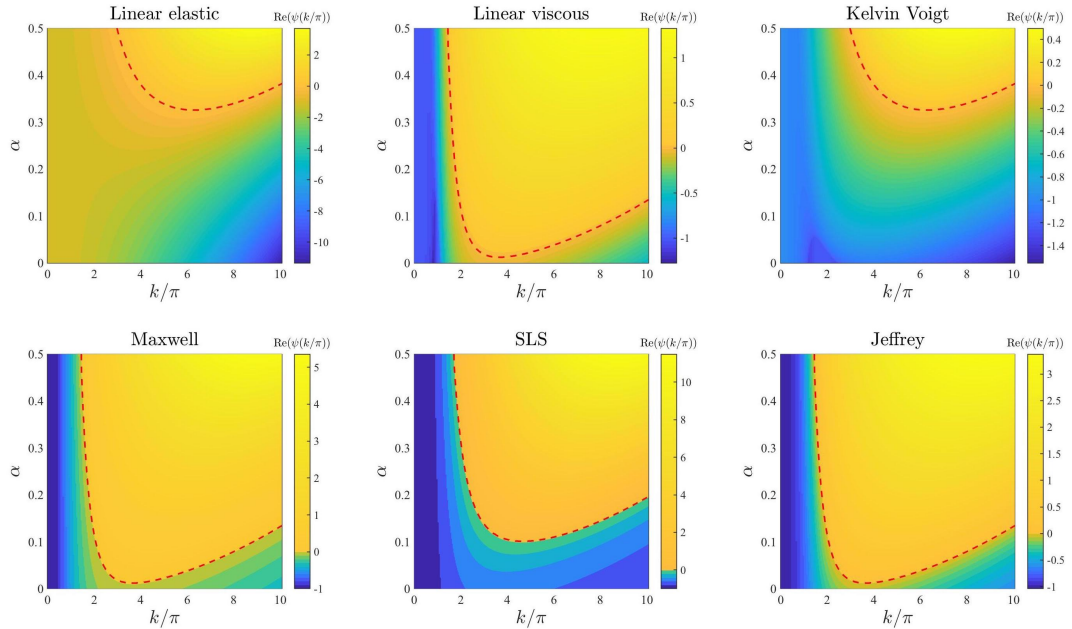


**Figure 8.9: Effects of varying the cell haptotactic sensitivity.** Dispersion relations corresponding to the stress-strain constitutive equations (7.1)-(7.6) for increasing values of the cell haptotactic sensitivity, that is for  $\alpha \in [0, 0.5]$ . The values of the other parameters are given by (8.20) and (8.21). Red dashed lines mark contour lines where  $\text{Re}(\psi(k^2)) = 0$ .

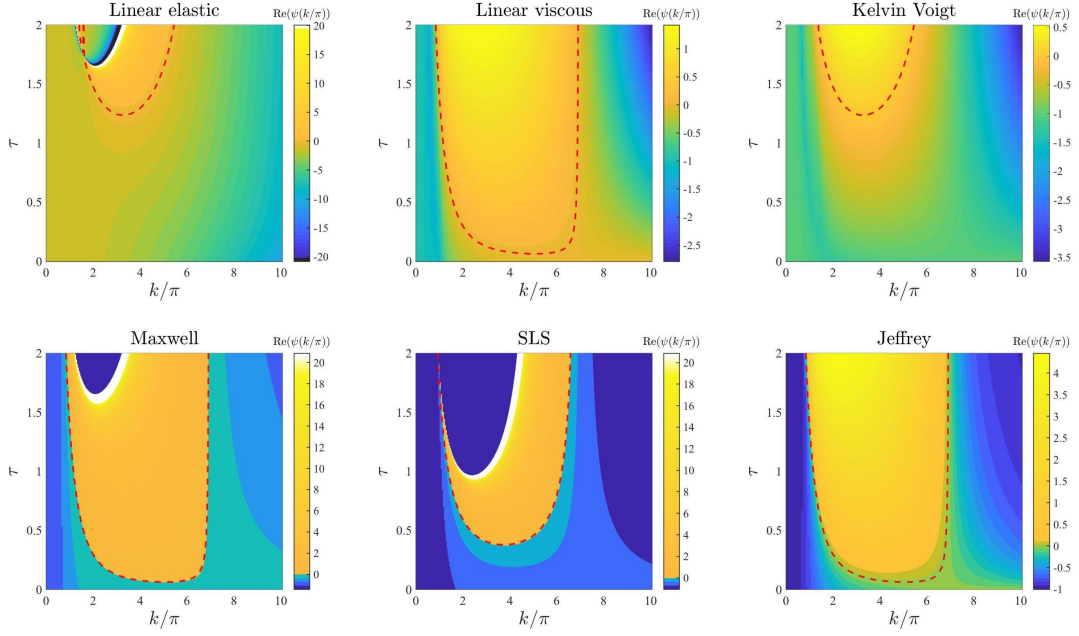


**Figure 8.10: Effects of varying the cell traction forces.** Dispersion relations corresponding to the stress-strain constitutive equations (7.1)-(7.6) for increasing cell traction forces, that is for  $\tau \in [0, 2]$ . The values of the other parameters are given by (8.20) and (8.21). White and black regions in the plots related to the linear elastic model, the Maxwell model and the SLS model correspond, respectively, to  $\text{Re}(\psi(k^2)) > 20$  and  $\text{Re}(\psi(k^2)) < -20$  (i.e. a vertical asymptote is present in the dispersion relation). Red dashed lines mark contour lines where  $\text{Re}(\psi(k^2)) = 0$ .

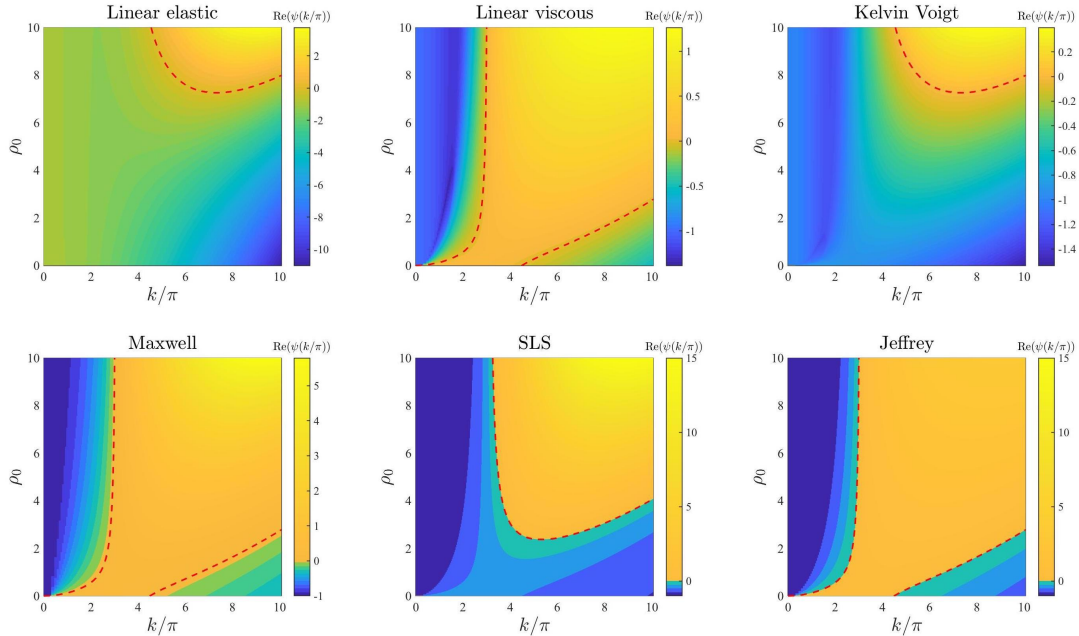


**Figure 8.11: Effects of varying the initial ECM density.** Dispersion relations corresponding to the stress-strain constitutive equations (7.1)-(7.6) for increasing values of the initial ECM density, that is for  $\rho_0 \in [0, 10]$ . The values of the other parameters are given by (8.20) and (8.21). Red dashed lines mark contour lines where  $\text{Re}(\psi(k^2)) = 0$ .

## 8.3 Numerical investigations

We verify key results of LSA presented in Section 8.2 by carrying out numerical simulations in 1D in Section 8.3.2. In particular, we report on numerical solutions obtained in the case where equation (8.7) is complemented with the Kelvin-Voigt model (7.3) or the Maxwell model (7.4). These results are complemented with the numerical simulations of the corresponding problem in 2D, reported in Section 8.3.3. The set-up of these numerical simulations and the methods employed to construct numerical solutions are described in Section 8.3.1.

### 8.3.1 Set-up of numerical simulations and numerical methods

**Set-up of numerical simulations in 1D.** We first solve numerically the 1D system of PDEs (8.1), (8.2) and (8.7) subject to boundary conditions (8.8) using the parameter values given by (8.20) and (8.21). We choose the endpoints of the spatial domain to be  $\ell = 0$  and  $L = 1$ , and the final time  $T$  is chosen sufficiently large so that distinct spatial patterns can be observed at the end of simulations. We consider the initial conditions

$$n(0, x) = 1 + 0.01 \epsilon(x), \quad \rho(0, x) \equiv \rho_0, \quad u(0, x) \equiv 0, \quad (8.22)$$

where  $\epsilon(x)$  is a normally distributed random variable with mean 0 and variance 1 for every  $x \in [0, 1]$ . Initial conditions (8.22) model a scenario where random small perturbations are superimposed to the cell density corresponding to the homogeneous steady state of components  $\bar{n} = 1$ ,  $\bar{\rho} = \rho_0$  and  $\bar{u} = 0$ . This is the steady state considered in the LSA undertaken in Section 8.2.1. Consistent initial conditions for  $\partial_t n(0, x)$ ,  $\partial_t \rho(0, x)$  and  $\partial_t u(0, x)$  are computed numerically – details provided in Appendix B.3.

**Set-up of numerical simulations in 2D.** Next, we solve numerically the system of PDEs (8.9) subject to the 2D version of the periodic boundary conditions (8.8) and complemented with (8.10)-(7.12). Numerical simulations are carried out using the following parameter values

$$E = 1, \quad \eta = 1, \quad D = 0.01, \quad \nu = 0.25, \quad (8.23)$$

$$\alpha = 0.05, \quad r = 1, \quad s = 10, \quad \lambda = 0.5, \quad \tau = 0.2, \quad \beta = 0.005, \quad (8.24)$$

which are chosen for illustrative purposes and are comparable with nondimensional parameter values that can be found in the extant literature (see Appendix C.3 for further details). We choose  $\Omega = [0, 1] \times [0, 1]$  and the final time  $T$  is chosen sufficiently large so that distinct spatial patterns can be observed at the end of simulations. We consider the

following 2D analogue of initial conditions (8.22)

$$n(0, x_1, x_2) = 1 + 0.01 \epsilon(x_1, x_2), \quad \rho(0, x_1, x_2) \equiv 1, \quad \mathbf{u}(0, x_1, x_2) \equiv \mathbf{0}, \quad (8.25)$$

where  $\epsilon(x_1, x_2)$  is a normally distributed random variable with mean 0 and variance 1 for each  $(x_1, x_2) \in [0, 1] \times [0, 1]$ . Consistent initial conditions for  $\partial_t n(0, x_1, x_2)$ ,  $\partial_t \rho(0, x_1, x_2)$  and  $\partial_t \mathbf{u}(0, x_1, x_2)$  are computed numerically, as similarly done in the 1D case.

**Numerical methods.** Numerical solutions are constructed on a uniform discretisation of the interval  $[0, 1]$  or the square  $[0, 1] \times [0, 1]$  as the computational domain of the independent variable  $\mathbf{x}$ , using the Method of Lines. Finite difference and finite volume approximations of the spatial derivatives are used, together with first order upwinding for the flux terms, to obtain a system of ODEs, solved implicitly with the MATLAB solver `ode15i`. All numerical computations are performed in MATLAB. Details of the numerical schemes are given in Appendix B.3.

### 8.3.2 1D patterns

The results obtained are summarised by the plots in Figure 8.12, which display the solution of the system of PDEs (8.1), (8.2) and (8.7) subject to the boundary conditions (8.8) and initial conditions (8.22) for the Kelvin-Voigt model and the Maxwell model when a steady state is reached. The supplementary Figure D.8 displays the solution of the same system of PDEs for the Maxwell model under alternative initial perturbations in the cell density, i.e. randomly distributed, periodic or randomly perturbed periodic initial perturbations.

The results in Figures 8.12 and D.8 demonstrate that, in agreement with the dispersion relations displayed in Figure 8.1, for the parameter values given by (8.20) and (8.21), small randomly distributed perturbations present in the initial cell density:

- Vanish in the case of the Kelvin-Voigt model, thus leading the cell density to relax to the homogeneous steady state  $\bar{n} = 1$  and attain numerical equilibrium at  $t = 100$  while leaving the ECM density unchanged;
- Grow in the case of the Maxwell model, resulting in the formation of spatial patterns both in the cell density  $n$  and in the ECM density  $\rho$ , which attain numerical equilibrium at  $t = 500$ .

Notice that the formation of spatial patterns correlates with the growth of the cell-ECM displacement  $u$ . In fact, the displacement remains close to zero (i.e.  $\sim O(10^{-11})$ ) for the Kelvin-Voigt model, whereas it grows with time for the Maxwell model. In addition, the steady state obtained for the Maxwell model in Figure 8.12, together with those obtained when considering alternative initial perturbations (*cf.* Figure D.8), demonstrate

that, in agreement with the dispersion relation displayed in Figure 8.1 for the Maxwell model, for the parameter values given by (8.20) and (8.21), under small perturbations in the cell density, be they randomly distributed, randomly perturbed periodic or periodic, the fourth mode is the fastest growing one within the range of unstable modes (*cf.*

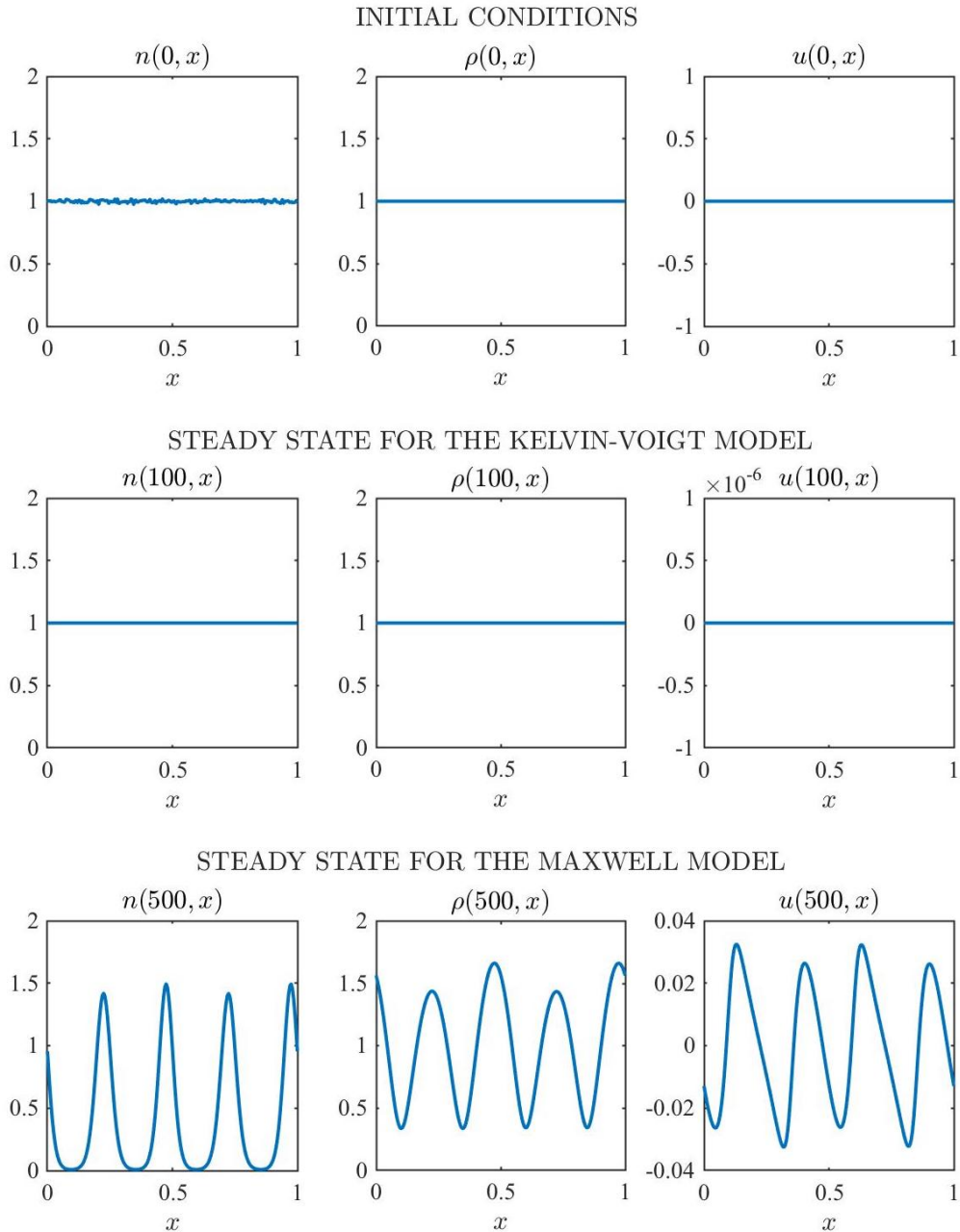


**Figure 8.12: 1D numerical results for the Kelvin-Voigt and the Maxwell models.** Cell density  $n(t, x)$  (left), ECM density  $\rho(t, x)$  (centre) and cell-ECM displacement  $u(t, x)$  (right) at  $t = 0$  (first row) and at steady state obtained solving numerically the system of PDEs (8.1), (8.2) and (8.7) complemented with the Kelvin-Voigt model (7.3) (second row) and with the Maxwell model (7.4) (third row), respectively, subject to boundary conditions (8.8) and initial conditions (8.22), for the parameter values given by (8.20) and (8.21).

$\text{Re}(\psi(k^2)) > 0$  for  $k/\pi$  between 2 and 6, with  $\max(\text{Re}(\psi(k^2))) \approx 4$  in Figure 8.1 for the Maxwell model). Moreover, all the obtained cellular patterns at steady state exhibit the same structure – up to a horizontal shift – consisting of four large peaks, independently of the initial conditions that is used (*cf.* left panel in the bottom row of Figure 8.12 and supplementary Figure D.8). This indicates robustness and consistency in the nature of the saturated nonlinear steady state under specific viscoelasticity assumptions and parameter choices.

### 8.3.3 2D patterns

The results obtained are summarised by the plots in Figures 8.13 and 8.14. Solutions of the system of PDEs (8.9), together with (8.10)-(7.12), subject to initial conditions (8.25) and periodic boundary conditions, for the parameter values given by (8.23) and (8.24), are calculated both for the Kelvin-Voigt model and the Maxwell model according to the parameter changes summarised in Table 7.3. The randomly generated initial perturbation in the cell density, together with the cell density at  $t = 200$  both for the Kelvin-Voigt and the Maxwell model are displayed in Figure 8.13, while the solution to the Maxwell model is plotted at a later time in Figure 8.14. Overall, these results demonstrate that, in the scenarios considered here, which are analogous to those considered for the corresponding 1D models, small randomly distributed perturbations present in the initial cell density (*cf.* first panel in Figure 8.13):

- Vanish in the case of the Kelvin-Voigt model, thus leading the cell density to relax to the homogeneous steady state  $\bar{n} = 1$  and attain numerical equilibrium at  $t = 260$  (*cf.* second panel of Figure 8.13) while leaving the ECM density unchanged;
- Grow in the case of the Maxwell model, leading to the formation of spatiotemporal patterns both in the cell density  $n$  and in the ECM density  $\rho$  (*cf.* third panel of Figure 8.13 and Figure 8.14), capturing spatiotemporal dynamic heterogeneity arising in the system.

Similarly to the 1D case, the formation of spatial patterns correlates with the growth of the cell-ECM displacement  $\mathbf{u}$ . In fact, the displacement remains close to zero (i.e.  $\sim O(10^{-11})$ ) for the Kelvin-Voigt model, whereas it grows with time for the Maxwell model – see Figure 8.14. Note that, while the observed pattern for the Maxwell model is not at steady state and we cannot therefore conclude that patterns exist at steady state, spatiotemporal heterogeneity and the emergence of transient patterns can sometimes be more biologically interesting than the existence of steady patterns.

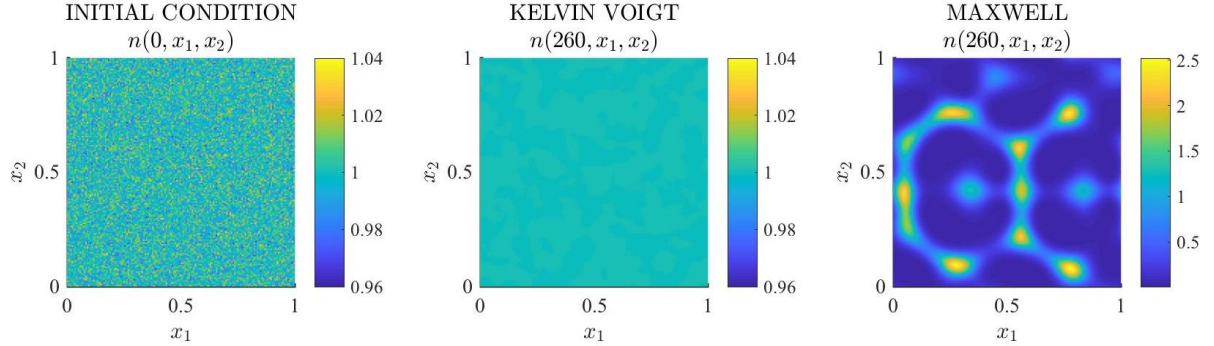


**Figure 8.13: 2D numerical results for the Kelvin-Voigt and the Maxwell models.** Cell density  $n(t, x_1, x_2)$  at  $t = 0$  (left panel) and at  $t = 260$  for the Kelvin-Voigt model (central panel) and the Maxwell model (right panel) obtained solving numerically the system of PDEs (8.9) subject to the 2D version of the periodic boundary conditions (8.8) and initial conditions (8.25), complemented with (8.10)-(7.12), for the parameter values given by (8.23) and (8.24).

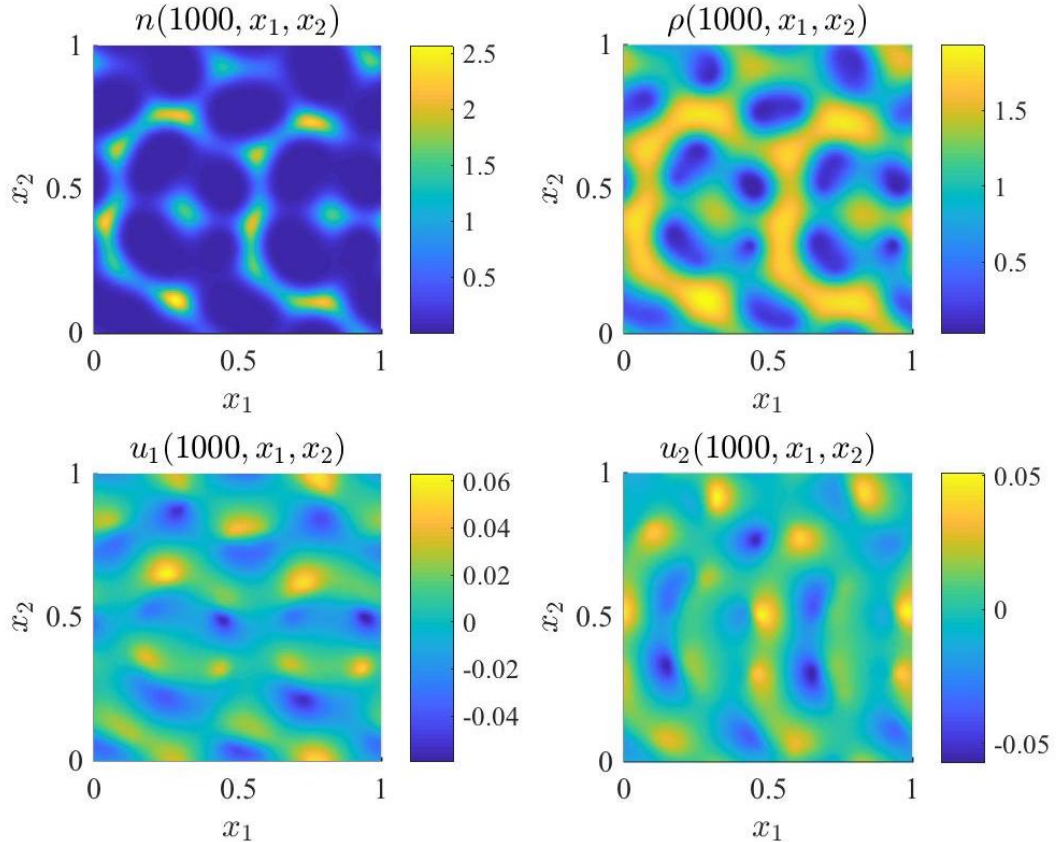


**Figure 8.14: 2D numerical results for the Maxwell model.** Cell density  $n(t, x_1, x_2)$  (top row, left panel), ECM density  $\rho(t, x_1, x_2)$  (top row, right panel), first and second components of the cell-ECM displacement  $\mathbf{u}(t, x_1, x_2)$  (bottom row, left panel and right panel, respectively) at  $t = 1000$  for the Maxwell model obtained solving numerically the system of PDEs (8.9) subject to the 2D version of the periodic boundary conditions (8.8) and initial conditions (8.25), complemented with (8.10)-(7.12), for the parameter values given by (8.23) and (8.24). The random initial perturbation of the cell density is displayed in the left panel of Figure 8.13.

# Chapter 9

## Discussion and research perspectives

### 9.1 Summary and discussion

In Chapter 7 we saw how mechanical and mechanochemical models of pattern formation have been used in a variety of applications in which the mechanical interaction between the cells and the ECM cannot be neglected. These models generally rely on linear viscoelasticity assumptions on the ECM, often making use of the Kelvin-Voigt model of linear viscoelasticity. However, a variety of linear viscoelasticity models that can better capture the rheological properties of the ECM exist, as outlined in Section 7.2. In Chapter 8 we therefore investigated the impact of considering different stress-strain constitutive equations in a generic mechanical model of pattern formation in biological tissue on the pattern formation potential of the system.

#### 9.1.1 Summary

We have investigated the pattern formation potential of different stress-strain constitutive equations for the ECM within a 1D mechanical model of pattern formation in biological tissues formulated as the system of implicit PDEs (8.1), (8.2) and (8.7). The results of LSA undertaken in Section 8.2 and the dispersion relations derived therefrom support the idea that fluid-like stress-strain constitutive equations (i.e. the linear viscous model (7.2), the Maxwell model (7.4) and the Jeffrey model (7.6)) have a pattern formation potential much higher than solid-like constitutive equations (i.e. the linear elastic model (7.1), the Kelvin-Voigt model (7.3) and the SLS model (7.5)). This is confirmed by the results of numerical simulations presented in Section 8.3, which demonstrate that, all else being

equal, spatial patterns emerge in the case where the Maxwell model (7.4) is used to represent the stress-strain relation of the ECM, while no patterns are observed when the Kelvin-Voigt model (7.3) is employed. In addition, the structure of the spatial patterns presented in Section 8.3 for the Maxwell model (7.4) is consistent with the fastest growing mode predicted by LSA. In Section 8.3.3, as an illustrative example, we have also reported on the results of numerical simulations of a 2D version of the model, which is given by the system of PDEs (8.9) complemented with the 2D Kelvin-Voigt and Maxwell models (7.10). These results demonstrate that key features of spatial pattern formation observed in one spatial dimension carry through when two spatial dimensions are considered, thus conferring additional robustness to the conclusions of our work.

### 9.1.2 Empirically informed mechanical models

These findings corroborate the conclusions of Byrne and Chaplain (1996) suggesting that prior studies on mechanochemical models of pattern formation relying on the Kelvin-Voigt model of viscoelasticity may have underestimated the pattern formation potential of biological tissues and advocating the need for further empirical work to acquire detailed quantitative information on the mechanical properties of single components of the ECM in different biological tissues, in order to furnish such models with stress-strain constitutive equations for the ECM that provide a more faithful representation of tissue rheology, *cf.* Fung (1993). This is particularly relevant as the Kelvin-Voigt model, typically selected in mathematical studies also thanks to its simple constitutive equation in 2D, is unlikely to give a faithful representation of the viscoelastic behaviour of biological or bio-engineered tissues, even in linear viscoelasticity regimes. These, in fact, generally display viscous flow during the creep test, as exemplified by the experimental creep curve reported in Figure 9.1a, and some form of stress relaxation during the stress relaxation test, as shown by the stress relaxation curves obtained fitting experimentally data reported in Figure 9.1b.

## 9.2 Research perspectives

### 9.2.1 Model extensions, further analytical and numerical work

The dispersion relations given in Section 8.2 indicate that there may be parameter regimes whereby solid-like constitutive models of linear viscoelasticity give rise to dispersion relations which exhibit a range of unstable modes, while the dispersion relations obtained using fluid-like constitutive models exhibit singularities, exiting the regime of validity of

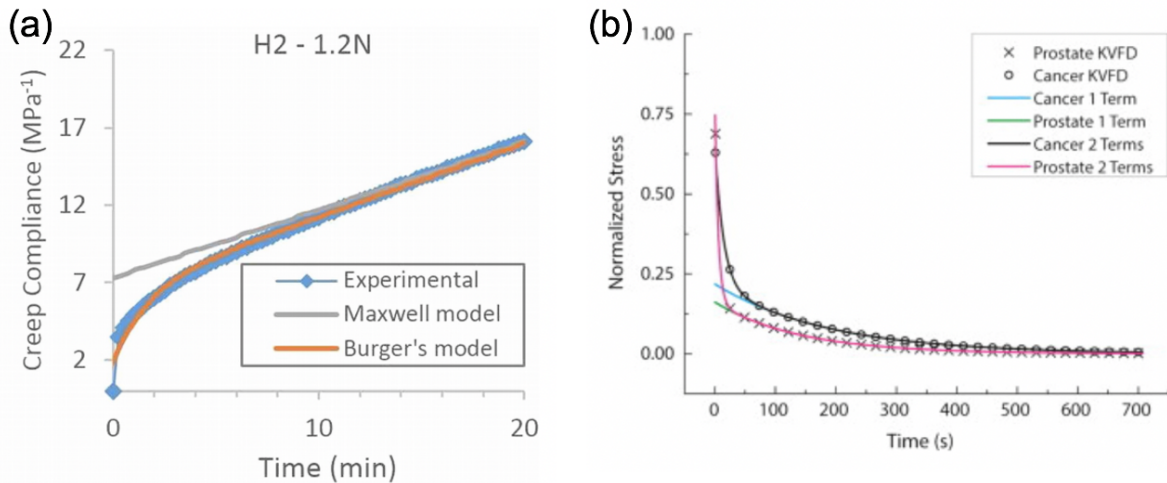


**Figure 9.1: Experimental creep and stress relaxation curves.** (a) Experimental creep curve of hydrogel-based engineered tissue, and comparison with creep curves captured by the Maxwell and Burger's models. Reprinted from Biomedical materials, 12(2), R. Kocen, M. Gasik, A. Gantar, S. Novak, Viscoelastic behaviour of hydrogel-based composites for tissue engineering under mechanical load, 025004, 2017, under Creative Commons licence <https://creativecommons.org/licenses/by/3.0/> (Kocen et al., 2017, Figure 8). (b) Fitted stress relaxation curves of experimental stress relaxation tests conducted by Hoyt et al. (2008) on normal prostatic and cancerous tissues. Reprinted from the Journal of the Mechanical Behavior of Biomedical Materials, 41, J. Palacio-Torralba, S. Hammer, D. W. Good, S. A. McNeill, G. D. Stewart, R. L. Reuben, Y. Chen, Quantitative diagnostics of soft tissue through viscoelastic characterization using time-based instrumented palpation, 149-160, 2015, under Creative Commons licence <https://creativecommons.org/licenses/by/3.0/> (Palacio-Torralba et al., 2015, Figure 1).

LSA. In this regard, it would be interesting to consider extended versions of the mechanical model of pattern formation defined by the system of PDEs (8.1), (8.2) and (8.7), in order to re-enter the regime of validity of LSA for the same parameter regimes and verify that in such regimes all constitutive models can produce patterns. For instance, it is known that including long-range effects, such as long-range diffusion or long-range haptotaxis, can promote the formation of stable spatial patterns (Moreo et al., 2010; Oster et al., 1983), which could be explored through nonlinear stability analysis, as previously done for the case in which the stress-strain relation of the ECM is represented by the Kelvin-Voigt model (Cruywagen and Murray, 1992; Lewis and Murray, 1991; Maini and Murray, 1988). In particular, weakly nonlinear analysis could provide information on the existence and stability of saturated nonlinear steady states, supercritical bifurcations or subcritical bifurcations, which may exist even when the homogeneous steady states are stable under small perturbations according to LSA (Cross and Greenside, 2009). Nonlinear analysis would further enable exploring the existence of possible differences in the spatial patterns obtained when different stress-strain constitutive equations for

the ECM are used – such as amplitude of patterns, perturbation mode selection and geometric structure in two spatial dimensions. In particular, the base-case dispersion relations given in Section 8.2 for different fluid-like models of viscoelasticity displayed the same range of unstable modes. This suggests that the investigation of similarities and differences in mode selection between the various models of viscoelasticity could yield interesting results. It would also be interesting to construct numerical solutions for the mechanical model defined by the system of PDEs (8.1), (8.2) and (8.7) complemented with the Jeffrey model (7.6). For this to be done, suitable extensions of the numerical schemes presented in Appendix B.3 need to be developed.

**2D constitutive equations.** It would also be relevant to systematically assess the pattern formation potential of different constitutive models of viscoelasticity in two spatial dimensions. This would require to relax the simplifying assumption (A.64) on the shear and bulk viscosities of the ECM, which we have used to derive the 2D Maxwell model in the form of (7.10), and, more in general, to find analytically and computationally tractable stress-strain-dilation relations, which still remains an open problem (Birman et al., 2002; Haghghi-Yazdi and Lee-Sullivan, 2011). In order to solve this problem, new methods of derivation and parameterisation for constitutive models of viscoelasticity might need to be developed (Valtorta and Mazza, 2005).

**Burger’s model of linear viscoelasticity.** Once appropriate 2D constitutive equations for the models of linear viscoelasticity presented in Section 7.2.2 have been derived, and the numerical methods further developed to address a constitutive equation in the form (7.7) – or (7.9) in 2D – it might be beneficial to focus on the Burger’s model of linear viscoelasticity. While this was not addressed in this study, it can capture all the rheological properties of linear viscoelastic materials introduced in Section 7.2.1 (cf. Table 7.2) and will therefore more easily fit any experimental creep and stress-relaxation data – e.g. see Figure 9.1a.

### 9.2.2 Experimentally motivated studies

As previously mentioned, the values of the model parameters used in this paper have been chosen for illustrative purposes only. Hence, it would be useful to re-compute the dispersion relations and the numerical solutions presented here for a calibrated version of the model based on real biological data. On a related note, in addition to the relevance this study has for *in vitro* vs. *in vivo* assays as briefly mentioned at the end of Chapter 6, there exists a variety of interesting applications that could be explored by varying parameter values in the generic constitutive equation (8.7) both in space and time. For

instance, cell monolayers appear to exhibit solid-like behaviours on small time scales, whereas they exhibit fluid-like behaviours on longer time scales (Tili et al., 2018), and spatiotemporal changes in basement membrane components are known to affect structural properties of tissues during development or ageing, as well as in a number of genetic and autoimmune diseases (Khalilgharibi and Mao, 2021). Amongst these, remarkable examples are Alport's syndrome, characterised by changes in collagen IV network due to genetic mutations associated with the disease, diabetes mellitus, whereby high levels of glucose induce significant basement membrane turnover, and cancer. In particular, cancer-associated fibrosis is a disease characterised by an excessive production of collagen, elastin and proteoglycans, which directly affects the structure of the ECM resulting in alterations of viscoelastic tissue properties (Ebihara et al., 2000). Such alterations in the ECM may facilitate tumour invasion and angiogenesis. Considering a calibrated mechanical model of pattern formation in biological tissues, whereby the values of the parameters in the stress-strain constitutive equation for the ECM change during fibrosis progression, may shed new light on the existing connections between structural changes in the ECM components and higher levels of malignancy in cancer (Chandler et al., 2019; Park et al., 2001).

# **Part V**

## **Potential future directions**

# Spatial sorting and the migratory phenotype

Throughout this thesis, a series of mathematical models comprising of systems of PDEs have been proposed to study different mechanisms at the basis of spatial sorting of cell populations at the tissue scale. In Part II this spatial sorting resulted from the nonlinear interaction between cells and abiotic factors which leads to the creation of distinct ecological niches in which cells in different phenotypic states can be selected. Here, cell spatial movement was either neglected or modelled as low diffusion in the quantity  $n(t, \mathbf{x}, y)$ , i.e. the cell phenotypic distribution. In Part III spatial sorting resulted from more complex forms of movement, such as chemotaxis and long-range cell adhesion, and interaction with the ECM, including matrix degradation. Finally, in Part IV it was a result of the mechanical interaction between cells and ECM, based on the cells' ability to exert traction forces on the ECM.

While in Parts III and IV it was assumed that all cells in the population were undergoing the same spatiotemporal dynamics, in reality cell populations are often composed of cells with different migratory abilities. In particular, it is known that mesenchymal-like cells, as opposed to amoeboid-like ones, have a more elongated morphology allowing them to sense environmental clues, including ECM binding sites, at larger distance and exert high traction forces on the ECM fibers to which they are bound (Friedl and Wolf, 2003; Friedl, 2004). In tumours, mesenchymal-like invasive cells are also characterised by invadopodia, protrusions associated with proteolytic degradation of the ECM (Alblazi and Siar, 2015). It might therefore be beneficial, for certain cell spatial sorting problems, to include a phenotype-structuring variable, say,  $y \in \mathcal{Y} \subset \mathbb{R}$  to model the cell morphologic and migratory phenotype, and define different terms in the equations as functions of  $y$ , similarly to as done in Part II for the metabolic phenotype. Below are discussed three problems, in cancer and development, which could benefit from this approach.

**Cancer invasion.** As hinted at in Section 1.1.1, EMT allows cells to switch to an invasive phenotype, capable of moving more easily though the ECM thanks to long-range adhesion and secretion of matrix-degrading enzymes. During EMT, moreover, tumour cells can display hybrid morphologies resulting in a range of motile behaviours within the same population (Jolly et al., 2015). Therefore, in a first instance, it would be interesting to study cancer invasion in a modelling framework similar to that recently proposed by Fiandaca et al. (2021a). The model would incorporate phenotype-dependent ECM-driven movement by considering local haptotaxis, as in equations (8.1) and (8.9), with heterogeneous haptotactic coefficient, e.g.  $\alpha(y)$ . Moreover, ECM degradation could be modelled by considering a phenotype-dependent degradation rate, e.g.  $\gamma(y)$ , and the

product  $\gamma(y)n(t, \mathbf{x}, y)$  would need to be integrated over  $\mathcal{Y}$  and multiplied by the ECM density. This way matrix degradation would introduce a nonlocal term in the balance equation for the ECM density, as opposed to the local term used in (5.10). In view of the results in (Bouin et al., 2012; Lorenzi et al., 2021; Lorenzi and Painter, 2022), and other works discussed in Section 1.2.4, we expect phenotype-dependent spatial movement to result in travelling wave solutions with the most motile individuals selected at the edge of the invading front. Moreover, these results could be combined with LSA to explore a potential emergence of spatial patterns, such as the finger-like patterns that are sometimes observed in invading tumours – see for instance (Bearer et al., 2009; Roche and Norris, 1975; Weinberg, 2013) and references therein.

**Cell migration by nonlocal adhesion.** In the cancer invasion problem introduced above, as well as in the cluster-based vasculogenesis one introduced in Part III, cell migration through the ECM could be guided by nonlocal adhesion thanks to cell protrusions. To capture the range of migratory abilities of cells in different phenotypic states, it would therefore be relevant to let the sensing radius of a cell be defined as a function of  $y$ , e.g.  $R(y)$ . Modelling nonlocal cell adhesion as in equations (5.5) and (5.6), this would introduce a  $y$ -dependence in the integration limits. A simpler first step in this direction would be to consider the approach of Loy and Preziosi (2020, 2021), where the sensing radius appears in the integrand, which is set to zero at spatial points further than the distance imposed by the sensing radius  $R$ .

**Cluster-based vasculogenesis.** As hinted at in Sections 4.1.4 and 6.2.3, during the early stages of cluster-based vasculogenesis EPCs display amoeboid-like features, and have been observed to extend protrusions and have an elongated morphology only after clusters have formed (Blatchley et al., 2019). The introduction of a phenotype-structuring variable would therefore allow for a comprehensive model including dynamics occurring at the early and late stages, without the need for separate modelling frameworks. In such model, local vs. nonlocal adhesion could be modelled as discussed in the previous paragraph. Moreover, mechanical clues relevant at the later stages could be modelled as in equations (8.3)-(8.5), or (8.9)-(8.10), of the mechanical models discussed in Part IV, with phenotype-dependent cell traction coefficient, e.g.  $\tau(y)$ . Note that it is still unclear what drives this phenotypic change after cluster formation, and mathematical modelling could therefore provide a great theoretical framework in which to test verbal hypotheses.

The interest of the mathematical community is indeed moving in this direction, as indicated by the fact that these modelling frameworks are increasingly being discussed – e.g. at seminars, workshops and conferences – and related papers are starting to be proposed

- e.g. [Fiandaca et al. (2021a); Lorenzi and Painter (2022)]. This will likely lead to new mathematical challenges at the interface of the fields of adaptive dynamics and pattern formation, which would feed back into related fields in physics and mathematics, and inspire new mathematical and interdisciplinary work.

# Appendices

# Appendix A

## Analytical details

We here report the details of the investigations conducted to support analytical results presented throughout the manuscript. In particular we include: the proof of Proposition 1 and that of Theorem 1 stated in Part II (Section 2.2.1) in Section A.1 and A.2 respectively; details of the formal analysis conducted in the asymptotic regime considered in Part II (Section 2.2.2) in Section A.3; details of the LSA conducted in Part III (Section 5.2) in Section A.4; rules of derivation of the constitutive equations in Part IV (Chapter 7) in Section A.5; examples of creep and stress relaxation tests presented in Part IV (Section 7.2.2) in Section A.6.

### A.1 Proof of Proposition 1 in Chapter 2

Substituting (2.6) and (2.15) into (2.5) yields

$$\frac{\partial n}{\partial t} = \beta \frac{\partial^2 n}{\partial y^2} + [a - b(y - h)^2 - \zeta \rho(t, \mathbf{x})] n, \quad (A.1)$$

$$n \equiv n(t, \mathbf{x}, y), \quad (t, \mathbf{x}, y) \in (0, \infty) \times \bar{\Omega} \times \mathbb{R}.$$

Building upon the results presented in (Almeida et al., 2019; Chisholm et al., 2016b; Lorenzi et al., 2015), we make the ansatz (2.29). Substituting this ansatz into (A.1) and introducing the notation  $v(t, \mathbf{x}) := 1/\sigma^2(t, \mathbf{x})$  we find

$$\frac{\partial_t \rho}{\rho} + \frac{\partial_t v}{2v} = \frac{\partial_t v}{2} (y - \mu)^2 - \partial_t \mu v (y - \mu) + \beta [v^2 (y - \mu)^2 - v] + a - b (y - h)^2 - \zeta \rho. \quad (A.2)$$

Equating the second-order terms in  $y$  gives the following differential equation for  $v$  alone

$$\partial_t v + 2\beta v^2 = 2b. \quad (A.3)$$

Moreover, equating the coefficients of the first-order terms in  $y$ , and eliminating  $\partial_t v$  from the resulting equation, yields

$$\partial_t \mu = \frac{2b(h - \mu)}{v}. \quad (\text{A.4})$$

Lastly, choosing  $y = \mu$  in (A.2) gives

$$\frac{\partial_t \rho}{\rho} + \frac{\partial_t v}{2v} = -\beta v + a - b(\mu - h)^2 - \zeta \rho \quad (\text{A.5})$$

and eliminating  $\partial_t v$  from (A.5) we obtain

$$\partial_t \rho = \left[ \left( a - \frac{b}{v} - b(\mu - h)^2 \right) - \zeta \rho \right] \rho. \quad (\text{A.6})$$

Under the initial condition (2.27), we have

$$v(0, \mathbf{x}) = v_0(\mathbf{x}), \quad \mu(0, \mathbf{x}) = \mu_0(\mathbf{x}), \quad \rho(0, \mathbf{x}) = \rho_0(\mathbf{x}),$$

and imposing these initial conditions for (A.3), (A.4) and (A.6) we arrive at the Cauchy problem (2.30) for the functions  $v(t, \mathbf{x})$ ,  $\mu(t, \mathbf{x})$  and  $\rho(t, \mathbf{x})$ .  $\square$

## A.2 Proof of Theorem 1 in Chapter 2

Under assumptions (2.24) and (2.25), Proposition 1 ensures that for any  $(t, \mathbf{x}) \in [0, \infty) \times \overline{\Omega}$  the solution of (2.5) subject to (2.27) and (2.28) is of the Gaussian form (2.29). Therefore, building upon the method of proof presented in (Ardaševa et al., 2020b; Chisholm et al., 2016b), we prove Theorem 1 by studying the behaviour of the components of the solution to the Cauchy problem (2.30) for  $t \rightarrow \infty$ .

**Step 1: asymptotic behaviour of  $v(t, \mathbf{x}) \equiv 1/\sigma^2(t, \mathbf{x})$  for  $t \rightarrow \infty$ .** Solving (2.30)<sub>1</sub> subject to the initial condition  $v(0, \mathbf{x}) = v_0(\mathbf{x})$  gives

$$v(t, \cdot) = \sqrt{\frac{b}{\beta}} \frac{\sqrt{\frac{b}{\beta}} + v_0 - \left( \sqrt{\frac{b}{\beta}} - v_0 \right) \exp(-4\sqrt{b\beta}t)}{\sqrt{\frac{b}{\beta}} + v_0 + \left( \sqrt{\frac{b}{\beta}} - v_0 \right) \exp(-4\sqrt{b\beta}t)}, \quad (\text{A.7})$$

which implies that

$$v(t, \cdot) \longrightarrow \sqrt{\frac{b}{\beta}} \quad \text{exponentially fast as } t \rightarrow \infty. \quad (\text{A.8})$$

**Step 2: asymptotic behaviour of  $\mu(t, \mathbf{x})$  for  $t \rightarrow \infty$ .** Solving  $(\text{[2.30]})_2$  subject to the initial condition  $\mu(0, \mathbf{x}) = \mu_0(\mathbf{x})$  yields

$$\mu(t, \cdot) = \mu_0 \exp \left( -2b \int_0^t \frac{dz}{v(z, \cdot)} \right) + h \left[ 1 - \exp \left( -2b \int_0^t \frac{dz}{v(z, \cdot)} \right) \right], \quad (\text{A.9})$$

which implies that

$$\mu(t, \cdot) \longrightarrow h \quad \text{exponentially fast as } t \rightarrow \infty. \quad (\text{A.10})$$

**Step 3: asymptotic behaviour of  $\rho(t, \mathbf{x})$  for  $t \rightarrow \infty$ .** We define

$$w(t, \mathbf{x}) \equiv w(v(t, \mathbf{x}), \mu(t, \mathbf{x}), S(\mathbf{x}), C(\mathbf{x})) := \left( \sqrt{b\beta} - \frac{b}{v} \right) - b(\mu - h)^2$$

and rewrite  $(\text{[2.30]})_3$  as

$$\partial_t \rho = \left[ \left( a - \sqrt{b\beta} + w \right) - \zeta \rho \right] \rho. \quad (\text{A.11})$$

Solving  $(\text{A.11})$  subject to the initial condition  $\rho(0, \mathbf{x}) = \rho_0(\mathbf{x})$  yields

$$\rho(t, \cdot) = \frac{\rho_0 \exp \left[ \left( a - \sqrt{b\beta} \right) t + \int_0^t w(z, \cdot) dz \right]}{1 + \zeta \rho_0 \int_0^t \exp \left[ \left( a - \sqrt{b\beta} \right) z + \int_0^z w(\tau, \cdot) d\tau \right] dz}. \quad (\text{A.12})$$

The asymptotic results  $(\text{A.8})$  and  $(\text{A.10})$  ensure that

$$w(t, \cdot) \longrightarrow 0 \quad \text{exponentially fast as } t \rightarrow \infty, \quad (\text{A.13})$$

and, therefore,  $(\text{A.12})$  allows us to conclude that

$$\text{if } \sqrt{b(S(\mathbf{x}), C(\mathbf{x}))\beta} \geq a(S(\mathbf{x}), C(\mathbf{x})) \text{ then } \rho(t, \mathbf{x}) \longrightarrow 0 \text{ as } t \rightarrow \infty. \quad (\text{A.14})$$

On the other hand, the asymptotic result  $(\text{A.13})$  implies that in the asymptotic regime  $t \rightarrow \infty$  we have

$$\exp \left[ \left( a - \sqrt{b\beta} \right) t + \int_0^t w(z, \cdot) dz \right] \sim A(S, C) \exp \left[ \left( a - \sqrt{b\beta} \right) t \right],$$

and also that, under the additional assumption  $\sqrt{b\beta} < a$ ,

$$\int_0^t \exp \left[ \left( a - \sqrt{b\beta} \right) z + \int_0^z w(\tau, \cdot) d\tau \right] dz \sim A(S, C) \frac{\exp \left[ \left( a - \sqrt{b\beta} \right) t \right]}{a - \sqrt{b\beta}},$$

for some positive function  $A(S, C)$ . These asymptotic relations, along with (A.12), allow us to conclude that

$$\begin{aligned} & \text{if } \sqrt{b(S(\mathbf{x}), C(\mathbf{x}))\beta} < a(S(\mathbf{x}), C(\mathbf{x})) \\ & \text{then } \rho(t, \mathbf{x}) \longrightarrow \frac{a(S(\mathbf{x}), C(\mathbf{x})) - \sqrt{b(S(\mathbf{x}), C(\mathbf{x}))\beta}}{\zeta} \quad \text{as } t \rightarrow \infty. \end{aligned} \quad (\text{A.15})$$

Taken together, the asymptotic results (A.14) and (A.15) ensure that

$$\rho(t, \cdot) \longrightarrow \max \left( 0, \frac{a - \sqrt{b\beta}}{\zeta} \right) \quad \text{as } t \rightarrow \infty. \quad (\text{A.16})$$

Claims (2.31)-(2.32) follow from the asymptotic results (A.8), (A.10) and (A.16).  $\square$

### A.3 Formal analysis presented in Chapter 2

We consider the asymptotic behaviour of the weak solution of (2.37) subject to the initial condition (2.38)-(2.39) in the asymptotic regime  $\varepsilon \rightarrow 0$ .

**Hamilton-Jacobi equation.** Having introduced the WKB ansatz (2.41), i.e.  $n_\varepsilon(t, \mathbf{x}, y) = \exp[u_\varepsilon(t, \mathbf{x}, y)/\varepsilon]$ , we have the following

$$\begin{aligned} \partial_t n_\varepsilon &= \varepsilon^{-1} n_\varepsilon \partial_t u_\varepsilon, \quad \nabla_{\mathbf{x}} n_\varepsilon = \varepsilon^{-1} n_\varepsilon \nabla_{\mathbf{x}} u_\varepsilon, \quad \partial_y n_\varepsilon = \varepsilon^{-1} n_\varepsilon \partial_y u_\varepsilon, \\ \Delta_{\mathbf{x}} n_\varepsilon &= \left( \varepsilon^{-1} |\nabla_{\mathbf{x}} u_\varepsilon| \right)^2 n_\varepsilon + \varepsilon^{-1} n_\varepsilon \Delta_{\mathbf{x}} u_\varepsilon, \quad \partial_{yy}^2 n_\varepsilon = \left( \varepsilon^{-1} \partial_y u_\varepsilon \right)^2 n_\varepsilon + \varepsilon^{-1} n_\varepsilon \partial_{yy}^2 u_\varepsilon. \end{aligned}$$

Substituting the ansatz (2.41) into (2.37)<sub>1</sub>, and using the identities listed above, we obtain

$$\partial_t u_\varepsilon = R(y, \rho_\varepsilon(t, \mathbf{x}), S(\mathbf{x}), C(\mathbf{x})) + (\partial_y u_\varepsilon)^2 + |\nabla_{\mathbf{x}} u_\varepsilon|^2 + \varepsilon (\partial_{yy}^2 u_\varepsilon + \Delta_{\mathbf{x}} u_\varepsilon) \quad (\text{A.17})$$

subject to the initial condition  $u_\varepsilon(0, \mathbf{x}, y) = u_\varepsilon^0(\mathbf{x}, y)$ , with  $u_\varepsilon^0(\mathbf{x}, y)$  given by (2.38).

Letting  $\varepsilon \rightarrow 0$  in (A.17) we formally obtain the following equation for the leading-order term  $u$  of the asymptotic expansion for  $u_\varepsilon$

$$\partial_t u = R(y, \rho(t, \mathbf{x}), S(\mathbf{x}), C(\mathbf{x})) + (\partial_y u)^2 + |\nabla_{\mathbf{x}} u|^2 \quad \text{in } \Omega, \quad (\text{A.18})$$

where  $\rho(t, \mathbf{x})$  is the leading-order term of the asymptotic expansion for  $\rho_\varepsilon(t, \mathbf{x})$ . This is the Hamilton-Jacobi equation (2.42)<sub>1</sub>.

**Bounds on  $\rho$ .** We here make use of the notation  $\underline{\rho}$  and  $\bar{\rho}$  to indicate the infimum and supremum of  $\rho$ , respectively (i.e.  $\underline{\rho}(t, \mathbf{x}) \leq \rho(t, \mathbf{x}) \leq \bar{\rho}(t, \mathbf{x})$ ). From the maximum-minimum principle of parabolic equations (Perthame, 2015) we obtain from (2.5)<sub>1</sub>, under assumption (2.24),

$$\partial_t \underline{\rho}(t, \mathbf{x}) \geq \left[ \min_{y \in \mathbb{R}} (p(y, S(\mathbf{x})) - k(y, C(\mathbf{x}))) - \zeta \underline{\rho} \right] \underline{\rho} \Big|_{\mathbf{x}} \quad (\text{A.19})$$

where both sides of the equation are evaluated at the minimum of  $\underline{\rho}$ , i.e.  $\underline{\mathbf{x}} = \arg \min_{\mathbf{x} \in \Omega} \underline{\rho}(t, \mathbf{x})$ , and

$$\partial_t \bar{\rho}(t, \bar{\mathbf{x}}) \leq \left[ \max_{y \in \mathbb{R}} (p(y, S(\mathbf{x})) - k(y, C(\mathbf{x}))) - \zeta \bar{\rho} \right] \bar{\rho} \Big|_{\bar{\mathbf{x}}} \quad (\text{A.20})$$

where both sides of the equation are evaluated at the maximum of  $\bar{\rho}$ , i.e.  $\bar{\mathbf{x}} = \arg \max_{\mathbf{x} \in \Omega} \bar{\rho}(t, \mathbf{x})$ . Equation (A.19), together with the lower bound on  $\rho(0, \mathbf{x})$  in (2.40), implies  $\underline{\rho}(t, \underline{\mathbf{x}}) \geq 0$  for all  $t \geq 0$ . Equation (A.20), together with the upper bound on  $\rho(0, \mathbf{x})$  in (2.40), implies  $\bar{\rho}(t, \bar{\mathbf{x}}) \leq \max \left( \bar{\rho}(0, \bar{\mathbf{x}}), \frac{1}{\zeta} \max_{y \in \mathbb{R}} (p(y, S(\mathbf{x})) - k(y, C(\mathbf{x})))|_{\bar{\mathbf{x}}} \right)$  for all  $t \geq 0$ . Thus, overall we have

$$0 \leq \rho(t, \mathbf{x}) < \infty. \quad (\text{A.21})$$

Note that the rest of the analysis is conducted on the support of  $\rho$ .

**Constraint on  $u$ .** Consider  $\mathbf{x} \in \Omega$  such that  $\rho(t, \mathbf{x}) > 0$ , i.e.  $\mathbf{x} \in \text{supp}(\rho)$ , and let  $\bar{y}(t, \mathbf{x})$  be a nondegenerate maximum point of  $u(t, \mathbf{x}, y)$ , i.e.  $\bar{y}(t, \mathbf{x}) \in \arg \max_{y \in \mathbb{R}} u(t, \mathbf{x}, y)$  with

$$\partial_{yy}^2 u(t, \mathbf{x}, \bar{y}(t, \mathbf{x})) < 0, \quad (\text{A.22})$$

and, by definition,

$$\partial_y u(t, \mathbf{x}, \bar{y}(t, \mathbf{x})) = 0. \quad (\text{A.23})$$

Moreover, the upper bound on  $\rho$  given by (A.21) gives the constraint

$$u(t, \mathbf{x}, \bar{y}(t, \mathbf{x})) = 0 \quad \text{for all } (t, \mathbf{x}) \in (0, \infty) \times \Omega. \quad (\text{A.24})$$

This is the constraint imposed on the Hamilton-Jacobi equation for  $u(t, \mathbf{x})$  in (2.42)<sub>2</sub>.

**Canonical equation for  $\bar{y}$ .** Evaluating (A.18) at  $y = \bar{y}(t, \mathbf{x})$  and using (A.23) along with (A.24) yields

$$R(\bar{y}(t, \mathbf{x}), \rho(t, \mathbf{x}), S(\mathbf{x}), C(\mathbf{x})) = 0. \quad (\text{A.25})$$

Differentiating (A.23) with respect to  $t$  yields

$$\partial_{ty} u(t, \mathbf{x}, \bar{y}(t, \mathbf{x})) + \partial_{yy}^2 u(t, \mathbf{x}, \bar{y}(t, \mathbf{x})) \partial_t \bar{y}(t, \mathbf{x}) = 0$$

and, using (A.22), we can formally rewrite the above equation as

$$\partial_t \bar{y}(t, \mathbf{x}) = -(\partial_{yy}^2 u(t, \mathbf{x}, \bar{y}(t, \mathbf{x})))^{-1} \partial_{ty} u(t, \mathbf{x}, \bar{y}(t, \mathbf{x})). \quad (\text{A.26})$$

Furthermore, differentiating both sides of (A.18) with respect to  $y$ , evaluating the resulting equation at  $y = \bar{y}(t, \mathbf{x})$  and using (A.23) along with (A.24) gives

$$\partial_{ty} u(t, \mathbf{x}, \bar{y}(t, \mathbf{x})) = \partial_y R(\bar{y}(t, \mathbf{x}), \rho(t, \mathbf{x}), S(\mathbf{x}), C(\mathbf{x})).$$

Substituting the latter equation into (A.26) we formally obtain the following canonical equation for  $\bar{y}(t, \mathbf{x})$

$$\partial_t \bar{y}(t, \mathbf{x}) = -(\partial_{yy}^2 u(t, \mathbf{x}, \bar{y}(t, \mathbf{x})))^{-1} \partial_y R(\bar{y}(t, \mathbf{x}), \rho(t, \mathbf{x}), S(\mathbf{x}), C(\mathbf{x})). \quad (\text{A.27})$$

**Equilibrium values of  $\rho$  and  $\bar{y}$ .** Combining (A.25) and (A.27) we find that the steady-state values of  $\rho(t, \mathbf{x})$  and  $\bar{y}(t, \mathbf{x})$ , say  $\rho_\infty(\mathbf{x})$  and  $\bar{y}_\infty(\mathbf{x})$ , need to satisfy

$$\begin{cases} R(\bar{y}_\infty(\mathbf{x}), \rho_\infty(\mathbf{x}), S(\mathbf{x}), C(\mathbf{x})) = 0, \\ \partial_y R(\bar{y}_\infty(\mathbf{x}), \rho_\infty(\mathbf{x}), S(\mathbf{x}), C(\mathbf{x})) = 0. \end{cases}$$

Substituting (2.6) into the above system of equations, we formally obtain

$$\begin{cases} p(\bar{y}_\infty(\mathbf{x}), S(\mathbf{x})) - k(\bar{y}_\infty(\mathbf{x}), C(\mathbf{x})) - \zeta \rho_\infty(\mathbf{x}) = 0, \\ \partial_y [p(\bar{y}_\infty(\mathbf{x}), S(\mathbf{x})) - k(\bar{y}_\infty(\mathbf{x}), C(\mathbf{x}))] = 0, \end{cases}$$

which implies the following equilibrium solution

$$\begin{cases} \rho_\infty(\mathbf{x}) = \frac{1}{\zeta} [p(\bar{y}_\infty(\mathbf{x}), S(\mathbf{x})) - k(\bar{y}_\infty(\mathbf{x}), C(\mathbf{x}))], \\ \bar{y}_\infty(\mathbf{x}) = \arg \max_{y \in \mathbb{R}} [p(y, S(\mathbf{x})) - k(y, C(\mathbf{x}))], \end{cases} \quad (\text{A.28})$$

valid in the support of  $\rho_\infty$ , i.e. as long as  $\rho_\infty(\mathbf{x}) > 0$  with  $\rho_\infty(\mathbf{x})$  given by (A.28)<sub>1</sub>. Under definitions (2.13) and (2.14), rewritten in the form (2.15), we obtain

$$\begin{cases} \rho_\infty(\mathbf{x}) = \frac{1}{\zeta} \left( a(\mathbf{x}) - b(\mathbf{x}) (\bar{y}_\infty(\mathbf{x}) - h(\mathbf{x}))^2 \right), \\ \bar{y}_\infty(\mathbf{x}) = \arg \max_{y \in \mathbb{R}} \left( a(\mathbf{x}) - b(\mathbf{x}) (y(\mathbf{x}) - h(\mathbf{x}))^2 \right), \end{cases} \implies \begin{cases} \rho_\infty(\mathbf{x}) = \frac{1}{\zeta} a(\mathbf{x}), \\ \bar{y}_\infty(\mathbf{x}) = h(\mathbf{x}), \end{cases} \quad (\text{A.29})$$

that is a unique value of  $\bar{y}_\infty(\mathbf{x})$  for each  $\mathbf{x}$ , dictated by the local values of  $S(\mathbf{x})$  and  $C(\mathbf{x})$  through (2.16)-(2.18). Taken together, these formal results lead to the weak solution given in (2.43) and (2.44).

## A.4 Linear stability analysis presented in Chapter 5

In Section A.4.1 we conduct a LSA of the 1D system (5.15) under definitions (5.5), (5.8) and (5.9), and either under definition (5.16) or (5.17). Similarly, in Section A.4.2 we conduct an analogous LSA of the 2D system (5.15) under definitions (5.6), (5.8) and (5.9), and either under definition (5.16) or (5.17).

### A.4.1 Linear stability analysis of the 1D problem

**Spatially homogeneous steady states.** The spatially homogeneous steady states of the system (5.15)  $\bar{\mathbf{v}} = (\bar{n}, \bar{\rho}, \bar{m}, \bar{c})^\top$  satisfy

$$\left\{ \begin{array}{l} p\bar{n}(1 - \bar{n} - \bar{\rho}) = 0 \\ \mu(1 - \bar{n} - \bar{\rho})_+ - \gamma\bar{\rho}\bar{m} = 0 \\ \alpha_m\bar{n} - \lambda_m\bar{m} = 0 \\ \alpha_c\bar{n} - \lambda_c\bar{c} = 0 \end{array} \right., \quad (\text{A.30})$$

giving either  $\bar{\mathbf{v}} = (0, 1, 0, 0)^\top$  or  $\bar{\mathbf{v}} = (1, 0, \alpha_m/\lambda_m, \alpha_c/\lambda_c)^\top$ . Each spatially homogeneous steady state is therefore in the form

$$\bar{\mathbf{v}} = \left( \bar{n}, 1 - \bar{n}, \frac{\alpha_m}{\lambda_m}\bar{n}, \frac{\alpha_c}{\lambda_c}\bar{n} \right)^\top \quad (\text{A.31})$$

with either  $\bar{n} = 0$  or  $\bar{n} = 1$ . The first one ('cell-free' steady state) corresponds to the absence of cells, with the whole volume occupied by the ECM. The second one ('cell-full' steady state) corresponds to the case in which the cells have completely degraded the ECM and are occupying the whole volume. Note that in the absence of matrix degradation (i.e.  $\gamma = 0$ ) the spatially homogeneous steady states are still in the form (A.31), but with  $0 \leq \bar{n} \leq 1$ . We thus have, in addition to the two already described, infinitely many steady states in which both cells and ECM are present, filling up the volume. These might be referred to as 'intermediate' steady states henceforth, as they correspond to intermediate values of  $\bar{n}$ , namely  $0 < \bar{n} < 1$ .

**Remark 7.** *We are going to assume that  $n + \rho \leq 1$  for our LSA investigations. That is indeed satisfied by the steady states and it can be justified through the biological argument that random perturbations to these states are likely to arise naturally if there is space available, while changes that would imply  $n + \rho > 1$  are much less likely as they would require high energy expenses to oppose a high pressure environment. Mathematically this allows us to avoid complications that arise when introducing perturbations in the typical ansatz (vid. below) due to definition (5.3) and equation (5.10). In fact, under this*

assumption the term  $(1 - n - \rho)_+ = (1 - n - \rho) \geq 0$  for all perturbations allowed.

**Remark 8.** During the LSA reported in the following sections, we are going to use the fact that  $\bar{n} + \bar{\rho} = 1$  and  $\gamma\bar{\rho}\bar{n} = \gamma\bar{\rho}\bar{m} = \gamma\bar{\rho}\bar{c} = 0$  for all spatially homogeneous steady states, as concluded above, to further simplify calculations.

**Remark 9.** In the following we are interested in the biologically significant steady states, that is, we are going to consider the stability of the steady states with  $\bar{n} > 0$ , focussing on the cell-full steady state with additional observations drawn on the intermediate steady states in the absence of matrix degradation. We will however also include results for the cell-free steady state, which will clearly indicate that such steady state is degenerate.

**Remark 10.** In the following we will encounter inconclusive LSA results – i.e. option (iii) described in Section 5.2 – particularly for the cell-free steady state. In such case the stability of the steady state under consideration could be investigated by considering the dynamics along a center manifold about the steady state, as LSA calculations reported below are inconclusive for this case. Such investigation, however, goes beyond the scope of this study and we leave the mathematical details to the interested reader, referring them to Carr (2012); Guckenheimer and Holmes (2013). We will instead briefly comment on the linear stability or instability of the steady state in question by means of ad hoc numerical simulations.

**Stability under spatially homogeneous perturbations.** Introducing a small spatially homogeneous perturbation  $\mathbf{v} = \bar{\mathbf{v}} + \tilde{\mathbf{v}}(t)$ , with  $|\tilde{\mathbf{v}}| \ll 1$ , in (5.15) and linearising leads to the following system for the perturbation  $\tilde{\mathbf{v}}(t)$ :

$$\begin{cases} \partial_t \tilde{n} = -p\bar{n}(\tilde{n} + \tilde{\rho}) \\ \partial_t \tilde{\rho} = -\gamma(\bar{\rho}\tilde{m} + \bar{m}\tilde{\rho}) - \mu(\tilde{n} + \tilde{\rho}) \\ \partial_t \tilde{m} = \alpha_m \tilde{n} - \lambda_m \tilde{m} \\ \partial_t \tilde{c} = \alpha_c \tilde{n} - \lambda_c \tilde{c} \end{cases}. \quad (\text{A.32})$$

Assuming small perturbations in the form  $\tilde{n}, \tilde{\rho}, \tilde{m}, \tilde{c} \propto \exp(\psi t)$ , the system (A.32) can be rewritten as

$$\mathbf{M}\tilde{\mathbf{v}} = \mathbf{0}, \quad \text{with} \quad \mathbf{M} = \begin{pmatrix} \psi + p\bar{n} & p\bar{n} & 0 & 0 \\ \mu & \psi + \gamma\bar{m} + \mu & \gamma\bar{\rho} & 0 \\ -\alpha_m & 0 & \psi + \lambda_m & 0 \\ -\alpha_c & 0 & 0 & \psi + \lambda_c \end{pmatrix}. \quad (\text{A.33})$$

For a non-trivial solution we require  $\det \mathbf{M} = 0$ , leading to the characteristic equation

$$(\psi + \lambda_m)(\psi + \lambda_c) \left[ \psi^2 + \psi(p\bar{n} + \gamma\bar{m} + \mu) + \gamma p\bar{n}\bar{m} \right] = 0, \quad (\text{A.34})$$

Note that these steps simply provide an alternative route to the calculation of the eigenvalues  $\psi_i$  ( $i = 1, \dots, 4$ ) of the Jacobian matrix of the ODE system

$$\begin{cases} \dot{n} = pn(1 - n - \rho) \\ \dot{\rho} = \mu(1 - n - \rho)_+ - \gamma m \rho \\ \dot{m} = \alpha_m n - \lambda_m m \\ \dot{c} = \alpha_c n - \lambda_c c \end{cases} \quad (\text{A.35})$$

which corresponds to the spatially homogeneous version of the PDE system (5.15). The eigenvalues are then given by the roots of the characteristic polynomial on the left-hand side of equation (A.34). For  $\bar{n} = 1$  we have that all eigenvalues  $\psi_i$  ( $i = 1, \dots, 4$ ) are such that  $\text{Re}(\psi_i) < 0$  indicating the cell-full spatially homogeneous steady state is stable under spatially homogeneous perturbations. On the other hand, for  $\bar{n} = 0$  we have one zero eigenvalue, thus LSA is inconclusive. We briefly investigate this by constructing numerical solutions for the ODE system (A.35) under the nondimensional baseline parameter set (BPS) in Table 5.1, complemented with initial conditions mimicking spatially homogeneous perturbations from the cell-free steady state, i.e. steady state (A.31) with  $\bar{n} = 0$ . From the numerical solutions displayed in Figure A.1 we observe that:

- If the perturbation is such that  $n_0 = 0$ , then the cell-free steady state is stable under spatially homogeneous perturbations (cf. Figure A.1a);
- If the perturbation is such that  $n_0 > 0$  (although in this case  $n_0 + \rho_0 > 1$ ), then the cell-free steady state is unstable under spatially homogeneous perturbations (cf. Figure A.1b).

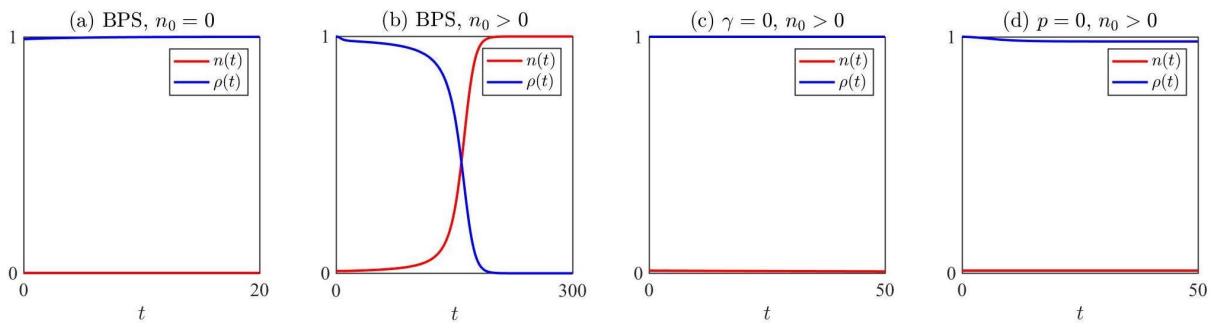


**Figure A.1:** Numerical solution for  $n$  and  $\rho$  of system (A.35), (a) under the BPS in Table 5.1 and initial conditions  $n_0 = 0$ ,  $\rho_0 = 0.99$ , (b) under the BPS and initial conditions  $n_0 = 0.01$ ,  $\rho_0 = 1$ , (c) same as in b except for  $\gamma = 0$ , (d) same as in b except for  $p = 0$ . Numerical solutions obtained using a finite difference scheme (forward in time).

Additional numerical tests with initial conditions such that  $n_0 > 0$  indicate that the cell-free steady state is stable under spatially-homogeneous perturbations also in the latter case if  $\gamma = 0$  (*cf.* Figure A.1c). Under the same initial condition, the solution also does not reach the cell-full steady state if  $p = 0$  (*cf.* Figure A.1d). In this case, however, it is because for  $p = 0$  there are infinitely many spatially homogeneous steady states of system (5.15) with  $0 \leq \bar{n} \leq 1$ ,  $\bar{\rho} = \mu(1 - \bar{\rho})/(\mu + \gamma\bar{m})$ ,  $\bar{m}$  and  $\bar{c}$  as in (A.31). Thus the initial condition considered in Figure A.1d may be seen as a spatially homogeneous perturbation (in  $\rho$ ) of the steady state  $\bar{n} = n_0$ , which is stable in this case. Overall these tests indicate that the cell-free steady state, which is unstable under spatially homogeneous perturbations with positive cell density, may owe such instability to cell proliferation and matrix degradation.

**Stability under spatially inhomogeneous perturbations.** We now introduce spatially inhomogeneous perturbations  $\mathbf{v} = \bar{\mathbf{v}} + \tilde{\mathbf{v}}(t, x)$ , with  $|\tilde{\mathbf{v}}| \ll 1$ . After linearisation, system (5.15) gives

$$\begin{cases} \partial_t \tilde{n} = D_n \Delta \tilde{n} - \bar{n} \nabla \cdot \mathcal{A}[\bar{\mathbf{v}} + \tilde{\mathbf{v}}(t, \cdot)] - p\bar{n}(\tilde{n} + \tilde{\rho}) \\ \partial_t \tilde{\rho} = -\gamma(\bar{\rho}\tilde{m} + \bar{m}\tilde{\rho}) - \mu(\tilde{n} + \tilde{\rho}) \\ \partial_t \tilde{m} = D_m \Delta \tilde{m} + \alpha_m \tilde{n} - \lambda_m \tilde{m} \\ \partial_t \tilde{c} = D_c \Delta \tilde{c} + \alpha_c \tilde{n} - \lambda_c \tilde{c} \end{cases}. \quad (\text{A.36})$$

We immediately notice that, as all steady states satisfy volume filling conditions, chemotaxis in the presence of saturating effects does not play a role in the dynamics of small perturbations from any of these states. After linearisation, for the 1D problem  $\mathcal{A}[\bar{\mathbf{v}} + \tilde{\mathbf{v}}(t, \cdot)]$  in equation (A.36)<sub>1</sub> becomes

$$\mathcal{A}[\bar{\mathbf{v}} + \tilde{\mathbf{v}}(t, \cdot)](x) = -\frac{1}{R}(S_{nn}\bar{n} + S_{n\rho}\bar{\rho}) \int_0^R \sum_{j=0}^1 \eta(j) \Gamma(r) (\tilde{n}(t, x + r\eta(j)) + \tilde{\rho}(t, x + r\eta(j))) dr \quad (\text{A.37})$$

with  $\Gamma(r)$  given by the corresponding definition in (5.8). Assuming small perturbations in the form  $\tilde{n}, \tilde{\rho}, \tilde{m}, \tilde{c} \propto \exp(\psi t + ikx)$ , we have that (A.37) can be rewritten as

$$\begin{aligned} \mathcal{A}[\bar{\mathbf{v}} + \tilde{\mathbf{v}}(t, \cdot)](x) &= -\frac{1}{R}(S_{nn}\bar{n} + S_{n\rho}\bar{\rho})(\tilde{n}(x) + \tilde{\rho}(x)) \int_0^R \Gamma(r) (\exp(ikr) - \exp(-ikr)) dr \\ &= -\frac{1}{R}(S_{nn}\bar{n} + S_{n\rho}\bar{\rho})(\tilde{n}(x) + \tilde{\rho}(x)) \frac{2i}{R} \int_0^R \left(1 - \frac{r}{R}\right) \sin(kr) dr \\ &= -\frac{2i}{R^2 k}(S_{nn}\bar{n} + S_{n\rho}\bar{\rho})(\tilde{n}(x) + \tilde{\rho}(x)) \left(1 - \frac{1}{Rk} \sin(Rk)\right). \end{aligned} \quad (\text{A.38})$$

We will make use of the notation

$$w_1(k) := \left(1 - \frac{1}{Rk} \sin(Rk)\right), \quad (\text{A.39})$$

for which we have that  $w_1(k) \geq 0$  for all  $k \in \mathbb{R}$ . Then, for small perturbations in the form introduced above, system (A.36) can be rewritten as  $\mathbf{M}\tilde{\mathbf{v}} = \mathbf{0}$  with  $\mathbf{M}$  given by

$$\mathbf{M} = \begin{pmatrix} \psi + D_n k^2 + A(k) + p\bar{n} & A(k) + p\bar{n} & 0 & 0 \\ \mu & \psi + \gamma\bar{m} + \mu & \gamma\bar{\rho} & 0 \\ -\alpha_m & 0 & \psi + D_m k^2 + \lambda_m & 0 \\ -\alpha_c & 0 & 0 & \psi + D_c k^2 + \lambda_c \end{pmatrix}, \quad (\text{A.40})$$

where

$$A(k) = \frac{2\bar{n}}{R^2} (S_{nn}\bar{n} + S_{n\rho}\bar{\rho}) w_1(k), \quad (\text{A.41})$$

with  $w_1(k)$  defined in (A.39). This immediately implies  $A(k) \geq 0$  for all steady states, those with, or without, matrix degradation. Imposing  $\det \mathbf{M} = 0$  for a non-trivial solution to  $\mathbf{M}\tilde{\mathbf{v}} = \mathbf{0}$ , we obtain the characteristic equation from which to infer the dispersion relation  $\psi(k^2)$  which, in its more general form, is given by

$$(\psi + D_c k^2 + \lambda_c)(p\bar{n} + A(k))[\psi + \gamma\bar{m} + (\psi + D_n k^2)(\psi + \gamma\bar{m} + \mu)] = 0. \quad (\text{A.42})$$

In order for the steady states to be unstable under spatially inhomogeneous perturbations – and patterns to arise – we require  $\operatorname{Re}(\psi(k^2)) > 0$  for some  $k^2 \in \mathbb{R}$ . It is clear from (A.42) that  $\operatorname{Re}(\psi(k^2)) < 0$  for all  $k^2$  and  $\bar{n} > 0$ . This indicates that the cell-full steady state (as well as the intermediate ones) is also stable under spatially inhomogeneous perturbations. We claim this to be due to saturation effects introduced in (5.16), while we may still expect chemotaxis and cell-to-cell or cell-to-matrix adhesion to play an important role for cell aggregation when the initially perturbed states are far from being volume filling, which will be investigated in the next paragraph. On the other hand, note that for  $\bar{n} = 0$  the second term in (A.42) is zero, thus any value of  $\psi$  will satisfy (A.42). However, substituting  $\bar{n} = 0$  from the beginning of this investigation would lead to the corresponding simpler version of matrix (A.40), the determinant of which would be given by the product of the entries in its main diagonal: in this case the dispersion relation would satisfy  $\operatorname{Re}(\psi(k^2)) < 0$  for all  $k^2$ , with the exception of  $k = 0$ , in which case we retrieve the results obtained above under spatially homogeneous perturbations.

**Considerations in the absence of saturation effects.** We here consider the pattern formation potential of the model in the absence of saturation effects, that is we make use

of definition (5.17) for the function  $f(n, \rho)$ , which influences both the chemotactic sensitivity of cells and their adhesion velocity. All results and considerations made earlier in this section on spatially homogeneous steady states and their stability under spatially homogeneous perturbations still hold. Introducing spatially inhomogeneous perturbations as done above leads to the following linearised system alternative to (A.36):

$$\left\{ \begin{array}{l} \partial_t \tilde{n} = D_n \Delta \tilde{n} - \chi \bar{n} \Delta \tilde{c} - \bar{n} \nabla \cdot \mathcal{A}[\bar{\mathbf{v}} + \tilde{\mathbf{v}}(t, \cdot)] - p \bar{n} (\tilde{n} + \tilde{\rho}) \\ \partial_t \tilde{\rho} = -\gamma(\bar{\rho} \tilde{m} + \bar{m} \tilde{\rho}) - \mu(\tilde{n} + \tilde{\rho}) \\ \partial_t \tilde{m} = D_m \Delta \tilde{m} + \alpha_m \tilde{n} - \lambda_m \tilde{m} \\ \partial_t \tilde{c} = D_c \Delta \tilde{c} + \alpha_c \tilde{n} - \lambda_c \tilde{c} \end{array} \right. \quad (\text{A.43})$$

in which, for the 1D problem,  $\mathcal{A}[\bar{\mathbf{v}} + \tilde{\mathbf{v}}(t, \cdot)]$  is given by

$$\mathcal{A}[\bar{\mathbf{v}} + \tilde{\mathbf{v}}(t, \cdot)](x) = \frac{1}{R} \int_0^R \sum_{j=0}^1 \eta(j) \Gamma(r) (S_{nn} \tilde{n}(t, x + r\eta(j)) + S_{n\rho} \tilde{\rho}(t, x + r\eta(j))) dr \quad (\text{A.44})$$

with  $\Gamma(r)$  given by the corresponding definition in (5.8). Then, assuming small perturbations in the form  $\tilde{n}, \tilde{\rho}, \tilde{m}, \tilde{c} \propto \exp(\psi t + ikx)$ , (A.44) can be rewritten as

$$\begin{aligned} \mathcal{A}[\bar{\mathbf{v}} + \tilde{\mathbf{v}}(t, \cdot)](x) &= \frac{1}{R} (S_{nn} \tilde{n}(x) + S_{n\rho} \tilde{\rho}(x)) \int_0^R \Gamma(r) (\exp(ikr) - \exp(-ikr)) dr \\ &= \frac{2i}{R^2 k} (S_{nn} \tilde{n}(x) + S_{n\rho} \tilde{\rho}(x)) w_1(k), \end{aligned} \quad (\text{A.45})$$

with  $w_1(k) \geq 0$  defined in (A.39). We can rewrite (A.43) as  $\mathbf{M} \tilde{\mathbf{v}} = \mathbf{0}$ , with  $\mathbf{M}$  given by

$$\mathbf{M} = \begin{pmatrix} \psi + D_n k^2 - A_n(k) + p \bar{n} & -A_\rho(k) + p \bar{n} & 0 & -\chi \bar{n} k^2 \\ \mu & \psi + \gamma \bar{m} + \mu & \gamma \bar{\rho} & 0 \\ -\alpha_m & 0 & \psi + D_m k^2 + \lambda_m & 0 \\ -\alpha_c & 0 & 0 & \psi + D_c k^2 + \lambda_c \end{pmatrix}, \quad (\text{A.46})$$

where

$$A_n(k) = \frac{2\bar{n}}{R^2} S_{nn} w_1(k) \quad \text{and} \quad A_\rho(k) = \frac{2\bar{n}}{R^2} S_{n\rho} w_1(k). \quad (\text{A.47})$$

We have both  $A_n(k) \geq 0$  and  $A_\rho(k) \geq 0$  for all  $k \in \mathbb{R}$ . Comparing these to (A.40) and (A.41), we see that in the absence of saturation effects the contributions from cell-to-cell and cell-to-matrix adhesion are decoupled and both give a negative contribution to  $\mathbf{M}$ . Furthermore, the contribution from chemotaxis does not vanish for any of the biologically significant steady states (i.e.  $\bar{n} > 0$ ). From this system the dispersion relation  $\psi(k^2)$

satisfies

$$(\psi + D_m k^2 + \lambda_m) \left\{ \left[ (\psi + D_n k^2) (\psi + \gamma \bar{n} + \mu) + (p \bar{n} - A_n(k)) (\psi + \gamma \bar{n}) \right. \right. \\ \left. \left. + \mu (A_\rho(k) - A_n(k)) \right] (\psi + D_c k^2 + \lambda_c) - \alpha_c \chi \bar{n} k^2 (\psi + \gamma \bar{n} + \mu) \right\} = 0. \quad (\text{A.48})$$

We now have that any biologically significant steady state – with or without matrix degradation – may be unstable under spatially inhomogeneous perturbations for strong enough cell-to-cell adhesion and/or chemotaxis, i.e. for large enough  $S_{nn}$  and  $\alpha_c$  and/or  $\chi$ . In addition, the magnitude of cell-to-cell adhesion  $A_n(k)$  in (A.47) will be larger for smaller values of the sensing radius  $R$  and larger values of  $\bar{n}$ , and the contribution from chemotactic movement will also increase for larger values of  $\bar{n}$ . Therefore in the absence of saturation effects steady states with  $\bar{n} > 0$  may be unstable under spatially inhomogeneous perturbations and patterns may form. This suggests that perturbed initial conditions far from being volume filling, so that saturation effects do not play a big role, might result in cell aggregation thanks to cell-to-cell adhesion and chemotaxis, as long as the initial cell density is large enough for these dynamics to play a significant role. On the other hand, for  $\bar{n} = 0$ , we reach the same conclusions as in the presence of saturation effects, that is the cell-free steady state is stable under spatially inhomogeneous perturbations, although we retrieve instability in the limit case of spatially homogeneous perturbations.

#### A.4.2 Linear stability analysis of the 2D problem

We here consider how the results obtained so far change in the 2D problem. Conclusions drawn in Section A.4.1 on the steady states of the system and their stability under spatially homogeneous perturbations remain unchanged and we report below the 2D calculations under spatially inhomogeneous perturbations.

**Considerations in the presence of saturation effects.** When introducing spatially inhomogeneous perturbations  $\mathbf{v} = \bar{\mathbf{v}} + \tilde{\mathbf{v}}(t, \mathbf{x})$ , after linearisation  $\mathcal{A}[\bar{\mathbf{v}} + \tilde{\mathbf{v}}(t, \cdot)](\mathbf{x})$  for the 2D problem is given by

$$\mathcal{A}[\bar{\mathbf{v}} + \tilde{\mathbf{v}}(t, \cdot)](\mathbf{x}) = -\frac{1}{R} (S_{nn} \bar{n} + S_{n\rho} \bar{\rho}) \int_0^R r \int_0^{2\pi} \boldsymbol{\eta}(\theta) \Gamma(r) (\tilde{n}(t, \mathbf{x} + r \boldsymbol{\eta}(\theta)) + \tilde{\rho}(t, \mathbf{x} + r \boldsymbol{\eta}(\theta))) d\theta dr \quad (\text{A.49})$$

with  $\Gamma(r)$  given by the corresponding definition in (5.8). Assuming small perturbations in the form  $\tilde{n}, \tilde{\rho}, \tilde{m}, \tilde{c} \propto \exp(\psi t + i \mathbf{k} \cdot \mathbf{x})$ , with  $\mathbf{k} = (k_1, k_2)^\top \in \mathbb{R}^2$ , then (A.49) can be

rewritten as

$$\begin{aligned}\mathcal{A}[\bar{\mathbf{v}} + \tilde{\mathbf{v}}(t, \cdot)](\mathbf{x}) &= -\frac{1}{R}(S_{nn}\bar{n} + S_{n\rho}\bar{\rho})(\tilde{n}(\mathbf{x}) + \tilde{\rho}(\mathbf{x})) \int_0^R r \int_0^{2\pi} \boldsymbol{\eta}(\theta) \Gamma(r) \exp(ir\mathbf{k} \cdot \boldsymbol{\eta}(\theta)) d\theta dr \\ &= \frac{3}{\pi R^3}(S_{nn}\bar{n} + S_{n\rho}\bar{\rho})(\tilde{n}(\mathbf{x}) + \tilde{\rho}(\mathbf{x})) [\Theta_I(\mathbf{k}) + i\Theta_R(\mathbf{k})]\end{aligned}\quad (\text{A.50})$$

where we have defined, with notation that will become more intuitive in a few steps,

$$\Theta_R(\mathbf{k}) = \int_0^{2\pi} \frac{\boldsymbol{\eta}(\theta)}{(\mathbf{k} \cdot \boldsymbol{\eta}(\theta))^2} \left[ \sin(R\mathbf{k} \cdot \boldsymbol{\eta}(\theta)) + \frac{2(\cos(R\mathbf{k} \cdot \boldsymbol{\eta}(\theta)) - 1)}{R\mathbf{k} \cdot \boldsymbol{\eta}(\theta)} \right] d\theta, \quad (\text{A.51})$$

$$\Theta_I(\mathbf{k}) = \int_0^{2\pi} \frac{\boldsymbol{\eta}(\theta)}{(\mathbf{k} \cdot \boldsymbol{\eta}(\theta))^2} \left[ 1 + \cos(R\mathbf{k} \cdot \boldsymbol{\eta}(\theta)) + \frac{2\sin(R\mathbf{k} \cdot \boldsymbol{\eta}(\theta))}{R\mathbf{k} \cdot \boldsymbol{\eta}(\theta)} \right] d\theta. \quad (\text{A.52})$$

We eventually obtain the system (A.40), in which  $k^2 = |\mathbf{k}|^2 = k_1^2 + k_2^2$  and, instead of  $A(k)$  as in (A.41), we have  $A(\mathbf{k})$  given by

$$A(\mathbf{k}) = -\frac{3\bar{n}}{\pi R^3}(S_{nn}\bar{n} + S_{n\rho}\bar{\rho}) \mathbf{k} \cdot [\Theta_R(\mathbf{k}) - i\Theta_I(\mathbf{k})], \quad (\text{A.53})$$

with  $\Theta_R(\mathbf{k})$  and  $\Theta_I(\mathbf{k})$  defined in (A.51) and (A.52). Despite the complexity of these integrals, we evaluated numerically the quantity  $-\mathbf{k} \cdot \Theta_R(\mathbf{k})$  – see Figure A.2 – which allowed us to conclude that, just like in the 1D case,  $\text{Re}(A(\mathbf{k})) \geq 0$  for all  $\mathbf{k} \in \mathbb{R}^2$ . For this problem we therefore obtain the corresponding version of equation (A.42) for the dispersion relation and reach the same conclusions as in section A.4.1 for the full system including saturation effects.

**Considerations in the absence of saturation effects.** In the absence of saturation effects,  $\mathcal{A}[\bar{\mathbf{v}} + \tilde{\mathbf{v}}(t, \cdot)](\mathbf{x})$  is given by the 2D correspondent of equation (A.44), that is

$$\mathcal{A}[\bar{\mathbf{v}} + \tilde{\mathbf{v}}(t, \cdot)](\mathbf{x}) = \frac{1}{R} \int_0^R r \int_0^{2\pi} \boldsymbol{\eta}(\theta) \Gamma(r) (S_{nn}\tilde{n}(t, \mathbf{x} + r\boldsymbol{\eta}(\theta)) + S_{n\rho}\tilde{\rho}(t, \mathbf{x} + r\boldsymbol{\eta}(\theta))) d\theta dr. \quad (\text{A.54})$$

Then assuming small perturbations in the form  $\tilde{n}, \tilde{\rho}, \tilde{m}, \tilde{c} \propto \exp(\psi t + i\mathbf{k} \cdot \mathbf{x})$ , with  $\mathbf{k} = (k_1, k_2)^\top \in \mathbb{R}^2$ , (A.54) can be rewritten as

$$\begin{aligned}\mathcal{A}[\bar{\mathbf{v}} + \tilde{\mathbf{v}}(t, \cdot)](\mathbf{x}) &= \frac{1}{R}(S_{nn}\tilde{n}(\mathbf{x}) + S_{n\rho}\tilde{\rho}(\mathbf{x})) \int_0^R r \int_0^{2\pi} \boldsymbol{\eta}(\theta) \Gamma(r) \exp(ir\mathbf{k} \cdot \boldsymbol{\eta}(\theta)) d\theta dr \\ &= -\frac{3}{\pi R^3}(S_{nn}\tilde{n}(\mathbf{x}) + S_{n\rho}\tilde{\rho}(\mathbf{x})) [\Theta_I(\mathbf{k}) + i\Theta_R(\mathbf{k})],\end{aligned}\quad (\text{A.55})$$

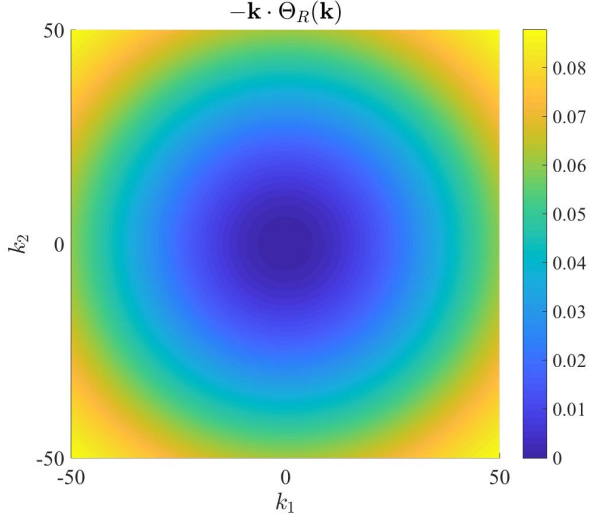


**Figure A.2:** Plot of the quantity  $-\mathbf{k} \cdot \Theta_R(\mathbf{k})$ , where  $\mathbf{k} = (k_1, k_2)^\top$  and  $\Theta_R(\mathbf{k})$  is defined in (A.51) for nondimensional  $R = 0.05$ . We clearly have  $-\mathbf{k} \cdot \Theta_R(\mathbf{k}) \geq 0$  for all  $\mathbf{k} \in \mathbb{R}^2$ , ensuring the real part of  $A(\mathbf{k})$  in (A.53), as well as those of  $A_n(\mathbf{k})$  and  $A_\rho(\mathbf{k})$  in (A.56) are non-negative. The integral in (A.51) was evaluated numerically using the composite trapezoidal rule for numerical integration.

with  $\Theta_R(\mathbf{k})$  and  $\Theta_I(\mathbf{k})$  defined in (A.51) and (A.52). We eventually end up with a system  $\mathbf{M}\tilde{\mathbf{v}} = \mathbf{0}$ , with  $\mathbf{M}$  defined as in (A.46), in which again we have  $k^2 = |\mathbf{k}|^2 = k_1^2 + k_2^2$  and, instead of  $A_n(k)$  and  $A_\rho(k)$  as in (A.47),  $A_n(\mathbf{k})$  and  $A_\rho(\mathbf{k})$  defined by

$$\begin{aligned} A_n(\mathbf{k}) &= -\frac{3\bar{n}}{\pi R^3} S_{nn} \mathbf{k} \cdot [\Theta_R(\mathbf{k}) - i\Theta_I(\mathbf{k})] \quad \text{and} \\ A_\rho(\mathbf{k}) &= -\frac{3\bar{n}}{\pi R^3} S_{n\rho} \mathbf{k} \cdot [\Theta_R(\mathbf{k}) - i\Theta_I(\mathbf{k})]. \end{aligned} \quad (\text{A.56})$$

Again, as demonstrated by the numerically evaluated quantity plot in Figure [A.2], we have that  $\text{Re}(A_n(\mathbf{k})) \geq 0$  and  $\text{Re}(A_\rho(\mathbf{k})) \geq 0$  for all  $\mathbf{k} \in \mathbb{R}^2$ , and can therefore reach analogous conclusions to those drawn in section [A.4.1] for the corresponding 2D problem.

## A.5 Derivation of the constitutive equations of the models of linear viscoelasticity in Chapter 7

In Section [A.5.1] are reported the rules of derivation of the constitutive equations of the 1D models of linear viscoelasticity presented in Section [7.2.2], using the Kelvin-Voigt and Maxwell models as illustrative examples. In Section [A.5.2] are reported the details of the derivation of the constitutive equations for the 2D Kelvin-Voigt and Maxwell models introduced in Section [7.2.3].

### A.5.1 Derivation of the 1D Kelvin-Voigt and Maxwell models

As presented in Section 7.2.2, the stress  $\sigma_e$  and strain  $\varepsilon_e$  of a purely elastic spring with elasticity  $E$  are related via Hooke's law

$$\sigma_e = E \varepsilon_e, \quad (\text{A.57})$$

which gives the constitutive equation (7.1) for the linear elastic model. Similarly, the stress  $\sigma_v$  and strain  $\varepsilon_v$  of a purely viscous damper with viscous modulus  $\eta$  are related via Newton's law

$$\sigma_v = \eta \partial_t \varepsilon_v, \quad (\text{A.58})$$

which gives the constitutive equation (7.2) for the linear viscous model. When two elements are connected in parallel the strain of each component is the same as the overall strain, while the overall stress is given by the sum of the stress of each component. For a Kelvin-Voigt arm, where a purely elastic spring and a purely viscous damper are connected in parallel, this means that the overall stress  $\sigma$  and strain  $\varepsilon$  are related via

$$\begin{cases} \varepsilon = \varepsilon_v = \varepsilon_e \\ \sigma = \sigma_v + \sigma_e \end{cases} \quad (\text{A.59})$$

where  $\sigma_e$  and  $\varepsilon_e$  satisfy (A.57), while  $\sigma_v$  and  $\varepsilon_v$  satisfy (A.58). Solving system (A.59) with (A.57) and (A.58) leads to the constitutive equation (7.3) for the Kelvin-Voigt model. On the other hand, when elements are connected in series the overall strain is given by the sum of the strain of each component, while the stress of each component is the same as the overall stress. For a Maxwell arm, where a purely elastic spring and a purely viscous damper are connected in series, this means that the overall stress  $\sigma$  and strain  $\varepsilon$  are related via

$$\begin{cases} \varepsilon = \varepsilon_v + \varepsilon_e \\ \sigma = \sigma_v = \sigma_e \end{cases} \quad (\text{A.60})$$

where  $\sigma_e$  and  $\varepsilon_e$  satisfy (A.57), while  $\sigma_v$  and  $\varepsilon_v$  satisfy (A.58). Solving system (A.60) with (A.57) and (A.58) leads to the constitutive equation (7.4) for the Maxwell model. The same rules can be applied to obtain the constitutive equations of any model of linear viscoelasticity starting from the system of purely elastic springs and purely viscous dampers that illustrates it, as was done to obtain (7.5) and (7.6) from Figures 7.1e and 7.1f respectively. Note that more complex models may be represented by different systems (e.g. the SLS model may be illustrated as a Maxwell arm connected in parallel with a purely elastic spring instead of as in Figure 7.1e), which lead to different constitutive equations but still capture the same properties characterising the model.

### A.5.2 Derivation of the 2D Kelvin-Voigt and Maxwell models

Landau & Lifshitz derived from first principles the stress-strain relations that give the 2D versions of the linear elastic model (7.1) and of the linear viscous model (7.2) in isotropic materials (Landau and Lifshitz, 1970), which read, respectively, as

$$\boldsymbol{\sigma}_e = \frac{E}{1+\nu} \left( \boldsymbol{\varepsilon}_e + \frac{\nu}{1-2\nu} \theta_e \mathbf{I} \right) \quad \text{and} \quad \boldsymbol{\sigma}_v = \eta \partial_t \boldsymbol{\varepsilon}_v + \mu \partial_t \theta_v \mathbf{I}. \quad (\text{A.61})$$

Here,  $E$  is Young's modulus,  $\nu$  is Poisson's ratio,  $\mathbf{I}$  is the identity tensor,  $\eta$  is the shear viscosity and  $\mu$  is the bulk viscosity. Moreover,  $\boldsymbol{\varepsilon}_e$  and  $\theta_e$  are the strain and dilation under a purely elastic deformation  $\mathbf{u}_e$  while  $\boldsymbol{\varepsilon}_v$  and  $\theta_v$  are the strain and dilation under a purely viscous deformation  $\mathbf{u}_v$ , which are all defined via (7.11).

In the case of a linearly viscoelastic material satisfying the Kelvin-Voigt model, the two dimensional analogue of (7.3) is simply given by

$$\boldsymbol{\sigma} = \boldsymbol{\sigma}_e + \boldsymbol{\sigma}_v = E' \boldsymbol{\varepsilon} + E' \nu' \theta \mathbf{I} + \eta \partial_t \boldsymbol{\varepsilon} + \mu \partial_t \theta \mathbf{I}. \quad (\text{A.62})$$

Here  $E'$  and  $\nu'$  are defined via (7.12) and there is no distinction between the strain or dilation associated with each component (i.e.  $\boldsymbol{\varepsilon} = \boldsymbol{\varepsilon}_e = \boldsymbol{\varepsilon}_v$  and  $\theta = \theta_e = \theta_v$ ), as the viscous and elastic components are connected in parallel. This is the stress-strain constitutive equation that is typically used to describe the contribution to the stress of the cell-ECM system coming from the ECM in 2D mechanochemical models of pattern formation (Cruywagen and Murray, 1992; Ferrenq et al., 1997; Javierre et al., 2009; Maini and Murray, 1988; Manoussaki, 2003; Murray, 2001; Murray et al., 1988; Murray and Oster, 1984a,b; Murray et al., 1983; Olsen et al., 1995; Oster et al., 1983; Perelson et al., 1986).

On the other hand, deriving the 2D analogues of Maxwell model (7.4), of the SLS model (7.5) and of the Jeffrey model (7.6) is more complicated due to the presence of elements connected in series. In the case of Maxwell model, using the fact that the overall strain and dilation will be distributed over the different components (i.e.  $\boldsymbol{\varepsilon} = \boldsymbol{\varepsilon}_e + \boldsymbol{\varepsilon}_v$  and  $\theta = \theta_e + \theta_v$ ) along with the fact that the stress on each component will be the same as the overall stress (i.e.  $\boldsymbol{\sigma} = \boldsymbol{\sigma}_e = \boldsymbol{\sigma}_v$ ), one finds

$$\frac{1}{\eta} \boldsymbol{\sigma} + \frac{1}{E'} \partial_t \boldsymbol{\sigma} = \partial_t \boldsymbol{\varepsilon} + \nu' \partial_t \theta \mathbf{I} + \left( \frac{\mu}{\eta} - \nu' \right) \partial_t \theta_v \mathbf{I}, \quad (\text{A.63})$$

with  $E'$  and  $\nu'$  being defined via (7.12). Under the simplifying assumption that

$$\frac{\mu}{\eta} = \nu' \quad (\text{A.64})$$

the stress-strain constitutive equation (A.63) can be rewritten in the form given by the generic 2D constitutive equation (7.10) under the parameter choices reported in Table 7.3. Dividing (A.62) by  $\eta$ , under the simplifying assumption (A.64), the stress-strain constitutive equation for the Kelvin-Voigt model (A.62) can be rewritten as

$$\frac{1}{\eta} \boldsymbol{\sigma} = \frac{E'}{\eta} \boldsymbol{\varepsilon} + \frac{E' \nu'}{\eta} \theta \mathbf{I} + \partial_t \boldsymbol{\varepsilon} + \nu' \partial_t \theta \mathbf{I},$$

which is in the form given by the generic 2D constitutive equation (7.10) under the parameter choices reported in Table 7.3.

## A.6 Creep and stress relaxation tests on the constitutive equations of the Kelvin-Voigt and Maxwell models in Chapter 7

We here report examples the mathematical procedures mimicking the creep and stress relaxation tests that can be used on the constitutive equations of linear viscoelastic models in order to identify the properties of linear viscoelastic materials captured by each model. The Kevin-Voigt and Maxwell models have been chosen as illustrative examples, and analogous methods have been used for the other models presented in Section 7.2.2.

**The creep test.** During a creep test we first impose a constant stress  $\sigma_a = \sigma_0$  at  $t = t_0$  and then remove it at  $t = t_1$ , and calculate the resulting strain  $\varepsilon(t)$  which can be plotted to give the creep curve (*cf.* left column in Figure A.3). For  $t < t_0$  we have  $\varepsilon = 0$ . For the Kelvin-Voigt model, the strain during the first phase of the creep test, here labelled  $\varepsilon_a(t)$  as resulting from the stress  $\sigma_a$ , satisfies the constitutive equation (7.3), i.e. we have

$$\dot{\varepsilon}_a + \frac{E}{\eta} \varepsilon_a = \frac{1}{\eta} \sigma_0 \quad \text{for } t_0 \leq t < t_1.$$

This can be solved using an integrating factor, yielding

$$\varepsilon_a(t) = \varepsilon(t_0 \leq t < t_1) = \frac{\sigma_0}{E} \left( 1 - \exp \left( \frac{E}{\eta} (t_0 - t) \right) \right), \quad (\text{A.65})$$

where we can identify a delayed elastic response. For the strain  $\varepsilon(t)$  during the second phase of the creep test, we note that removing the stress  $\sigma_0$  at  $t = t_1$  is the same as applying a stress  $\sigma_b = -\sigma_0$ , and by linearity we have that the strain  $\varepsilon_b$  due to stress removal is given by  $\varepsilon_b(t) = -\varepsilon_a(t - t_1)$ . Using Boltzmann's superposition principle, i.e.

$\varepsilon(\sigma_a + \sigma_b) = \varepsilon(\sigma_a) + \varepsilon(\sigma_b)$ , we can compute the overall strain

$$\varepsilon(t \geq t_1) = \varepsilon_a(t) - \varepsilon_a(t - t_1) = \frac{\sigma_0}{E} \left( \exp\left(\frac{Et_1}{\eta}\right) - 1 \right) \exp\left(\frac{E}{\eta}(t_0 - t)\right) \xrightarrow[t \rightarrow \infty]{} 0, \quad (\text{A.66})$$

where we can identify a delayed elastic recovery, eventually observing a total recovery – see also Figure A.3 (first column, second row). On the other hand, for the Maxwell model, the strain  $\varepsilon_a(t)$  during the first phase of the creep test satisfies the constitutive equation (7.4), and we have

$$\varepsilon_a(t) = \int_{t_0}^t \dot{\varepsilon}_a(s) ds = \int_{t_0}^t \left( \frac{\dot{\sigma}_a}{E} + \frac{\sigma_a}{\eta} \right) ds \quad \text{for } t_0 \leq t < t_1,$$

where we have used that  $\varepsilon(t < t_0) = 0$ . This can be integrated, using that  $\sigma_a = \sigma_0$  and that  $\dot{\sigma}_a(t) = \sigma_0 \delta(t - t_0)$  in the interval considered, and we obtain

$$\varepsilon_a(t) = \varepsilon(t_0 \leq t < t_1) = \frac{\sigma_0}{E} + \frac{\sigma_0}{\eta}(t - t_0), \quad (\text{A.67})$$

where we can identify an instantaneous elastic response and viscous flow. Following the same principles introduced above for the Kelvin-Voigt model, we have that the strain in the second phase of the creep test is given by

$$\varepsilon(t \geq t_1) = \varepsilon_a(t) - \varepsilon_a(t - t_1) = \frac{\sigma_0}{E} + \frac{\sigma_0}{\eta}t - \frac{\sigma_0}{E} - \frac{\sigma_0}{\eta}(t - t_1) = \frac{\sigma_0}{\eta}t_1 \xrightarrow[t \rightarrow \infty]{} \frac{\sigma_0}{\eta}t_1 \quad (\text{A.68})$$

where we can recognise an instantaneous elastic recovery (*cf.* cancelled out terms) and a permanent set (residual strain) – see also Figure A.3 (first column, third row). Note that this is exactly due to viscous flow, and therefore specifically characterises viscoelastic fluid models such as Maxwell's (viscous flow and permanent set are observed in the same way repeating the test for the linear viscous and the Jeffrey model).

**The stress relaxation test.** During a stress relaxation test we impose a constant strain  $\varepsilon_0$  at  $t = t_0$ , and calculate the resulting stress  $\sigma(t)$  which can be plotted to give the stress relaxation curve (*cf.* left column in Figure A.3). For  $t < t_0$  we have  $\sigma = 0$ . For the Kelvin-Voigt model we can apply the constitutive equation (7.3) directly and obtain

$$\sigma(t \geq t_0) = E \varepsilon_0 + \eta \varepsilon_0 \delta(t - t_0), \quad (\text{A.69})$$

which implies  $\dot{\sigma}(t \geq t_0) = 0$  and we observe no stress relaxation – see also Figure A.3 (second column, second row). Note that the singularity in  $\sigma$  is due to the presence of the viscous damper, since it is unphysical to impose an instantaneous strain on a purely viscous damper. For this reason, we have indicated stress relaxation as N.A. for the linear viscous model in Table 7.2. For the Maxwell model, on the other hand, we have that the

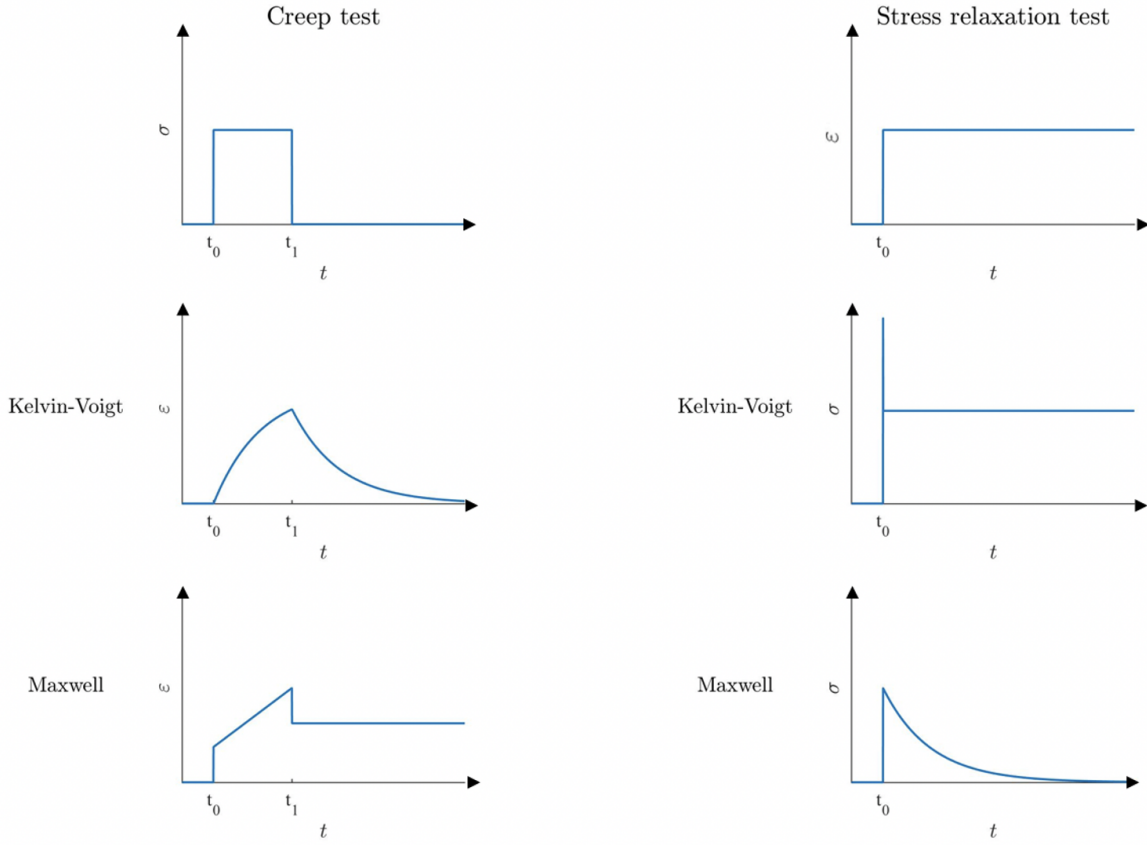


**Figure A.3:** *Left column:* Creep curve for the Kelvin-Voigt model (second row) and the Maxwell model (third row) obtained under a constant stress (first row) applied during a creep test. The curves are obtained plotting functions (A.65) and (A.66) for the Kelvin-Voigt model, and (A.67) and (A.68) for the Maxwell model. *Right column:* Stress relaxation curve for the Kelvin-Voigt model (second row) and the Maxwell model (third row) obtained under a constant strain (first row) applied during a stress relaxation test. The curves are obtained plotting functions (A.69) and (A.70) for the Kelvin-Voigt and Maxwell models respectively.

stress satisfies

$$\dot{\sigma} + \frac{E}{\eta} \sigma = E \dot{\varepsilon} \quad \text{for } t \geq t_0 .$$

Using an integrating factor and the fact that  $\dot{\varepsilon} = \varepsilon_0 \delta(t - t_0)$ , we obtain

$$\sigma(t \geq t_0) = E \varepsilon_0 \exp \left( \frac{E}{\eta} (t_0 - t) \right) , \quad (\text{A.70})$$

which implies  $\dot{\sigma}(t \geq t_0) < 0$  so we observe stress relaxation – see also Figure A.3 (second column, third row).

# Appendix B

## Numerical details

The numerical schemes used to construct numerical solutions to the models studied in this thesis are based on finite difference and finite volume methods. We first give a brief introduction of these methods, for 1D problems, followed by details of the schemes used in each part: the scheme developed for the numerical simulations reported in Part II is described in detail in Section B.1; the scheme developed by Alf Gerisch (TU Darmstadt) used for the numerical simulations in Part III is described in Section B.2; the scheme developed for the numerical simulations reported in Part IV is described in detail in Section B.3.

### Spatial discretisation: finite differences, finite volumes, numerical integration.

Consider a 1D domain  $\Omega = [0, L]$ . Finite difference and finite volume methods rely on a discretisation of the domain, similarly to as illustrated in Figure B.1. The methods used in this thesis rely on homogeneous discretisations of the domain, therefore certain details provided below may not apply to schemes developed on unstructured meshes.

Consider a domain discretised into a grid of, say,  $K + 1$  grid points, similar to the one illustrated in Figure B.1a. **Finite difference methods** (LeVeque, 2007) rely on the approximation of derivatives in the differential equation by finite difference formulas at each grid point. These can be obtained from Taylor expansions of the function whose derivative we need to approximate centred at different points on the grid, and truncating the obtained expression by ignoring terms of order  $\Delta x^N$  ( $\Delta x = L/K$  is the distance between two grid points) for an approximation of order  $N$ . The approximations may be ‘backward’, ‘forward’ or ‘central’, depending on which points of the grid are used to obtain the approximation. This gives a large but finite algebraic system of equations to be solved in place of the differential equation, which can often be done efficiently using programming and numeric computing platforms (e.g. MATLAB). Finite difference approximations are used in the schemes presented in Sections B.1 and B.3.

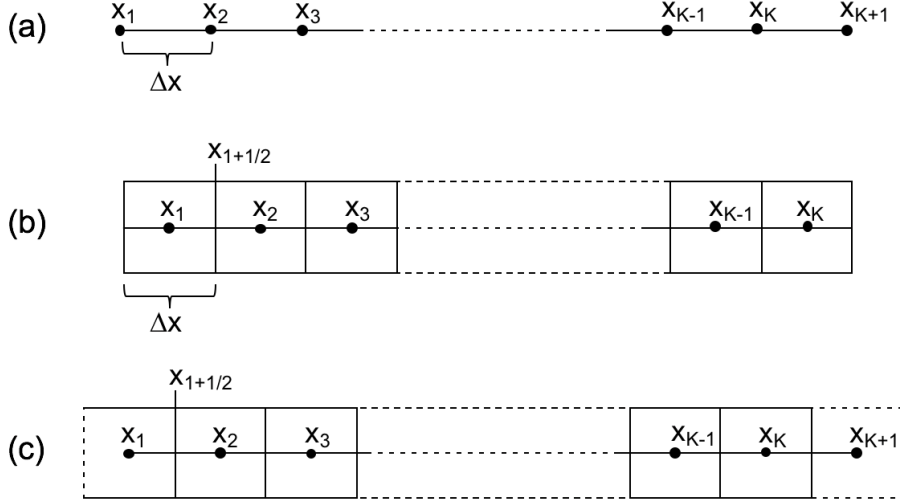


**Figure B.1:** Schematic illustration of the spatial discretisation of the (1D) domain used in this thesis: (a) grid with  $K + 1$  grid points  $x_i$  ( $i = 1, \dots, K + 1$ ) used for the finite difference scheme presented in Section B.1; (b) grid made up of  $K$  cells (finite volumes) of centres  $x_i$  ( $i = 1, \dots, K$ ), left and right grid cell interfaces  $x_{i-1/2}$  and  $x_{i+1/2}$  ( $i = 1, \dots, K$ ), used for the finite volume scheme described in Section B.2; (c) grid with  $K + 1$  grid points  $x_i$  ( $i = 1, \dots, K + 1$ ) with cells constructed centred at each  $x_i$  used for the mixed finite difference and finite volume scheme presented in Section B.3.

**Finite volume methods** (Eymard et al., 2000), on the other hand, rely on the discretisation of the domain into, say,  $K$  grid cells (i.e. finite volumes), similar to as illustrated in Figure B.1b. The finite volume approximations are derived by integrating the differential equation over each cell (control volume) and using the divergence theorem to obtain an integral formulation of the fluxes over the boundary of the control volume. Then numerical fluxes can be computed at the grid cell interfaces, which is particularly helpful when solving transport equations. In this case a popular approach is to define the approximate advective flux at each interface according to the sign of its velocity, a method known as ‘upwinding’ that helps to avoid spurious oscillations and negative solution values often introduced by large advective fluxes. Finite volume methods are at the basis of the scheme described in Section B.2, as well as in the mixed finite difference and finite volume scheme presented in Section B.3 for the advective/taxis terms.

Finally, for the **numerical approximation of the integral terms** found in Parts II and III, we make use of finite difference schemes based on a weighted sum of the values of the integrand at a finite set of integration points. The method described in Section B.2, in particular, relies on the composite trapezoidal rule of numerical integration. This consists of applying the trapezoidal rule, i.e. the approximation of an integral by calculating the area of the trapezoid fitting under the curve of the integrand, over a partition of the integration interval and summing up the results.

**Time integration: explicit and implicit schemes.** Time integration is computed via explicit or implicit numerical methods. These can be obtained by approximating the time derivatives using, respectively, forward and backward difference approximations. Explicit schemes, such as the one presented in Section B.1, allow for the calculation of the solution at the next timestep solely relying on the solution at the current and/or previous timesteps. Implicit schemes, such as the one presented in Section B.3 which relies on the Method of Lines (MOL), require an implicit equation involving the solution at the next and current (and/or previous) timesteps to be solved instead. Implicit methods are computationally more expensive than explicit ones, but are better suited to solve stiff systems of equations, for which explicit schemes require extremely small step sizes for numerical stability (LeVeque, 2007).

## B.1 Numerical schemes used in Chapter 2

As introduced in Section 2.3.1, we construct numerical solutions both to system (2.26) and system (2.30) in 1D under stationary distributions of  $s(t, x) \equiv S(x)$  and  $c(t, x) \equiv C(x)$  for Section 2.3.2. Then we construct numerical solutions both to system (2.26) and system (2.5) in 2D, each coupled with equations (2.19) and (2.20), for Section 2.3.3 and 2.3.4 respectively. Therefore, Appendix B.1 is organised as follows: the schemes developed for simulation in 1D spatial domains, both to solve (2.26) and (2.30) for given  $S(x)$  and  $C(x)$ , are reported in Section B.1.1; the scheme developed for simulations in 2D spatial domains, to solve (2.5) together with (2.19) and (2.20), are reported in Section B.1.2. Comments on how the scheme changes to solve (2.26), together with (2.19) and (2.20), in 2D will be made throughout Section B.1.2. Files containing the code corresponding to the schemes is available on GitLab<sup>1</sup>

### B.1.1 Numerical schemes for 1D spatial domains

Numerical simulations in 1D rely on a uniform discretisation of the spatial domain  $[0, 0.05]$  consisting of  $K_x + 1 = 101$  grid points and a uniform discretisation of the computational domain  $[-L, L]$  ( $L = 7$ ) for the independent variable  $y$  consisting of  $K_y + 1 = 1000$  grid points, in a similar fashion to the example grid (a) in Figure B.1. We denote the spatial grid width with  $\Delta x$  and the grid width of the computational domain for the independent variable  $y$  as  $\Delta y$ . We also consider a uniform discretisation of the time interval  $[0, T]$  with grid width  $\Delta t = 0.01$  and denote the total number of grid points by  $K_t + 1$ .

---

<sup>1</sup><https://github.com/ChiaraVilla/VillaEtAl2021Phenotypes>

The phenotypic distribution  $n(t, x, y)$  is approximated as

$$n(t_i, x_j, y_m) \approx n_{j,m}^i \quad \text{for } i = 0, \dots, K_t, \quad j = 0, \dots, K_x, \quad m = 0, \dots, K_y,$$

while the cell density  $\rho(t, x)$ , the local mean trait  $\mu(t, x)$  and the inverse variance  $v(t, x) = 1/\sigma^2(t, x)$  are approximated as

$$\rho(t_i, x_j) \approx \rho_j^i, \quad \mu(t_i, x_j) \approx \mu_j^i, \quad v(t_i, x_j) \approx v_j^i \quad \text{for } i = 0, \dots, K_t, \quad j = 0, \dots, K_x.$$

Finally we make use of the notation  $S_j := S(x_j)$  and  $C_j := C(x_j)$  for the stationary distributions of oxygen  $S(x)$  and chemotherapeutic agent  $C(x)$  at each grid point  $j = 0, \dots, K_x$ .

**Numerical scheme for the nonlocal reaction-diffusion equation (2.26).** We rewrite the 1D version of the reaction-diffusion equation (2.26) under stationary distributions of oxygen and chemotherapeutic agent as

$$\partial_t n = \beta \partial_{yy}^2 n + R(y, \rho(t, x), S(x), C(x))n, \quad \text{with } \rho(t, x) = \int_{-L}^L n(t, x, y) dy,$$

where  $R$  is defined as in (2.6) with (2.15)-(2.18). We discretise the equation as

$$n_{j,m}^{i+1} = n_{j,m}^i + \Delta t \left[ \frac{\beta}{\Delta y^2} (n_{j,m+1}^i - 2n_{j,m}^i + n_{j,m-1}^i) + R_{j,m}^i n_{j,m}^i \right], \quad (\text{B.1})$$

where we have used the notation  $R_{j,m}^i := R(y_m, \rho_j^i, S_j, C^j)$ , with

$$\rho_j^i = \sum_{m=0}^{K_y} n_{j,m}^i \Delta y. \quad (\text{B.2})$$

In particular, equation (B.1) is based on a first order forward difference approximation for the time derivative, thus yielding an explicit scheme, and a second order central difference approximation for the diffusion term in  $y$ . For this reason, the scheme (B.1) is based on a three-point stencil and can only be solved for  $m = 2, \dots, K_y - 1$ . The solution for  $m = 1$  and  $m = K_y$  is calculated using a first order (forward and backward, respectively) difference approximation of the derivative  $\partial_y$ , which is set to zero at the boundary (i.e. at  $y = -L$  and  $y = L$ ) under the zero-flux boundary conditions (2.52). This yields

$$n_{j,1}^i = n_{j,2}^i \quad \text{and} \quad n_{j,K_y}^i = n_{j,K_y-1}^i. \quad (\text{B.3})$$

**Numerical scheme for the system (2.30).** Note first of all that, thanks to absence of spatial derivatives, the PDE system (2.30) is *de facto* an ODE system to be solved at each point in space. Therefore, we rewrite the 1D version of the system (2.30) under

stationary distributions of oxygen and chemotherapeutic agent as

$$\begin{cases} v' = 2(b(S, C) - \beta v^2), \\ \mu' = (2b(S, C)/v)(h(S, C) - \mu), \\ \rho' = [(a(S, C) - (b(S, C)/v) - b(S, C)(\mu - h(S, C))^2) - \zeta\rho]\rho. \end{cases}$$

Where  $a$ ,  $b$  and  $h$  are defined as in (2.18)-(2.18). Introducing the notation  $a_j := a(S_j, C_j)$ ,  $b_j := b(S_j, C_j)$  and  $h_j := h(S_j, C_j)$ , we discretise system (2.30) as

$$\begin{cases} v_j^{i+1} = v_j^i + \Delta t [2(b_j - \beta(v_j^i)^2)], \\ \mu_j^{i+1} = \mu_j^i + \Delta t [(2b_j/v_j^i)(h_j - \mu_j^i)], \\ \rho_j^{i+1} = \rho_j^i + \Delta t \left\{ \left[ (a_j - (b_j/v_j^i)) - b_j(\mu_j^i - h_j)^2 \right] - \zeta\rho_j^i \right\}. \end{cases} \quad (\text{B.4})$$

System (B.4) is based on a first order forward difference approximation of the time derivative corresponding, at each point in space, to what is known as the explicit Euler method for solving systems of ODEs.

**Remark 11.** System (B.4) is complemented with initial conditions (2.49) with exactly  $\rho_0 = 10^8$ . On the other hand system (B.1)-(B.3) is complemented with initial conditions (2.27) with (2.49), where  $\rho_0 \approx 10^8$ . This is because we seek to have corresponding numerical initial conditions for the two problems, in order to compare the numerical solutions of the two systems and verify the analytical results of Section 2.2.1. Initial condition (2.27) is defined as a Gaussian-like function with support  $\mathbb{R}$ , integrating to  $\rho_0$ . However, integrating the Gaussian-like function over the finite computational domain  $[-L, L]$  introduces an approximation error and the resulting quantity does not match the required initial cell density of  $10^8$ . In order for these to match,  $\rho_0$  in (2.27) needs to be defined as

$$\rho_0 = 10^8 \frac{\sqrt{2\pi\sigma_0^2(\mathbf{x})}}{\int_{-L}^L \exp\left[-\frac{1}{2\sigma_0^2(\mathbf{x})}(y - \mu_0(\mathbf{x}))^2\right] dy} \approx 10^8$$

for the numerical initial condition complementing scheme (B.1)-(B.3).

### B.1.2 Numerical schemes for 2D spatial domains

Numerical simulations in 2D rely on a uniform discretisation of the spatial domain  $[0, 0.05] \times [0, 0.05]$  consisting of  $(K_x + 1) \times (K_x + 1) = 101 \times 101$  grid points and, as in the 1D case, a uniform discretisation of the computational domain  $[-L, L]$  ( $L = 7$ ) for the independent variable  $y$  consisting of  $K_y + 1 = 1000$  grid points. Again, we denote the spatial grid width in each direction with  $\Delta x$  and the grid width of the computational domain for the independent variable  $y$  as  $\Delta y$ . We again consider a uniform discretisation

of the time interval  $[0, T]$  with grid width  $\Delta t = 0.01$  and denote the total number of grid points by  $K_t + 1$ . The phenotypic distribution  $n(t, \mathbf{x}, y)$  is approximated as

$$n(t_i, x_j, x_l, y_m) \approx n_{j,l,m}^i \quad \text{for } i = 0, \dots, K_t, \quad j, l = 0, \dots, K_x, \quad m = 0, \dots, K_y,$$

while the cell density  $\rho(t, \mathbf{x})$ , oxygen concentration  $s(t, \mathbf{x})$  and chemotherapeutic agent concentration  $c(t, \mathbf{x})$  are approximated as

$$\rho(t_i, x_j, x_l) \approx \rho_{j,l}^i, \quad s(t_i, x_j, x_l) \approx s_{j,l}^i, \quad c(t_i, x_j, x_l) \approx c_{j,l}^i \quad \text{for } i = 0, \dots, K_t, \quad j, l = 0, \dots, K_x.$$

**Numerical scheme for the nonlocal reaction-diffusion equation (2.5).** We rewrite the 2D version of the reaction-diffusion equation (2.5) as

$$\partial_t n = D_n \Delta_{\mathbf{x}} n + \beta \partial_{yy}^2 n + R(y, \rho(t, \mathbf{x}), s(t, \mathbf{x}), c(t, \mathbf{x})) n, \quad \text{with } \rho(t, \mathbf{x}) = \int_{-L}^L n(t, \mathbf{x}, y) dy,$$

where  $R$  is defined as in (2.6) with (2.15)-(2.18). We discretise the equation as

$$\begin{aligned} n_{j,l,m}^{i+1} &= n_{j,l,m}^i + \Delta t \left[ \frac{D_n}{\Delta x^2} (n_{j+1,l,m}^i + n_{j,l+1,m}^i - 4n_{j,l,m}^i + n_{j-1,l,m}^i + n_{j,l-1,m}^i) \right. \\ &\quad \left. + \frac{\beta}{\Delta y^2} (n_{j,l,m+1}^i - 2n_{j,l,m}^i + n_{j,l,m-1}^i) + R_{j,l,m}^i n_{j,l,m}^i \right], \end{aligned} \quad (\text{B.5})$$

where we have used the notation  $R_{j,l,m}^i := R(y_m, \rho_{j,l}^i, s_{j,l}^i, c_{j,l}^i)$ , with

$$\rho_{j,l}^i = \sum_{m=0}^{K_y} n_{j,l,m}^i \Delta y. \quad (\text{B.6})$$

In particular, equation (B.5) is based on a first order forward difference approximation for the time derivative, thus yielding an explicit scheme, and a second order central difference approximation for the diffusion terms in  $\mathbf{x}$  and  $y$ . For this reason, the scheme (B.5) is based on a seven-point stencil and can only be solved for  $j, l = 2, \dots, K_x - 1$  and  $m = 2, \dots, K_y - 1$ . The solution at the end points of the grid is calculated using a first order (forward and backward, respectively) difference approximation of the derivatives  $\partial_{x_1}$ ,  $\partial_{x_2}$  and  $\partial_y$ , which are set to zero at the boundary under the zero-flux boundary conditions (2.5)<sub>3</sub> and (2.52). This yields, at each timestep  $i$ ,

$$\begin{aligned} n_{1,l,m}^i &= n_{1,l,m}^i \quad \text{and} \quad n_{K_x,l,m}^i = n_{K_x-1,l,m}^i \quad \text{for } l = 2, \dots, K_x - 1, \quad m = 2, \dots, K_y - 1, \\ n_{j,1,m}^i &= n_{j,2,m}^i \quad \text{and} \quad n_{j,K_x,m}^i = n_{j,K_x-1,m}^i \quad \text{for } j = 1, \dots, K_x, \quad m = 2, \dots, K_y - 1, \\ n_{j,l,1}^i &= n_{j,l,2}^i \quad \text{and} \quad n_{j,l,K_y}^i = n_{j,l,K_y-1}^i \quad \text{for } j, l = 1, \dots, K_x. \end{aligned} \quad (\text{B.7})$$

In the absence of spatial diffusion, i.e. for the 2D system (2.26) coupled with (2.19) and (2.20), we obtain a scheme analogous to (B.5) with  $D_n = 0$ , together with (B.6),

and boundary conditions  $(B.7)_3$  as in such case the scheme for  $n_{j,l,m}^{i+1}$  is valid for all  $j, l = 1, \dots, K_x$ .

**Numerical scheme for the balance equations (2.19) and (2.19).** We rewrite equation (2.19), together with definitions (2.22)-(2.23), as

$$\partial_t s = D_s \Delta_{\mathbf{x}} s - \int_{\mathbb{R}} r_s(y, s) n(t, \mathbf{x}, y) dy - \lambda_s s + I_s \mathbf{1}_{\omega}(\mathbf{x})$$

where  $r_s$  is defined as in (2.21). This is discretised as

$$s_{j,l}^{i+1} = s_{j,l}^i + \Delta t \left[ \frac{D_s}{\Delta x^2} (s_{j+1,l}^i + s_{j,l+1}^i - 4s_{j,l}^i + s_{j-1,l}^i + s_{j,l-1}^i) - \sum_{m=0}^{K_y} (r_s)_{j,l,m}^i n_{j,l,m}^i - \lambda_s s_{j,l}^i + I_s W_{i,j} \right], \quad (B.8)$$

where we have used the notation  $(r_s)_{j,l,m}^i := r_s(y_m, s_{j,l}^i)$ , and where  $W_{i,j}$  is a  $(K_x + 1) \times (K_x + 1)$  matrix of ones in correspondence of the blood vessel positions and zeros otherwise. As for (B.5), equation (B.8) is based on a finite difference scheme that is first order forward in time and second order central in space, computed on a five-point stencil. The solution at boundary grid points are computed, as in (B.7), from the zero-flux boundary conditions (2.19)<sub>2</sub> using a first order finite difference approximation in space, i.e.

$$\begin{aligned} s_{1,l}^i &= s_{1,l}^i \text{ and } s_{K_x,l}^i = s_{K_x-1,l}^i \text{ for } l = 2, \dots, K_x - 1, \\ s_{j,1}^i &= s_{j,2}^i \text{ and } s_{j,K_x}^i = s_{j,K_x-1}^i \text{ for } j = 1, \dots, K_x. \end{aligned} \quad (B.9)$$

The scheme for the numerical computation of the solution  $c(t, \mathbf{x})$  to equation (2.20), together with definitions (2.22)-(2.23), is analogous to that here described for  $s(t, \mathbf{x})$ .

## B.2 Numerical method used in Chapter 5

The code used for the numerical simulations reported in Section 5.3 for the nonlocal PDE model introduced in Section 5.1 was developed by Alf Gerisch, from the Technical University of Darmstadt. We here describe the main features of the scheme and refer the interested reader to publications which report its sophisticated details – e.g. Gerisch (2010); Gerisch and Chaplain (2006, 2008). As introduced in Section 5.3.1, we solve the nondimensional system (5.15)-(5.16) in  $\Omega = (0, 1)$  in 1D and  $\Omega = (0, 1) \times (0, 1)$  in 2D, with zero-flux boundary conditions and initial conditions (5.13)-(5.14).

**Spatial discretisation.** The numerical solution is constructed following the MOL by first discretising the nonlocal model in space, yielding an initial value problem for a large system of stiff ODEs. This is obtained using a second-order finite volume approach, described in detail by Gerisch and Chaplain (2006) and references therein. First, the spatial domain  $\Omega$  is discretised by an equi-spaced linear grid of  $K = 1000$  grid cells in 1D, in a similar fashion to the example grid (b) in Figure B.1 and  $K \times K = 100 \times 100$  grid cells in 2D. Reaction terms are computed using approximations at the grid cell centres. Diffusion terms are calculated using a second-order finite difference approximation of the diffusion operator within each grid cell (e.g. in 1D the three-point stencil used is made up of the left grid cell interface, the grid cell centre and the right grid cell interface). Advection (chemotaxis and adhesion) terms exploit the calculation of the advective flux at the grid cell interfaces using first-order upwinding – see Section B.3 (equations (B.16)–(B.18)) – with the additional use of flux limiter functions in order to ensure an accurate and at the same time non-negative approximation of the taxis and adhesion terms; note that here in particular we employ the Koren flux limiter ( $k = 1/3$ ,  $\delta = 0.25$ ) (Gerisch and Chaplain, 2006; Koren, 1993). Zero-flux boundary conditions are simply implemented by imposing the flux to be zero at the interfaces corresponding to the boundary of  $\Omega$ .

**Computation of the nonlocal term.** In order to calculate the adhesion terms, we require a computation of the nonlocal adhesion velocity at each grid cell interface. A detailed account of the approximation of the nonlocal term in a periodic boundary condition setting is given by Gerisch (2010). The integral needs to be computed over integration domains which can be discretised by means of finer stencils overlapping the main spatial grid; note in particular that for the sensing region in 2D a circular stencil is used – see (Gerisch, 2010, Figure 6). A piecewise-constant reconstruction of the quantity  $g(\mathbf{v})$  in (5.5) is used to approximate the function within the sensing region starting from the approximation evaluated at the grid cell interfaces. Then the composite trapezoidal rule of numerical integration is applied over the discretised integration domain. The combination of these two steps gives rise to a matrix-vector product resulting in a vector for the adhesion velocity at each grid cell interface. In the case of periodic boundary conditions the matrix involved in this product is a circulant<sup>2</sup> matrix. Under zero-flux boundary conditions the matrices involved in this product have Toeplitz<sup>3</sup> structure, and can be embedded in slightly larger circulant matrices (Domschke et al., 2014; Villa et al., 2022). Then the matrix-vector product involving a circulant matrix can be evaluated efficiently using fast Fourier transform techniques. This efficient approximation of the nonlocal term, simultaneously on the full computational grid, is key to an overall efficient numerical scheme for the full PDE system.

---

<sup>2</sup>A circulant matrix is a Toeplitz matrix where each row is a right cyclic shift of the row above it.

<sup>3</sup>A Toeplitz matrix is an  $n \times n$  matrix  $M$  such that  $M_{i,j} = M_{i+1,j+1}$  for all  $i, j = 1, \dots, n - 1$ .

**Time integration.** The above methods yield an initial value problem for a large system of stiff ODEs. This system is solved using the linearly-implicit time integration scheme ROWMAP (Weiner et al., 1997), implemented in a Fortran subroutine and called from MATLAB. ROWMAP is specifically designed for the numerical solution of stiff initial value problems of ODEs of large dimension, and implements automatic time step size control ensuring that the temporal discretisation error of the numerical solution is negligible in comparison with the spatial error introduced during the spatial discretisation (Gerisch and Chaplain, 2008).

## B.3 Numerical schemes used in Chapter 7

Details of the numerical schemes for the 1D and 2D problems presented in Chapter B.3 are given in Section B.3.1 and B.3.2 respectively. The files containing the code corresponding to the schemes is available on GitLab<sup>4</sup>. The following schemes and available code have been developed in collaboration with Alf Gerisch (TU Darmstadt).

### B.3.1 Numerical schemes for the 1D problem

Numerical solutions for the system of implicit, time-dependent and spatially 1D PDEs (8.1), (8.2) and (8.7) are obtained exploiting the Method of Lines. We make use of a uniform discretisation of the spatial domain  $[l, L]$  consisting of  $K + 1$  grid points, or grid cell centres, while, at first, leaving the time variable continuous. We denote the spatial grid width by  $\Delta x$ . The normalised cell density  $n(t, x)$ , the normalised ECM density  $\rho(t, x)$  and the displacement of a material point of the cell-ECM system  $u(t, x)$  are approximated as

$$n(t, x_i) \approx N_i(t), \quad \rho(t, x_i) \approx P_i(t), \quad u(t, x_i) \approx U_i(t) \quad \text{for } i = 0, \dots, K.$$

Thanks to the periodic boundary conditions we have

$$N_0(t) = N_K(t), \quad P_0(t) = P_K(t) \quad \text{and} \quad U_0(t) = U_K(t),$$

and consequently have  $3 \times K$  time-continuous approximations to determine. We collect them in the vectors  $N(t)$ ,  $P(t)$ ,  $U(t)$  and denote their time-derivatives by  $N'(t)$ ,  $P'(t)$ ,  $U'(t)$ . The discretization of the spatial derivatives in the PDE system will then result in an implicit system of  $3 \times K$  ODEs for the variables  $N(t)$ ,  $P(t)$ ,  $U(t)$  and their time-

---

<sup>4</sup><https://git-ce.rwth-aachen.de/alf.gerisch/VillaEtAl2021BullMathBiol>

derivatives of the following form

$$F(N, P, U, N', P', U') = \begin{bmatrix} f_n(N, P, N', U') \\ f_\rho(P, P', U') \\ f_u(N, P, U, N', P', U') \end{bmatrix} = 0. \quad (\text{B.10})$$

In this system  $f_n(N, P, N', U') = 0$ ,  $f_\rho(P, P', U') = 0$  and  $f_u(N, P, U, N', P', U') = 0$  are each systems of  $K$  ODEs obtained, respectively, from PDEs (8.1), (8.2) and (8.7), using second-order central finite difference approximations for the spatial derivatives and the first-order upwind scheme for the advection terms, as detailed below for each equation.

In order to solve system (B.10), we make use of the MATLAB solver `ode15i`, which uses a variable-order (orders 1 to 5) backward difference formula (BDF) method in a form suitable to an implicit system of ODEs. Initial conditions  $N(0)$ ,  $P(0)$  and  $U(0)$  are given by the appropriate equivalent of initial conditions (8.22), and we make use of the MATLAB function `decic` to obtain consistent initial conditions  $N'(0)$ ,  $P'(0)$  and  $U'(0)$  such that (B.10) is satisfied at initial time  $t = 0$ .

**Useful matrices.** In order to apply the first-order upwind scheme we need to compute variables and derivatives at the grid cell interfaces, i.e. half-way between grid points, in addition to those at the grid cell centres. We here clarify the notation adopted throughout the rest of this document. The  $K \times K$  matrices  $\mathbf{M}_x$  and  $\mathbf{M}_{xx}$  are used to approximate, using second-order finite differences, the first-order and the second-order derivatives in space, respectively, of a periodic grid function at the grid cell centres and are therefore given by

$$\mathbf{M}_x := \frac{1}{2\Delta x} \begin{bmatrix} 0 & 1 & & -1 \\ -1 & 0 & 1 & \\ & \ddots & \ddots & \ddots \\ 1 & & -1 & 0 \end{bmatrix} \quad \text{and} \quad \mathbf{M}_{xx} := \frac{1}{\Delta x^2} \begin{bmatrix} -2 & 1 & & 1 \\ 1 & -2 & 1 & \\ & \ddots & \ddots & \ddots \\ 1 & & 1 & -2 \end{bmatrix}. \quad (\text{B.11})$$

We make use of the notation  $\vec{\cdot}$  to indicate a shift from the grid cell centres to the (right) grid cell interfaces. In particular to approximate the value of a periodic grid function at these grid cell interfaces we multiply it by the  $K \times K$  matrix

$$\vec{\mathbf{M}} := \frac{1}{2} \begin{bmatrix} 1 & 1 & & & \\ & 1 & 1 & & \\ & & \ddots & \ddots & \\ 1 & & & & 1 \end{bmatrix}. \quad (\text{B.12})$$

In addition, the  $K \times K$  matrices  $\vec{\mathbf{M}}_x$  and  $\hat{\mathbf{M}}_x$  are used to approximate the first-order derivatives in space of a periodic grid function at the (right) grid cell interfaces, when the grid function is given in the grid cell centres, and at the grid cell centres, when the grid function is given in the (right) grid cell interfaces, respectively. These are given by

$$\vec{\mathbf{M}}_x := \frac{1}{\Delta x} \begin{bmatrix} -1 & 1 & & & \\ & -1 & 1 & & \\ & & \ddots & \ddots & \\ & & & -1 & \\ 1 & & & & \end{bmatrix}, \quad \hat{\mathbf{M}}_x := \frac{1}{\Delta x} \begin{bmatrix} 1 & & & & -1 \\ -1 & 1 & & & \\ & \ddots & \ddots & & \\ & & & -1 & 1 \end{bmatrix}. \quad (\text{B.13})$$

Note that, even though these two matrices are multiplied by  $1/\Delta x$ , they still stem from second-order finite difference approximations, calculated on a staggered grid shifted by half the grid cell width.

**Convention:** In the formulas which follow below, we use the convention that any product of a matrix from above with a vector of length  $K$  is a matrix-vector product but any operation between two vectors, in particular multiplication, division, or exponentiation, are understood element-wise.

**Numerical scheme for the balance equation (8.1).** We rewrite the balance equation (8.1) as

$$\partial_t n - D \partial_{xx}^2 n + \nabla_{\mathbf{x}}(\phi n) - rn(1-n) = 0 \quad \text{with } \phi = \alpha \nabla_{\mathbf{x}} \rho + \partial_t u,$$

which, upon spatial discretisation, leads to the following system of  $K$  ODEs

$$f_n(N, P, N', U') = N' - D \vec{\mathbf{M}}_{xx} N + A(\vec{\Phi}, N) - rN(1-N) = 0 \quad (\text{B.14})$$

with  $\vec{\Phi}$  indicating the advective velocity computed at the grid cell interfaces, that is

$$\vec{\Phi} = \alpha \vec{\mathbf{M}}_x P + \vec{\mathbf{M}} U', \quad (\text{B.15})$$

and the matrices  $\vec{\mathbf{M}}_{xx}$ ,  $\vec{\mathbf{M}}$  and  $\hat{\mathbf{M}}_x$  are defined in (B.11), (B.12) and (B.13), respectively. The function  $A(\vec{\Phi}, N)$  computes the contribution of advection, given advective velocity and advected quantity as inputs, at the grid cell centres as

$$A(\vec{\Phi}, N) := \hat{\mathbf{M}}_x \vec{\mathcal{F}}(\vec{\Phi}, N) \quad (\text{B.16})$$

where the matrix  $\overleftarrow{\mathbf{M}}_x$  is defined in (B.13) and the advective flux  $\overrightarrow{\mathcal{F}}$  at the grid cell interfaces is computed using first-order upwinding, i.e.

$$\left[ \overrightarrow{\mathcal{F}}(\overrightarrow{\Phi}, N) \right]_i := \begin{cases} (\overrightarrow{\Phi}_i)^+ N_i + (\overrightarrow{\Phi}_i)^- N_{i+1} & \text{for } i = 1, \dots, K-1 \\ (\overrightarrow{\Phi}_K)^+ N_K + (\overrightarrow{\Phi}_K)^- N_1 & \text{for } i = K \end{cases} \quad (\text{B.17})$$

with  $(\cdot)^+$  and  $(\cdot)^-$  being the positive and negative parts of the input variable, i.e.

$$(\Phi)^+ := \max(0, \Phi) \quad \text{and} \quad (\Phi)^- := \min(0, \Phi). \quad (\text{B.18})$$

**Numerical scheme for the transport equation (8.2).** We rewrite the transport equation (8.2) as

$$\partial_t \rho + \nabla_{\mathbf{x}}(\partial_t u \rho) = 0$$

which, upon spatial discretisation, leads to the following system of  $K$  ODEs

$$f_\rho(P, P', U') = P' + \mathbf{A}(\overrightarrow{\mathbf{M}} U', P) = 0, \quad (\text{B.19})$$

where the function  $\mathbf{A}(\overrightarrow{\mathbf{M}} U', P)$  is defined in (B.16), together with definitions (B.17) and (B.18), with advection velocity given by  $U'$  calculated at the cell interfaces using  $\overrightarrow{\mathbf{M}}$  defined in (B.12).

**Numerical scheme for the force-balance equation (8.7).** We solve the system of PDEs (8.1), (8.2) and (8.7) for the Kelvin-Voigt (7.3) and the Maxwell (7.4) models. In these cases we have  $b_2 = a_2 = 0$ , and the force-balance equation (8.7) reads as

$$\begin{aligned} b_1 \partial_{xxt}^3 u + b_0 \partial_{xx}^2 u - a_1 s \partial_t(\rho u) - a_0 s \rho u + \nabla_{\mathbf{x}}(a_1 \partial_t \sigma_c + a_0 \sigma_c) &= 0 \\ \text{with } \sigma_c = \tau \frac{n}{1 + \lambda n^2} (\rho + \beta \partial_{xx}^2 \rho) &. \end{aligned}$$

Upon spatial discretisation, this leads to the following system of  $K$  ODEs

$$\begin{aligned} f_u(N, P, U, N', P', U') &= b_1 \mathbf{M}_{xx} U' + b_0 \mathbf{M}_{xx} U - a_1 s(PU)' \\ &\quad - a_0 s PU + \mathbf{M}_x \mathbf{T}_1(N, P, N', P') = 0 \end{aligned} \quad (\text{B.20})$$

with

$$\mathbf{T}_1(N, P, N', P') = \tau [a_1 \Lambda_2(N) N' \mathbf{M}_{T1} P + a_1 \Lambda_1(N) \mathbf{M}_{T1} P' + a_0 \Lambda_1(N) \mathbf{M}_{T1} P], \quad (\text{B.21})$$

where the functions  $\Lambda_1$  and  $\Lambda_2$  are defined as

$$\Lambda_1(N) := \frac{N}{1 + \lambda N^2} \quad \text{and its derivative} \quad \Lambda_2(N) := \frac{1 - \lambda N^2}{(1 + \lambda N^2)^2}, \quad (\text{B.22})$$

while the  $K \times K$  matrix  $\mathbf{M}_{T1}$  is given by

$$\mathbf{M}_{T1} := \mathbf{I} + \beta \mathbf{M}_{xx}, \quad (\text{B.23})$$

where  $\mathbf{I}$  is the  $K \times K$  identity matrix and  $\mathbf{M}_x$  is defined in (B.11).

This scheme is valid as long as  $b_2 = a_2 = 0$  and can therefore also be applied when considering the linear elastic model (7.1), the linear viscous model (7.2), and the SLS model (7.5). On the other hand, in the case where  $b_2 \neq 0$  (i.e. when the Jeffrey model (7.6) is considered) the above numerical scheme cannot be directly employed due to the presence of a second-order derivative in  $t$ . We could still, however, take a similar approach and make use of the `ode15i` solver by introducing extra variables for the first-order derivatives in  $t$  of  $n$  and  $\rho$ , thus formally reducing the PDE (8.7) to first-order in time, at the cost of increasing the number of equations in the Method of Lines ODE system.

### B.3.2 Numerical scheme for the 2D problem

Similarly as done for the spatially 1D model, numerical solutions for the system of implicit, time-dependent and spatially 2D PDEs (8.9), together with (30)-(32), are obtained exploiting the Method of Lines. We make use of a uniform discretisation of the square spatial domain  $[l, L] \times [l, L]$  consisting of  $(K+1) \times (K+1)$  grid points, while leaving the time variable continuous. The spatial grid width, in both spatial directions, is denoted by  $\Delta x$  again. The normalised cell density  $n(t, x_1, x_2)$ , the normalised ECM density  $\rho(t, x_1, x_2)$  and the displacement of a material point of the cell-ECM system  $\mathbf{u}(t, x_1, x_2) = (u_1(t, x_1, x_2), u_2(t, x_1, x_2))^\top$  are approximated as

$$n(t, x_i, x_j) \approx N_{i,j}(t), \quad \rho(t, x_i, x_j) \approx P_{i,j}(t) \quad \text{for } i, j = 0, \dots, K,$$

$$u_1(t, x_i, x_j) \approx (U_1)_{i,j}(t), \quad u_2(t, x_i, x_j) \approx (U_2)_{i,j}(t) \quad \text{for } i, j = 0, \dots, K.$$

Thanks to the periodic boundary conditions, we can drop the index values  $i = 0$  and  $j = 0$  and consequently have  $4 \times K^2$  time-continuous approximations to determine. We collect them in the matrices  $N(t)$ ,  $P(t)$ ,  $U_1(t)$ ,  $U_2(t)$  and denote their time-derivatives by  $N'(t)$ ,  $P'(t)$ ,  $U'_1(t)$ ,  $U'_2(t)$ . The discretization of the spatial derivatives in the PDE system will then result in an implicit system of  $4 \times K^2$  ODEs for the variables  $N(t)$ ,  $P(t)$ ,  $U_1(t)$ ,

$U_2(t)$  and their time-derivatives of the following form

$$F(N, P, U_1, U_2, N', P', U'_1, U'_2) = \begin{bmatrix} f_n(N, P, N', U'_1, U'_2) \\ f_\rho(P, P', U'_1, U'_2) \\ f_{u_1}(N, P, U_1, U_2, N', P', U'_1, U'_2) \\ f_{u_2}(N, P, U_1, U_2, N', P', U'_1, U'_2) \end{bmatrix} = 0. \quad (\text{B.24})$$

In this system  $f_n = 0$ ,  $f_\rho = 0$ ,  $f_{u_1} = 0$  and  $f_{u_2} = 0$  are each systems of  $K^2$  ODEs obtained from the system of PDEs (8.9), using second-order central finite difference approximations for the spatial derivatives and the first-order upwind scheme for the advection terms, as detailed below for each equation.

In order to solve system (B.24), we make, similarly to the spatially 1D case, use of the MATLAB solver `ode15i`. Initial conditions  $N(0)$ ,  $P(0)$ ,  $U_1(0)$  and  $U_2(0)$  are given by the appropriate equivalent of initial conditions (8.25), and we make use of the MATLAB function `decic` to obtain consistent initial conditions  $N'(0)$ ,  $P'(0)$ ,  $U'_1(0)$  and  $U'_2(0)$  such that (B.24) is satisfied at initial time  $t = 0$ .

**Useful functions** In order to solve the system (B.24) we need to compute variables and derivatives at the grid cell centres and interfaces, both in the  $x_1$ - and the  $x_2$ -direction. We here introduce the functions that will be used in the rest of this document to compute the aforementioned quantities in the different directions. These rely on the fact that the matrices (B.11)-(B.13) act on column vectors and therefore, when applied to an  $K \times K$  argument matrix, they will act on each column of that, which in our framework corresponds to computing the quantity of interest in the  $x_1$ -direction. In order to compute the same quantities in the  $x_2$ -direction, we need the operating matrix to act on each row of the argument matrix of interest, which can be achieved by matrix transposition of the argument matrix before and of the product matrix after matrix multiplication. Hence the functions  $\mathbf{M}_{x1}(N)$  and  $\mathbf{M}_{x2}(N)$  are used to approximate the first-order derivative of the variable of interest, say  $N$ , at the grid cell centres in the  $x_1$ - and  $x_2$ -directions respectively, and are defined as

$$\mathbf{M}_{x1}(N) := \mathbf{M}_x N, \quad \text{and} \quad \mathbf{M}_{x2}(N) := [\mathbf{M}_x N^\top]^\top, \quad (\text{B.25})$$

where the matrix  $\mathbf{M}_x$  is defined in (B.11). Similarly, the functions  $\mathbf{M}_{xx1}(N)$  and  $\mathbf{M}_{xx2}(N)$  are used to approximate the second-order derivative of the variable of interest at the grid cell centres in the  $x_1$ - and  $x_2$ -directions, respectively, and are defined as

$$\mathbf{M}_{xx1}(N) := \mathbf{M}_{xx} N, \quad \text{and} \quad \mathbf{M}_{xx2}(N) := [\mathbf{M}_{xx} N^\top]^\top, \quad (\text{B.26})$$

where the matrix  $\mathbf{M}_{xx}$  is defined in (B.11). Then the function  $\mathbf{M}_{x1x2}(N)$  is used to approximate the second-order mixed derivative in space at the grid cell centres and is defined as

$$\mathbf{M}_{x1x2}(N) := \mathbf{M}_{x2}(\mathbf{M}_{x1}(N)) = [\mathbf{M}_x (\mathbf{M}_x N)^\top]^\top. \quad (\text{B.27})$$

In order to approximate the value of a variable in the centres of the (right or upper) grid cell interfaces in the  $x_1$ - and  $x_2$ -direction, we make use of the functions  $\vec{\mathbf{M}}_1$  and  $\vec{\mathbf{M}}_2$ , respectively, which are defined as

$$\vec{\mathbf{M}}_1(N) := \vec{\mathbf{M}} N, \quad \text{and} \quad \vec{\mathbf{M}}_2(N) := [\vec{\mathbf{M}} N^\top]^\top, \quad (\text{B.28})$$

with the matrix  $\vec{\mathbf{M}}$  defined in (B.12). In a similar fashion we define the functions  $A_1(\vec{v}_1, N)$  and  $A_2(\vec{v}_2, N)$  which approximate the contribution of advection in the  $x_1$ - and  $x_2$ -direction, respectively, given as input the advective velocity at the grid cell interfaces in the direction of interest – say  $v_1$  and  $v_2$  are, respectively, the first and second components of the advective velocity – and the advected quantity. These are given by

$$A_1(\vec{v}_1, N) := A(\vec{v}_1, N) \quad \text{and} \quad A_2(\vec{v}_2, N) := [A(\vec{v}_2^\top, N^\top)]^\top, \quad (\text{B.29})$$

with the function  $A(\vec{v}, N)$  given by (B.16) together with definitions (B.17) and (B.18).

**Convention:** With the definitions above, we have hidden all applications of the matrices from the spatially 1D case in newly defined functions. Consequently, in the formulas which follow below, we use the convention that any further operation between matrices, in particular multiplication, division, or exponentiation, are understood element-wise.

**Numerical scheme for the balance equation (8.9)<sub>1</sub>.** We rewrite the balance equation (8.9)<sub>1</sub> as

$$\begin{aligned} \partial_t n - D[\partial_{x_1 x_1}^2 n + \partial_{x_2 x_2}^2 n] + \partial_{x_1}(\phi_1 n) + \partial_{x_2}(\phi_2 n) - rn(1-n) &= 0 \\ \text{with } \phi_i = \alpha \partial_{x_i} \rho + \partial_t u_i \quad i = 1, 2, \end{aligned}$$

which, upon spatial discretisation, leads to the following system of  $K^2$  ODEs

$$\begin{aligned} f_n(N, P, N', U'_1, U'_1) &= N' - D[\mathbf{M}_{xx1}(N) + \mathbf{M}_{xx2}(N)] + A_1(\vec{\Phi}_1, N) \\ &\quad + A_2(\vec{\Phi}_2, N) - rN(1-N) = 0 \end{aligned} \quad (\text{B.30})$$

with the functions  $\mathbf{M}_{xx1}(\cdot)$  and  $\mathbf{M}_{xx2}(\cdot)$  defined in (B.26), and the components of the advective velocity at the grid cell interfaces given by

$$\vec{\Phi}_1 = \alpha \vec{\mathbf{M}}_{x1}(P) + \vec{\mathbf{M}}_1(U'_1) \quad \text{and} \quad \vec{\Phi}_2 = \alpha \vec{\mathbf{M}}_{x2}(P) + \vec{\mathbf{M}}_2(U'_2), \quad (\text{B.31})$$

where functions  $\vec{\mathbf{M}}_{x1}(\cdot)$  and  $\vec{\mathbf{M}}_{x2}(\cdot)$  are defined in (B.25),  $\vec{\mathbf{M}}_1(\cdot)$  and  $\vec{\mathbf{M}}_2(\cdot)$  are defined in (B.28), and functions  $A_1(\cdot, \cdot)$  and  $A_2(\cdot, \cdot)$  are defined in (B.29).

**Numerical scheme for the transport equation (8.9)<sub>2</sub>.** We rewrite the transport equation (8.9)<sub>2</sub> as

$$\partial_t \rho + \partial_{x_1} (\partial_t u_1 \rho) + \partial_{x_2} (\partial_t u_2 \rho) = 0$$

which, upon spatial discretisation, leads to the following system of  $K^2$  ODEs

$$f_\rho(P, P', U'_1, U'_2) = P' + A_1(\vec{\mathbf{M}}_1(U'_1), P) + A_2(\vec{\mathbf{M}}_2(U'_2), P) = 0, \quad (\text{B.32})$$

where the functions  $A_1(\cdot, \cdot)$  and  $A_2(\cdot, \cdot)$  are defined in (B.29) and functions  $\vec{\mathbf{M}}_1(\cdot)$  and  $\vec{\mathbf{M}}_2(\cdot)$  are defined in (B.28).

**Numerical scheme for the force balance equation (8.9)<sub>3</sub>.** We rewrite the first component of the force balance equation (8.9)<sub>3</sub>, complemented with (30)-(32), as

$$\begin{aligned} & b_1 \left( \partial_{x_1 x_1}^2 \partial_t u_1 + \frac{1}{2} [\partial_{x_2 x_2}^2 \partial_t u_1 + \partial_{x_1 x_2}^2 \partial_t u_2] \right) + b_0 \left( \partial_{x_1 x_1}^2 u_1 + \frac{1}{2} [\partial_{x_2 x_2}^2 u_1 + \partial_{x_1 x_2}^2 u_2] \right) \\ & + c_1 (\partial_{x_1 x_1}^2 \partial_t u_1 + \partial_{x_1 x_2}^2 \partial_t u_2) + c_0 (\partial_{x_1 x_1}^2 u_1 + \partial_{x_1 x_2}^2 u_2) \\ & + \partial_{x_1} [a_1 \partial_t \sigma_c + a_0 \sigma_c] - a_1 s (u_1 \partial_t \rho + \rho \partial_t u_1) - a_0 s \rho u_1 = 0, \end{aligned} \quad (\text{B.33})$$

and, similarly, we rewrite the second component as

$$\begin{aligned} & b_1 \left( \partial_{x_2 x_2}^2 \partial_t u_2 + \frac{1}{2} [\partial_{x_1 x_2}^2 \partial_t u_1 + \partial_{x_1 x_1}^2 \partial_t u_2] \right) + b_0 \left( \partial_{x_2 x_2}^2 u_2 + \frac{1}{2} [\partial_{x_1 x_2}^2 u_1 + \partial_{x_1 x_1}^2 u_2] \right) \\ & + c_1 (\partial_{x_2 x_2}^2 \partial_t u_2 + \partial_{x_1 x_2}^2 \partial_t u_1) + c_0 (\partial_{x_2 x_2}^2 u_2 + \partial_{x_1 x_2}^2 u_1) \\ & + \partial_{x_2} [a_1 \partial_t \sigma_c + a_0 \sigma_c] - a_1 s (u_2 \partial_t \rho + \rho \partial_t u_2) - a_0 s \rho u_2 = 0, \end{aligned} \quad (\text{B.34})$$

where  $\sigma_c$  is defined by

$$\sigma_c = \tau \frac{n}{1 + \lambda n^2} (\rho + \beta \partial_{x_1 x_1}^2 \rho + \beta \partial_{x_2 x_2}^2 \rho). \quad (\text{B.35})$$

Upon spatial discretisation, these lead to the following systems of  $K^2$  ODEs

$$\begin{aligned} f_{u1}(N, P, U, N', P', U') = & b_1 (\mathbf{M}_{xx1}(U'_1) + \frac{1}{2} (\mathbf{M}_{xx2}(U'_1) + \mathbf{M}_{x1x2}(U'_2))) \\ & + b_0 (\mathbf{M}_{xx1}(U_1) + \frac{1}{2} (\mathbf{M}_{xx2}(U_1) + \mathbf{M}_{x1x2}(U_2))) + c_1 (\mathbf{M}_{xx1}(U'_1) + \mathbf{M}_{x1x2}(U'_2)) \\ & + c_0 (\mathbf{M}_{xx1}(U_1) + \mathbf{M}_{x1x2}(U_2)) + \mathbf{M}_{x1} (\mathbf{T}_2(N, P, N', P')) \\ & - a_1 s (P U'_1 + P' U_1) - a_0 s P U_1 = 0 \end{aligned} \quad (\text{B.36})$$

and

$$\begin{aligned}
f_{u2}(N, P, U, N', P', U') = & \ b_1 \left( \mathbf{M}_{xx2}(U'_2) + \frac{1}{2} (\mathbf{M}_{x1x2}(U'_1) + \mathbf{M}_{xx1}(U'_2)) \right) \\
& + b_0 \left( \mathbf{M}_{xx2}(U_2) + \frac{1}{2} (\mathbf{M}_{x1x2}(U_1) + \mathbf{M}_{xx1}(U_2)) \right) + c_1 \left( \mathbf{M}_{xx2}(U'_2) + \mathbf{M}_{x1x2}(U'_1) \right) \quad (\text{B.37}) \\
& + c_0 \left( \mathbf{M}_{xx2}(U_2) + \mathbf{M}_{x1x2}(U_1) \right) + \mathbf{M}_{x2}(\mathbf{T}_2(N, P, N', P')) \\
& - a_1 s(PU'_2 + P'U_2) - a_0 sPU_2 = 0 .
\end{aligned}$$

Here

$$\begin{aligned}
\mathbf{T}_2(N, P, N', P') = & \tau \left[ a_1 \Lambda_2(N) N' \mathbf{M}_{T2}(P) + a_1 \Lambda_1(N) \mathbf{M}_{T2}(P') \right. \\
& \left. + a_0 \Lambda_1(N) \mathbf{M}_{T2}(P) \right], \quad (\text{B.38})
\end{aligned}$$

where the functions  $\Lambda_1$  and  $\Lambda_2$  are defined as in (B.22), while the function  $\mathbf{M}_{T2}(P)$  is given by

$$\mathbf{M}_{T2}(P) := P + \beta [\mathbf{M}_{xx1}(P) + \mathbf{M}_{xx2}(P)], \quad (\text{B.39})$$

where the functions  $\mathbf{M}_{xx1}(\cdot)$  and  $\mathbf{M}_{xx2}(\cdot)$  are defined in (B.26).

**Remark 12.** *The MATLAB solver `ode15i` allows for the specification of the sparsity pattern of Jacobian matrices. In particular in the spatially 2D simulations this leads, in comparison to not specifying these patterns, to substantial savings in required CPU time. For details on these patterns we refer to the available MATLAB implementation for the numerical solution of the PDE systems.*

# Appendix C

## Parameter details

### C.1 Parameter values used in Chapter 2

Numerical solutions are computed in a domain of length  $L = 0.5$  cm, which in 2D corresponds to a region of tumour tissue of area  $2.5 \times 10^{-3}$  cm<sup>2</sup>, chosen in agreement with clinical images provided by Schuh et al. (2017).

**Cancer cells.** As discussed in Section 2.2, typical values of the epimutation rate  $\beta$  are one or two orders of magnitude larger than the rate of somatic DNA mutation (Doerfler and Böhm, 2006, p.45), which is about  $10^{-12}$  s<sup>-1</sup> (Duesberg et al., 2000), and typical values of the cell diffusivity  $D_n$  are about  $10^{-12}$  cm<sup>2</sup>s<sup>-1</sup> (Smith et al., 2004; Wang et al., 2009). Given the various sources of spontaneous phenotypic changes, discussed in Section 1.1.3, and the wide range of observable mutation rates (Duesberg et al., 2000), higher rates of spontaneous phenotypic variation have been considered in the literature (Ardaševa et al., 2020c; Chisholm et al., 2015). In view of the analytical choices made in Section 2.2 we make different choices of these parameters for two parameter sets. (A) We take  $\beta = 0^{-6}$  s<sup>-1</sup> as proposed by Chisholm et al. (2015), and  $D_0 = 0$  cm<sup>2</sup>s<sup>-1</sup> to match assumptions made for the analysis in Section 2.2.1. (B) We take  $\beta = D_n = 10^{-13}$  for consistency with assumptions made for the formal analysis in Section 2.2.2, i.e. parametrising these quantities as the square of a small parameter  $\varepsilon$ , and this way we have  $D_n = 10^{-13}$  cm<sup>2</sup>s<sup>-1</sup> close to the estimate of Wang et al. (2009) using an experimentally calibrated model, and  $\beta = 10^{-13}$  s<sup>-1</sup> closer to the order of magnitude discussed above (Doerfler and Böhm, 2006; Duesberg et al., 2000). The maximal background fitness of anaerobic phenotypic variants  $\varphi$  can be estimated from the experimental data reported by Gordan et al. (2007) on the proliferation of the control culture in hypoxic conditions using the logistic growth, where the death rate is assumed to be  $10^9$  orders of magnitude smaller

than the proliferation rate for consistency with the parameter choices of Lorenzi et al. (2018). Moreover, in agreement with experimental results of Gordan et al. (2007) and the choices made by Lorenzi et al. (2018), we choose the maximum proliferation rate via aerobic energy pathways to be one order of magnitude higher than via anaerobic energy pathways. This results in about  $\varphi = 1 \times 10^{-5} \text{ s}^{-1}$  and  $\gamma_s = 1 \times 10^{-4} \text{ s}^{-1}$ . We take the rate of cell death due to competition for space  $\zeta = 2 \times 10^{-13} \text{ cm}^3 \text{s}^{-1} \text{cells}^{-1}$ , for consistency with the parameter choices made by Lorenzi et al. (2018), who considered experimental values reported in Li (1982). Finally, we chose the maximal reduction of the background fitness due to chemotherapy  $\gamma_c = 1.8 \times 10^{-4} \text{ s}^{-1}$  as chosen by Lorenzi et al. (2018) referring back to Ward and King (1997).

**Oxygen.** In agreement with the choices made by Lorenzi et al. (2018), in view of the considerations made by Ward and King (1997) and the experimental results reported by Casciari et al. (1992), we take the Michaelis-Menten constant of oxygen  $\alpha_s = 1.5 \times 10^{-7} \text{ g cm}^{-3}$  and the diffusivity of oxygen  $D_s = 2 \times 10^{-5} \text{ cm}^2 \text{s}^{-1}$  with reference to the experimental results of Hlatky and Alpen (1985). In view of definitions (2.21) and (2.13), and the parameter choice for  $\gamma_s$ , we take the conversion factor for cell consumption of oxygen  $\eta_s = 2 \times 10^{-11} \text{ g cells}^{-1}$ , so that the maximum consumption rate of oxygen  $\max r_s = \eta_s \gamma_s$  matches that of Lorenzi et al. (2018), who refer back to the considerations made by Ward and King (1997) and the experimental results reported by Casciari et al. (1992). We take the rate of natural decay of oxygen  $\lambda_s = 2.78 \times 10^{-6} \text{ s}^{-1}$  matching the value used by Cumsille et al. (2015). Similarly to as chosen by Lorenzi et al. (2018), we pick the reference value for the concentration of oxygen  $S_0 = 6.3996 \times 10^{-7} \text{ g cm}^{-3}$ , consistent with experimental data on oxygen concentration reported by Kumosa et al. (2014). We pick the constant rate of inflow of oxygen through blood vessels  $I_s$  to match this value, i.e.  $I_s = 6.3996 \times 10^{-7} \text{ g cm}^{-3} \text{s}^{-1}$ .

**Chemotherapeutic agent.** We follow the parameter choices made by Lorenzi et al. (2018), who take the Michaelis-Menten constant of chemotherapeutic agent  $\alpha_c = 2 \times 10^{-6} \text{ g cm}^{-3}$  following considerations made by Norris et al. (2006) and experimental results of Kwok and Twentyman (1985). For consistency with the choice made for  $\eta_s$ , we take the conversion factor for cell consumption of chemotherapeutic agent  $\eta_c = 4 \times 10^{-11} \text{ g cells}^{-1}$ , cf. Norris et al. (2006); Lorenzi et al. (2018). We take average values in the range of estimates reported by Powathil et al. (2012b) for the diffusivity of chemotherapeutic agent, yielding and the rate of natural decay of chemotherapeutic agent , yielding  $D_c = 4.4 \times 10^{-6} \text{ cm}^2 \text{s}^{-1}$  and  $\lambda_c = 2.3 \times 10^{-4} \text{ s}^{-1}$ . Norris et al. (2006) reported reference values for the concentration of chemotherapeutic agent in the range  $5 \times 10^{-8} - 2 \times 10^{-5} \text{ g cm}^{-3}$ , thus we chose  $C_0 = 2.5 \times 10^{-6} \text{ g cm}^{-3}$ , although other parameter values in that range

are considered for the study in Section 2.3. Similarly to as chosen for  $I_s$ , we take the constant rate of inflow of chemotherapeutic agent through blood vessels  $I_c$  to match  $C_0$ , i.e.  $I_c = 2.5 \times 10^{-6} \text{ g cm}^{-3}\text{s}^{-1}$ .

## C.2 Parameter values used in Chapter 5

As already indicated in Section 5.1.4, we use  $L = 0.1 \text{ cm}$  as characteristic length scale, in accordance with previous vasculogenesis works (Manoussaki, 2003; Serini et al., 2003) and for easy visual comparison with the experimental results reported by Blatchley et al. (2019). We then take reference time scale  $\tau := L^2/D$ , where  $D$  is a characteristic diffusion coefficient  $D \sim 10^{-6} \text{ cm}^2\text{s}^{-1}$  (Bray, 2000), resulting in a reference time scale  $\tau = 10^4 \text{ s}$ .

**Endothelial progenitor cells (or endothelial cells).** The reference cell density is chosen to be  $N := n_M = \vartheta_1^{-1}$  and we take  $\vartheta_1$  to be the average volume occupied by an EC. (Rubin et al., 1989) measured the average ECs volume during different phases of the cell cycle, registering values in the range of  $800 - 1800 \mu\text{m}^3$ , with a predominance of measurements around  $1000 \mu\text{m}^3$ . Hence we take  $\vartheta_1 = 10^{-9} \text{ cm}^3/\text{cell}$ , corresponding to an average cell diameter of approximately  $a = 10^{-3} \text{ cm}$ . Measures and estimates of the diffusion coefficient of ECs fall in the range  $10^{-6}\text{-}10^{-12} \text{ cm}^2\text{s}^{-1}$  (Ambrosi et al., 2005), so we take  $D_n = 10^{-9} \text{ cm}^2\text{s}^{-1}$ . We consider the chemotactic sensitivity coefficient estimated by Jain and Jackson (2013), corresponding to  $\chi = 1.4 \times 10^{-7} \text{ cm}^5\text{ng}^{-1}\text{s}^{-1}$ . Sen et al. (2009) estimated a maximum cell surface radius, upon morphological changes to better adhere to the underlying gel, of about  $50 \mu\text{m}$ . Given cell-to-cell and cell-to-matrix adhesion occurs via adhesion molecules on the cell surface, we take the sensing radius  $R = 0.5 \times 10^{-2} \text{ cm}$ . While the nonlocal term introduced in equations (5.5) and (5.6) allows us to consider cell-to-cell and cell-to-matrix adhesion dynamics at tissue level, these are the result of smaller scale dynamics between adhesion molecules and receptors on cell surfaces – *vid.* for instance Albelda and Buck (1990); Berrier and Yamada (2007); Garrod (1993) – of which our modelling choice is a simplification. As a result, good estimates for cell-to-cell and cell-to-matrix coefficients  $S_{nn}$  and  $S_{n\rho}$  are currently lacking. We therefore consider nondimensional values chosen by Gerisch and Chaplain (2008) for our baseline parameter set which correspond to  $S_{nn} = 10^{-16} \text{ cm}^5 \text{ s}^{-1}$  and  $S_{n\rho} = 10^{-6} \text{ cm}^2 \text{ nM}^{-1} \text{ s}^{-1}$  respectively, acknowledging that model fitting to experimental data is required. Kinev et al. (2013) reported doubling times of non-irradiated ECFCs – the same class of EPCs employed by Blatchley et al. (2019) – of about 19.5 hours, estimated from measured growth rates assuming exponential growth. Following their calculations, this corresponds to proliferation rates of about  $p = 10^{-5} \text{ s}^{-1}$ .

**Extracellular matrix.** We use a reference matrix density of  $P = 10^{-1}$  nM (Anderson, 2005; Anderson et al., 2000; Terranova et al., 1985) and define the parameter  $\vartheta_2 := P^{-1}$ . Since the LSA suggest that a domain not too densely packed with cells and ECM may facilitate the emergence of spatial patterns (see Section 5.2 and Appendix A.4), we take the initial ECM density in (5.13) to be  $\rho_0 = 0.5$  in our nondimensional baseline parameter set, corresponding to  $\rho_0 = 0.5 \times 10^{-1}$  nM. We take the ECM degradation rate by MMPs proposed by Kim and Friedman (2010), i.e.  $\gamma = 9 \times 10^5$  cm<sup>3</sup>g<sup>-1</sup>s<sup>-1</sup>. ECM remodelling is a complex process involving a variety of cells and molecules (Chang, 2016; Daley et al., 2008; Lefebvre et al., 1999; Streuli, 1999), so the remodelling term introduced in equation (5.10) is an oversimplification of the underlying dynamics. Therefore the lack of experimental values or estimates for the remodelling rate  $\mu$  is not surprising, and we take the nondimensional value 0.2 as similarly considered in Deakin and Chaplain (2013); Domschke et al. (2014); Gerisch and Chaplain (2008) for our baseline parameter set. Under the defined nondimensional parameters this corresponds to the dimensional value  $\mu = 0.2 \times 10^{-5}$  nM s<sup>-1</sup>.

**Matrix degrading enzyme (MMP).** Blatchley et al. (2019) reported concentrations of MMP-1 in the range  $1 - 100$  µg ml<sup>-1</sup>, so we take the intermediate concentration as reference MMP density, i.e.  $M = 10$  µg cm<sup>-3</sup>. We let the diffusion coefficient for the MMP be given by  $D_m = 8 \times 10^{-9}$  cm<sup>2</sup>s<sup>-1</sup>, which was experimentally determined by Saffarian et al. (2004), although diffusion rates have been observed in the range  $10^{-10} - 10^{-8}$  cm<sup>2</sup>s<sup>-1</sup> (Collier et al., 2011; Kumar et al., 2018). While MMPs secretion rates by cells have been reported in a variety of works, these fail to provide parameter values in the appropriate unit of  $\alpha_m$  in this model. For instance Kumar et al. (2018) considered secretion rates varying between  $0.01 - 0.5$  s<sup>-1</sup> but the associated MMP concentration is unspecified, while Ruggiero et al. (2017) estimated secretion rates by stromal cells and macrophages to be  $5.75 \times 10^{-10}$  and  $4.44 \times 10^{-10}$  g cm<sup>-3</sup> respectively, without an indication of the considered time frame. We here consider that molecular dynamics are generally faster than cellular ones and therefore the observed average MMP concentration satisfies (5.11) at equilibrium, i.e.  $m = \alpha_m n / \lambda_m$ . Under the chosen reference values  $N$ ,  $M$  and  $\lambda_m$ , this corresponds to an MMP production rate of  $\alpha_m = 0.5 \times 10^{-12}$  µg s<sup>-1</sup> per cell. Note that the resulting nondimensional parameter value is close to that chosen in previous mathematical models – *vid.* for instance Anderson et al. (2000); Deakin and Chaplain (2013); Domschke et al. (2014); Gerisch and Chaplain (2008). Nonetheless, we will also consider higher values of  $\alpha_m$ , since Deem and Cook-Mills (2004) have reported up to a 4-fold increase in MMP production in the presence of reactive oxygen species, and in addition MMP production levels have been shown to be significantly upregulated in human cancers (Shiomi and Okada, 2003). Finally, Kim and Friedman (2010) estimated

– from its half life – the decay rate of MMP  $\lambda_m = 5 \times 10^{-5} \text{ s}^{-1}$ .

**Chemoattractant (VEGF).** We take the reference VEGF density to be  $C = 20 \text{ ng cm}^{-3}$ , in the range of values generally considered in *in vitro* set ups – *vid.* for instance [Hanjaya-Putra and Gerecht (2009); Lee et al. (2007); Serini et al. (2003)]. Measures and estimates of the diffusion coefficient of the chemoattractant, usually identified as VEGF, are in the range  $10^{-6} - 10^{-9} \text{ cm}^2\text{s}^{-1}$  (Ambrosi et al., 2005; Gamba et al., 2003; Merks et al., 2008; Miura and Tanaka, 2009; Serini et al., 2003; Singh et al., 2015), so we take  $D_c = 10^{-7} \text{ cm}^2\text{s}^{-1}$ . Yen et al. (2011) reported a VEGF secretion rate of  $0.068 \text{ molecules cell}^{-1}\text{s}^{-1}$ , which in combination with Avogadro’s number ( $6.022 \times 10^{23} \text{ molecules per mole}$ ) and a molecular weight of 45kDa (Yen et al., 2011) results in a VEGF production rate of about  $\alpha_c = 0.5 \times 10^{-11} \text{ ng s}^{-1}$  per cell. Serini et al. (2003) reported the half-life of VEGF-A to be approximately 64 minutes, corresponding to a decay rate of about  $\lambda_c = 2.7 \times 10^{-4} \text{ s}^{-1}$ , in line with the values chosen in Merks et al. (2008); Singh et al. (2015).

## C.3 Parameter values used in Chapter 7

In order not to limit the conclusions of our work by selecting a specific biological scenario, we identified possible ranges of values for each parameter of our model on the basis of the existing literature on mechanochemical models of pattern formation and then define our baseline parameter set by selecting values in the middle of such ranges. In the sensitivity analysis presented in Section 8.2.2, we then consider the effect of varying the parameter values within an appropriate range. We first consider the parameters appearing in equations (8.1), (8.2) and (8.7), as well as in the initial conditions (8.22), and then consider additional parameters appearing in the 2D system (8.9)-(7.12), and the associated initial conditions (8.25).

**Parameters in the balance equation (8.1).** Nondimensional parameter values for the cell motility coefficient  $D$  in the literature appear as low as  $D = 10^{-8}$  (Gilmore et al., 2012), and as high as  $D = 10$  (Murray and Oster, 1984b), but are generally taken in the range  $[10^{-5}, 1]$  (Bentil and Murray, 1991; Byrne and Preziosi, 2003; Cruywagen and Murray, 1992; Ferrenq et al., 1997; Maini et al., 2002; Murray et al., 1988; Namy et al., 2004; Olsen et al., 1995; Perelson et al., 1986). Hence, we take  $D = 0.01$  for our baseline parameter set. The nondimensional haptotactic sensitivity of cells  $\alpha$  takes values in the range  $[10^{-5}, 5]$  (Bentil and Murray, 1991; Cruywagen and Murray, 1992; Gilmore et al., 2012; Murray et al., 1988; Namy et al., 2004; Olsen et al., 1995; Perelson et al., 1986),

and we take  $\alpha = 0.05$  for our baseline parameter set. While most authors ignore cell proliferation dynamics, i.e. consider  $r = 0$  (Ambrosi et al., 2005; Byrne and Preziosi, 2003; Gilmore et al., 2012; Murray et al., 1988; Perelson et al., 1986), when present, the rate of cell proliferation takes nondimensional value in the range  $[0.02, 5]$  (Cruywagen and Murray, 1992; Olsen et al., 1995; Perelson et al., 1986). Hence, we choose  $r = 1$  for our baseline parameter set.

**Parameters in the balance equation (8.2).** While no parameters appear in the balance equation (8.2), the value of the parameter  $\rho_0$  introduced in Section 8.2 as the spatially homogeneous steady state  $\bar{\rho} = \rho_0$ , and successively specified to be the initial ECM density in (8.22) for our numerical simulations, stems from neglected terms in equation (8.2). With the exception of Cruywagen and Murray (1992) and Maini et al. (2002) who, respectively, have  $\rho_0 = 100.2$  and  $\rho_0 = 0.1$ , this parameter is usually taken to be  $\rho_0 = 1$  in mechanochemical models ignoring additional ECM dynamics (Bentil and Murray, 1991; Cruywagen and Murray, 1992; Harris et al., 1981; Manoussaki, 2003; Moreo et al., 2010; Murray and Oster, 1984a,b; Olsen et al., 1995; Oster et al., 1983; Perelson et al., 1986). This is generally justified by assuming the steady state  $\rho_0$  of equation (8.2) that is introduced by the additional term, say  $S(n, \rho)$ , is itself used to nondimensionalise  $\rho$ , before assuming the dynamics modelled by  $S(n, \rho)$  to occur on a much slower timescale than convection driven by the cell-ECM displacement, thus neglecting this term (Murray, 2001), resulting in the nondimensional parameter  $\hat{\rho}_0 = 1$ . Hence, we take  $\rho_0 = 1$ .

**Parameters in the force balance equation (8.7).** The elastic modulus, or Young modulus,  $E$  is usually itself used to nondimensionalise the other parameters in the dimensional correspondent of equation (8.7) and, therefore, does not appear in the nondimensional system (Bentil and Murray, 1991; Gilmore et al., 2012; Murray and Oster, 1984b,b; Murray et al., 1988; Olsen et al., 1995; Perelson et al., 1986). This corresponds to the nondimensional value  $E = 1$ , which is what we take for our baseline parameter set. The viscosity coefficient  $\eta$  has been taken with nondimensional values in low orders of magnitude, such as  $\eta \sim 10^{-3} - 10^{-1}$  (Bentil and Murray, 1991; Cruywagen and Murray, 1992; Gilmore et al., 2012; Perelson et al., 1986), as well as in high orders of magnitude, such as  $\eta \sim 10^2 - 10^3$  (Gilmore et al., 2012; Olsen et al., 1995). It is, however, generally taken to be  $\eta = 1$  (Bentil and Murray, 1991; Byrne and Chaplain, 1996; Cruywagen and Murray, 1992; Murray and Oster, 1984b; Murray et al., 1988; Perelson et al., 1986), which is what we choose for our baseline parameter set. When the constitutive model includes two elastic moduli, i.e. for the SLS model (7.5), or two viscosity coefficients, i.e. for the Jeffrey model (7.6), we take  $E_1 = E_2 = E/2 = 0.5$  and  $\eta_1 = \eta_2 = \eta/2 = 0.5$  as done by Alonso et al. (2017). The cell traction parameter  $\tau$  takes nondimensional values

spanning many orders of magnitude: it can be found as low as  $\tau = 10^{-5}$  (Ferrenq et al., 1997) and as high as  $\tau = 10$  (Bentil and Murray, 1991; Cruywagen and Murray, 1992; Perelson et al., 1986), but it is generally taken to be of order  $\tau \sim 1$  (Bentil and Murray, 1991; Byrne and Chaplain, 1996; Gilmore et al., 2012; Murray et al., 1988; Perelson et al., 1986) and many works consider  $\tau \sim 10^{-2} - 10^{-1}$  (Byrne and Chaplain, 1996; Ferrenq et al., 1997; Murray and Oster, 1984b; Olsen et al., 1995). Hence, for our baseline parameter set we choose  $\tau = 0.2$ . The cell-cell contact inhibition parameter  $\lambda$  generally takes nondimensional values in the range  $[10^{-2}, 1]$  (Bentil and Murray, 1991; Byrne and Chaplain, 1996; Murray et al., 1988; Perelson et al., 1986), so we choose  $\lambda = 0.5$  for our baseline parameter set. The long-range cell traction parameter  $\beta$ , when present, takes nondimensional values in the range  $[10^{-3}, 10^{-2}]$  (Bentil and Murray, 1991; Cruywagen and Murray, 1992; Gilmore et al., 2012; Moreo et al., 2010; Murray et al., 1988; Perelson et al., 1986) so we choose  $\beta = 0.005$  for our baseline parameter set. The elasticity of the external elastic substratum  $s$ , which is sometimes ignored or substituted with a viscous drag, has been taken to have nondimensional values as low as  $s \in [10^{-1}, 1]$  (Byrne and Chaplain, 1996; Murray and Oster, 1984b; Olsen et al., 1995) but is generally chosen in the range  $[10, 400]$  (Bentil and Murray, 1991; Gilmore et al., 2012; Murray et al., 1988; Perelson et al., 1986). Hence, we take  $s = 10$  for our baseline parameter set.

**Parameters in the 2D system (8.9)-(7.12).** For the parameters in the 2D system (8.9)-(7.12) and initial condition (8.25) that also appear in the equations (8.1), (8.2), (8.7) and initial conditions (8.22), we make use of the same nondimensional values selected in the 1D case (see previous paragraphs). The Poisson ratio  $\nu$ , which can only take values in the range  $[0.1, 0.45]$ , has been estimated to be in the range  $[0.2, 0.3]$  for the biological tissue considered in mechanochemical models in the current literature (Ambrosi et al., 2005; Cruywagen and Murray, 1992; Manoussaki, 2003; Moreo et al., 2010). Hence, we choose  $\nu = 0.25$  for our baseline parameter set. This results in  $E' = E/(1 + \nu) = 0.8$  and  $\nu' = \nu/(1 - 2\nu) = 0.5$  according to definitions (7.12). In addition, under the simplifying assumption (A.64) introduced in Appendix A.5.2, the bulk viscosity takes the value  $\mu = \nu'\eta = 0.5\eta = 0.5$ , which is in agreement with the fact that the bulk and shear viscosities are usually assumed to take values of a similar order of magnitude in the extant literature (Ambrosi et al., 2005; Manoussaki, 2003; Moreo et al., 2010; Murray, 2003).

# Appendix D

## Supplementary figures

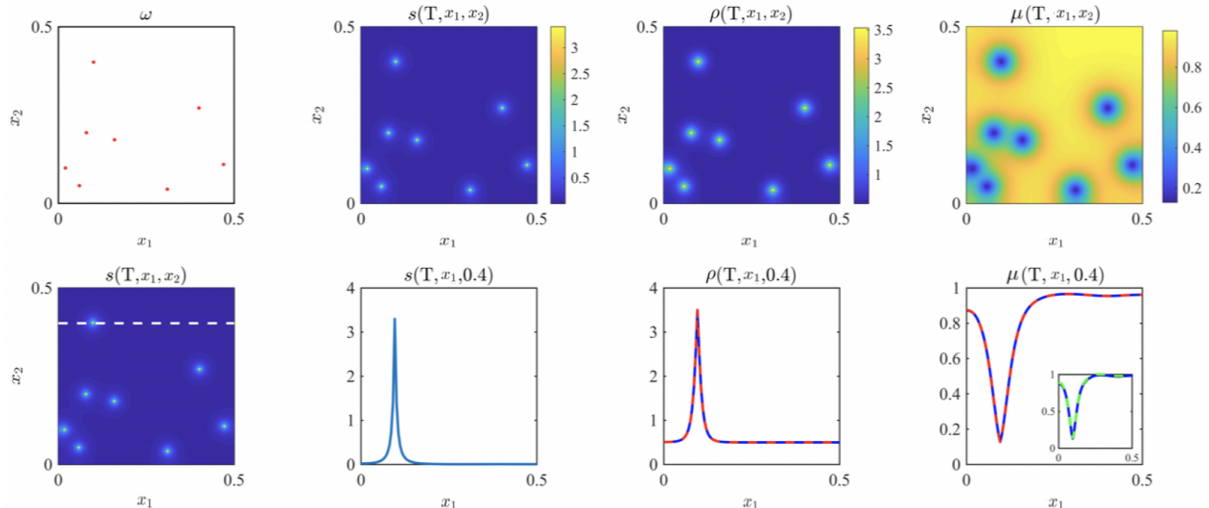


**Figure D.1:** *First row:* Plots of the oxygen concentration  $s(T, \mathbf{x})$  (second panel), the cell density  $\rho(T, \mathbf{x})$  (third panel) and the local mean phenotypic state  $\mu(T, \mathbf{x})$  (fourth panel), with  $T = 5 \times 10^5 s$ , obtained by solving numerically (2.5) and (2.19) imposing the initial conditions defined via (2.27), (2.51) and (2.50), and assuming  $c(t, \mathbf{x}) \equiv 0$  (i.e. in the absence of chemotherapeutic agent). The set  $\omega$  in (2.22) consists of the parts of  $\Omega$  highlighted in red in the first panel. *Second row:* Plots of the oxygen concentration  $s(T, x_1, 0.4)$  (second panel), the cell density  $\rho(T, x_1, 0.4)$  (third panel, blue line) and the local mean phenotypic state  $\mu(T, x_1, 0.4)$  (fourth panel, blue line). The plot of the oxygen concentration  $s(T, \mathbf{x})$  is displayed in the first panel, where the white, dashed line highlights the 1D cross-section corresponding to  $x_2 = 0.4$ . The red lines in the third and fourth panels highlight  $\rho_\infty(x_1, 0.4)$  and  $\mu_\infty(x_1, 0.4)$  computed through (2.47) and (2.48) with  $s_\infty(x_1, 0.4) := s(T, x_1, 0.4)$  and  $c_\infty \equiv 0$ . The insets in the fourth panel display the plot of the mean phenotypic state  $\mu(T, x_1, 0.4)$  (blue line) and of the maximum point of  $n(T, x_1, 0.4, y)$  (green line). The oxygen concentration  $s(T, \mathbf{x})$  is in units of  $10^{-7} g cm^{-2}$ , the cell density  $\rho(T, \mathbf{x})$  is in units of  $10^8 cells cm^{-2}$  the spatial variables  $x_1$  and  $x_2$  are in units of  $cm$ , and the parameters values used are those listed in Table 2.1 ( $D_n = 0 = \beta = 10^{-13}$ ).

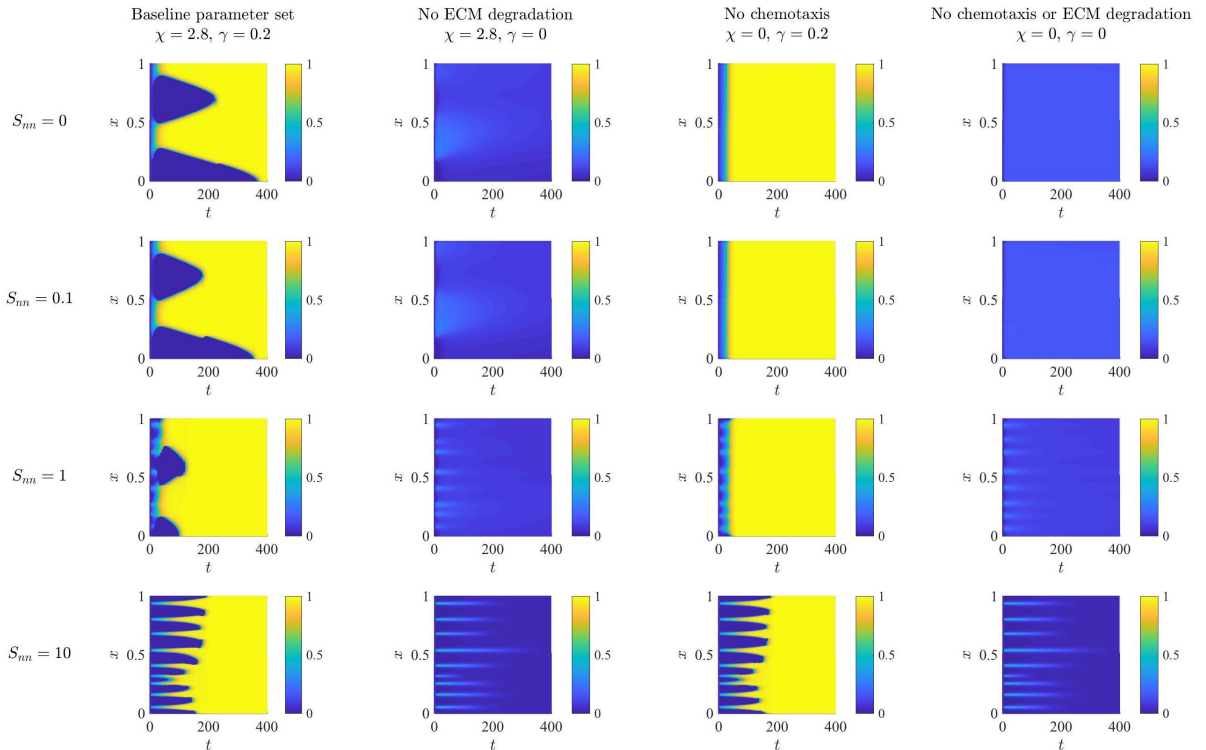


**Figure D.2:** *First row:* Plots of the cell density  $n(t, x)$  up to  $t = 400$  obtained solving the system (5.15), together with definitions (5.6), (5.8) and (5.16), initial conditions (5.13) and (5.14), complemented with zero-flux boundary conditions, in the absence of cell-to-cell adhesion, *i.e.* for  $S_{nn} = 0$ : under the baseline parameter set (first column), in the absence of matrix degradation, *i.e.* for  $\gamma = 0$  (second column), in the absence of chemotaxis, *i.e.*  $\chi = 0$  (third column), and in the absence of both chemotaxis and matrix degradation, *i.e.*  $\chi = \gamma = 0$  (fourth column). *Second, third and fourth rows:* Same as first row but in the presence of cell-to-cell adhesion, with  $S_{nn} = 0.1$  (second row),  $S_{nn} = 1$  (third row) and  $S_{nn} = 10$  (fourth row) respectively.

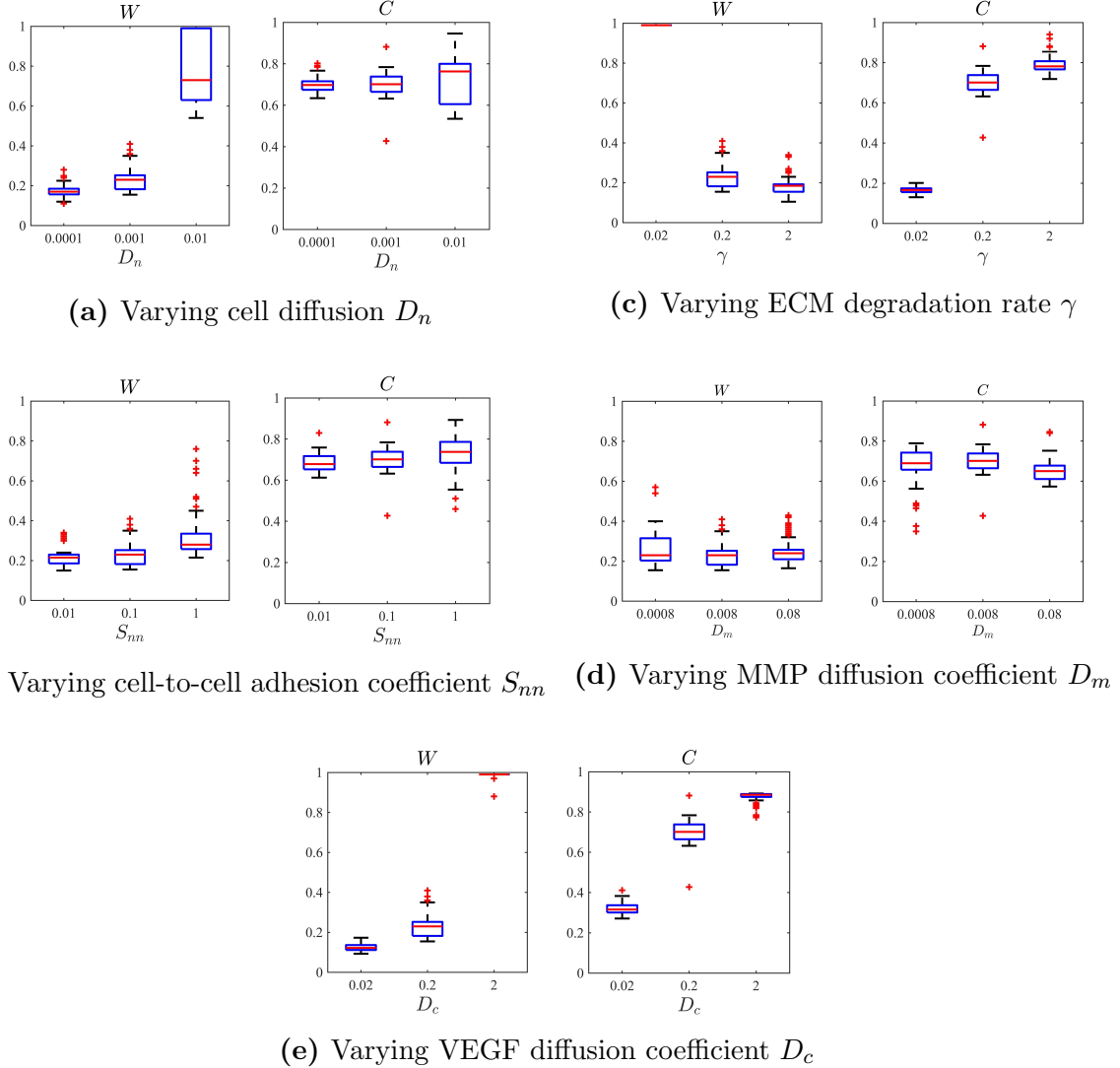


**Figure D.3:** Cluster width  $W$  and compactness  $C$ , defined in (5.20) and (5.21), under alterations of certain parameters from the baseline parameter set (BPS), in Table 5.1. In (a) we have boxplots of  $W$  and  $C$  measured on the numerical solution of the system (5.15) at  $t = 50$ , for  $D_n$  taking its value in the BPS (center), one order of magnitude higher (left) and one order of magnitude lower (right) than the one in the BPS. Each boxplot collects data from 100 simulations under randomised initial conditions (5.13) and (5.14). In (b)-(e) we have the same as in (a) but varying parameters  $S_{nn}$  (b),  $\gamma$  (c),  $D_m$  (d) and  $D_c$  (e).

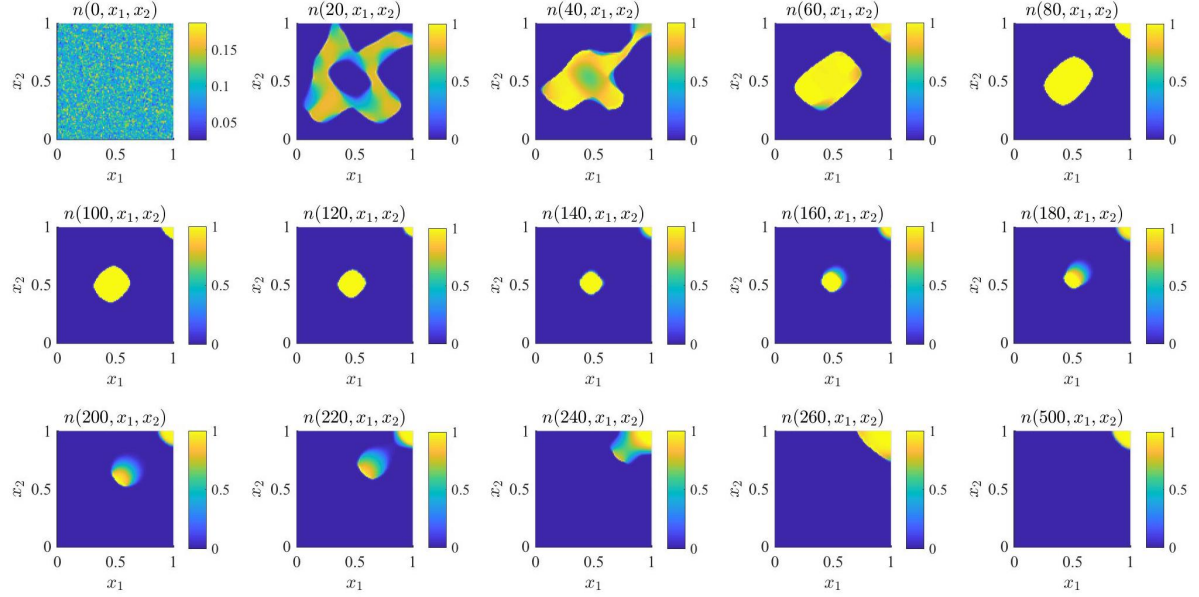


**Figure D.4:** Plots of the cell density  $n(t, \mathbf{x})$  obtained solving the system (5.15), together with definitions (5.6), (5.8) and (5.16), initial conditions (5.13) and (5.14), complemented with zero-flux boundary conditions, under the parameter choices reported in Table 5.1. The solution is plotted at time  $t = 0, 20, 40, 60, 80$  (first row, left to right),  $t = 100, 120, 140, 160, 180$  (second row, left to right) and  $t = 200, 220, 240, 260, 500$  (third row, left to right).

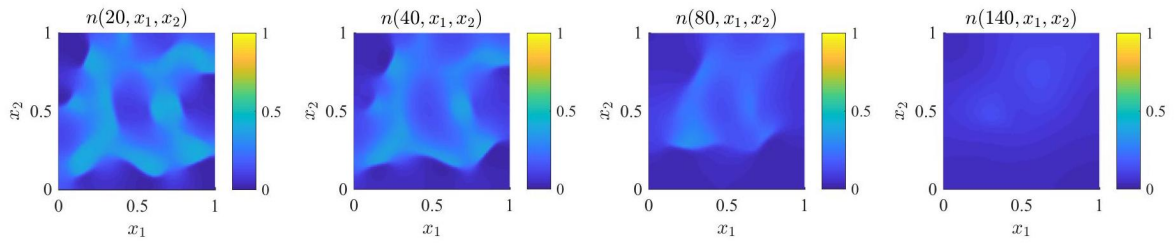


**Figure D.5:** Plots of the cell density  $n(t, \mathbf{x})$  obtained solving the system (5.15), together with definitions (5.6), (5.8) and (5.16), initial conditions (5.13) and (5.14), complemented with zero-flux boundary conditions, under the parameter choices reported in Table 5.1, except for  $\gamma = 0$ . The solution is plotted at time  $t = 20$  (first panel),  $t = 40$  (second panel),  $t = 80$  (third panel) and  $t = 140$  (fourth panel).

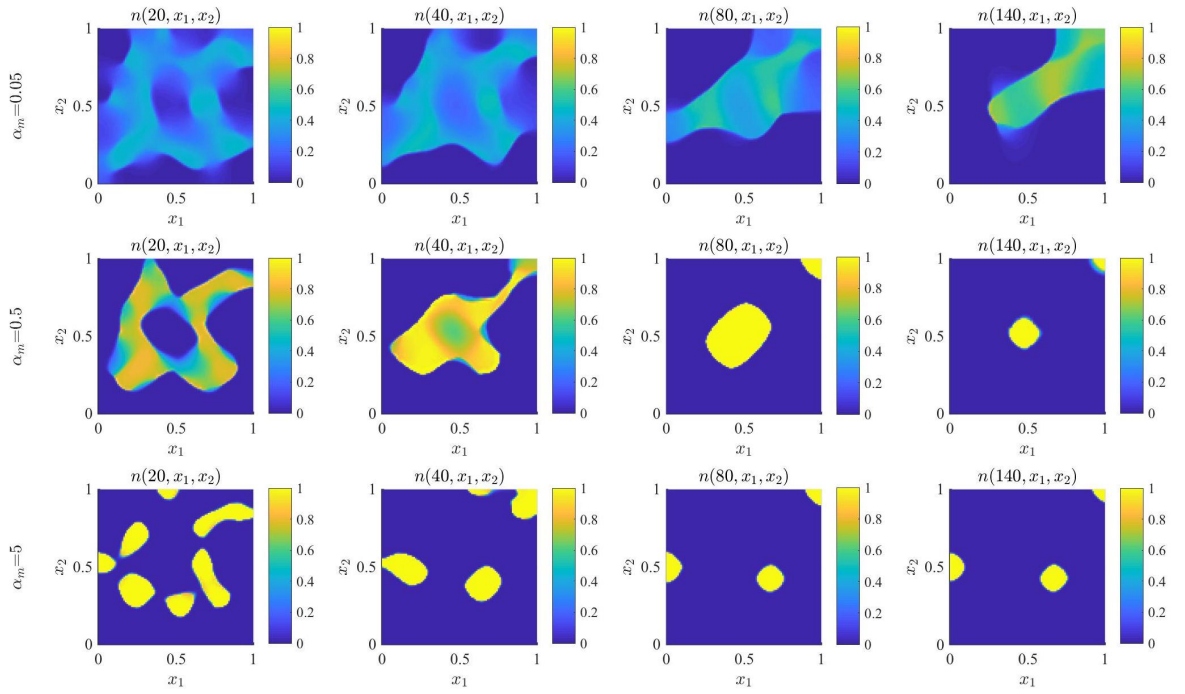


**Figure D.6:** *First row:* Plots of the cell density  $n(t, \mathbf{x})$  obtained solving the system (5.15), together with definitions (5.6), (5.8) and (5.16), initial conditions (5.13) and (5.14), complemented with zero-flux boundary conditions, under the parameter choices reported in Table 5.1, except for  $\alpha_m = 0.05$ . The solution is plotted at time  $t = 20$  (first panel),  $t = 40$  (second panel),  $t = 80$  (third panel) and  $t = 140$  (fourth panel). *Second and third row:* Same as first row, except for  $\alpha_m = 0.5$  (second row) and  $\alpha_m = 5$  (third row).

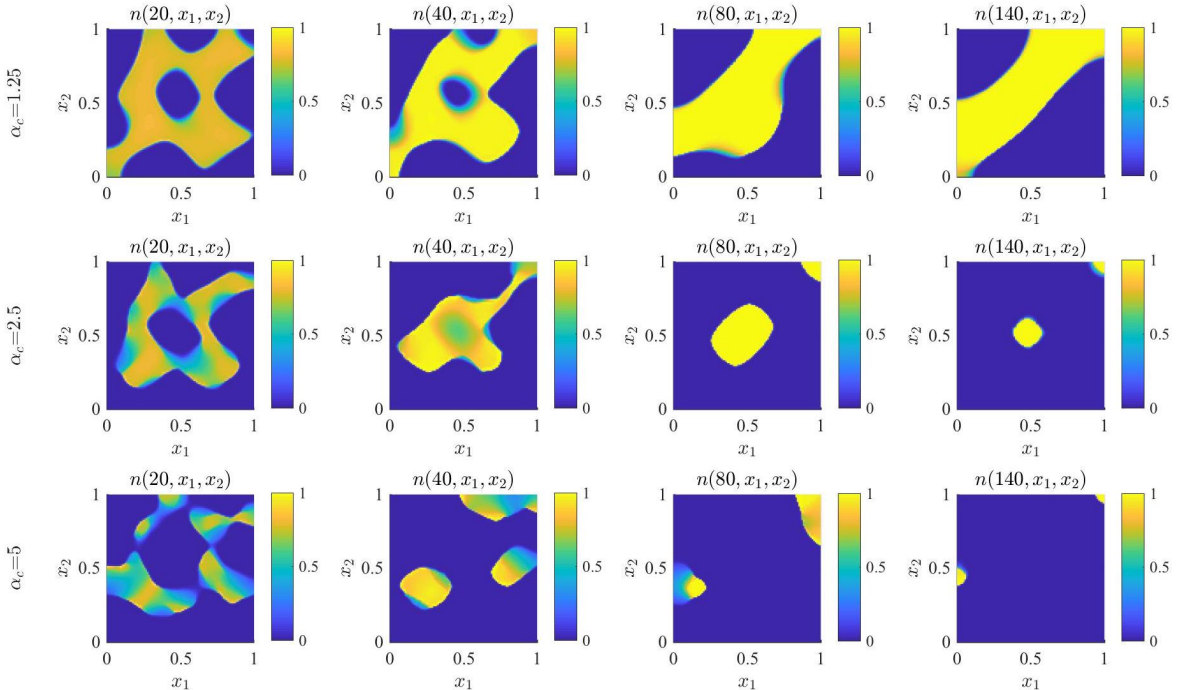


**Figure D.7:** First row: Plots of the cell density  $n(t, \mathbf{x})$  obtained solving the system (5.15), together with definitions (5.6), (5.8) and (5.16), initial conditions (5.13) and (5.14), complemented with zero-flux boundary conditions, under the parameter choices reported in Table 5.1, except for  $\alpha_c = 1.25$ . The solution is plotted at time  $t = 20$  (first panel),  $t = 40$  (second panel),  $t = 80$  (third panel) and  $t = 140$  (fourth panel). Second and third row: Same as first row, except for  $\alpha_c = 2.5$  (second row) and  $\alpha_c = 5$  (third row).

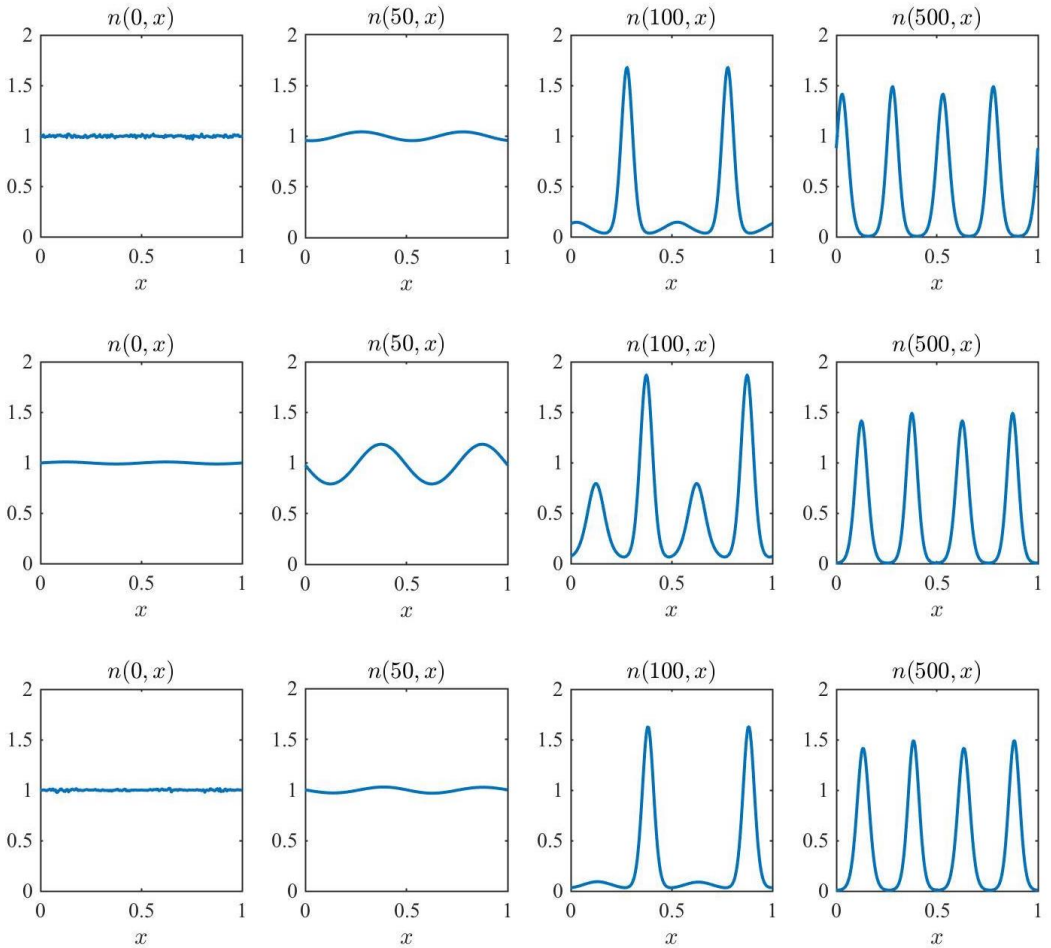


**Figure D.8:** *First row:* Cell density  $n(t,x)$  obtained solving numerically the system of PDEs (8.1), (8.2) and (8.7) complemented with the Maxwell model (7.4) subject to boundary conditions (8.8) and initial conditions (8.22), for the parameter values given by (8.20) and (8.21). The solution is plotted at time  $t = 0$  (first panel),  $t = 50$  (second panel),  $t = 100$  (third panel) and  $t = 500$  (fourth panel). *Second row:* Same as first row, but under sinusoidal initial perturbations, i.e. with  $n(0,x) = 1 + 0.01 \sin(4\pi x)$  in (8.22). *Thirds row:* Same as first row, but under randomly perturbed sinusoidal initial perturbations, i.e. with  $n(0,x) = 1 + 0.01\epsilon(x) \sin(4\pi x)$  in (8.22).

# Bibliography

- T. H. Adair and J.-P. Montani. Angiogenesis. In *Colloquium series on integrated systems physiology: from molecule to function*, volume 2, pages 1–84. Morgan & Claypool Life Sciences, 2010.
- J. Adamski, A. Price, C. Dive, and G. Makin. Hypoxia-induced cytotoxic drug resistance in osteosarcoma is independent of hif-1alpha. *PloS One*, 8(6):e65304, 2013.
- T. Akita, T. Murohara, H. Ikeda, K.-i. Sasaki, T. Shimada, K. Egami, and T. Imaizumi. Hypoxic preconditioning augments efficacy of human endothelial progenitor cells for therapeutic neovascularization. *Laboratory Investigation*, 83(1):65–73, 2003.
- C. A. Aktipis and R. M. Nesse. Evolutionary foundations for cancer biology. *Evolutionary Applications*, 6(1):144–159, 2013.
- S. M. Albelda and C. A. Buck. Integrins and other cell adhesion molecules. *The FASEB Journal*, 4(11):2868–2880, 1990.
- K. M. O. Alblazi and C. H. Siar. Cellular protrusions-lamellipodia, filopodia, invadopodia and podosomes-and their roles in progression of orofacial tumours: current understanding. *Asian Pacific Journal of Cancer Prevention*, 16(6):2187–2191, 2015.
- M. Alfaro and R. Carles. Explicit solutions for replicator-mutator equations: extinction versus acceleration. *SIAM Journal on Applied Mathematics*, 74(6):1919–1934, 2014.
- M. Alfaro and M. Veruete. Evolutionary branching via replicator–mutator equations. *Journal of Dynamics and Differential Equations*, 31(4):2029–2052, 2019.
- M. Alfaro, J. Coville, and G. Raoul. Travelling waves in a nonlocal reaction-diffusion equation as a model for a population structured by a space variable and a phenotypic trait. *Communications in Partial Differential Equations*, 38(12):2126–2154, 2013.
- M. Alfaro, H. Berestycki, and G. Raoul. The effect of climate shift on a species submitted to dispersion, evolution, growth, and nonlocal competition. *SIAM Journal on Mathematical Analysis*, 49(1):562–596, 2017.

- K. O. Alfarouk, M. E. Ibrahim, R. A. Gatenby, and J. S. Brown. Riparian ecosystems in human cancers. *Evolutionary Applications*, 6(1):46–53, 2013.
- L. Almeida, P. Bagnerini, G. Fabrini, B. D. Hughes, and T. Lorenzi. Evolution of cancer cell populations under cytotoxic therapy and treatment optimisation: insight from a phenotype-structured model. *ESAIM: Mathematical Modelling and Numerical Analysis (ESAIM: M2AN)*, 53(4):1157–1190, 2019.
- S. Alonso, M. Radszuweit, H. Engel, and M. Bär. Mechanochemical pattern formation in simple models of active viscoelastic fluids and solids. *Journal of Physics D: Applied Physics*, 50(43):434004, 2017.
- P. M. Altrock, L. L. Liu, and F. Michor. The mathematics of cancer: integrating quantitative models. *Nature Reviews Cancer*, 15(12):730–745, 2015.
- D. Ambrosi, A. Gamba, and G. Serini. Cell directional and chemotaxis in vascular morphogenesis. *Bulletin of Mathematical Biology*, 66(6):1851–1873, 2004.
- D. Ambrosi, F. Bussolino, and L. Preziosi. A review of vasculogenesis models. *Journal of Theoretical Medicine*, 6(1):1–19, 2005.
- A. R. A. Anderson. A hybrid mathematical model of solid tumour invasion: the importance of cell adhesion. *Mathematical Medicine and Biology*, 22(2):163–186, 2005.
- A. R. A. Anderson and P. K. Maini. Mathematical oncology. *Bulletin of Mathematical Biology*, 80(5):945–953, 2018.
- A. R. A. Anderson and V. Quaranta. Integrative mathematical oncology. *Nature Reviews Cancer*, 8(3):227–234, 2008.
- A. R. A. Anderson, M. A. J. Chaplain, E. L. Newman, R. J. C. Steele, and A. M. Thompson. Mathematical Modelling of Tumour Invasion and Metastasis. *Journal of Theoretical Medicine*, 2(2):129–154, 2000. ISSN 1027-3662.
- A. R. A. Anderson, A. M. Weaver, P. T. Cummings, and V. Quaranta. Tumor morphology and phenotypic evolution driven by selective pressure from the microenvironment. *Cell*, 127(5):905–915, 2006.
- A. R. A. Anderson, M. A. J. Chaplain, and K. Rejniak (editors). Single-cell-based models in biology and medicine. In *Mathematics and Biosciences in Interaction*. Springer Science & Business Media, Birkhäuser, 2007.
- H. Anderson, P. Price, M. Blomley, M. Leach, and P. Workman. Measuring changes in human tumour vasculature in response to therapy using functional imaging techniques. *British Journal of Cancer*, 85(8):1085–1093, 2001.

- F. Andreu, V. Caselles, and J. M. Mazón. Diffusion equations with finite speed of propagation. In *Functional Analysis and Evolution Equations*, pages 17–34. Springer, 2007.
- A. Ardaševa, A. R. A. Anderson, R. A. Gatenby, H. M. Byrne, P. K. Maini, and T. Lorenzi. Comparative study between discrete and continuum models for the evolution of competing phenotype-structured cell populations in dynamical environments. *Physical Review E*, 102(4):042404, 2020a.
- A. Ardaševa, R. A. Gatenby, A. R. A. Anderson, H. M. Byrne, P. K. Maini, and T. Lorenzi. Evolutionary dynamics of competing phenotype-structured populations in periodically fluctuating environments. *Journal of Mathematical Biology*, 80(3):775–807, 2020b.
- A. Ardaševa, R. A. Gatenby, A. R. A. Anderson, H. M. Byrne, P. K. Maini, and T. Lorenzi. A mathematical dissection of the adaptation of cell populations to fluctuating oxygen levels. *Bulletin of Mathematical Biology*, 82(6):81, 2020c.
- N. J. Armstrong, K. J. Painter, and J. A. Sherratt. A continuum approach to modelling cell-cell adhesion. *Journal of Theoretical Biology*, 243(1):98–113, 2006.
- N. J. Armstrong, K. J. Painter, and J. A. Sherratt. Adding adhesion to a chemical signaling model for somite formation. *Bulletin of Mathematical Biology*, 71(1):1–24, 2009.
- A. Arnold, L. Desvillettes, and C. Prévost. Existence of nontrivial steady states for populations structured with respect to space and a continuous trait. *Communications on Pure and Applied Analysis*, 11(1):83–96, 2012.
- T. Asahara and A. Kawamoto. Endothelial progenitor cells for postnatal vasculogenesis. *American Journal of Physiology-Cell Physiology*, 287(3):C572–C579, 2004.
- T. Asahara, T. Murohara, A. Sullivan, M. Silver, R. Van Der Zee, T. Li, B. Witzenbichler, G. Schatteman, and J. M. Isner. Isolation of Putative Progenitor Endothelial Cells for Angiogenesis. *Science*, 275(5302):964–966, 1997.
- T. Asahara, H. Masuda, T. Takahashi, C. Kalka, C. Pastore, M. Silver, M. Kearne, M. Magner, and J. M. Isner. Bone marrow origin of endothelial progenitor cells responsible for postnatal vasculogenesis in physiological and pathological neovascularization. *Circulation Research*, 85(3):221–228, 1999.
- H. Axelsson, E. Fredlund, M. Ovenberger, G. Landberg, and S. Pählman. Hypoxia-induced dedifferentiation of tumor cells – a mechanism behind heterogeneity and aggressiveness of solid tumors. *Seminars in Cell & Developmental Biology*, 16(5):554–563, 2005.

- M. Bachmann, S. Kukkurainen, V. P. Hytönen, and B. Wehrle-Haller. Cell adhesion by integrins. *Physiological reviews*, 99(4):1655–1699, 2019.
- R. E. Baker, A. Parker, and M. J. Simpson. A free boundary model of epithelial dynamics. *Journal of Theoretical Biology*, 481(1):61–74, 2019.
- J. Bard and I. Lauder. How well does turing’s theory of morphogenesis work? *Journal of Theoretical Biology*, 45(2):501–531, 1974.
- H. E. Barker, J. T. Paget, A. A. Khan, and K. J. Harrington. The tumour microenvironment after radiotherapy: mechanisms of resistance and recurrence. *Nature Reviews Cancer*, 15(7):409–425, 2015.
- G. Barles, L. C. Evans, and P. E. Souganidis. Wavefront propagation for reaction-diffusion systems of PDE. *Duke Mathematical Journal*, 61(3):835–858, 1989.
- G. Barles, S. Mirrahimi, B. Perthame, et al. Concentration in Lotka-Volterra parabolic or integral equations: a general convergence result. *Methods and Applications of Analysis*, 16(3):321–340, 2009.
- V. H. Barocas and R. T. Tranquillo. Biphasic theory and in vitro assays of cell-fibril mechanical interactions in tissue-equivalent gels. In *Cell Mechanics and Cellular Engineering*, pages 185–209. Springer, 1994.
- V. H. Barocas, A. G. Moon, and R. T. Tranquillo. The Fibroblast-Populated Collagen Microsphere Assay of Cell Traction Force—Part 2: Measurement of the Cell Traction Parameter. *Journal of Biomechanical Engineering*, 117(2):161–170, 1995.
- D. Basanta and A. R. A. Anderson. Exploiting ecological principles to better understand cancer progression and treatment. *Interface Focus*, 3(4):20130020, 2013.
- D. Basanta, M. Simon, H. Hatzikirou, and A. Deutsch. Evolutionary game theory elucidates the role of glycolysis in glioma progression and invasion. *Cell Proliferation*, 41(6):980–987, 2008.
- D. Basanta, R. A. Gatenby, and A. R. A. Anderson. Exploiting evolution to treat drug resistance: combination therapy and the double bind. *Molecular Pharmaceutics*, 9(4):914–921, 2012a.
- D. Basanta, J. G. Scott, M. N. Fishman, G. Ayala, S. W. Hayward, and A. R. A. Anderson. Investigating prostate cancer tumour–stroma interactions: clinical and biological insights from an evolutionary game. *British Journal of Cancer*, 106(1):174–181, 2012b.

- M. U. Baumann, S. Zamudio, and N. P. Illsley. Hypoxic upregulation of glucose transporters in human choriocarcinoma cells is mediated by hypoxia-inducible factor-1. *American Journal of Physiology - Cell Physiology*, 293(1):C477–C485, 2007.
- E. L. Bearer, J. S. Lowengrub, H. B. Frieboes, Y.-L. Chuang, F. Jin, S. M. Wise, M. Ferrari, D. B. Agus, and V. Cristini. Multiparameter computational modeling of tumor invasion. *Cancer Research*, 69(10):4493–4501, 2009.
- N. Beerenswinkel, T. Antal, D. Dingli, A. Traulsen, K. W. Kinzler, V. E. Velculescu, B. Vogelstein, and M. A. Nowak. Genetic progression and the waiting time to cancer. *PLoS Computational Biology*, 3(11):e225, 2007.
- A. Bellini and S. Mattoli. The role of the fibrocyte, a bone marrow-derived mesenchymal progenitor, in reactive and reparative fibroses. *Laboratory Investigation*, 87(9):858–870, 2007.
- O. Benichou, V. Calvez, N. Meunier, and R. Voituriez. Front acceleration by dynamic selection in fisher population waves. *Physical Review E*, 86(4):041908, 2012.
- D. E. Bentil and J. D. Murray. Pattern selection in biological pattern formation mechanisms. *Applied Mathematics Letters*, 4(3):1–5, 1991.
- H. Berestycki, G. Nadin, B. Perthame, and L. Ryzhik. The non-local Fisher–KPP equation: travelling waves and steady states. *Nonlinearity*, 22(12):2813, 2009.
- A. L. Berrier and K. M. Yamada. Cell–matrix adhesion. *Journal of Cellular Physiology*, 213(3):565–573, 2007.
- L. Bianchetti, M. Barczyk, J. Cardoso, M. Schmidt, A. Bellini, and S. Mattoli. Extracellular matrix remodelling properties of human fibrocytes. *Journal of Cellular and Molecular Medicine*, 16(3):483–495, 2012.
- L. E. Bilston, Z. Liu, and N. Phan-Thien. Linear viscoelastic properties of bovine brain tissue in shear. *Biorheology*, 34(6):377–385, 1997.
- V. B. Birman, W. K. Binienda, and G. Townsend. 2D Maxwell model. *Journal of Macromolecular Science, Part B*, 41(2):341–356, 2002.
- J. E. Bischoff, E. M. Arruda, and K. Grosh. A rheological network model for the continuum anisotropic and viscoelastic behavior of soft tissue. *Biomechanics and Modeling in Mechanobiology*, 3(1):56–65, 2004.
- V. Bitsouni, M. A. J. Chaplain, and R. Eftimie. Mathematical modelling of cancer invasion: the multiple roles of TGF- $\beta$  pathway on tumour proliferation and cell adhesion. *Mathematical Models and Methods in Applied Sciences*, 27(10):1929–1962, 2017.

- M. R. Blatchley, F. Hall, S. Wang, H. C. Pruitt, and S. Gerecht. Hypoxia and matrix viscoelasticity sequentially regulate endothelial progenitor cluster-based vasculogenesis. *Science Advances*, 5(3):eaau7518, 2019.
- S. E. Boas, Y. Jiang, R. M. Merks, S. A. Prokopiou, and E. G. Rens. Cellular potts model: applications to vasculogenesis and angiogenesis. In *Probabilistic Cellular Automata*, pages 279–310. Springer, 2018.
- N. Boonkorkuea, Y. Lenbury, F. Alvarado, and D. Wollkind. Nonlinear stability analyses of vegetative pattern formation in an arid environment. *Journal of Biological Dynamics*, 4(4):346–380, 2010.
- E. Bouin and V. Calvez. Travelling waves for the cane toads equation with bounded traits. *Nonlinearity*, 27(9):2233, 2014.
- E. Bouin and S. Mirrahimi. A Hamilton-Jacobi approach for a model of population structured by space and trait. *Communications in Mathematical Sciences*, 13(6):1431–1452, 2015.
- E. Bouin, V. Calvez, N. Meunier, S. Mirrahimi, B. Perthame, G. Raoul, and R. Voituriez. Invasion fronts with variable motility: phenotype selection, spatial sorting and wave acceleration. *Comptes Rendus Mathematique*, 350(15-16):761–766, 2012.
- D. A. Brafman. Constructing stem cell microenvironments using bioengineering approaches. *Physiological Genomics*, 45(23):1123–1135, 2013.
- D. Bray. *Cell movements: from molecules to motility*. Garland Science, 2000.
- F. Brinkmann, M. Mercker, T. Richter, and A. Marciniak-Czochra. Post-Turing tissue pattern formation: Advent of mechanochemistry. *PLoS Computational Biology*, 14(7):e1006259, 2018.
- J. M. Brown and A. J. Giaccia. The unique physiology of solid tumors: opportunities (and problems) for cancer therapy. *Cancer Research*, 58(7):1408–1416, 1998.
- J. S. Brown, J. J. Cunningham, and R. A. Gatenby. Aggregation effects and population-based dynamics as a source of therapy resistance in cancer. *IEEE Transactions on Biomedical Engineering*, 64(3):512–518, 2016.
- R. Brown, E. Curry, L. Magnani, C. S. Wilhelm-Benartzi, and J. Borley. Poised epigenetic states and acquired drug resistance in cancer. *Nature Reviews Cancer*, 14(11):747–753, 2014.

- F. Bubba, C. Pouchol, N. Ferrand, G. Vidal, L. Almeida, B. Perthame, and M. Sabbah. A chemotaxis-based explanation of spheroid formation in 3D cultures of breast cancer cells. *Journal of Theoretical Biology*, 479(1):73–80, 2019. ISSN 10958541.
- F. Bubba, T. Lorenzi, and F. R. Macfarlane. From a discrete model of chemotaxis with volume-filling to a generalized Patlak–Keller–Segel model. *Proceedings of the Royal Society A*, 476(2237):20190871, 2020.
- M. Burger, J. A. Carrillo, J.-F. Pietschmann, and M. Schmidtchen. Segregation effects and gap formation in cross-diffusion models. *Interfaces and Free Boundaries*, 22(2):175–203, 2020.
- R. Bürger. *The mathematical theory of selection, recombination, and mutation*. John Wiley & Sons, 2000.
- R. A. Burrell and C. Swanton. Tumour heterogeneity and the evolution of polyclonal drug resistance. *Molecular Oncology*, 8(6):1095–1111, 2014.
- A. Buttenschön, T. Hillen, A. Gerisch, and K. J. Painter. A space-jump derivation for non-local models of cell–cell adhesion and non-local chemotaxis. *Journal of Mathematical Biology*, 76(1):429–456, 2018.
- H. Byrne and D. Drasdo. Individual-based and continuum models of growing cell populations: a comparison. *Journal of Mathematical Biology*, 58(4):657–687, 2009.
- H. Byrne and L. Preziosi. Modelling solid tumour growth using the theory of mixtures. *Mathematical Medicine and Biology: A Journal of the IMA*, 20(4):341–366, 2003.
- H. M. Byrne and M. A. J. Chaplain. The importance of constitutive equations in mechanochemical models of pattern formation. *Applied Mathematics Letters*, 9(6):85–90, 1996.
- C. Carmona-Fontaine, M. Deforet, L. Akkari, C. B. Thompson, J. A. Joyce, and J. B. Xavier. Metabolic origins of spatial organization in the tumor microenvironment. *Proceedings of the National Academy of Sciences*, 114(11):2934–2939, 2017.
- J. Carr. *Applications of centre manifold theory*, volume 35. Springer Science & Business Media, 2012.
- J. A. Carrillo, S. Cuadrado, and B. Perthame. Adaptive dynamics via Hamilton–Jacobi approach and entropy methods for a juvenile-adult model. *Mathematical Biosciences*, 205(1):137–161, 2007.

- J. A. Carrillo, H. Murakawa, M. Sato, H. Togashi, and O. Trush. A population dynamics model of cell-cell adhesion incorporating population pressure and density saturation. *Journal of Theoretical Biology*, 474(1):14–24, 2019.
- J. J. Casciari, S. V. Sotirchos, and R. M. Sutherland. Variations in tumor cell growth rates and metabolism with oxygen concentration, glucose concentration, and extracellular pH. *Journal of Cellular Physiology*, 151(2):386–394, 1992.
- V. Castets, E. Dulos, J. Boissonade, and P. De Kepper. Experimental evidence of a sustained standing Turing-type nonequilibrium chemical pattern. *Physical Review Letters*, 64(24):2953, 1990.
- N. Champagnat and S. Méléard. Polymorphic evolution sequence and evolutionary branching. *Probability Theory and Related Fields*, 151(1-2):45–94, 2011.
- N. Champagnat, R. Ferrière, and S. Méléard. Unifying evolutionary dynamics: from individual stochastic processes to macroscopic models. *Theoretical Population Biology*, 69(3):297–321, 2006.
- N. Champagnat, R. Ferrière, and S. Méléard. From individual stochastic processes to macroscopic models in adaptive evolution. *Stochastic Models*, 24(sup1):2–44, 2008.
- C. Chandler, T. Liu, R. Buckanovich, and L. Coffman. The double edge sword of fibrosis in cancer. *Translational Research*, 209:55–67, 2019.
- M. Chang. Restructuring of the extracellular matrix in diabetic wounds and healing: A perspective. *Pharmacological Research*, 107:243–248, 2016.
- M. A. Chaplain, T. Lorenzi, and F. R. Macfarlane. Bridging the gap between individual-based and continuum models of growing cell populations. *Journal of Mathematical Biology*, 80(1):343–371, 2020.
- M. A. J. Chaplain, M. Lachowicz, Z. Szymańska, and D. Wrzosek. Mathematical modelling of cancer invasion: the importance of cell–cell adhesion and cell–matrix adhesion. *Mathematical Models and Methods in Applied Sciences*, 21(04):719–743, 2011.
- L. Chen, K. Painter, C. Surulescu, and A. Zhigun. Mathematical models for cell migration: a non-local perspective. *Philosophical Transactions of the Royal Society B*, 375 (1807):20190379, 2020.
- R. H. Chisholm, T. Lorenzi, A. Lorz, A. K. Larsen, L. Almeida, A. Escargueil, and J. Clairambault. Emergence of drug tolerance in cancer cell populations: an evolutionary outcome of selection, non-genetic instability and stress-induced adaptation. *Cancer Research*, 75(6):930–939, 2015.

- R. H. Chisholm, T. Lorenzi, and J. Clairambault. Cell population heterogeneity and evolution towards drug resistance in cancer: Biological and mathematical assessment, theoretical treatment optimisation. *Biochimica et Biophysica Acta (BBA)-General Subjects*, 1860(11):2627–2645, 2016a.
- R. H. Chisholm, T. Lorenzi, L. Desvillettes, and B. D. Hughes. Evolutionary dynamics of phenotype-structured populations: from individual-level mechanisms to population-level consequences. *Zeitschrift für Angewandte Mathematik und Physik*, 67(4):100, 2016b.
- R. H. Chisholm, T. Lorenzi, and A. Lorz. Effects of an advection term in nonlocal lotka–volterra equations. *Communications in Mathematical Sciences*, 14(4):1181–1188, 2016c.
- H. Cho and D. Levy. Modeling the dynamics of heterogeneity of solid tumors in response to chemotherapy. *Bulletin of mathematical biology*, 79(12):2986–3012, 2017.
- H. Cho and D. Levy. Modeling the chemotherapy-induced selection of drug-resistant traits during tumor growth. *Journal of Theoretical Biology*, 436(1):120–134, 2018a.
- H. Cho and D. Levy. Modeling continuous levels of resistance to multidrug therapy in cancer. *Applied Mathematical Modelling*, 64(1):733–751, 2018b.
- H. Cho and D. Levy. The impact of competition between cancer cells and healthy cells on optimal drug delivery. *Mathematical Modelling of Natural Phenomena*, 15(42):42, 2020.
- E. Chu and A. Sartorelli. Cancer chemotherapy. *Basic & Clinical Pharmacology*, 9: 898–930, 2004.
- J. Clairambault and C. Pouchol. A survey of adaptive cell population dynamics models of emergence of drug resistance in cancer, and open questions about evolution and cancer. *Biomath*, 8(1):23, 2019.
- I. E. Collier, W. Legant, B. Marmer, O. Lubman, S. Saffarian, T. Wakatsuki, E. Elson, and G. I. Goldberg. Diffusion of MMPs on the surface of collagen fibrils: the mobile cell surface–collagen substratum interface. *PloS One*, 6(9):e24029, 2011.
- A. Coniglio, A. De Candia, S. Di Talia, and A. Gamba. Percolation and burgers’ dynamics in a model of capillary formation. *Physical Review E*, 69(5):051910, 2004.
- P. G. Corrie. Cytotoxic chemotherapy: clinical aspects. *Medicine*, 39(12):717–722, 2011.
- B. Crespi and K. Summers. Evolutionary biology of cancer. *Trends in Ecology & Evolution*, 20(10):545–552, 2005.

- M. Cross and H. Greenside. *Pattern formation and dynamics in nonequilibrium systems*. Cambridge University Press, 2009.
- G. C. Cruywagen and J. D. Murray. On a tissue interaction model for skin pattern formation. *Journal of Nonlinear Science*, 2(2):217–240, 1992.
- P. Cumille, A. Coronel, C. Conca, C. Quiñinao, and C. Escudero. Proposal of a hybrid approach for tumor progression and tumor-induced angiogenesis. *Theoretical Biology and Medical Modelling*, 12(1):13, 2015.
- J. Cunningham, F. Thuijsman, R. Peeters, Y. Viossat, J. Brown, R. Gatenby, and K. Staňková. Optimal control to reach eco-evolutionary stability in metastatic castrate-resistant prostate cancer. *Plos One*, 15(12):e0243386, 2020.
- J. J. Cunningham, J. S. Brown, R. A. Gatenby, and K. Staňková. Optimal control to develop therapeutic strategies for metastatic castrate resistant prostate cancer. *Journal of Theoretical Biology*, 459(1):67–78, 2018.
- A. Czirok. Endothelial cell motility, coordination and pattern formation during vasculogenesis. *Wiley Interdisciplinary Reviews: Systems Biology and Medicine*, 5(5):587–602, 2013.
- W. P. Daley, S. B. Peters, and M. Larsen. Extracellular matrix dynamics in development and regenerative medicine. *Journal of Cell Science*, 121(3):255–264, 2008.
- J. T. Daub and R. M. Merks. A cell-based model of extracellular-matrix-guided endothelial cell migration during angiogenesis. *Bulletin of Mathematical Biology*, 75(8):1377–1399, 2013.
- N. E. Deakin and M. A. J. Chaplain. Mathematical modeling of cancer invasion: The role of membrane-bound matrix metalloproteinases. *Frontiers in Oncology*, 3:70, 2013. ISSN 2234943X.
- T. L. Deem and J. M. Cook-Mills. Vascular cell adhesion molecule 1 (VCAM-1) activation of endothelial cell matrix metalloproteinases: role of reactive oxygen species. *Blood*, 104(8):2385–2393, 2004.
- T. S. Deisboeck, Z. Wang, P. Macklin, and V. Cristini. Multiscale cancer modeling. *Annual Review of Biomedical Engineering*, 13:127–155, 2011.
- N. C. Denko. Hypoxia, HIF1 and glucose metabolism in the solid tumour. *Nature Reviews Cancer*, 8(9):705–713, 2008.

- L. Desvillettes, P.-E. Jabin, S. Mischler, G. Raoul, et al. On selection dynamics for continuous structured populations. *Communications in Mathematical Sciences*, 6(3):729–747, 2008.
- M. W. Dewhirst, Y. Cao, and B. Moeller. Cycling hypoxia and free radicals regulate angiogenesis and radiotherapy response. *Nature Reviews Cancer*, 8(6):425, 2008.
- L. Diaz-Flores, R. Gutierrez, M. Garcia, F. Sáez, F. Valladares, J. Madrid, et al. CD34+ stromal cells/fibroblasts/fibrocytes/telocytes as a tissue reserve and a principal source of mesenchymal cells. location, morphology, function and role in pathology. *Histology and Histopathology: Cellular and Molecular Biology*, 29:831–870, 2014.
- A. Diaz-Santana, M. Shan, and A. D. Stroock. Endothelial cell dynamics during anastomosis in vitro. *Integrative Biology*, 7(4):454–466, 2015.
- O. Diekmann, P.-E. Jabin, S. Mischler, and B. Perthame. The dynamics of adaptation: an illuminating example and a hamilton–jacobi approach. *Theoretical Population Biology*, 67(4):257–271, 2005.
- W. Doerfler and P. Böhm. *DNA methylation: development, genetic disease and cancer*, volume 310. Springer Science & Business Media, 2006.
- P. Domschke, D. Trucu, A. Gerisch, and M. A. J. Chaplain. Mathematical modelling of cancer invasion: implications of cell adhesion variability for tumour infiltrative growth patterns. *Journal of Theoretical Biology*, 361(1):41–60, 2014.
- P. Domschke, D. Trucu, A. Gerisch, and M. A. J. Chaplain. Structured models of cell migration incorporating molecular binding processes. *Journal of Mathematical Biology*, 75(6-7):1517–1561, 2017.
- P. Duesberg, R. Stindl, and R. Hehlmann. Explaining the high mutation rates of cancer cells to drug and multidrug resistance by chromosome reassortments that are catalyzed by aneuploidy. *Proceedings of the National Academy of Sciences*, 97(26):14295–14300, 2000.
- A. M. Dujon, A. Aktipis, C. Alix-Panabières, S. R. Amend, A. M. Boddy, J. S. Brown, J.-p. Capp, J. DeGregori, P. Ewald, R. Gatenby, et al. Identifying key questions in the ecology and evolution of cancer. *Evolutionary Applications*, 14(4):877–892, 2021.
- R. Durrett and S. Levin. The importance of being discrete (and spatial). *Theoretical Population Biology*, 46(3):363–394, 1994.
- K. Eales, K. Hollinshead, and D. Tenant. Hypoxia and metabolic adaptation of cancer cells. *Oncogenesis*, 5(1):e190–e190, 2016.

- T. Ebihara, N. Venkatesan, R. Tanaka, and M. S. Ludwig. Changes in extracellular matrix and tissue viscoelasticity in bleomycin-induced lung fibrosis: Temporal aspects. *American Journal of Respiratory and Critical Care Medicine*, 162(4):1569–1576, 2000.
- M. Egeblad, E. S. Nakasone, and Z. Werb. Tumors as organs: complex tissues that interface with the entire organism. *Developmental Cell*, 18(6):884–901, 2010.
- J. A. Espina, C. L. Marchant, and E. H. Barriga. Durotaxis: the mechanical control of directed cell migration. *The FEBS Journal*, 2021.
- L. C. Evans and P. E. Souganidis. A PDE approach to geometric optics for certain semilinear parabolic equations. *Indiana University Mathematics Journal*, 38(1):141–172, 1989.
- R. Eymard, T. Gallouët, and R. Herbin. Finite volume methods. *Handbook of Numerical Analysis*, 7:713–1018, 2000.
- I. Ferrenq, L. Tranqui, B. Vailhe, P. Y. Gumery, and P. Tracqui. Modelling biological gel contraction by cells: mechanocellular formulation and cell traction force quantification. *Acta Biotheoretica*, 45(3-4):267–293, 1997.
- G. Fiandaca, S. Bernardi, M. Scianna, and M. E. Delitala. A phenotype-structured model to reproduce the avascular growth of a tumor and its interaction with the surrounding environment. *Journal of Theoretical Biology*, page 110980, 2021a.
- G. Fiandaca, M. Delitala, and T. Lorenzi. A mathematical study of the influence of hypoxia and acidity on the evolutionary dynamics of cancer. *Bulletin of Mathematical Biology*, 83(7):1–29, 2021b.
- W. N. Findley, J. S. Lai, and K. Onaran. *Creep and relaxation of nonlinear viscoelastic materials - with an introduction to linear viscoelasticity*. Dover Publications, 1976.
- R. A. Fisher. The wave of advance of advantageous genes. *Annals of Eugenics*, 7(4):355–369, 1937.
- W. H. Fleming and P. E. Souganidis. PDE-viscosity solution approach to some problems of large deviations. *Annali della Scuola Normale Superiore di Pisa-Classe di Scienze*, 13(2):171–192, 1986.
- L. C. Franssen, T. Lorenzi, A. E. F. Burgess, and M. A. J. Chaplain. A mathematical framework for modelling the metastatic spread of cancer. *Bulletin of Mathematical Biology*, 81(6):1965–2010, 2019.
- C. Frantz, K. Stewart, and V. M. Weaver. The extracellular matrix at a glance. *Journal of Cell Science*, 123(24):4195–4200, 2010. ISSN 00219533.

- P. Friedl. Prespecification and plasticity: shifting mechanisms of cell migration. *Current Opinion in Cell Biology*, 16(1):14–23, 2004.
- P. Friedl and K. Wolf. Tumour-cell invasion and migration: diversity and escape mechanisms. *Nature Reviews Cancer*, 3(5):362–374, 2003.
- D. Fukumura, D. G. Duda, L. L. Munn, and R. K. Jain. Tumor microvasculature and microenvironment: novel insights through intravital imaging in pre-clinical models. *Microcirculation*, 17(3):206–225, 2010.
- Y. C. Fung. *Biomechanics Mechanical Properties of Living Tissues (2nd Edition)*. Springer-Verlag New York, 1993.
- J. Gallaher and A. R. A. Anderson. Evolution of intratumoral phenotypic heterogeneity: the role of trait inheritance. *Interface Focus*, 3(4):20130016, 2013.
- A. Gamba, D. Ambrosi, A. Coniglio, A. De Candia, S. Di Talia, E. Giraudo, G. Serini, L. Preziosi, and F. Bussolino. Percolation, morphogenesis, and Burgers dynamics in blood vessels formation. *Physical Review Letters*, 90(11):118101, 2003.
- S. N. Gardner. Modeling multi-drug chemotherapy: tailoring treatment to individuals. *Journal of Theoretical Biology*, 214(2):181–207, 2002.
- D. R. Garrod. Cell to cell and cell to matrix adhesion. *BMJ: British Medical Journal*, 306(6879):703, 1993.
- L. P. Gartner. *Textbook of Histology E-Book*. Elsevier Health Sciences, 2020.
- R. Gatenby, K. Smallbone, P. Maini, F. Rose, J. Averill, R. Nagle, L. Worrall, and R. Gillies. Cellular adaptations to hypoxia and acidosis during somatic evolution of breast cancer. *British Journal of Cancer*, 97(5):646, 2007.
- R. A. Gatenby and J. Brown. Mutations, evolution and the central role of a self-defined fitness function in the initiation and progression of cancer. *Biochimica et Biophysica Acta (BBA)-Reviews on Cancer*, 1867(2):162–166, 2017.
- R. A. Gatenby and R. J. Gillies. Glycolysis in cancer: a potential target for therapy. *The International Journal of Biochemistry & Cell Biology*, 39(7-8):1358–1366, 2007.
- R. A. Gatenby and R. J. Gillies. A microenvironmental model of carcinogenesis. *Nature Reviews Cancer*, 8(1):56–61, 2008.
- R. A. Gatenby and T. L. Vincent. Application of quantitative models from population biology and evolutionary game theory to tumor therapeutic strategies. *Molecular Cancer Therapeutics*, 2(9):919–927, 2003a.

- R. A. Gatenby and T. L. Vincent. An evolutionary model of carcinogenesis. *Cancer Research*, 63(19):6212–6220, 2003b.
- L. Gay, A.-M. Baker, and T. A. Graham. Tumour cell heterogeneity. *F1000Research*, 5:238, 2016.
- A. Gerisch. On the approximation and efficient evaluation of integral terms in PDE models of cell adhesion. *IMA Journal of Numerical Analysis*, 30(1):173–194, 2010.
- A. Gerisch and M. A. J. Chaplain. Robust numerical methods for taxis–diffusion–reaction systems: Applications to biomedical problems. *Mathematical and Computer Modelling*, 43(1):49–75, 2006.
- A. Gerisch and M. A. J. Chaplain. Mathematical modelling of cancer cell invasion of tissue: local and non-local models and the effect of adhesion. *Journal of Theoretical Biology*, 250(4):684–704, 2008.
- A. Gerisch and K. J. Painter. Mathematical modeling of cell adhesion and its applications to developmental biology and cancer invasion. In *Cell Mechanics*, pages 337–368. Chapman and Hall/CRC, 2010.
- A. Giatromanolaki, M. Koukourakis, E. Sivridis, H. Turley, K. Talks, F. Pezzella, K. Gatter, and A. Harris. Relation of hypoxia inducible factor 1  $\alpha$  and 2  $\alpha$  in operable non-small cell lung cancer to angiogenic/molecular profile of tumours and survival. *British Journal of Cancer*, 85(6):881–890, 2001.
- A. Gierer and H. Meinhardt. A theory of biological pattern formation. *Kybernetik*, 12:30–39, 1972.
- R. J. Gillies and R. A. Gatenby. Hypoxia and adaptive landscapes in the evolution of carcinogenesis. *Cancer and Metastasis Reviews*, 26(2):311–317, 2007.
- R. J. Gillies, D. Verduzco, and R. A. Gatenby. Evolutionary dynamics of carcinogenesis and why targeted therapy does not work. *Nature Reviews Cancer*, 12(7):487, 2012.
- R. J. Gillies, J. S. Brown, A. R. A. Anderson, and R. A. Gatenby. Eco-evolutionary causes and consequences of temporal changes in intratumoural blood flow. *Nature Reviews Cancer*, page 1, 2018.
- S. J. Gilmore, B. L. Vaughan Jr, A. Madzvamuse, and P. K. Maini. A mechanochemical model of striae distensae. *Mathematical Biosciences*, 240(2):141–147, 2012.
- J. D. Gordan, J. A. Bertout, C.-J. Hu, J. A. Diehl, and M. C. Simon. HIF-2 $\alpha$  promotes hypoxic cell proliferation by enhancing c-myc transcriptional activity. *Cancer Cell*, 11(4):335–347, 2007.

- M. Greaves and C. C. Maley. Clonal evolution in cancer. *Nature*, 481(7381):306–313, 2012.
- J. Greene, O. Lavi, M. M. Gottesman, and D. Levy. The impact of cell density and mutations in a model of multidrug resistance in solid tumors. *Bulletin of Mathematical Biology*, 76(3):627–653, 2014.
- D. R. Grimes, P. Kannan, D. R. Warren, B. Markelc, R. Bates, R. Muschel, and M. Partridge. Estimating oxygen distribution from vasculature in three-dimensional tumour tissue. *Journal of The Royal Society Interface*, 13(116):20160070, 2016.
- J. Guckenheimer and P. Holmes. *Nonlinear oscillations, dynamical systems, and bifurcations of vector fields*, volume 42. Springer Science & Business Media, 2013.
- M. Haghghi-Yazdi and P. Lee-Sullivan. Modeling linear viscoelasticity in glassy polymers using standard rheological models, 2011.
- Y. Han, Z. Li, J. Tao, and M. Ma. Pattern formation for a volume-filling chemotaxis model with logistic growth. *Journal of Mathematical Analysis and Applications*, 448(2):885–907, 2017.
- D. Hanahan and R. A. Weinberg. The hallmarks of cancer. *Cell*, 100(1):57–70, 2000.
- D. Hanahan and R. A. Weinberg. Hallmarks of cancer: the next generation. *Cell*, 144(5):646–674, 2011.
- D. Hanjaya-Putra and S. Gerecht. Vascular engineering using human embryonic stem cells. *Biotechnology Progress*, 25(1):2–9, 2009.
- K. D. Hansen, W. Timp, H. C. Bravo, S. Sabunciyan, B. Langmead, O. G. McDonald, B. Wen, H. Wu, Y. Liu, D. Diep, et al. Increased methylation variation in epigenetic domains across cancer types. *Nature Genetics*, 43(8):768–775, 2011.
- A. K. Harris, D. Stopak, and P. Wild. Fibroblast traction as a mechanism for collagen morphogenesis. *Nature*, 290(5803):249–251, 1981.
- A. Harris Jr. Tissue culture cells on deformable substrata: biomechanical implications. *Journal of Biomechanical Engineering*, 106(1):19–24, 1984.
- G. Helmlinger, F. Yuan, M. Dellian, and R. K. Jain. Interstitial pH and pO<sub>2</sub> gradients in solid tumors in vivo: high-resolution measurements reveal a lack of correlation. *Nature Medicine*, 3(2):177, 1997.
- H. Heloterä and K. Alitalo. The VEGF family, the inside story. *Cell*, 130(4):591–592, 2007.

- F. Hillen and A. W. Griffioen. Tumour vascularization: sprouting angiogenesis and beyond. *Cancer and Metastasis Reviews*, 26(3):489–502, 2007.
- T. Hillen and K. J. Painter. Global Existence for a Parabolic Chemotaxis Model with Prevention of Overcrowding. *Advances in Applied Mathematics*, 26(4):280–301, 2001. ISSN 01968858.
- T. Hillen and K. J. Painter. A user’s guide to PDE models for chemotaxis. *Journal of Mathematical Biology*, 58(1):183–217, 2009.
- L. Hlatky and E. Alpen. Two-dimensional diffusion limited system for cell growth. *Cell Proliferation*, 18(6):597–611, 1985.
- M. Hockel and P. Vaupel. Tumor hypoxia: definitions and current clinical, biologic, and molecular aspects. *Journal of the National Cancer Institute*, 93(4):266–276, 2001.
- A. Hodgkinson, G. Uzé, O. Radulescu, and D. Trucu. Signal propagation in sensing and reciprocating cellular systems with spatial and structural heterogeneity. *Bulletin of Mathematical Biology*, 80(7):1900–1936, 2018.
- M. Holmes and B. Sleeman. A mathematical model of tumour angiogenesis incorporating cellular traction and viscoelastic effects. *Journal of Theoretical Biology*, 202(2):95–112, 2000.
- T. Hoshiba and T. Yamaoka. *Decellularized Extracellular Matrix: Characterization, Fabrication and Applications*, volume 6. Royal Society of Chemistry, 2019.
- R. Hoyle and R. B. Hoyle. *Pattern formation: an introduction to methods*. Cambridge University Press, 2006.
- K. Hoyt, B. Castaneda, M. Zhang, P. Nigwekar, P. A. di Sant’Agnese, J. V. Joseph, J. Strang, D. J. Rubens, and K. J. Parker. Tissue elasticity properties as biomarkers for prostate cancer. *Cancer Biomarkers*, 4(4-5):213–225, 2008.
- L. E. Huang. How HIF-1 $\alpha$  handles stress. *Science*, 339(6125):1285–1286, 2013a.
- S. Huang. Genetic and non-genetic instability in tumor progression: link between the fitness landscape and the epigenetic landscape of cancer cells. *Cancer and Metastasis Reviews*, 32:423–448, 2013b.
- Y.-P. Huang, Y.-P. Zheng, and S.-F. Leung. Quasi-linear viscoelastic properties of fibrotic neck tissues obtained from ultrasound indentation tests in vivo. *Clinical Biomechanics*, 20(2):145–154, 2005.

- A. Ibrahim-Hashim, M. Robertson-Tessi, P. Enrizues-Navas, M. Damaghi, Y. Balagurunathan, J. W. Wojtkowiak, S. Russell, K. Yoonseok, M. C. Lloyd, M. M. Bui, et al. Defining cancer subpopulations by adaptive strategies rather than molecular properties provides novel insights into intratumoral evolution. *Cancer Research*, 77(9):2242–2254, 2017.
- D. E. Ingber. Mechanical control of tissue morphogenesis during embryological development. *International Journal of Developmental Biology*, 50(2-3):255–266, 2003.
- P.-E. Jabin and R. S. Schram. Selection-Mutation dynamics with spatial dependence. *arXiv preprint arXiv:1601.04553*, 2016. To appear in the *Journal de Mathématiques Pures et Appliquées*.
- H. Jain and T. Jackson. A hybrid model of the role of VEGF binding in endothelial cell migration and capillary formation. *Frontiers in Oncology*, 3:102, 2013.
- R. K. Jain. Determinants of tumor blood flow: a review. *Cancer Research*, 48(10):2641–2658, 1988.
- R. K. Jain, R. T. Tong, and L. L. Munn. Effect of vascular normalization by antiangiogenic therapy on interstitial hypertension, peritumor edema, and lymphatic metastasis: insights from a mathematical model. *Cancer Research*, 67(6):2729–2735, 2007.
- E. Javierre, P. Moreo, M. Doblaré, and J. M. García-Aznar. Numerical modeling of a mechano-chemical theory for wound contraction analysis. *International Journal of Solids and Structures*, 46(20):3597–3606, 2009.
- J. Jernvall, S. A. Newman, et al. Mechanisms of pattern formation in development and evolution. *Development*, 130(10):2027–2037, 2003.
- M. K. Jolly, M. Boareto, B. Huang, D. Jia, M. Lu, E. Ben-Jacob, J. N. Onuchic, and H. Levine. Implications of the hybrid epithelial/mesenchymal phenotype in metastasis. *Frontiers in Oncology*, 5:155, 2015.
- B. F. Jordan and P. Sonveaux. Targeting tumor perfusion and oxygenation to improve the outcome of anticancer therapy1. *Frontiers in Pharmacology*, 3:94, 2012.
- A. Kaznatcheev, R. Vander Velde, J. G. Scott, and D. Basanta. Cancer treatment scheduling and dynamic heterogeneity in social dilemmas of tumour acidity and vasculature. *British Journal of Cancer*, 116(6):785, 2017.
- E. F. Keller and L. A. Segel. Initiation of slime mold aggregation viewed as an instability. *Journal of Theoretical Biology*, 26(3):399–415, 1970.

- N. Khalilgharibi and Y. Mao. To form and function: on the role of basement membrane mechanics in tissue development, homeostasis and disease. *Open Biology*, 11(2):200360, 2021.
- Y. Kim and A. Friedman. Interaction of tumor with its micro-environment: A mathematical model. *Bulletin of Mathematical Biology*, 72(5):1029–1068, 2010.
- A. V. Kinev, V. Levering, K. Young, F. Ali-Osman, G. A. Truskey, M. W. Dewhirst, and D. Il'yasova. Endothelial colony forming cells (ECFCs) as a model for studying effects of low-dose ionizing radiation: growth inhibition by a single dose. *Cancer Investigation*, 31(5):359–364, 2013.
- R. Kocen, M. Gasik, A. Gantar, S. Novak, et al. Viscoelastic behaviour of hydrogel-based composites for tissue engineering under mechanical load. *Biomedical Materials*, 12(2): 025004, 2017.
- D. Kolte, J. A. McClung, and W. S. Aronow. Vasculogenesis and Angiogenesis. In *Translational Research in Coronary Artery Disease: Pathophysiology to Treatment*, chapter 6, pages 49–65. Elsevier Inc., 2016. ISBN 9780128023853.
- N. L. Komarova and D. Wodarz. Drug resistance in cancer: principles of emergence and prevention. *Proceedings of the National Academy of Sciences*, 102(27):9714–9719, 2005.
- S. Kondo and R. Asai. A reaction–diffusion wave on the skin of the marine angelfish pomacanthus. *Nature*, 376(6543):765–768, 1995.
- B. Koren. *A robust upwind discretization method for advection, diffusion and source terms*. Centrum voor Wiskunde en Informatica Amsterdam, 1993.
- B. P. Kotler and J. S. Brown. Cancer community ecology. *Cancer Control*, 27(1): 1073274820951776, 2020.
- R. Kowalczyk. Preventing blow-up in a chemotaxis model. *Journal of Mathematical Analysis and Applications*, 305(2):566–588, 2005.
- R. Kowalczyk, A. Gamba, and L. Preziosi. On the stability of homogeneous solutions to some aggregation models. *Discrete & Continuous Dynamical Systems-B*, 4(1):203, 2004.
- A. Krtolica and J. W. Ludlow. Hypoxia arrests ovarian carcinoma cell cycle progression, but invasion is unaffected. *Cancer Research*, 56(5):1168–1173, 1996.
- M. Kukumberg, A. M. Zaw, D. H. Wong, C. M. Toh, B. P. Chan, R. Seet, P. T. Wong, and E. K. Yim. Characterization and functional assessment of endothelial progenitor cells in ischemic stroke patients. *Stem Cell Reviews and Reports*, 17(3):952–967, 2021.

- J. K. Kular, S. Basu, and R. I. Sharma. The extracellular matrix: structure, composition, age-related differences, tools for analysis and applications for tissue engineering. *Journal of Tissue Engineering*, 5:2041731414557112, 2014.
- S. Kumar, A. Das, A. Barai, and S. Sen. MMP secretion rate and inter-invadopodia spacing collectively govern cancer invasiveness. *Biophysical Journal*, 114(3):650–662, 2018.
- L. S. Kumosa, T. L. Routh, J. T. Lin, J. Y. Lucisano, and D. A. Gough. Permeability of subcutaneous tissues surrounding long-term implants to oxygen. *Biomaterials*, 35(29):8287–8296, 2014.
- M. Kuznetsov, J. Clairambault, and V. Volpert. Improving cancer treatments via dynamical biophysical models. *Physics of Life Reviews*, 2021.
- T. Kwok and P. Twentyman. The response to cytotoxic drugs of EMT6 cells treated either as intact or disaggregated spheroids. *British Journal of Cancer*, 51(2):211, 1985.
- A. W. Lambert, D. R. Pattabiraman, and R. A. Weinberg. Emerging biological principles of metastasis. *Cell*, 168(4):670–691, 2017.
- E. Lammert and J. Axnick. Vascular lumen formation. *Cold Spring Harbor perspectives in medicine*, 2(4):a006619, 2012.
- L. D. Landau and E. M. Lifshitz. *Theory of Elasticity*. Pergamon Press, 1970.
- R. Lande and S. J. Arnold. The measurement of selection on correlated characters. *Evolution*, 37(6):1210–1226, 1983.
- O. Lavi, M. M. Gottesman, and D. Levy. The dynamics of drug resistance: a mathematical perspective. *Drug Resistance Updates*, 15(1-2):90–97, 2012.
- O. Lavi, J. M. Greene, D. Levy, and M. M. Gottesman. The role of cell density and intratumoral heterogeneity in multidrug resistance. *Cancer Research*, 73(24):7168–7175, 2013.
- B. Laviña. Brain vascular imaging techniques. *International Journal of Molecular Sciences*, 18(1):70, 2016.
- J.-W. Lee, S.-H. Bae, J.-W. Jeong, S.-H. Kim, and K.-W. Kim. Hypoxia-inducible factor (hif-1)  $\alpha$ : its protein stability and biological functions. *Experimental & Molecular Medicine*, 36(1):1, 2004.
- S. Lee, T. T. Chen, C. L. Barber, M. C. Jordan, J. Murdock, S. Desai, N. Ferrara, A. Nagy, K. P. Roos, and M. L. Iruela-Arispe. Autocrine VEGF signaling is required for vascular homeostasis. *Cell*, 130(4):691–703, 2007.

- O. Lefebvre, L. Sorokin, M. Kedinger, and P. Simon-Assmann. Developmental Expression and Cellular Origin of the Laminin 2, 4, and 5 Chains in the Intestine. *Developmental Biology*, 210:135–150, 1999.
- C. T. Leung and J. S. Brugge. Tumor self-seeding: bidirectional flow of tumor cells. *Cell*, 139(7):1226–1228, 2009.
- R. J. LeVeque. *Finite difference methods for ordinary and partial differential equations: steady-state and time-dependent problems*. Society for Industrial and Applied Mathematics (SIAM), Philadelphia, 2007.
- H. Levine, M. K. Jolly, P. Kulkarni, and V. Nanjundiah. *Phenotypic Switching: Implications in Biology and Medicine*. Academic Press, 2020.
- M. A. Lewis and J. D. Murray. Analysis of stable two-dimensional patterns in contractile cytogel. *Journal of Nonlinear Science*, 1(3):289–311, 1991.
- C. K. Li. The glucose distribution in 9l rat brain multicell tumor spheroids and its effect on cell necrosis. *Cancer*, 50(10):2066–2073, 1982.
- K. A. Lipinski, L. J. Barber, M. N. Davies, M. Ashenden, A. Sottoriva, and M. Gerlinger. Cancer evolution and the limits of predictability in precision cancer medicine. *Trends in Cancer*, 2(1):49–63, 2016.
- Q. Liu, H. Peng, and Z.-A. Wang. Asymptotic stability of diffusion waves of a quasi-linear hyperbolic-parabolic model for vasculogenesis. *arXiv preprint arXiv:2103.11301*, 2021.
- Z. Liu and L. Bilston. On the viscoelastic character of liver tissue: experiments and modelling of the linear behaviour. *Biorheology*, 37(3):191–201, 2000.
- M. C. Lloyd, J. J. Cunningham, M. M. Bui, R. J. Gillies, J. S. Brown, and R. A. Gatenby. Darwinian dynamics of intratumoral heterogeneity: not solely random mutations but also variable environmental selection forces. *Cancer Research*, 76:3136–3144, 2016.
- L. A. Loeb. A mutator phenotype in cancer. *Cancer Research*, 61(8):3230–3239, 2001.
- T. Lorenzi and K. J. Painter. Trade-offs between chemotaxis and proliferation shape the phenotypic structuring of invading waves. *International Journal of Non-Linear Mechanics*, 139:103885, 2022.
- T. Lorenzi, R. H. Chisholm, L. Desvillettes, and B. D. Hughes. Dissecting the dynamics of epigenetic changes in phenotype-structured populations exposed to fluctuating environments. *Journal of Theoretical Biology*, 386(1):166–176, 2015.

- T. Lorenzi, R. H. Chisholm, and J. Clairambault. Tracking the evolution of cancer cell populations through the mathematical lens of phenotype-structured equations. *Biology Direct*, 11(1):43, 2016.
- T. Lorenzi, C. Venkataraman, A. Lorz, and M. A. J. Chaplain. The role of spatial variations of abiotic factors in mediating intratumour phenotypic heterogeneity. *Journal of Theoretical Biology*, 451(1):101–110, 2018.
- T. Lorenzi, F. R. Macfarlane, and C. Villa. Discrete and continuum models for the evolutionary and spatial dynamics of cancer: a very short introduction through two case studies. In *International Symposium on Mathematical and Computational Biology*, pages 359–380. Springer, 2019.
- T. Lorenzi, P. J. Murray, and M. Ptashnyk. From individual-based mechanical models of multicellular systems to free-boundary problems. *Interfaces and Free Boundaries*, 22(2):205–244, 2020.
- T. Lorenzi, B. Perthame, and X. Ruan. Invasion fronts and adaptive dynamics in a model for the growth of cell populations with heterogeneous mobility. *European Journal of Applied Mathematics*, pages 1–18, 2021. doi:10.1017/S0956792521000218.
- A. Lorz, S. Mirrahimi, and B. Perthame. Dirac mass dynamics in multidimensional nonlocal parabolic equations. *Communications in Partial Differential Equations*, 36(6):1071–1098, 2011.
- A. Lorz, T. Lorenzi, M. E. Hochberg, J. Clairambault, and B. Perthame. Populational adaptive evolution, chemotherapeutic resistance and multiple anti-cancer therapies. *ESAIM: Mathematical Modelling and Numerical Analysis*, 47(2):377–399, 2013.
- A. Lorz, T. Lorenzi, J. Clairambault, A. Escargueil, and B. Perthame. Modeling the effects of space structure and combination therapies on phenotypic heterogeneity and drug resistance in solid tumors. *Bulletin of Mathematical Biology*, 77(1):1–22, 2015.
- N. Loy and L. Preziosi. Kinetic models with non-local sensing determining cell polarization and speed according to independent cues. *Journal of Mathematical Biology*, 80(1):373–421, 2020.
- N. Loy and L. Preziosi. Stability of a non-local kinetic model for cell migration with density-dependent speed. *Mathematical Medicine and Biology: A Journal of the IMA*, 38(1):83–105, 2021.
- F. R. Macfarlane, M. A. Chaplain, and T. Lorenzi. A hybrid discrete-continuum approach to model Turing pattern formation. *Mathematical Biosciences and Engineering*, 17(6):7442–7479, 2020.

- A. Madzvamuse, R. Barreira, and A. Gerisch. Cross-diffusion in reaction-diffusion models: Analysis, numerics, and applications. In P. Quintela, P. Barral, D. Gómez, F. J. Pena, J. Rodríguez, P. Salgado, and M. E. Vázquez-Méndez, editors, *Progress in Industrial Mathematics at ECMI 2016*, pages 385–392, Cham, 2017. Springer International Publishing.
- A. L. Magnussen and I. G. Mills. Vascular normalisation as the stepping stone into tumour microenvironment transformation. *British Journal of Cancer*, pages 1–13, 2021.
- P. Maini, K. Painter, and H. P. Chau. Spatial pattern formation in chemical and biological systems. *Journal of the Chemical Society, Faraday Transactions*, 93(20):3601–3610, 1997.
- P. K. Maini. Morphogenesis, biological. In A. Scott, editor, *Morphogenesis, Biological, Encyclopedia of Nonlinear Science*, pages 587–589. Routledge, 2005.
- P. K. Maini and J. D. Murray. A nonlinear analysis of a mechanical model for biological pattern formation. *SIAM Journal on Applied Mathematics*, 48(5):1064–1072, 1988.
- P. K. Maini and T. E. Woolley. The Turing Model for Biological Pattern Formation. In *The Dynamics of Biological Systems*, pages 189–204. Springer, 2019.
- P. K. Maini, L. Olsen, and J. A. Sherratt. Mathematical models for cell-matrix interactions during dermal wound healing. *International Journal of Bifurcation and Chaos*, 12(09):2021–2029, 2002.
- P. K. Maini, T. E. Woolley, R. E. Baker, E. A. Gaffney, and S. S. Lee. Turing’s model for biological pattern formation and the robustness problem. *Interface Focus*, 2(4):487–496, 2012.
- V. S. Manem, K. Kaveh, M. Kohandel, and S. Sivaloganathan. Modeling invasion dynamics with spatial random-fitness due to micro-environment. *PloS One*, 10(10):e0140234, 2015.
- D. Manoussaki. A mechanochemical model of angiogenesis and vasculogenesis. *ESAIM: Mathematical Modelling and Numerical Analysis*, 37(4):581–599, 2003.
- S. Marino, I. B. Hogue, C. J. Ray, and D. E. Kirschner. A methodology for performing global uncertainty and sensitivity analysis in systems biology. *Journal of Theoretical Biology*, 254(1):178–196, 2008.
- A. Marusyk, V. Almendro, and K. Polyak. Intra-tumour heterogeneity: a looking glass for cancer? *Nature Reviews Cancer*, 12(5):323, 2012.
- G. E. Mase. *Continuum mechanics*. McGraw-Hill New York, 1970.

- R. J. McAnulty. Fibroblasts and myofibroblasts: their source, function and role in disease. *The International Journal of Biochemistry & Cell Biology*, 39(4):666–671, 2007.
- H. Meinhardt. *Models of Biological Pattern Formation*. Academic Press, London, 1982.
- H. Meinhardt. *The algorithmic beauty of sea shells*. Springer Science & Business Media, 2009.
- I. Mellman, G. Coukos, and G. Dranoff. Cancer immunotherapy comes of age. *Nature*, 480(7378):480–489, 2011.
- R. M. Merks and J. A. Glazier. Dynamic mechanisms of blood vessel growth. *Nonlinearity*, 19(1):C1, 2005.
- R. M. Merks, S. A. Newman, and J. A. Glazier. Cell-oriented modeling of in vitro capillary development. In *International Conference on Cellular Automata*, pages 425–434. Springer, 2004.
- R. M. Merks, S. V. Brodsky, M. S. Goligorsky, S. A. Newman, and J. A. Glazier. Cell elongation is key to in silico replication of in vitro vasculogenesis and subsequent remodeling. *Developmental Biology*, 289(1):44–54, 2006.
- R. M. H. Merks, E. D. Perryn, A. Shirinifard, and J. A. Glazier. Contact-inhibited chemotaxis in de novo and sprouting blood-vessel growth. *PLoS Computational Biology*, 4(9), 2008.
- L. M. Merlo, J. W. Pepper, B. J. Reid, and C. C. Maley. Cancer as an evolutionary and ecological process. *Nature Reviews Cancer*, 6(12):924–935, 2006.
- J. Metzcar, Y. Wang, R. Heiland, and P. Macklin. A review of cell-based computational modeling in cancer biology. *JCO Clinical Cancer Informatics*, 2:1–13, 2019.
- F. Michor and K. Polyak. The origins and implications of intratumor heterogeneity. *Cancer Prevention Research*, 3(11):1361–1364, 2010.
- S. Mirrahimi. A Hamilton–Jacobi approach to characterize the evolutionary equilibria in heterogeneous environments. *Mathematical Models and Methods in Applied Sciences*, 27(13):2425–2460, 2017.
- S. Mirrahimi and S. Gandon. Evolution of specialization in heterogeneous environments: equilibrium between selection, mutation and migration. *Genetics*, 214(2):479–491, 2020.
- S. Mirrahimi and B. Perthame. Asymptotic analysis of a selection model with space. *Journal de Mathématiques Pures et Appliquées*, 104(6):1108–1118, 2015.

- T. Miura and R. Tanaka. In vitro vasculogenesis models revisited-measurement of vegf diffusion in matrigel. *Mathematical Modelling of Natural Phenomena*, 4(4):118–130, 2009.
- H. R. Molavian, M. Kohandel, M. Milosevic, and S. Sivaloganathan. Fingerprint of cell metabolism in the experimentally observed interstitial ph and po<sub>2</sub> in solid tumors. *Cancer Research*, 69(23):9141–9147, 2009.
- A. G. Moon and R. T. Tranquillo. Fibroblast-populated collagen microsphere assay of cell traction force: Part 1. Continuum model. *AICHE Journal*, 39(1):163–177, 1993.
- P. Moreo, E. A. Gaffney, J. M. Garcia-Aznar, and M. Doblaré. On the modelling of biological patterns with mechanochemical models: insights from analysis and computation. *Bulletin of Mathematical Biology*, 72(2):400–431, 2010.
- K. T. Morin and R. T. Tranquillo. In vitro models of angiogenesis and vasculogenesis in fibrin gel. *Experimental Cell Research*, 319(16):2409–2417, 2013.
- H. Murakawa and H. Togashi. Continuous models for cell-cell adhesion. *Journal of Theoretical Biology*, 374(1):1–12, 2015.
- J. Murray. A mechanical theory of vascular network formation. In *Mathematical Biology*, pages 416–440. Springer, 1993.
- J. D. Murray. A pre-pattern formation mechanism for animal coat markings. *Journal of Theoretical Biology*, 88(1):161–199, 1981.
- J. D. Murray. *Mathematical biology. II Spatial models and biomedical applications {Interdisciplinary Applied Mathematics V. 18}*. Springer-Verlag New York Incorporated New York, 2001.
- J. D. Murray. On the mechanochemical theory of biological pattern formation with application to vasculogenesis. *Comptes Rendus Biologies*, 326(2):239–252, 2003.
- J. D. Murray and P. K. Maini. A new approach to the generation of pattern and form in embryology. *Scientific Programme, Oxford*, 1986.
- J. D. Murray and P. K. Maini. Pattern formation mechanisms—a comparison of reaction-diffusion and mechanochemical models. In *Cell to Cell Signalling*, pages 159–170. Elsevier, 1989.
- J. D. Murray and G. F. Oster. Cell traction models for generating pattern and form in morphogenesis. *Journal of Mathematical Biology*, 19(3):265–279, 1984a.

- J. D. Murray and G. F. Oster. Generation of biological pattern and form. *Mathematical Medicine and Biology: A Journal of the IMA*, 1(1):51–75, 1984b.
- J. D. Murray, G. F. Oster, and A. K. Harris. A mechanical model for mesenchymal morphogenesis. *Journal of Mathematical Biology*, 17(1):125–129, 1983.
- J. D. Murray, P. K. Maini, and R. T. Tranquillo. Mechanochemical models for generating biological pattern and form in development. *Physics Reports*, 171(2):59–84, 1988.
- P. Namy, J. Ohayon, and P. Tracqui. Critical conditions for pattern formation and in vitro tubulogenesis driven by cellular traction fields. *Journal of Theoretical Biology*, 227(1):103–120, 2004.
- J. T. Nardini, R. E. Baker, M. J. Simpson, and K. B. Flores. Learning differential equation models from stochastic agent-based model simulations. *Journal of the Royal Society Interface*, 18(176):20200987, 2021.
- K. Nargess and M. Yanlan. To form and function: on the role of basement membrane mechanics in tissue development, homeostasis and disease. *Open Biology*, 11(2):200360, 2021.
- S. Nasseri, L. E. Bilston, and N. Phan-Thien. Viscoelastic properties of pig kidney in shear, experimental results and modelling. *Rheologica Acta*, 41(1-2):180–192, 2002.
- A. R. Nobre, D. Entenberg, Y. Wang, J. Condeelis, and J. A. Aguirre-Ghiso. The different routes to metastasis via hypoxia-regulated programs. *Trends in Cell Biology*, 28(11):941–956, 2018.
- E. Norris, J. R. King, and H. M. Byrne. Modelling the response of spatially structured tumours to chemotherapy: Drug kinetics. *Mathematical and Computer Modelling*, 43 (7-8):820–837, 2006.
- P. C. Nowell. The clonal evolution of tumor cell populations. *Science*, 194(4260):23–28, 1976.
- J. Olsen, J. Holmes, and G. B. Jemec. Advances in optical coherence tomography in dermatology – a review. *Journal of Biomedical Optics*, 23(4):040901, 2018.
- L. Olsen, J. A. Sherratt, and P. K. Maini. A mechanochemical model for adult dermal wound contraction and the permanence of the contracted tissue displacement profile. *Journal of Theoretical Biology*, 177(2):113–128, 1995.
- G. F. Oster, J. D. Murray, and A. K. Harris. Mechanical aspects of mesenchymal morphogenesis. *Development*, 78(1):83–125, 1983.

- J. Otwinowski and J. B. Plotkin. Inferring fitness landscapes by regression produces biased estimates of epistasis. *Proceedings of the National Academy of Sciences*, 111(22):E2301–E2309, 2014.
- A. R. Padhani, K. A. Krohn, J. S. Lewis, and M. Alber. Imaging oxygenation of human tumours. *European Radiology*, 17(4):861–872, 2007.
- K. M. Page and M. A. Nowak. Unifying evolutionary dynamics. *Journal of Theoretical Biology*, 219(1):93–98, 2002.
- K. J. Painter. Mathematical models for chemotaxis and their applications in self-organisation phenomena. *Journal of Theoretical Biology*, 481(1):162–182, 2019. ISSN 10958541.
- K. J. Painter and T. Hillen. Volume-filling and quorum-sensing in models for chemosensitive movement. *Canadian Applied Mathematics Quarterly*, 10(4):501–543, 2002.
- K. J. Painter, N. J. Armstrong, and J. A. Sherratt. The impact of adhesion on cellular invasion processes in cancer and development. *Journal of Theoretical Biology*, 264(3):1057–1067, 2010.
- K. J. Painter, J. Bloomfield, J. Sherratt, and A. Gerisch. A nonlocal model for contact attraction and repulsion in heterogeneous cell populations. *Bulletin of Mathematical Biology*, 77(6):1132–1165, 2015.
- J. Palacio-Torralba, S. Hammer, D. W. Good, S. A. McNeill, G. D. Stewart, R. L. Reuben, and Y. Chen. Quantitative diagnostics of soft tissue through viscoelastic characterization using time-based instrumented palpation. *Journal of the Mechanical Behavior of Biomedical Materials*, 41:149–160, 2015.
- M. M. Palm and R. M. Merks. Vascular networks due to dynamically arrested crystalline ordering of elongated cells. *Physical Review E*, 87(1):012725, 2013.
- R. Palmer, S. Pratontep, and H.-G. Boyen. Nanostructured surfaces from size-selected clusters. *Nature Materials*, 2(7):443–448, 2003.
- J. Park, D. S. Kim, T. S. Shim, C. M. Lim, Y. Koh, S. D. Lee, W. S. Kim, W. D. Kim, J. S. Lee, and K. S. Song. Lung cancer in patients with idiopathic pulmonary fibrosis. *European Respiratory Journal*, 17(6):1216–1219, 2001.
- A. S. Perelson, P. K. Maini, J. D. Murray, J. M. Hyman, and G. F. Oster. Nonlinear pattern selection in a mechanical model for morphogenesis. *Journal of Mathematical Biology*, 24(5):525–541, 1986.
- B. Perthame. *Transport equations in biology*. Springer Science & Business Media, 2006.

- B. Perthame. Parabolic equations in biology. In *Parabolic Equations in Biology*, pages 1–21. Springer, 2015.
- B. Perthame and G. Barles. Dirac concentrations in lotka-volterra parabolic pdes. *Indiana University Mathematics Journal*, pages 3275–3301, 2008.
- V. Petrolli, M. Le Goff, M. Tadrous, K. Martens, C. Allier, O. Mandula, L. Hervé, S. Henkes, R. Sknepnek, T. Boudou, et al. Confinement-induced transition between wavelike collective cell migration modes. *Physical Review Letters*, 122(16):168101, 2019.
- A. O. Pisco and S. Huang. Non-genetic cancer cell plasticity and therapy-induced stemness in tumour relapse: ‘what does not kill me strengthens me’. *British Journal of Cancer*, 112(11):1725, 2015.
- J. Poleszczuk, P. Hahnfeldt, and H. Enderling. Evolution and phenotypic selection of cancer stem cells. *PLoS Computational Biology*, 11(3):e1004025, 2015.
- T. J. Poole, E. B. Finkelstein, and C. M. Cox. The role of FGF and VEGF in angioblast induction and migration during vascular development. *Developmental Dynamics*, 220(1):1–17, 2001. ISSN 10588388.
- C. Pouchol, J. Clairambault, A. Lorz, and E. Trélat. Asymptotic analysis and optimal control of an integro-differential system modelling healthy and cancer cells exposed to chemotherapy. *Journal de Mathématiques Pures et Appliquées*, 116:268–308, 2018.
- G. Powathil, M. Kohandel, M. Milosevic, and S. Sivaloganathan. Modeling the spatial distribution of chronic tumor hypoxia: implications for experimental and clinical studies. *Computational and Mathematical Methods in Medicine*, 2012:410602, 2012a.
- G. G. Powathil, K. E. Gordon, L. A. Hill, and M. A. J. Chaplain. Modelling the effects of cell-cycle heterogeneity on the response of a solid tumour to chemotherapy: biological insights from a hybrid multiscale cellular automaton model. *Journal of Theoretical Biology*, 308(1):1–19, 2012b.
- M. Pressley, M. Salvioli, D. B. Lewis, C. L. Richards, J. S. Brown, and K. Staňková. Evolutionary dynamics of treatment-induced resistance in cancer informs understanding of rapid evolution in natural systems. *Frontiers in Ecology and Evolution*, 9:460, 2021.
- L. Preziosi and A. Tosin. Multiphase and multiscale trends in cancer modelling. *Mathematical Modelling of Natural Phenomena*, 4(3):1–11, 2009.
- K. Proulx, A. Lu, and S. Sumanas. Cranial vasculature in zebrafish forms by angioblast cluster-derived angiogenesis. *Developmental Biology*, 348(1):34–46, 2010. ISSN 1095564X.

- G. Qian and A. Mahdi. Sensitivity analysis methods in the biomedical sciences. *Mathematical Biosciences*, 323:108306, 2020.
- N. Rahimi. The ubiquitin-proteasome system meets angiogenesis. *Molecular Cancer Therapeutics*, 11(3):538–548, 2012.
- J. R. Ramos, R. Travasso, and J. Carvalho. Capillary network formation from dispersed endothelial cells: Influence of cell traction, cell adhesion, and extracellular matrix rigidity. *Physical Review E*, 97(1):012408, 2018.
- A. Rauff, S. A. Labelle, H. A. Strobel, J. B. Hoying, and J. A. Weiss. Imaging the dynamic interaction between sprouting microvessels and the extracellular matrix. *Frontiers in Physiology*, 10:1011, 2019. ISSN 1664042X.
- M. Renardy, C. Hult, S. Evans, J. J. Linderman, and D. E. Kirschner. Global sensitivity analysis of biological multiscale models. *Current Opinion in Biomedical Engineering*, 11:109–116, 2019.
- S. H. Rice. *Evolutionary theory: mathematical and conceptual foundations*. Sinauer Associates Sunderland, MA, 2004.
- W. Risau and I. Flamme. Vasculogenesis. *Annual Review of Cell and Developmental Biology*, 11(1):73–91, 1995.
- K. Roberts, B. Alberts, A. Johnson, P. Walter, and T. Hunt. Molecular biology of the cell. New York: Garland Science, 32(2), 2002.
- M. Robertson-Tessi, R. J. Gillies, R. A. Gatenby, and A. R. A. Anderson. Impact of metabolic heterogeneity on tumor growth, invasion, and treatment outcomes. *Cancer Research*, 75(8):1567–1579, 2015.
- W. D. Roche and H. J. Norris. Microinvasive carcinoma of the cervix the significance of lymphatic invasion and confluent patterns of stromal growth. *Cancer*, 36(1):180–186, 1975.
- S. Romero-Garcia, J. S. Lopez-Gonzalez, J. L. B’ez Viveros, D. Aguilar-Cazares, and H. Prado-Garcia. Tumor cell metabolism: an integral view. *Cancer Biology & Therapy*, 12(11):939–948, 2011.
- D. B. Rubin, E. A. Drab, and K. D. Bauer. Endothelial cell subpopulations in vitro: Cell volume, cell cycle, and radiosensitivity. *Journal of Applied Physiology*, 67(4):1585–1590, 1989. ISSN 01617567.
- S. M. Ruggiero, M. R. Pilvankar, and A. N. Ford Versypt. Mathematical Modeling of Tuberculosis Granuloma Activation. *Processes*, 5(4):79, 2017.

- E. Ruoslahti et al. Integrins. *The Journal of Clinical Investigation*, 87(1):1–5, 1991.
- F. R. Sabin. Origin and development of the primitive vessels of the chick and of the pig. *Contributions to Embryology*, 6:61–124, 1917.
- S. Saffarian, I. E. Collier, B. L. Marmer, E. L. Elson, and G. Goldberg. Interstitial collagenase is a Brownian ratchet driven by proteolysis of collagen. *Science*, 306(5693):108–111, 2004.
- A. Saltelli and P. Annoni. How to avoid a perfunctory sensitivity analysis. *Environmental Modelling & Software*, 25(12):1508–1517, 2010.
- A. Saltelli, K. Aleksankina, W. Becker, P. Fennell, F. Ferretti, N. Holst, S. Li, and Q. Wu. Why so many published sensitivity analyses are false: A systematic review of sensitivity analysis practices. *Environmental Modelling & Software*, 114:29–39, 2019.
- J. Sandoval and M. Esteller. Cancer epigenomics: beyond genomics. *Current Opinion in Genetics & Development*, 22(1):50–55, 2012.
- D. Sasaki, H. Nakajima, Y. Yamaguchi, R. Yokokawa, S.-I. Ei, and T. Miura. Mathematical modeling for meshwork formation of endothelial cells in fibrin gels. *Journal of Theoretical Biology*, 429(1):95–104, 2017.
- S. Schuh, J. Holmes, M. Ulrich, L. Themstrup, G. B. Jemec, N. De Carvalho, G. Pellacani, and J. Welzel. Imaging blood vessel morphology in skin: dynamic optical coherence tomography as a novel potential diagnostic tool in dermatology. *Dermatology and Therapy*, 7(2):187–202, 2017.
- M. Scianna and L. Preziosi. *Cellular Potts Models: Multiscale Extensions and Biological Applications*. CRC Press, 2013.
- M. Scianna, L. Munaron, and L. Preziosi. A multiscale hybrid approach for vasculogenesis and related potential blocking therapies. *Progress in Biophysics and Molecular Biology*, 106(2):450–462, 2011.
- M. Scianna, C. G. Bell, and L. Preziosi. A review of mathematical models for the formation of vascular networks. *Journal of Theoretical Biology*, 333(1):174–209, 2013.
- J. G. Scott, A. G. Fletcher, A. R. A. Anderson, and P. K. Maini. Spatial metrics of tumour vascular organisation predict radiation efficacy in a computational model. *PLoS Computational Biology*, 12(1):e1004712, 2016.
- G. L. Semenza. Targeting HIF-1 for cancer therapy. *Nature Reviews Cancer*, 3(10):721, 2003.

- G. L. Semenza. HIF-1: upstream and downstream of cancer metabolism. *Current Opinion in Genetics & Development*, 20(1):51–56, 2010.
- S. Sen, A. J. Engler, and D. E. Discher. Matrix strains induced by cells: computing how far cells can feel. *Cellular and Molecular Bioengineering*, 2(1):39–48, 2009.
- G. Serini, D. Ambrosi, E. Giraudo, A. Gamba, L. Preziosi, and F. Bussolino. Modeling the early stages of vascular network assembly. *The EMBO Journal*, 22(8):1771–1779, 2003.
- X. Serra-Picamal, V. Conte, R. Vincent, E. Anon, D. T. Tambe, E. Bazellieres, J. P. Butler, J. J. Fredberg, and X. Trepat. Mechanical waves during tissue expansion. *Nature Physics*, 8(8):628–634, 2012.
- M. R. Servedio, Y. Brandvain, S. Dhole, C. L. Fitzpatrick, E. E. Goldberg, C. A. Stern, J. Van Cleve, and D. J. Yeh. Not just a theory—the utility of mathematical models in evolutionary biology. *PLoS Biology*, 12(12), 2014.
- M. A. Shah and G. K. Schwartz. Cell cycle-mediated drug resistance: an emerging concept in cancer therapy. *Clinical Cancer Research*, 7(8):2168–2181, 2001.
- A. M. Shannon, D. J. Bouchier-Hayes, C. M. Condron, and D. Toomey. Tumour hypoxia, chemotherapeutic resistance and hypoxia-related therapies. *Cancer Treatment Reviews*, 29(4):297–307, 2003.
- C. E. Shannon. A mathematical theory of communication. *Bell System Technical Journal*, 27(3):379–423, 1948.
- J. A. Sherratt, S. A. Gourley, N. J. Armstrong, and K. J. Painter. Boundedness of solutions of a non-local reaction–diffusion model for adhesion in cell aggregation and cancer invasion. *European Journal of Applied Mathematics*, 20(1):123–144, 2009.
- Q. Shi, S. Rafii, M. H.-D. Wu, E. S. Wijelath, C. Yu, A. Ishida, Y. Fujita, S. Kothari, R. Mohle, L. R. Sauvage, and Others. Evidence for circulating bone marrow-derived endothelial cells. *Blood, The Journal of the American Society of Hematology*, 92(2):362–367, 1998.
- T. Shiomi and Y. Okada. MT1-MMP and MMP-7 in invasion and metastasis of human cancers. *Cancer and Metastasis Reviews*, 22(2-3):145–152, 2003.
- E. H. Simpson. Measurement of diversity. *Nature*, 163(4148):688, 1949.
- M. J. Simpson and R. E. Baker. Corrected mean-field models for spatially dependent advection-diffusion-reaction phenomena. *Physical Review E*, 83(5):051922, 2011.

- J. Singh, F. Hussain, and P. Decuzzi. Role of differential adhesion in cell cluster evolution: from vasculogenesis to cancer metastasis. *Computer Methods in Biomechanics and Biomedical Engineering*, 18(3):282–292, 2015. ISSN 14768259.
- J. T. Smith, J. K. Tomfohr, M. C. Wells, T. P. Beebe, T. B. Kepler, and W. M. Reichert. Measurement of cell migration on surface-bound fibronectin gradients. *Langmuir*, 20(19):8279–8286, 2004.
- J. G. Snedeker, P. Niederer, F. Schmidlin, M. Farshad, C. Demetropoulos, J. Lee, and K. Yang. Strain-rate dependent material properties of the porcine and human kidney capsule. *Journal of Biomechanics*, 38(5):1011–1021, 2005.
- R. E. Stace, T. Stiehl, M. A. J. Chaplain, A. Marciniak-Czochra, and T. Lorenzi. Discrete and continuum phenotype-structured models for the evolution of cancer cell populations under chemotherapy. *Mathematical Modelling of Natural Phenomena*, 15:14, 2020.
- K. Staňková, J. S. Brown, W. S. Dalton, and R. A. Gatenby. Optimizing cancer treatment using game theory: A review. *JAMA Oncology*, 5(1):96–103, 2019.
- K. R. Stenmark, E. Gerasimovskaya, R. A. Nemenoff, and M. Das. Hypoxic activation of adventitial fibroblasts: role in vascular remodeling. *Chest*, 122(6):326S–334S, 2002.
- A. Stevens. The derivation of chemotaxis equations as limit dynamics of moderately interacting stochastic many-particle systems. *SIAM Journal on Applied Mathematics*, 61(1):183–212, 2000.
- A. Stevens and H. G. Othmer. Aggregation, blowup, and collapse: the ABC’s of taxis in reinforced random walks. *SIAM Journal on Applied Mathematics*, 57(4):1044–1081, 1997.
- T. Stiehl, N. Baran, A. D. Ho, and A. Marciniak-Czochra. Clonal selection and therapy resistance in acute leukaemias: mathematical modelling explains different proliferation patterns at diagnosis and relapse. *Journal of The Royal Society Interface*, 11(94):20140079, 2014.
- S. Strese, M. Fryknäs, R. Larsson, and J. Gullbo. Effects of hypoxia on human cancer cell line chemosensitivity. *BMC Cancer*, 13(1):331, 2013.
- C. Streuli. Extracellular matrix remodelling and cellular differentiation. *Current Opinion in Cell Biology*, 11(5):634–640, 1999.
- R. Sullivan, G. C. Pare, L. J. Frederiksen, G. L. Semenza, and C. H. Graham. Hypoxia-induced resistance to anticancer drugs is associated with decreased senescence and requires hypoxia-inducible factor-1 activity. *Molecular Cancer Therapeutics*, 7(7):1961–1973, 2008.

- X.-x. Sun and Q. Yu. Intra-tumor heterogeneity of cancer cells and its implications for cancer treatment. *Acta Pharmacologica Sinica*, 36(10):1219, 2015.
- H. Sung, J. Ferlay, R. L. Siegel, M. Laversanne, I. Soerjomataram, A. Jemal, and F. Bray. Global cancer statistics 2020: GLOBOCAN estimates of incidence and mortality worldwide for 36 cancers in 185 countries. *CA: a Cancer Journal for Clinicians*, 71(3):209–249, 2021.
- A. Szabó and A. Czirók. The role of cell-cell adhesion in the formation of multicellular sprouts. *Mathematical Modelling of Natural Phenomena*, 5(1):106–122, 2010.
- A. Szabo, E. D. Perryn, and A. Czirok. Network formation of tissue cells via preferential attraction to elongated structures. *Physical Review Letters*, 98(3):038102, 2007.
- A. Szabo, E. Mehes, E. Kosa, and A. Czirok. Multicellular sprouting in vitro. *Biophysical Journal*, 95(6):2702–2710, 2008.
- I. Tannock. The relation between cell proliferation and the vascular system in a transplanted mouse mammary tumour. *British Journal of Cancer*, 22(2):258, 1968.
- O. M. Tepper, J. M. Capla, R. D. Galiano, D. J. Ceradini, M. J. Callaghan, M. E. Kleinman, and G. C. Gurtner. Adult vasculogenesis occurs through in situ recruitment, proliferation, and tubulization of circulating bone marrow-derived cells. *Blood*, 105(3):1068–1077, 2005. ISSN 00064971.
- V. P. Terranova, R. DiFlorio, R. M. Lyall, S. Hic, R. Friesel, and T. Maciag. Human endothelial cells are chemotactic to endothelial cell growth factor and heparin. *Journal of Cell Biology*, 101(6):2330–2334, 1985. ISSN 15408140.
- D. W. Thompson. *On growth and form*. Cambridge University Press, Cambridge, 1917.
- S. Tlili, E. Gauquelin, B. Li, O. Cardoso, B. Ladoux, H. Delanoë-Ayari, and F. Graner. Collective cell migration without proliferation: density determines cell velocity and wave velocity. *Royal Society Open Science*, 5(5):172421, 2018.
- C. J. Tomlin and J. D. Axelrod. Biology by numbers: mathematical modelling in developmental biology. *Nature Reviews Genetics*, 8(5):331–340, 2007.
- A. Tosin, D. Ambrosi, and L. Preziosi. Mechanics and chemotaxis in the morphogenesis of vascular networks. *Bulletin of Mathematical Biology*, 68(7):1819–1836, 2006.
- L. Tranqui and P. Tracqui. Mechanical signalling and angiogenesis. the integration of cell-extracellular matrix couplings. *Comptes Rendus de l'Académie des Sciences-Series III-Sciences de la Vie*, 323(1):31–47, 2000.

- R. T. Tranquillo and J. D. Murray. Continuum model of fibroblast-driven wound contraction: inflammation-mediation. *Journal of Theoretical Biology*, 158(2):135–172, 1992.
- A.-M. Tsimerman. Targeted therapy in cancer. *Cancer Chemotherapy and Pharmacology*, 76(6):1113–1132, 2015.
- A. M. Turing. The chemical basis of morphogenesis. *Philosophical Transactions of the Royal Society of London B*, 237:37–72, 1952.
- S. Turner and J. A. Sherratt. Intercellular adhesion and cancer invasion: a discrete simulation using the extended potts model. *Journal of Theoretical Biology*, 216(1):85–100, 2002.
- S. Turner, J. A. Sherratt, K. J. Painter, and N. J. Savill. From a discrete to a continuous model of biological cell movement. *Physical Review E*, 69(2):021910, 2004.
- P. K. Upputuri, K. Sivasubramanian, C. S. K. Mark, and M. Pramanik. Recent developments in vascular imaging techniques in tissue engineering and regenerative medicine. *BioMed Research International*, 2015, 2015.
- S. Urdy. On the evolution of morphogenetic models: mechano-chemical interactions and an integrated view of cell differentiation, growth, pattern formation and morphogenesis. *Biological Reviews*, 87(4):786–803, 2012.
- P. Vajkoczy, S. Blum, M. Lamparter, R. Mailhammer, R. Erber, B. Engelhardt, D. Vestweber, and A. K. Hatzopoulos. Multistep nature of microvascular recruitment of ex vivo-expanded embryonic endothelial progenitor cells during tumor angiogenesis. *Journal of Experimental Medicine*, 197(12):1755–1765, 2003. ISSN 00221007.
- D. Valtorta and E. Mazza. Dynamic measurement of soft tissue viscoelastic properties with a torsional resonator device. *Medical Image Analysis*, 9(5):481–490, 2005.
- S. Van Helvert, C. Storm, and P. Friedl. Mechanoreciprocity in cell migration. *Nature Cell Biology*, 20(1):8–20, 2018.
- R. F. van Oers, E. G. Rens, D. J. LaValley, C. A. Reinhart-King, and R. M. Merks. Mechanical cell-matrix feedback explains pairwise and collective endothelial cell behavior in vitro. *PLoS Computational Biology*, 10(8):e1003774, 2014.
- M. G. Vander Heiden, L. C. Cantley, and C. B. Thompson. Understanding the Warburg effect: the metabolic requirements of cell proliferation. *Science*, 324(5930):1029–1033, 2009.

- A. Vartanian, S. K. Singh, S. Agnihotri, S. Jalali, K. Burrell, K. D. Aldape, and G. Zadeh. GBM's multifaceted landscape: highlighting regional and microenvironmental heterogeneity. *Neuro-Oncology*, 16(9):1167–1175, 2014.
- P. Vaupel. Tumor microenvironmental physiology and its implications for radiation oncology. *Seminars in Radiation Oncology*, 14(3):198–206, 2004.
- P. Vaupel, F. Kallinowski, and P. Okunieff. Blood flow, oxygen and nutrient supply, and metabolic microenvironment of human tumors: a review. *Cancer Research*, 49(23):6449–6465, 1989.
- J. Vera, C. Lischer, M. Nenov, S. Nikolov, X. Lai, and M. Eberhardt. Mathematical modelling in biomedicine: A primer for the curious and the skeptic. *International Journal of Molecular Sciences*, 22(2):547, 2021.
- C. Verdier. Rheological properties of living materials. From cells to tissues. *Computational and Mathematical Methods in Medicine*, 5(2):67–91, 2003.
- D. Vestweber, M. Winderlich, G. Cagna, and A. F. Nottebaum. Cell adhesion dynamics at endothelial junctions: VE-cadherin as a major player. *Trends in Cell Biology*, 19(1):8–15, 2009.
- C. Villa, M. A. Chaplain, A. Gerisch, and T. Lorenzi. Mechanical models of pattern and form in biological tissues: The role of stress–strain constitutive equations. *Bulletin of Mathematical Biology*, 83(7):1–38, 2021a.
- C. Villa, M. A. Chaplain, and T. Lorenzi. Evolutionary dynamics in vascularised tumours under chemotherapy: Mathematical modelling, asymptotic analysis and numerical simulations. *Vietnam Journal of Mathematics*, 49(1):143–167, 2021b.
- C. Villa, M. A. Chaplain, and T. Lorenzi. Modeling the emergence of phenotypic heterogeneity in vascularized tumors. *SIAM Journal on Applied Mathematics*, 81(2):434–453, 2021c.
- C. Villa, A. Gerisch, and M. A. Chaplain. A novel nonlocal partial differential equation model of endothelial progenitor cell cluster formation during the early stages of vasculogenesis. *Journal of Theoretical Biology*, 534(1):110963, 2022.
- P. Villa Martín, M. A. Muñoz, and S. Pigolotti. Bet-hedging strategies in expanding populations. *PLoS Computational Biology*, 15(4):e1006529, 2019.
- C. Waddington. The Strategy of the Genes, 1957.

- S. E. Wang, P. Hinow, N. Bryce, A. M. Weaver, L. Estrada, C. L. Arteaga, and G. F. Webb. A mathematical model quantifies proliferation and motility effects of TGF- $\beta$  on cancer cells. *Computational and Mathematical Methods in Medicine*, 10(1):71–83, 2009.
- J. P. Ward and J. King. Mathematical modelling of avascular-tumour growth. *Mathematical Medicine and Biology: A Journal of the IMA*, 14(1):39–69, 1997.
- M. Wartenberg, F. C. Ling, M. Möschel, F. Klein, H. Acker, M. Gassmann, K. Petrat, V. Pütz, J. Hescheler, and H. Sauer. Regulation of the multidrug resistance transporter P-glycoprotein in multicellular tumor spheroids by hypoxia-inducible factor (HIF-1) and reactive oxygen species. *The FASEB Journal*, 17(3):503–505, 2003.
- R. A. Weinberg. *The biology of cancer*. Garland science, 2013.
- R. Weiner, B. A. Schmitt, and H. Podhaisky. ROWMAP—a ROW-code with Krylov techniques for large stiff ODEs. *Applied Numerical Mathematics*, 25(2-3):303–319, 1997.
- K. Wolf and P. Friedl. Extracellular matrix determinants of proteolytic and non-proteolytic cell migration. *Trends in Cell Biology*, 21(12):736–744, 2011.
- B. Wölf, H. te Rietmole, M. Salvioli, A. Kaznatcheev, F. Thuijsman, J. S. Brown, B. Burgering, and K. Staňková. The contribution of evolutionary game theory to understanding and treating cancer. *Dynamic Games and Applications*, pages 1–30, 2021.
- H.-C. Wu, D.-K. Chang, and C.-T. Huang. Targeted therapy for cancer. *Journal of Cancer Molecules*, 2(2):57–66, 2006.
- T. A. Yap, M. Gerlinger, P. A. Futreal, L. Pusztai, and C. Swanton. Intratumor heterogeneity: seeing the wood for the trees. *Science Translational Medicine*, 4(127):127ps10–127ps10, 2012.
- P. L. Yeagle. *The membranes of cells*. Academic Press, 2016.
- P. Yen, S. D. Finley, M. O. Engel-Stefanini, and A. S. Popel. A two-compartment model of VEGF distribution in the mouse. *PloS One*, 6(11):e27514, 2011.
- J. Zhang, J. J. Cunningham, J. S. Brown, and R. A. Gatenby. Integrating evolutionary dynamics into treatment of metastatic castrate-resistant prostate cancer. *Nature Communications*, 8(1):1–9, 2017.
- M. Zhang, J. Rehman, and A. B. Malik. Endothelial progenitor cells and vascular repair. *Current Opinion in Hematology*, 21(3):224, 2014.

Y. Zhao, E. B. Butler, and M. Tan. Targeting cellular metabolism to improve cancer therapeutics. *Cell Death & Disease*, 4(3):e532, 2013.